Institut de Physique de l'Université de Neuchâtel

The Hubbard Model with Attractive Nearest Neighbor Interaction

Thèse présentée à la Faculté des Sciences
de l'Université de Neuchâtel
pour l'obtention du grade de docteur ès sciences

par

Thomas F. Meintrup
Physician diplôme de l'Université de Heidelberg/Allemagne

Commitée
Prof. Dr. H. Beck
Prof. Dr. T. Schneider
Prof. Dr. P. F. Meier
Prof. Dr. P. Martinoli

Neuchâtel 1995

IMPRIMATUR POUR LA THÈSE

The Hubbard model with attractive nearest-neighbor interaction

de M. Thomas Meintrup

UNIVERSITÉ DE NEUCHÂTEL

FACULTÉ DES SCIENCES

La Faculté des sciences de l'Université de Neuchâtel sur le rapport des membres du jury,

Messieurs H. Beck, P. Martinoli, T. Schneider (IBM, Rüschlikon) et P. Meier (Zürich)

autorise l'impression de la présente thèse.

Neuchâtel, le 21 novembre 1995

Le doyen:

R. Dändliker

The Hubbard Model with Attractive Nearest Neighbor Interaction

Thèse pour l'obtention du grade de docteur ès sciences par Thomas F. Meintrup

Commitée:

Prof. Dr. H. Beck, Prof. Dr. P. Martinoli

Université de Neuchâtel, CH-6000 Neuchâtel

Prof. Dr. T. Schneider

IBM Zürich Research Laboratory, CH-8803 Rüschlikon

Prof. Dr. P. F. Meier

Université de Zürich, CH-8057 Zürich

for Beate

Contents

List of Figures

List of Tables

Chapter 1

Introduction

Although this work is trying to approach the field of high temperature superconductivity, we do not want to begin the introduction with

Since the discovery of high temperature superconductivity by Muller and Bednorz...

as many of the publications in this field. Nevertheless the fundamental work of Muller and Bednorz [Bednorz86] needs to be mentioned, because it caused a tremendous wave of experimental and theoretical effort in order to understand these materials, in particular in comparison to the well known conventional superconductors. Questions about the role of antiferromagnetic fluctuations, the pairing mechanism and the symmetry of the superconducting order parameter are currently of great interest. But it is not only the field of high temperature superconductivity that we are interested in and that this work is dealing with, it is also the more general problem of the interplay, competition or coexistence of different types of order in highly correlated electron systems. In fact, the competition of antiferromagnetism and superconductivity, or charge order and superconductivity plays an important role in high temperature superconductivity. The coexistence of antiferromagnetism and superconductivity is also of interest in the framework of heavy fermion superconductors. However, this work is mainly focused on the features of copper oxide materials. Nevertheless, some of the results might also be applicable to heavy fermion compounds. Starting from a tight binding model with attractive nearest neighbor singlet pairing interaction, which we have called the NNSP model, we derive the phase diagram of high temperature superconductors, including both their antiferromagnetic and superconducting properties. For the first time their phase diagram can be qualitatively reproduced starting from a simple semi–microscopical model. This causes some implications, such as the unconventional character of the superconducting order parameter with d– or extended s–wave (xs–wave) symmetry, which is in contrast to the classical BCS–superconductors.

Moreover, the normal state behavior is strongly influenced by antiferromagnetic correlations. However, we do not want to anticipate any results before the model has been defined and motivated, which is the aim of this introductory chapter. In section 1.1, some basic features of high temperature superconductors are summarized, which are used in section 1.2 to motivate the NNSP model. In section 1.3, two extreme limits are discussed: the free case and the "atomic" limit. Both limits show the metallic, and on the other hand, the antiferromagnetic and insulating features of the NNSP model. The last section 1.4 presents an overview of this dissertation.

1.1 High Temperature Superconductivity

The most astonishing point of high temperature superconductors is their transition temperature into the superconducting state. It ranges from 24 K for the $(Nd, Ce)_2CuO_{4-\delta}$-compounds [Tokura89] up to 125 K for $Tl_2Ba_2Ca_3Cu_4O_{10}$ [Cox88]. A common feature of high temperature superconductors is their extremely anisotropic structure including CuO_2 layers as their main components. It is widely accepted that the electronic activity takes place within these layers. For this reason they are often called copper–oxide superconductors. Their phase diagram is another common feature. A generic phase diagram is shown in figure 1.1 , where δ is the hole concentration in the CuO_2 planes and T the temperature. The left–hand side for $\delta = 0$ corresponds to the undoped or parent material, such as $YBa_2Cu_3O_6$ [Jorgensen90] or La_2CuO_4 [Bednorz86, Jorgensen87]. They are insulating and show antiferromagnetic long–range order and no superconductivity. In these materials, the copper ions in the CuO_2 planes are in a Cu^{2+} state with a $Cu(3d^9)$ electronic configuration, which corresponds to a half–filled $d_{x^2-y^2}$ band. From this point of view one should expect a metal, but a strong on–site repulsion splits the band into a lower and an upper Hubbard band [HubbardI, HubbardII, HubbardIII]. In this dissertation, we show that this splitting can also be achieved by a weak singlet nearest neighbor pairing interaction which drives the system into the antiferromagnetic state for half–filling. As the copper–oxide superconductors are doped by cationic substitution ($La_{2-x}Sr_xCuO_4$) or by oxygen intercalation (La_2CuO_{6+y}), the Néel temperature drops very rapidly and they exhibit a metal–insulator transition at $\delta \approx 0.05$. Beyond this threshold the antiferromagnetic long–range order disappears and superconductivity occurs. There is no coexistence of superconductivity and antiferromagnetism like in heavy fermion compounds [Steglich85, Steglich93]. However, it has been shown by NMR [Slichter93, Kitaoka93], angle resolved photoemmission [Aebi94] and inelastic neutron scattering experiments [Birgenau88a, Birgenau88b, Birgenau89a, Birgenau89b], that above and even below the superconducting critical temperature strong antiferromagnetic fluctuations exist for hole concentrations well above the insulator–metal transition line.

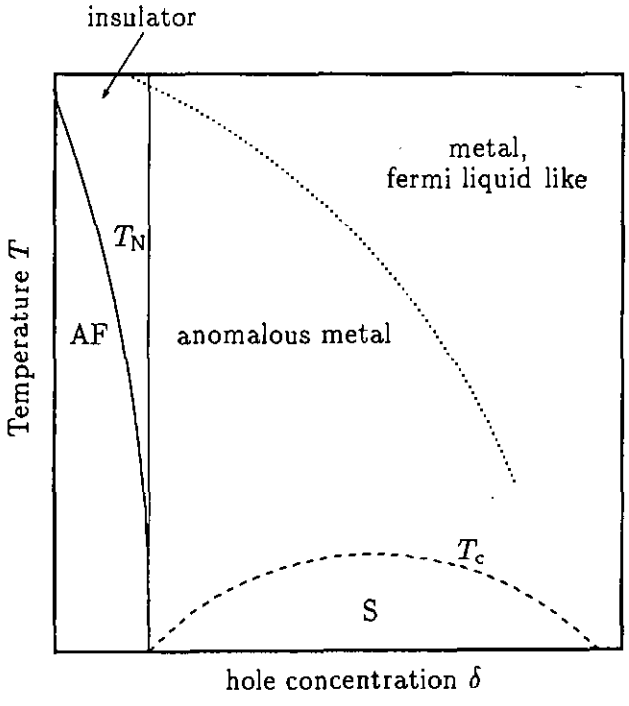

Figure 1.1: Generic phase diagram of high temperature superconductors like the YBaCuO– and LaSrCuO–compounds, where δ is the hole concentration within the CuO_2–planes and T the temperature. The solid curve marks the antiferromagnetic phase boundary, below which antiferromagnetic long range order exists. The dashed curve is the superconducting phase boundary as a function of doping. An insulator–metal transition occurs at $\delta \approx 0.05$, which is indicated by the thin vertical line. The dotted curve marks the area below which short range antiferromagnetic fluctuations are important and control the normal state behavior.

These fluctuations give rise to a spin gap and are responsible for the anomalous normal state behavior in this regime [Mangelschots92a, Mangelschots92b, Torrence89]. It has been extensively discussed at the workshops on "Phase Separation in Cuprate Superconductors" [PS92, PS93] that these fluctuations are accompanied by an electronic phase separation of antiferromagnetic domains and itinerant electrons, which become superconducting below the transition temperature. The decrease of the Néel temperature is due to the addition of holes which enter predominantly in the oxygen $2p\sigma$ orbitals [Bianconi87, Nucker88, Alloul90] and act in a frustrating way onto the antiferromagnetic exchange coupling between neighboring Cu ions. This leads to a spin–glass phase at low temperatures [Aharony89]. It should be noted, although the holes reside predominantly at the oxygen sites, that there is a strong hybridization between the copper $3d_{x^2-y^2}$ and oxygen $2p\sigma$ orbitals. This has for instance been observed in NMR experiments where the Knight shift and the nuclear relaxation rate for both the Cu and O ions has been compared [Mangelschots92a, Mangelschots92b]. These results show that the electron distribution around the Cu and O sites are similar. For this reason there is no sharp distinction between the electrons in the Cu $3d_{x^2-y^2}$ and O $2p\sigma$ orbitals and single band models are therefore possible [Anderson87]. The superconducting critical temperature first increases with increasing hole concentration, reaches an optimum value at $\delta \approx 0.15$ and finally drops to zero as δ approaches 0.3. Accordingly the region on the left and right hand side of the optimal hole concentration is often called underdoped and overdoped regime, respectively. It is a challenging question why T_c shows this behavior and what the physical origin of it

is. A simple explanation is possible for the model discussed in this work. Comparing the maximum Néel temperature for the undoped material and the optimal superconducting critical temperature, one observes that T_N is about four to six times larger than T_c^{max}. For instance in the case of $YBa_2Cu_2O_6$, the Néel temperature is about $600K$, while the critical temperature for $YBa_2Cu_2O_{6.15}$, which corresponds to optimal doping, is $90K$. Note that for La_2CuO_4, $T_N = 250K$ and $T_c^{max} = 40K$.

Besides the phase diagram and the normal state behavior of high temperature superconductors, there is another important question of interest in current research, which is the origin of the pairing interaction and the symmetry of the superconducting order parameter [Annett90a, Annett90b, Coffey93, Anderson93, Li93, Levi93, Dynes94, Schrieffer94]. There exists strong evidence from NMR experiments [Slichter93] that the pairing state of high temperature superconductors is a spin singlet state. This rules out p–wave pairing with $S = 1$ and $l = 1$, where S is the total spin of the electron pair and l is its relative angular momentum. More generally, only pairing states where l is an even number are allowed. This is, for instance, in contrast to superfluid ^{3}He, where triplet pairing with $S = 1$ and $l = 1$ is the most stable state [Vollhardt90, Mahan90]. The classical superconductors may be well described by the BCS–theory with an effective, attractive electron–electron interaction which originates from electron–phonon coupling and yields an s–wave superconducting order parameter [BCS57], while in heavy fermion superconductors like UPt_3 and UBe_{13} $S = 0$ and $l = 2$ pairing is present [Rice87a, Rice87b, Sigrist91]. For high temperature superconductors, several different experiments have been carried out in order to answer this question. Tunneling experiments which probe the density of states of the quasiparticle excitations show for some materials, such as $YBa_2Cu_3O_{7-\delta}$ [Valles91], a pseudo–gap which is consistent with d–wave pairing. On the other hand, for $Nd_{2-x}Ce_xCuO_4$ [Tralshawala91] or the newly discoverd Hg–compounds [Chen94], a real gap is observed which favors conventional s–wave symmetry. Other materials lie in between those two extreme limits. Measurements of the nuclear relaxation rate in NMR experiments on several copper–oxide superconductors show no coherence peak (Hebel–Slichter–peak) and a power law behavior in the low temperature regime [Kitaoka93, Thelen93]. Both results support d–wave pairing. In addition, angular resolved photoemisson experiments [Shen93, YokoyaPP, Aebi94] might be explained assuming anisotropic d–wave pairing and antiferromagnetic fluctuations. However, from these experiments one cannot clearly distinguish between d–, xs– or a mixed state with $xs + id$–wave symmetry. The SQUID–experiments by Chaudhari and Lin [Chaudhari94] and the single Josephson tunneling experiments by Sun et al. [Sun94] favor a strong s–wave component to the superconducting order parameter, while other SQUID experiments [Wollman93] indicate d–wave pairing. Overall, there is a great controversy about the symmetry of the order parameter in high temperature superconductors. It has been reported that theoretical models which start from antiferromagnetic

fluctuations [Monien90, Pines91, Monthoux91], or assume an antiferromagnetic exchange coupling [Dagotta94, Dagotto90, Liu92] show d–wave superconductivity. From this point of view it seems surprising that, although most of the cuprates apparently are antiferromagnetic insulators in the undoped case and show strong antiferromagnetic fluctuations in the doped region, some of them are d– and others conventional s–wave superconductors. In this dissertation we will show that there is no contradiction between antiferromagnetic pairing interactions and different kinds of symmetries for the superconducting order parameter. We also show that the symmetry might depend on carrier density, temperature and coupling strength. Moreover, we show that even for a pure d–wave superconductor a real gap is possible due to the competition of antiferromagnetism and superconductivity.

There are other experiments which are also important in order to understand the nature of high temperature superconductors. Examples are measurements of the specific heat, Pauli susceptibility, transport experiments or measurements of the upper critical field, to name only a few of them. This work, however, concentrates on the correlations between antiferromagnetic and superconducting order and the symmetry of the superconducting order parameter, which is why the above mentioned experiments are not reported here. Moreover, the experiments described above reveal some basic features which are common properties of nearly all high temperature superconductors and which are used in the next section to introduce and motivate the NNSP model.

1.2 The NNSP Model

The basic characteristics which are shared by most high temperature superconductors can be summarized as follows:

- Extremely anisotropic structure including CuO_2–layers in which the electronic activity takes place.
- Strong hybridization between the Cu $3d_{x^2-y^2}$ and O $2p\sigma$ orbitals.
- The undoped material is an antiferromagnetic insulator.
- An insulator–metal transition occurs at low carrier densities.
- Strong antiferromagnetic fluctuations exist well beyond the insulator–metal transition line.
- The superconducting critical temperature depends on doping, shows an optimal value at $\delta \approx 0.15$ and vanishes for $\delta < 0.05$ and $\delta > 0.3$.

- The electron pairing in the superconducting state is of singlet type.

These features should somehow be incorporated in any realistic model for copper oxide superconductors [Dynes94]. Some of them can be used to define the model, others must be derived and explained. For the NNSP model, the layered structure, the strong hybridization, the essential role of antiferromagnetic correlations and the existence of superconductivity of singlet type can be considered as the starting points. In fact, from the first point follows that high temperature superconductors can be treated as quasi two-dimensional systems. The second point shows that the antiferromagnetic electrons and the superconducting holes or electrons form one band, so that a unit cell of a CuO_2-plane can be considered as one site of a square lattice. Moreover, it suggests a tight-binding description. Finally in order to allow for antiferromagnetic fluctuations and singlet superconductivity, a singlet pairing interaction between nearest neighbors is assumed. Combining this, the Hamiltonian of the NNSP model then reads in particle number representation in real space [Negele88]:

$$\mathcal{H} = \sum_{i,j,\sigma} t_{ij} c^{\dagger}_{i\sigma} c_{j\sigma} + \sum_{i,j} W_{ij} n_{i\uparrow} n_{j\downarrow} - \mu \sum_{i} (n_{i\uparrow} + n_{i\downarrow}) \quad , \tag{1.1}$$

where $c^{\dagger}_{i\sigma}$ creates and $c_{i\sigma}$ destroys an electron with spin σ at site i and $n_{i\sigma} = c^{\dagger}_{i\sigma} c_{i\sigma}$. The term t_{ij} is the hopping integral between site i and site j. It is spin independent and incorporates the kinetic energy of the electrons as well as the electron lattice interaction [HubbardI]. For this reason it is usually negative. Here we will assume $t_{ij} = -t$ $(t > 0)$ for i and j on neighboring lattice sites and $t_{ij} = 0$ otherwise. The implications of next nearest neighbor hopping is briefly discussed in the last chapter of this dissertation. The interaction term is assumed to be an attractive nearest neighbor interacion with $W_{ij} = W$ $(W < 0)$. The last term in the Hamiltonian above accounts for a grand canonicle description which is used throughout the entire dissertation and is therefore added to the Hamiltonian. μ represents the chemical potential determined selfconistently from

$$n = \frac{1}{L} \sum_{i} \langle n_{i\uparrow} + n_{i\downarrow} \rangle \quad , \tag{1.2}$$

which is the mean electron density per unit cell. As most of the properties of high temperature superconductors are controlled by the number of carriers per unit cell measured from half-filling, this quantity is, besides W, the most important parameter. The hopping parameter t is used as energy unit, i. e. the coupling constant, temperature and all other energies are measured in units of t.

The NNSP model is a special case of the extended Hubbard model with attractive, spin independent nearest neighbor interaction [Micnas88a, Micnas88b], which can be written

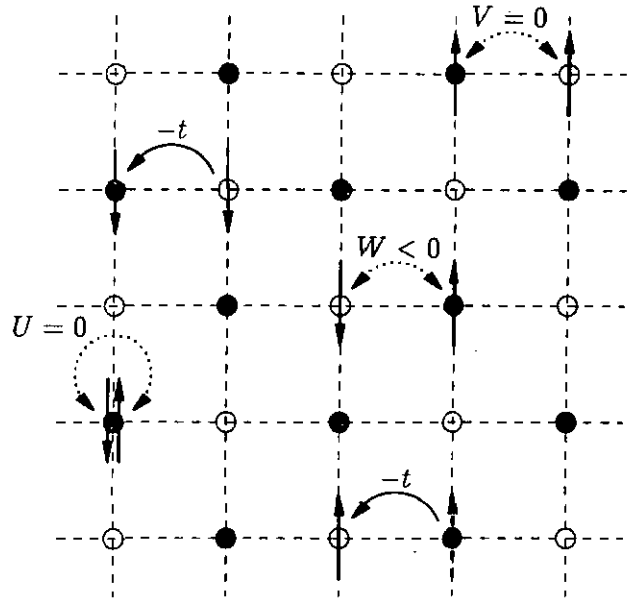

Figure 1.2: Hopping and interaction of the NNSP model in two dimensions. The filled • and open ○ circles define the sublattices A and B, respectively. The solid arrows ↑ and ↓ represent electrons with either spin up or spin down, while a dashed arrow marks a previous site of an electron. t is the hopping amplitude and W the nearest neighbor pairing interaction. Both, onsite repulsion U and nearest neighbor interaction between electrons of equal spin are assumed to be zero within the NNSP model.

as follows:

$$H = \sum_{i,j,\sigma} t_{ij} c^{\dagger}_{i\sigma} c_{j\sigma} + U \sum_{i} n_{i\uparrow} n_{i\downarrow} + V \sum_{i,j} n_{i\uparrow} n_{j\uparrow} + W \sum_{i,j} n_{i\uparrow} n_{j\downarrow} - \mu \sum_{i} (n_{i\uparrow} + n_{i\downarrow}) \tag{1.3}$$

with $V = W$, $U \geq 0$ and $V, W \leq 0$. From this point of view, the NNSP model corresponds to $U = 0$ and $V = 0$ which is shown in figure 1.2, where the hopping and interaction terms are visualized on a two–dimensional square lattice. The white and black nodes are the neighboring sites of the lattice. An up(down)–arrow symbolizes an electron with spin up(down). A dashed arrow signals a previous site of an electron. Accordingly the hopping term connects a dashed arrow at one site with an arrow of the same direction at one of its neighboring sites, while the interaction terms are given by nondirected relations between electrons of different spin at the same site (U–term), of equal spin at neighboring sites (V–term) and of opposite spin at neighboring sites (W–term). Only the W–term is included in the NNSP model.

The Hamiltonian in equation (1.1) is valid for any dimension. In fact, most of the general results are derived independently of dimension or can easily be generalized. To take the layered structure of the copper oxide materials into account, the two–dimensional case is assumed for the numerical calculations. This is a somewhat dangerous assumption because of the nonexistence of long–range order in strictly two–dimensional quantummechanical systems [Hohenberg67, Binney92, Nolting86]. A brief discussion on this issue is presented in chapter 8.

Although the real–space representation of the Hamiltonian of the NNSP model in equation (1.1) yields a better visualization of the meaning of the hopping and interaction

terms, its Fourier representation is often more practical in calculations. The following transformation rules are used:

$$c_{k\sigma} = \frac{1}{\sqrt{L}} \sum_i c_{i\sigma} e^{-ikR_i} \quad (1.4)$$

$$c_{i\sigma} = \frac{1}{\sqrt{L}} \sum_k c_{k\sigma} e^{ikR_i} \quad , \quad (1.5)$$

where L is the lattice size and R_i and k are D–dimensional lattice vectors in real space and Fourier space, respectively. Within the first Brioullin zone, the components of k are given by

$$k_\alpha = \frac{2\pi}{L_\alpha} n_\alpha \quad \text{for} \quad \alpha = 1 \ldots D \quad , \quad (1.6)$$

where L_α is the linear lattice size in dimension α with $\prod_{\alpha=1}^{D} L_\alpha = L$ and n_α is an integral number in the range

$$-\frac{L_\alpha}{2} \leq n_\alpha \leq \frac{L_\alpha}{2} \quad . \quad (1.7)$$

The Fourier representation of the NNSP model now reads

$$\mathcal{H} = \sum_{k\sigma} (\epsilon_k - \mu) n_{k\sigma} + \frac{zW}{L} \sum_{kk'q} S(q) c^\dagger_{k+q\uparrow} c_{k\uparrow} c^\dagger_{k'-q\downarrow} c_{k'\downarrow} \quad , \quad (1.8)$$

where $z = 2D$ is the number of nearest neighbors. The tight–binding band energy ϵ_k is given by

$$\epsilon_k = -2t \sum_{\alpha=1}^{D} \cos(k_\alpha) \quad (1.9)$$

and the nearest neighbor structure factor for the interaction term is

$$S(q) = \frac{1}{z} \sum_{\alpha=1}^{z} e^{iq\delta_\alpha} \quad (1.10)$$

$$= \frac{1}{D} \sum_{\alpha=1}^{D} \cos(q_\alpha) \quad , \quad (1.11)$$

where δ_α is a relative lattice vector pointing to one of the z nearest neighbors of each lattice point. Comparing both representations, it becomes obvious that it is advantageous to work in Fourier space in the weak coupling regime, because the hopping term is diagonal, and to use the real space representation, where the interaction term is diagonal, in the strong coupling limit.

Related models have been extensively studied in the past. Schneider et al. [Schneider89, Schneider90a, Schneider90b, Frick90] considered a three–dimensional layered model with anisotropic hopping and attractive nearest neighbor pairing interaction like in the NNSP model. In their approach they modelled the crystal structure of high temperature superconductors in a superior way than just assuming a two–dimensional lattice, but they entirely neglect the antiferromagnetic implications of the nearest neighbor interaction. Accordingly their interpretations are misleading. Teubel et al. [Teubel90], who have studied the NNSP model from a functional integral point of view, neglect the antiferromagnetic component, too. The trio Micnas, Robaszkiewicz and Ranninger have studied the extended Hubbard model as it is given in equation (1.3) ([Micnas88a, Micnas88b, Micnas89, Micnas90], [Robaszkiewicz81a] – [Robaszkiewicz81d], [Robaszkiewicz82]). Although they discussed the antiferromagnetic instability, they did not take the competition between superconductivity and antiferromagnetism into account. For this reason their results indeed show the importance of the antiferromagnetic component but are still wrong, especially in the neighborhood of half–filling. It is one of the major points of this work to show that the interplay between antiferromagnetic and superconducting correlations cannot be neglected. Moreover, it is precisely its incorporation that leads to results which are comparable to the real world of high temperature superconductors.

A semi–phenomenological approach to the relation of antiferromagnetic fluctuations and superconductivity in copper oxide compounds has been presented by Monthoux and Pines [Pines91, Monthoux91]. They start from experimental data for the spin susceptibility which shows a peak at the antiferromagnetic reciprocal lattice vector $Q = (\pi, \pi)$ and model an effective quasiparticle interaction mediated by antiferromagnetic spin fluctuations [Monthoux91]. They perform both a weak coupling calculation using the BCS approach [Monthoux92a, Leggett75] and a strong coupling treatment using the Eliashberg formalism [Monthoux92b, Monthoux93, Eliashberg60]. Both calculations lead to superconductivity with d–wave symmetry. Moreover, the incorporation of lifetime effects and a selfconsistent calculation of the chemical potential in the Eliashberg approach leads to results which are comparable to those measured for $YBa_2Cu_3O_7$. Nevertheless, they were neither able to derive a doping–dependent phase diagram including both the antiferromagnetic and superconducting properties of the copper oxide materials, nor to explain their results from a microscopical point of view.

1.3 Two Extreme Limits

Two limits of the NNSP model can be exactly solved, the free case ($W = 0$) and the "atomic" limit ($t = 0$). Both cases show two different and somehow excluding properties,

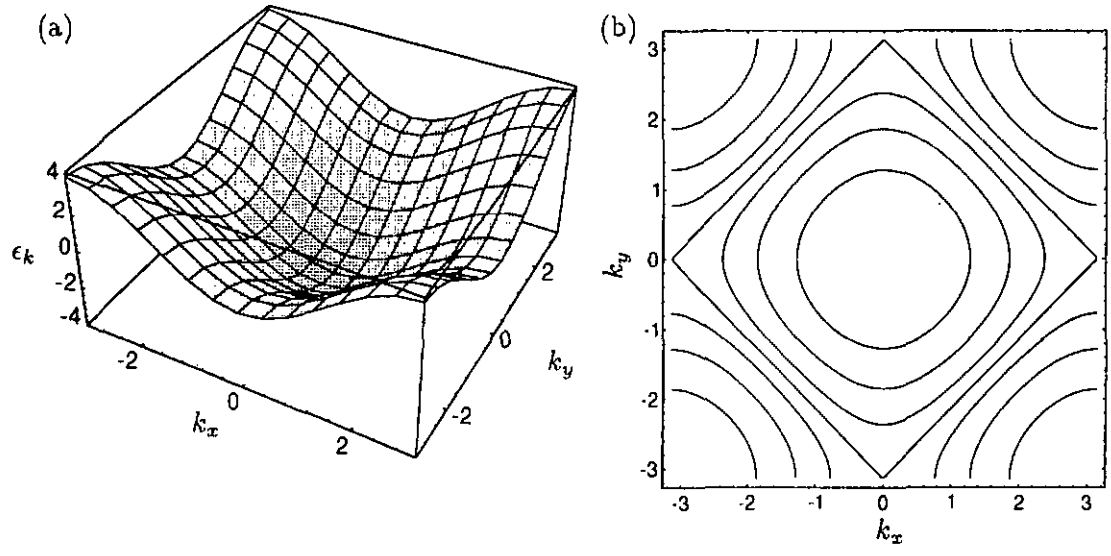

Figure 1.3: Tight binding band (a) for nearest neighbor hopping on a two dimensional square lattice and Fermi surface (b) for $n = 0.25, 0.5 \ldots, 1.75$, starting from the inner surface. For half-filling, the Fermi surface is a square and nested.

the metallic behavior on one hand and the antiferromagnetic and insulating behavior on the other hand.

1.3.1 Free Electrons

In the limit $W = 0$, the Hamiltonian in equation (1.8) becomes

$$\mathcal{H}_0 = \sum_{k\sigma} (\epsilon_k - \mu) n_{k\sigma} \quad . \tag{1.12}$$

This Hamiltonian is diagonal in Fourier space and describes a metal with a single s-band in a tight binding picture [Ashcroft76]. For nearest neighbor hopping on a square lattice, the dispersion relation is given in equation (1.9). For $D = 2$ it is shown in figure 1.3 (a). The bandwidth $B = 8t$. According to the Pauli principle, the groundstate is given by filling the one-particle energy states $|k\sigma\rangle$ from below up to the Fermi energy. The Fermi surface for various band fillings n are shown in figure 1.3 (b). For half-filling it is a square and it is "nested", which means that a reciprocal lattice vector ((π, π) or $(-\pi, \pi)$) maps an entire section of the Fermi surface onto another. This is due to the fact that the lattice is bipartite[1] and that nearest neighbor hopping only joins sublattice A

[1] A bipartite graph is a graph whose vertex-set can be split into two sets A and B in such a way that each edge of the graph joins a vertex in A to a vertex in B.

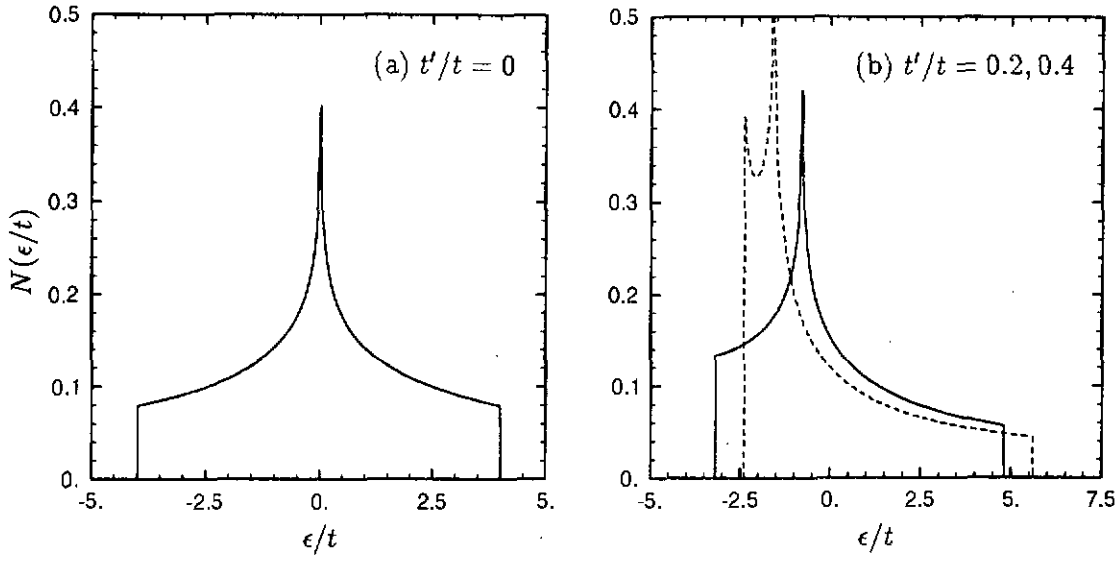

Figure 1.4: Density of states for the tight binding band given in equation (1.14). On the left hand side (a) only nearest neighbor hopping is assumed, while the curves on the right hand side (b) are calculated for $t'/t = 0.2$ (solid line) and $t'/t = 0.4$ (dotted line).

to sublattice B [Hirsch85c]. Implications of the nesting property on the Hubbard model have been discussed by several authors [Richmond69, Mattis70, Chaikin75]. In the low density limit the Fermi surface is more or less a circle and shows the s–wave symmetry of the band.

Besides the Fermi surface, the density of states is an important feature of the free Hamiltonian. It is defined by

$$N(\epsilon/t) = \frac{1}{L}\sum_{k\sigma}\delta(\epsilon_k/t - \epsilon/t) \quad . \tag{1.13}$$

For nearest neighbor hopping and in two dimensions it is shown in figure 1.4(a). The symmetry of the density of states reflects the particle hole symmetry of the nearest–neighbor–hopping model. Moreover, in this model the logarithmic van Hoove singularity ($\sim \ln(\epsilon/4t)$), which is typical for two-dimensional systems for topological reasons, occurs at the same energy where the Fermi surface is nested. In fact, including for instance a next nearest hopping term via

$$\epsilon_k = -2t(\cos(k_x) + \cos(k_y)) + 4t'\cos(k_x)\cos(k_y) \quad , \tag{1.14}$$

the van Hove singularity will shift to the left or right according to the sign of t'. Furthermore, two singularities may occur. This is shown in figure 1.4(b) for $t'/t = 0.2, 0.4$. In this work, however, nearly all calculations assume nearest neighbor hopping. Nevertheless,

most of the results can be easily generalized. Some implications of next nearest neighbor hopping are discussed in the last chapter of this disseration.

1.3.2 The Atomic Limit; A Monte Carlo Study

We first need to explain the notion "atomic limit". For the usual Hubbard model the case $t = 0$ is correctly called an atomic limit, for there is no more interaction between electrons on neighboring sites and the problem becomes a one–site problem. For the NNSP model this is not the case. Even for $t = 0$, the problem is a lattice problem because of the nearest neighbor interaction. However, all electrons are immobile, so that we are still using the term "atomic limit" to name this case. For $t = 0$, the NNSP Hamiltonian reads

$$\mathcal{H}_1 = \sum_{i,j} W_{ij} n_{i\uparrow} n_{j\downarrow} - \mu \sum_i (n_{i\uparrow} + n_{i\downarrow}) \quad . \tag{1.15}$$

In one dimension a transfer matrix method [Reichl80] can be used to calculate the partition function [Tanner94]. In two dimensions one can try a similar technique as it has been used to solve the two–dimensional Ising model [Onsager44, Kaufmann49a, Kaufmann49b]. Using the local particle number and the z–components of the local spin operators

$$n_i = (n_{i\uparrow} + n_{i\downarrow}) \quad \text{and} \tag{1.16}$$

$$s_i^z = \frac{1}{2}(n_{i\uparrow} - n_{i\downarrow}) \quad , \tag{1.17}$$

the Hamiltonian of the atomic limit can be rewritten as follows:

$$\mathcal{H}_1 = W \sum_{<i,j>} \left(\frac{1}{4} n_i n_j - s_i^z s_j^z \right) - \mu \sum_i n_i \quad , \tag{1.18}$$

which shows the similarity to the Ising model. The interaction term, however, includes both a density–density interaction and a spin–spin interaction of the z–components of the local spin operators and neither the number of electrons is fixed nor their position. This last feature is in sharp contrast with respect to the Ising model. For this reason and for simplicity we have not tried to find the exact solution by analytical means. Instead we have used a classical Monte Carlo technique, which also yields exact results for the thermodynamic limit in a finite size scaling procedure. Because both, Monte Carlo Simulation and finite size scaling analysis are standared techniques, a discussion of the details implemented for the atomic limit of the NNSP model is omitted here. It should be noted that for the atomic limit all energies can be measured in units of T.

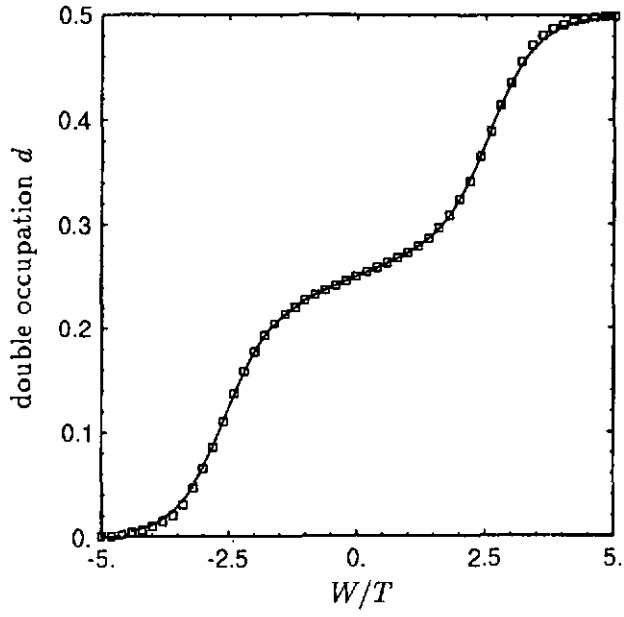

Figure 1.5: Mean double occupation number per lattice site on an 8 site ring with $N = 8$ electrons (half–filling) for W/T between -5 and 5. The solid line is estimated using an exact diagonalization technique and the square dots show the Monte Carlo results. Both calculations agree closely, which indicates the validity of the Monte Carlo algorithm.

To test the algorithm, the Monte Carlo results for the mean double occupation number

$$d = \frac{1}{L} \sum_i \langle n_{i\uparrow} n_{i\downarrow} \rangle \tag{1.19}$$

has been compared with exact diagonalization results [Tanner94]. This is shown in figure 1.5 for a one dimensional ring of $L = 8$ sites and $N = 8$ electrons, where the solid line is obtained by exact diagonalization, while the square dots are the Monte carlo results. The agreement is obvious. In addition, the same algorithm has been used to calculate the atomic limit of the usual Hubbard model, which is even for finite lattice sizes and fixed particle numbers analytically solvable. The comparison of these calculations also show exact agreement.

Because of the negative sign of the coupling constant, the interaction Hamiltonian in equation (1.18) favors antiferromagnetic order. Due to the classical character of the interaction Hamiltonian, antiferromagnetic long range order is possible for dimensions greater than or equal to two. In one dimension, thermal fluctuations destroy any long range order for finite temperatures. The phase diagram for the two–dimensional square lattice is shown in figure 1.6 . It displays the Néel temperature as a function of filling. Due to particle hole symmetry it is plotted versus $|n - 1|$. The dots are obtained by the Monte Carlo technique including a finite size scaling procedure, while the solid line is evaluated by a simple mean field approximation, where the Hamiltonian in equation (1.15) has been replaced by a one particle Hamiltonian including an antiferromagnetic mean field parameter. For the half–filled system the ground state is the perfect Néel state, whereas away from half-filling it is characterized by a phase separation between an antiferromagneti-

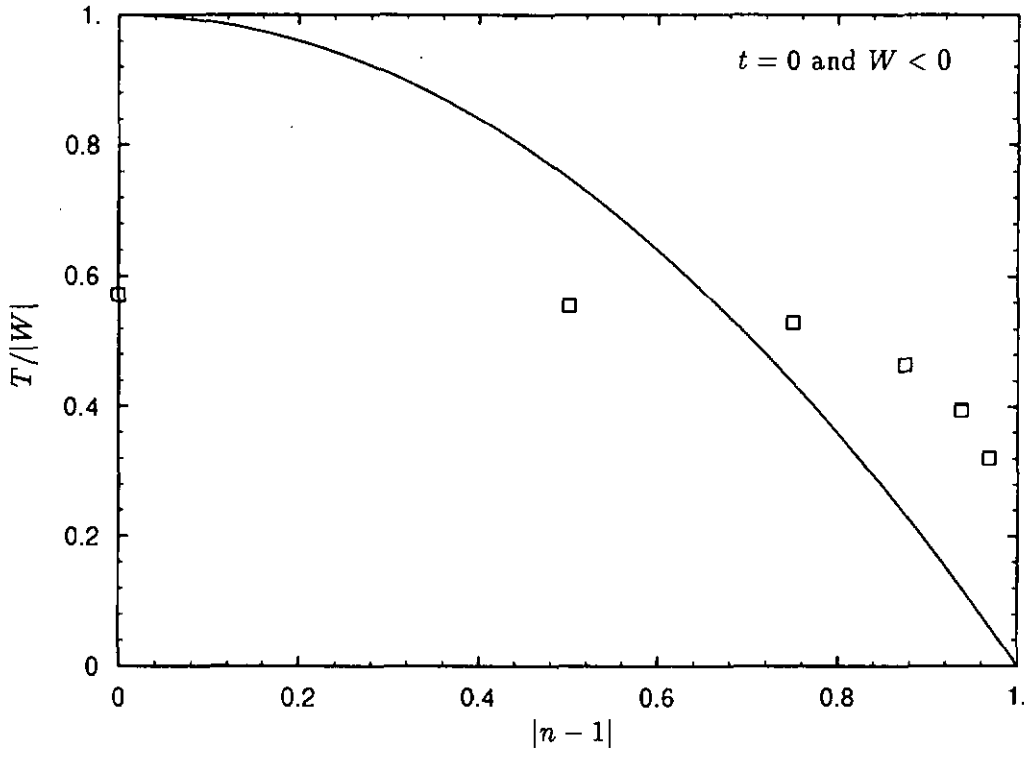

Figure 1.6: $T/|W|$ versus $|n-1|$ phase diagram for $t = 0$ and $W < 0$. The square dots are the Monte Carlo results, while the solid line is estimated using the Mean Field approximation.

cally ordered and an empty domain. The message of the phase diagram is twofold. First it shows the antiferromagnetic properties of the interaction of the NNSP model for all fillings and that they cannot be neglected in any calculation. Second it shows that the simple mean field approximation yields qualitatively correct results. Both calculations show antiferromagnetic long range order for all fillings. The deviation must be attributed to neglecting thermal fluctuations and to the fact that the mean-field approximation does not provide a realistic description of a phase separation. This issue is discussed in more detail in chapter 6.

1.4 Overview

Two extreme limits were discussed in the previous section, which can both be exactly solved because the Hamiltonian becomes diagonal either in Fourier or real space. The general case ($t \neq 0$ and $W < 0$) is not exactly solvable, so that approximation approaches have to be used. The functional integral formalism which is introduced in chapter 2 is quite a good starting point for studying phase transitions in highly correlated electron systems. Even the competition between different kinds of orders enters in a natural way.

The functional integral description is a one–to–one map of the original problem and therefore not exactly solvable either. It yields, however, a different point of consideration, from which approximations which are more suitable to the problem of phase transitions, as for instance a traditional perturbation theory, can be derived. Some of them are discussed in chapter 3. The symmetry–broken Hartree Fock Bogoliubov approximation is related to the time–independent saddle point approximation and is therefore also discussed in chapter 3. Starting from the functional integral formalism, the approximations can be interpreted in a better way and it becomes obvious what is neglected and what has to be included to improve them. Both the derivation of the functional integral formalism and the approximations are very general, so that the results from chapters 2 and 3 can be used for a large class of models, including for instance all modifications of the Hubbard model, attractive as well as repulsive ones. The symmetry–broken Hartree Fock Bogoliubov approximation is one of the simplest methods for studying the competition between different order parameters. In chapters 4 – 6 this method is applied to the NNSP model. To allow for superconductivity and antiferromagnetism, both superconducting and antiferromagnetic variational parameters are included in the effective Hamiltonian. In chapter 4 the selfconsistent equations are derived using a Greens function technique. They are coupled nonlinear equations of all variational parameters and reflect their interdependence on each other. The notion of d– and xs–wave pairing is introduced. In addition, the possibillity of mixed symmetry, where the superconducting order parameter has a nonzero d– and xs–wave component, is discussed. Chapter 5 presents and analyzes the numeric solutions for all order parameters as a function of coupling strength, electron density and temperature, in particular the competition between antiferromagnetism and superconductivity and its implications. Moreover, a comparison to the BCS approximation, where the antiferromagnetic features are neglected, yields some interesting information. Chapter 6 considers several types of phase diagrams: ground state, temperature versus filling and temperature versus coupling strength phase diagrams. They are obtained by linearizing the self consistent equations, for all phase transitions are of second order. Based on the chemical potential and its behavior as a function of filling, the existence of an electronic phase separation is revealed and discussed. Chapter 7 includes a discussion about the application of the NNSP model to reality, in particular the phase diagram of high temperature superconductors. It starts from fixing the model parameters and ends with interesting implications, such as the d–wave symmetry of the superconducting order parameter or the shape of the density of states. We conclude this dissertation with a global summary of the results obtained and some suggestions for further research.

Chapter 2

The Functional Integral Formalism

In this chapter we derive a general framework for studying phase transitions from a microscopical point of view, that is, starting from a microscopicl model defined by a Hamiltonian such as in equation (1.1). This method is known as the functional integral description of quantum mechanical systems and was first used by Feynman [Feynman65]. There are several ways to introduce this method (see e. g. [Amit84, Negele88]). We are using the direct approach for the partition function which can be summarized in four steps:

1. Writing the interaction as a quadratic form,

2. Dividing $\beta = 1/T$ in N imaginary time slices and introducing a time-ordered product, i. e. applying a *Trotter–Suzuki* [Trotter59] decomposition,

3. Using the *Stratanovich–Hubbard* [Stratonovich57, Stratonovich58, Hubbard59] transformation for every time slice, and

4. taking the limit $N \to \infty$.

In section 2.1 we show several ways to write the interaction of the NNSP model as a quadratic form ending with a general form which may also be applied to other models. Using this general form, the functional integral representation of the partition function is derived in section 2.2. It leads to the definition of a free energy functional based on an effective one–particle Hamiltonian. In section 2.3 we derive a procedure for calculating the free energy functional, using a generalization of the Nambu formalism. Finally, all of this development is applied to the NNSP model.

2.1 Quadratic Form of the Pairing Interaction of the NNSP Model

Although it is possible and for some reasons easier to derive the following decompositions in real space, we are using the Fourier representation of the Hamiltonian in equation (1.8). The resulting formula will be more suitable for approximations derived in chapter 3. The interaction part is a two–particle operator and writing it in quadratic form means writing it in quadratic form of one–particle operators. There exist three different ways to do this, leading to three possible quadratic representations of $\mathcal{H}_1$ and describing four different types of order which are presented in the following sections 2.1.1 - 2.1.3.

2.1.1 The Charge– and Spin–Density Wave Representation

The first decomposition leads to the notion of charge– and spin–density waves. The interaction Hamiltonian may be written as follows:

$$\mathcal{H}_1 = \frac{Wz}{L} \sum_q S(q) \left(\sum_k c^\dagger_{k+q\uparrow} c_{k\uparrow} \right) \left(\sum_{k'} c^\dagger_{k'-q\downarrow} c_{k'\downarrow} \right) \quad , \tag{2.1}$$

which appears to be more or less a quadratic form. The operators in the parentheses are the Fourier transforms of the local particle number operators $n_{i\sigma}$:

$$\frac{1}{L} \sum_j n_{j\sigma} \mathrm{e}^{-iqR_j} = \frac{1}{L} \sum_k c^\dagger_{k-q\sigma} c_{k\sigma} =: \eta_{q\sigma} \quad . \tag{2.2}$$

In order to obtain a quadratic representation, one has to introduce spin–independent entities, which are the *Charge–Density–Wave* (CDW) operator

$$\eta_q := \left(\eta_{q\uparrow} + \eta_{q\downarrow} \right) = \eta^\dagger_{-q} = \eta^\dagger_q \quad , \tag{2.3}$$

and the *Spin–Density–Wave* (SDW) operator

$$s_q := \frac{1}{2} \left(\eta_{q\uparrow} - \eta_{q\downarrow} \right) = s^\dagger_{-q} = s^\dagger_q \quad . \tag{2.4}$$

The last equality signs in equation (2.3) and equation (2.4) are valid due to the inversion symmetry of the lattice. Hence both operators are selfadjoint. The meaning of these operators becomes clear, when using the real space representation given in equation (2.2). A nonzero value of $\langle \eta_q \rangle$ or $\langle s_q \rangle$ describes a system with charge density or spin density order

with respect to the wave vector q. Two special cases are important: $q = 0$ and $q = Q$, where Q maps one sublattice onto the other presuming a bipartite lattice. For $q = 0$, $\langle \eta_0 \rangle \neq 0$ describes a uniform charge distribution while $\langle s_0 \rangle \neq 0$ inidicates Ferromagnetism. A finite value for $\langle \eta_Q \rangle$ describes a system where the mean charge on one sublattice is different from the one on the other sublattice. On the other hand, $\langle s_Q \rangle \neq 0$ represents antiferromagnetic long range order. In this case the mean magnetization on both sublattices are different. Chiral structures are described by $\langle \eta_q \rangle \neq 0$ or $\langle s_q \rangle \neq 0$ for intermediate wave vectors q. With the definition of CDW and SDW operators, the interaction Hamiltonian finally becomes

$$\mathcal{H}_1 = WzL \sum_q S(q) \left(\frac{1}{4} \eta_q^\dagger \eta_q - s_q^\dagger s_q \right) \quad , \tag{2.5}$$

which is obviously a quadratic form.

2.1.2 Electron Pairing Representation

The second way to write the interaction term as a quadratic form leads to pairing operators with different internal symmetry and finite center of mass momentum. Commuting the $\uparrow$- and $\downarrow$-operators, the interaction Hamiltonian may be written as follows:

$$\mathcal{H}_1 = \frac{Wz}{L} \sum_{k,k',q} S(q) c_{k+q\uparrow}^\dagger c_{k'-q\downarrow}^\dagger c_{k'\downarrow} c_{k\uparrow} \quad , \tag{2.6}$$

and after some variable transformations:

$$\mathcal{H}_1 = \frac{Wz}{L} \sum_{k,k',q} S(k-k') c_{k'\uparrow}^\dagger c_{-k'+q\downarrow}^\dagger c_{-k+q\downarrow} c_{k\uparrow} \quad . \tag{2.7}$$

The forthcoming treatment of this expression depends on how one factorizes the structure factor $S(k-k')$ into terms which depend only on k and k'.

Cartesian Decomposition

The most simple case is the cartesian decomposition using the definition of $S(q)$ in equation (1.10). The interaction Hamiltonian then reads:

$$\mathcal{H}_1 = WL \sum_q \sum_\alpha^z P_\alpha^\dagger(q) P_\alpha(q) \tag{2.8}$$

with

$$P_\alpha(q) := \frac{1}{L}\sum_k c_{-k+q\downarrow}c_{k\uparrow}\,e^{ik\delta_\alpha} \quad , \tag{2.9}$$

where δ_α is a relative lattice vector pointing to one of the z nearest neighbors enumerated by $\alpha = 1\ldots z$. $P_\alpha^\dagger(q)$ is the adjoint operator to $P_\alpha(q)$. Note: these operators are not selfadjoint, even when the lattice has inversion symmetry. Again, the meaning of these operators needs to be discussed. For this reason it is very useful to transform them back into real space representation:

$$P_\alpha^\dagger(q) = \frac{1}{L}\sum_j P_\alpha^\dagger(j)\,e^{iqR_j} \quad \text{with} \quad P_\alpha^\dagger(j) = c_{j+\alpha\uparrow}^\dagger c_{j\downarrow}^\dagger \quad . \tag{2.10}$$

The operator $c_{j+\alpha\uparrow}^\dagger c_{j\downarrow}^\dagger$ creates an electron pair with one electron at site j and the other electron at the neighboring site in α–direction. Therefore this index characterizes the internal structure of the pair, i. e. its symmetry. The definition of $P_\alpha^\dagger(q)$ includes a Fourier transformation of $P_\alpha^\dagger(j)$ with respect to j, so that q becomes the center of mass momentum of the pair.

Group–Theoretical Decomposition

Instead of using the cartesian symmetry characterization, one often uses a group–theoretical classification. What does this mean? In a system with a total symmetry group G, any non–retarded two particle potential which respects this symmetry can be expanded in basisfunctions $f_{\Gamma,m_\Gamma}(k)$ of the irreducible representations of G as follows:

$$S_{\alpha\beta\gamma\delta}(k,k') = \sum_{\Gamma,m_\Gamma} S_{\alpha\beta\gamma\delta}^{\Gamma,m_\Gamma} f_{\Gamma,m_\Gamma}(k) f_{\Gamma,m_\Gamma}(k') \quad , \tag{2.11}$$

where the indices $\alpha,\ldots,\delta$ are spin or pseudospin variables. Γ labels the irreducible representations induced by G acting on the two–particle Hilbert space and m_Γ is an additional index needed for representations with dimension greater than one. This decomposition leads directly to a quadratic representation of the interaction Hamiltonian with generalized pairing operators defined by the basisfunctions $f_{\Gamma,m_\Gamma}(k)$. Within the NNSP model a two–dimensional square lattice is assumed. Its point group D_4 has eight elements in five classes. Accordingly there exist five irreducible representations $\Gamma_1,\ldots,\Gamma_5$, where $\Gamma_1,\ldots,\Gamma_4$ are one–dimensional and Γ_5 is two–dimensional [Sigrist87]. For the two-dimensional square lattice basisfunctions can be chosen so they are related to the coordination shells of the

Table 2.1: Basisfunctions of the irreducible representations of the point group D_4 corresponding to the first coordination shell.

representation	basisfunction	state
Γ_2	$f_{xs}(k) = \cos(k_x) + \cos(k_y)$	extended s–wave
Γ_3	$f_d(k) = \cos(k_x) - \cos(k_y)$	d–wave
Γ_5	$f_{p_x}(k) = \sqrt{2}\sin(k_x)$	p_x–wave
	$f_{p_y}(k) = \sqrt{2}\sin(k_y)$	p_y–wave

lattice. Within the NNSP model only the first coordination shell is involved. The corresponding basisfunctions are summarized in table 2.1. Using these basisfunctions the potential for the NNSP model then reads:

$$S(k-k') = \frac{1}{z}\sum_{\alpha} f_\alpha(k)\, f_\alpha^*(k') \quad , \tag{2.12}$$

where α sums over d, xs, p_x and p_y. With this decomposition, the interaction Hamiltonian becomes:

$$\mathcal{H}_1 = WL\sum_q \sum_\alpha P_\alpha^\dagger(q) P_\alpha(q) \quad , \tag{2.13}$$

with pairing operators defined by:

$$P_\alpha(q) := \frac{1}{L}\sum_k c_{-k+q\downarrow} c_{k\uparrow}\, f_\alpha(k) \quad . \tag{2.14}$$

These have the same form as the pairing operators in equation (2.9), but the structure functions have changed. Their real space representations are given by:

$$P_\alpha^\dagger(j) = \sum_\delta g_\alpha(\delta)\, c_{j+\delta\uparrow}^\dagger c_{j\downarrow}^\dagger \quad . \tag{2.15}$$

Here the sum over δ ranges over all nearest neighbors and $g_\alpha(\delta)$ are weight functions corresponding to the index α. Again, we can interpret the index α as an internal symmetry index and $P_\alpha^\dagger(j)$ as the creation operator for a pair of symmetry α at site j. Within

the same interpretation, the Fourier transformed operator $P^{\dagger}_{\alpha}(q)$ is the creation operator for a pair of symmetry α and center of mass momentum q. For the nearest neighbor pairing interaction, there are always z different symmetries corresponding to the number of nearest neighbors. Using the general formula above, it is very easy to generalize this result to other pairing interactions and higher dimensions. For instance, a local attractive interaction yields only one pairing operator with $f_s = 1$, which corresponds to the s–wave symmetry in the group–theoretical classification.

As is known from the general considerations of Yang [Yang62], a nonzero value of the pair wave function

$$\Psi(j,\rho) := \left\langle c^{\dagger}_{j+\rho/2\uparrow} c^{\dagger}_{j-\rho/2\downarrow} \right\rangle \tag{2.16}$$

is equivalent to the existence of *Off Diagonal Long Range Order* (ODLRO) and indicates singlet superconductivity. Here j and ρ denote the center of mass and the relative coordinate of the electron pair created by $c^{\dagger}_{j+\rho/2\uparrow} c^{\dagger}_{j-\rho/2\downarrow}$, respectively. Again, the Fourier transform of this anomalous expectation value with respect to both the internal coordinate ρ and the center of mass coordinate j may be expanded in terms of basisfunctions of the irreducible representations of the symmetry group G. This yields:

$$\Psi(q,k) = \sum_{\Gamma,m_\Gamma} \Psi_{\Gamma,m_\Gamma}(q)\, f_{\Gamma,m_\Gamma}(k) \tag{2.17}$$

with

$$\Psi_{\Gamma,m_\Gamma}(q) = \left\langle P^{\dagger}_{\Gamma,m_\Gamma}(q) \right\rangle \tag{2.18}$$

and

$$P_{\Gamma,m_\Gamma}(q) = \frac{1}{L} \sum_{k} f_{\Gamma,m_\Gamma}(k)\, c_{-k+q\downarrow} c_{k\uparrow} \tag{2.19}$$

From this point of view, the meaning of a nonzero expectation value $\langle P_{\Gamma,m_\Gamma}(q) \rangle$ becomes clear. It indicates superconductivity of electron pairs with symmetry Γ, m_Γ and center of mass momentum q. The latter describes a spatial modulation of the superconducting order parameter. Note that the expansion of the pair wave function in equation (2.17) also includes components which are not included in the expansion of the pairing interaction. This means that the symmetry of the superconducting state might be different from the symmetries mediated by the interaction potential. As we will show in chapter 3, within a saddle point approximation. the possible symmetries are exactly those for which S^{Γ,m_Γ} is

nonzero. Consider for instance the attractive Hubbard model with only on–site interaction, which might also exhibit d–wave superconductivity, although this is very unlikely. In the BCS–treatment of this model only s–wave superconductivity appears.

2.1.3 The Spin–Flip Representation

This last possibility to write the interaction term as a quadratic from arises from the combination of the first and the fourth and of the third and the second fermion operator of the interaction Hamiltonian in equation (1.8). In order to obtain the proper order one needs to commute the fermion operators. There are two possibilities:

$$\mathcal{H}_1 = \frac{Wz}{L} \sum_{k,k',q} S(q) \left\{ n_{k'\downarrow} \delta_{q,0} - c^\dagger_{k'-q\downarrow} c_{k\uparrow} c^\dagger_{k+q\uparrow} c_{k'\downarrow} \right\} \tag{2.20}$$

$$= \frac{Wz}{L} \sum_{k,k',q} S(q) \left\{ n_{k\uparrow} \delta_{q,0} - c^\dagger_{k+q\uparrow} c_{k'\downarrow} c^\dagger_{k'-q\downarrow} c_{k\uparrow} \right\} \quad . \tag{2.21}$$

Adding both equations and using some variable transformations and $S(q) = S(-q)$, the interaction Hamiltonian becomes:

$$\mathcal{H}_1 = \frac{Wz}{2} \sum_k n_k - \frac{Wz}{L} \sum_{k,k',q} S(k-k') c^\dagger_{k'\uparrow} c_{k'+q\downarrow} c^\dagger_{k+q\downarrow} c_{k\uparrow} \quad . \tag{2.22}$$

In this form $\mathcal{H}_1$ may be treated as in section 2.1.2. Introducing spin flip operators

$$Q_\alpha(q) := \frac{1}{L} \sum_k c^\dagger_{k+q\downarrow} c_{k\uparrow} f_\alpha(k) \quad \text{for} \quad \alpha = 1, \ldots, z \quad , \tag{2.23}$$

where the $f_\alpha(k)$ are either the cartesian or the group theoretical structure functions, yields:

$$\mathcal{H}_1 = \frac{Wz}{2} \sum_k n_k - WL \sum_q \sum_\alpha^z Q^\dagger_\alpha(q) Q_\alpha(q) \quad . \tag{2.24}$$

The first term has one–particle character and can be added to $\mathcal{H}_0$ while the second term has the desired quadratic form. As explained before in section 2.1.2, the index α can be interpreted as a general symmetry index and $Q_\alpha(q)$ as a spin–flip operator corresponding to this symmetry.

A finite expectation value of one of these spin–flip operators breaks the spin symmetry because one electron of spin $\uparrow$ is destroyed and another electron of spin $\downarrow$ is created. Hence the total spin is not conserved. For this reason this representation becomes less important. Nevertheless, for other Hamilton operators including spin–independent density–density

interactions, it might be important. For such Hamiltonians this representation includes also spin conserving components which yields the Fock exchange terms in a saddle point approximation.

2.1.4 The General Form

In the previous sections 2.1.1 - 2.1.3, we described several ways of writing the interaction Hamiltonian in a quadratic form such as

$$\mathcal{H}_1 = \sum_{q\alpha} g_{i\alpha}(q) h^\dagger_{i\alpha}(q) h_{i\alpha}(q) \quad . \tag{2.25}$$

Here i indicates one of the representations and the q–, α–sum includes the sum over all wave vectors in the first Brioullin zone and over all components $h_{i\alpha}(q)$, respectively. $g_{i\alpha}(q)$ is a representation–specific coupling constant which may also depend on q and α as is the case for the CDW/SDW–representation. Instead of using only one of the representations, one can add two or more of them. That is, for all families of real constants $\{\lambda_i\}$ with $\sum_i \lambda_i = 1$, the interaction Hamiltonian is given by

$$\mathcal{H}_1 = \sum_{i,q,\alpha} \lambda_i g_{i\alpha}(q) h^\dagger_{i\alpha}(q) h_{i\alpha}(q) \quad . \tag{2.26}$$

Note that the constants $\{\lambda_i\}$ may be arbitrarily chosen. The only condition they must satisfy is the sum rule mentioned above. However, it is very useful to restrict oneself to positive values of all λ_i in order to maintain the sign of the coupling constants $g_{i\alpha}(q)$. With this additional constraint the interaction Hamiltonian is, mathematically spoken, the convex envelope of all possible representations.

In the forthcoming considerations we do not pay any attention to the parameters $\{\lambda_i\}$. Therefore it is useful to redefine the index i including the component index α and the coupling constants via $\lambda_i g_{i\alpha}(q) \to g_i(q)$. Within this definition the interaction Hamiltonian becomes finally:

$$\mathcal{H}_1 = \sum_{i,q} g_i(q) h^\dagger_i(q) h_i(q) \quad . \tag{2.27}$$

This is quite a general form which may also be applied to many other models. Hence, the final formula for the partition function derived in the next section 2.2 is also very general. However, for any specific calculations one has to remember the definition of the coupling constants $g_i(q)$, particularly the arbitrariness of the parameters $\{\lambda_i\}$. In fact, it is an

interesting question whether for approximate treatments there exists an optimum choice of these parameters. We will discuss this problem within the mean field approximation in section 3.2.3.

2.2 The Functional Integral Representation of the Partition Function

2.2.1 Introducing a Time–Ordered Product

Within the Schrödinger or Heisenberg picture of quantum mechanics the partition function of the grand canonical ensemble is defined by:

$$Z = \mathrm{Tr}\, e^{-\beta \mathcal{H}} = \mathrm{Tr}\, \mathcal{S}(\beta) \quad , \tag{2.28}$$

where $\mathcal{S}(\beta)$ is the evolution operator in imaginary time evaluated at $\tau = \beta$. In order to get rid of the noncommutivity of $\mathcal{H}_0$ and $\mathcal{H}_1$, one uses a Trotter–Suzuki decomposition [Trotter59], i. e. one divides β into N time slices of length $\Delta\tau_r = \beta/N$, labeled by an index r, yielding:

$$\mathcal{S}(\beta) = \prod_{r=1}^{N} e^{-\mathcal{H}\,\Delta\tau_r} \quad . \tag{2.29}$$

As N approaches infinity and hence $\Delta\tau_r$ becomes infinitesimally small, the exponential function in equation (2.29) may be decomposed due to the Baker–Hausdorff theorem:

$$e^{-\mathcal{H}\Delta\tau_r} = e^{-\mathcal{H}_0\,\Delta\tau_r}\, e^{-\mathcal{H}_1\,\Delta\tau_r} \qquad \text{for} \qquad \Delta\tau_r \to 0 \quad . \tag{2.30}$$

This decomposition has to be carried out for each time slice r. Since commuting the resulting factors of different time slices is not permitted, it is necessary to introduce a time ordered product[1]:

$$\mathcal{S}(\beta) = \lim_{N\to\infty} \mathrm{T}_r \prod_{r=1}^{N} \exp\left(-\mathcal{H}_0\,\Delta\tau_r\right) \exp\left(-\mathcal{H}_1\,\Delta\tau_r\right) \quad . \tag{2.31}$$

In the same manner noncommutative contributions of $\mathcal{H}_1$ may be treated. For every time slice they can be considered as commutative. In this sense the introduction of the time ordered product maps the quantum mechanical system onto a classical system. The price to pay is the increase of the dimension by one.

[1] Neglecting the time order yields $\mathcal{S}(\beta) = \exp(\beta\mathcal{H}_0)\exp(\beta\mathcal{H}_1)$, which is obviously wrong!

2.2.2 The Stratanovich–Hubbard Transformation

As for every time slice r where the contributions of $\mathcal{H}_1$ may be considered as commutative operators, a classical formula may be applied. In its general form for complex numbers $a, z \in \mathbb{C}$ it reads:

$$e^{-|a|^2} = \int \frac{d^2z}{\pi} e^{-|z|^2 \pm i(a^* z + a z^*)} \tag{2.32}$$

$$e^{|a|^2} = \int \frac{d^2z}{\pi} e^{-|z|^2 \pm (a^* z + a z^*)} \quad . \tag{2.33}$$

For real $a \in \mathbb{R}$ it suffices to introduce a real field $x \in \mathbb{R}$. In this case one has to perform the following replacement

$$\int \frac{d^2z}{\pi} \longrightarrow \int \frac{dx}{\sqrt{\pi}} \quad \text{and} \quad (a^* z + a z^*) \longrightarrow 2ax \quad . \tag{2.34}$$

It should be emphasized that the sign of the linear term in z is arbitrary. In order to use this formula for the quadratic representation of the interaction Hamiltonian derived in the previous section 2.I, it has to be modified including the coupling constant and the time slice $\Delta\tau_r$. Both have to be treated differently because $\Delta\tau_r$ is always positive while the sign of $g_i(q)$ depends on q and i. For one term in equation (2.27) of the form $gh^\dagger h \Delta\tau_r$ one obtains

$$e^{-gh^\dagger h \Delta\tau_r} = \int \frac{d^2v}{\pi} \exp\left(- |v|^2 \pm \sqrt{\mathrm{sgn}(-g)} \sqrt{|g|\,\Delta\tau_r}\,(h^\dagger v + h v^*) \right) \quad , \tag{2.35}$$

and after the variable substitution $v \longrightarrow v\sqrt{|g|\,\Delta\tau_r}$

$$e^{-gh^\dagger h \Delta\tau_r} = \int \frac{d^2v}{\pi} |g|\,\Delta\tau_r \exp\left(- \left[|g|\,|v|^2 + \sqrt{\mathrm{sgn}(-g)}\, g\,(h^\dagger v + h v^*) \right] \Delta\tau_r \right) \quad . \tag{2.36}$$

In this formula we have chosen the free sign of the linear terms so that $\pm|g|$ becomes $-g$, i.e. for negative g the positive and for positive coupling constant the negative sign. Finally, this Stratanovich–Hubbard transformation has to be applied for all q, i and all time slices r. That is, for every set of indices $\{q, i, r\}$ one has to integrate over a corresponding field variable $v_i(q, \tau_r)$, which yields:

$$\mathcal{S}(\beta) = \lim_{N\to\infty} \mathrm{T}_\tau \prod_{r=1}^{N} \int \left(\prod_{q,i} \frac{d^2 v_i(q,\tau_r)}{\pi} |g_i(q)|\,\Delta\tau_r \right) \times \exp\left(-\mathcal{H}^{\#}[v]\,\Delta\tau_r \right) \tag{2.37}$$

with

$$\mathcal{H}^{\#}[v] = \mathcal{H}_0 + \sum_{i,q} \Big\{ |g_i(q)|\,|v_i(q,\tau_r)|^2 + \sqrt{\mathrm{sgn}(-g_i(q))}\, g_i(q) \left(h_i^{\dagger}(q) v_i(q,\tau_r) + h_i(q) v_i^{*}(q,\tau_r) \right) \Big\} \quad , \tag{2.38}$$

where $\mathcal{H}^{\#}[v]$ means that $\mathcal{H}^{\#}$ is a functional of the τ–, q– and i–dependent field $v_i(q,\tau_r)$. The expressions in equation (2.37) and (2.38) are not very handy, so it is useful to define a shortcut:

$$\mathcal{S}(\beta) = \int \mathcal{D}^2 v \; \mathrm{T}_\tau \exp\left(- \int_0^\beta \mathcal{H}^{\#}[v] d\tau \right) \quad . \tag{2.39}$$

Here the functional integral measure is given by:

$$\int \mathcal{D}^2 v := \lim_{N\to\infty} \prod_{r=1}^{N} \prod_{q,i} \frac{d^2 v_i(q,\tau_r)}{\pi} |g_i(q)|\, \Delta\tau_r \quad . \tag{2.40}$$

Note that for a selfadjoint operator the introduction of a real field is sufficient.

2.2.3 Definition of the Free Energy Functional

The partition function is defined as the trace of $\mathcal{S}(\beta)$. Hence, interchanging the functional integration with the trace operation – both are linear operations – yields:

$$Z = \int \mathcal{D}^2 v \; \exp\left(-\beta F^{\#}[v] \right) \tag{2.41}$$

with

$$F^{\#}[v] := -\frac{1}{\beta} \ln\left(\mathrm{Tr}\, \mathrm{T}_\tau \exp\left(- \int_0^\beta \mathcal{H}^{\#}[v] d\tau \right) \right) \quad , \tag{2.42}$$

which is called the "free energy functional" of the system. It should not be confused with the free energy, which is given by the natural logarithm of Z:

$$F = -\frac{1}{\beta} \ln(Z) \quad . \tag{2.43}$$

In fact, $F^{\#}$ and F are only identical in a saddle point approximation where the functional integral is replaced by the integrand evaluated at the minimum of $F^{\#}$. It is very practical to decompose $F^{\#}[v]$ into two parts:

$$F^{\#}[v] = F_{\mathrm{eff}}[v] + \frac{1}{\beta} \int_0^\beta \sum_{i,q} |g_i(q)|\, |v_i(q,\tau)|^2 \, d\tau \quad , \tag{2.44}$$

with

$$F_{\text{eff}}[v] = -\frac{1}{\beta} \ln \left(\text{Tr}\, \text{T}_\tau \exp \left(- \int_0^\beta \mathcal{H}_{\text{eff}}[v] d\tau \right) \right) \tag{2.45}$$

and

$$\mathcal{H}_{\text{eff}}[v] := \mathcal{H}_0 + \sum_{i,q} \sqrt{\text{sgn}(-g_i(q))}\, g_i(q) \left(h_i^\dagger(q) v_i(q,\tau) + h_i(q) v_i^*(q,\tau) \right) \quad . \tag{2.46}$$

The first term $F_{\text{eff}}[v]$ is just the free energy of the field–dependent Hamilton operator $\mathcal{H}_{\text{eff}}[v]$, whereas the second term leads to a Gaussian weight factor:

$$g[v] = \exp \left(-\frac{1}{\beta} \int_0^\beta \sum_{i,q} |g_i(q)|\, |v_i(q,\tau)|^2 \, d\tau \right) \tag{2.47}$$

in the functional integral in equation (2.41).

2.3 The Computation of the Free Energy Functional

Because the effective Hamiltonian $\mathcal{H}_{\text{eff}}[v]$ is a one–particle operator, the free energy functional may be computed exactly. From the decomposition above it becomes clear that it suffices to determine $F_{\text{eff}}[v]$. In this section we shall show how this can be done in principle. The basic idea behind the calculation scheme described below is that one takes the functional derivatives of F_{eff} with respect to some properly defined variables, calculates the resulting expressions using a Greens function method and finally integrates them back.

2.3.1 The Nambu Representation

First of all one has to rearrange the operators in $\mathcal{H}_{\text{eff}}[v]$ so that it becomes explicitly a quadratic form. For this task note that the quadratic representation of the interaction Hamiltonian is based on a complete set of one–particle creation and annihilation operators and all field operators are linear combinations of product of two of them. In the forthcoming sections the corresponding one–particle states are labeled by a single roman index including momentum and spin, or, as one works in a real space representation, the lattice site and spin or any other one–particle state description. On the other hand, the set of all creation and annihilation operators is enumerated by a greek index which ranges

from 1 to $4L$. Accordingly all these operators may be combined into one column vector with $4L$ components:

$$\bar{\mathbf{c}} := \begin{pmatrix} \mathbf{c} \\ \mathbf{c}^\dagger \end{pmatrix} \quad , \tag{2.48}$$

where $\mathbf{c} = \{c_i\}_{i=1,\ldots,2L}$ and $\mathbf{c}^\dagger = \{c_i^\dagger\}_{i=1,\ldots,2L}$ are the collections of all annihilation and creation operators, respectively. The adjoint operator of $\bar{\mathbf{c}}$ is a row vector given by

$$\bar{\mathbf{c}}^\dagger = \begin{pmatrix} \mathbf{c}^\dagger \, \mathbf{c} \end{pmatrix} \quad . \tag{2.49}$$

This represention is a straightforward generalization of the Nambu representation which is very often used in the theory of superconductivity [Nambu60], which is why we shall call it the Nambu representation as well. Within the context of this work both vectors are considered as matrices, namely $\bar{\mathbf{c}}$ as a $4L \times 1$ and $\bar{\mathbf{c}}^\dagger$ as a $1 \times 4L$ matrix. The transpose matrices $\bar{\mathbf{c}}$ and $\bar{\mathbf{c}}^\dagger$ are:

$$\begin{aligned} \bar{\mathbf{c}}^{\mathrm{T}} &= \begin{pmatrix} \mathbf{c} \; \mathbf{c}^\dagger \end{pmatrix} = \bar{\mathbf{c}}^\dagger \boldsymbol{\Gamma} \\ \bar{\mathbf{c}}^{\dagger \mathrm{T}} &= \begin{pmatrix} \mathbf{c}^\dagger \\ \mathbf{c} \end{pmatrix} = \boldsymbol{\Gamma} \bar{\mathbf{c}} \quad , \end{aligned} \tag{2.50}$$

with

$$\boldsymbol{\Gamma} = \begin{pmatrix} \mathbf{0} & \mathbf{1} \\ \mathbf{1} & \mathbf{0} \end{pmatrix} \quad , \tag{2.51}$$

where $\mathbf{1}$ is an identity matrix of size $2L \times 2L$ and $\mathbf{0}$ is a matrix of the same size but with all entries equal to zero. The anticommutation rules for the components of the Nambu vectors are given by:

$$\begin{aligned} \left[\bar{c}_\alpha^\dagger, \bar{c}_\beta\right]_+ &= \delta_{\alpha\beta} \\ \left[\bar{c}_\alpha, \bar{c}_\beta\right]_+ &= \Gamma_{\alpha\beta} \quad , \end{aligned} \tag{2.52}$$

where $\delta_{\alpha\beta}$ is the Kronecker Delta and $\Gamma_{\alpha\beta}$ is the $\alpha\beta$–component of $\boldsymbol{\Gamma}$.

Because the effective Hamiltonian is a linear combination of biproducts of creation and annihilation operators and these products are in normal order, i. e. the creation operators are always on the right hand side of the annihilation operators, there exists a traceless matrix $\mathbf{M}[v]$ with

$$\mathcal{H}_{\mathrm{eff}}[v] = \frac{1}{2} \bar{\mathbf{c}}^\dagger \, \mathbf{M}[v] \, \bar{\mathbf{c}} + \frac{1}{2} \mathrm{Tr} \, \mathbf{M}^1[v] \quad , \tag{2.53}$$

where $\mathbf{M}^1[v]$ is defined by the $2L \times 2L$ block matrix representation

$$\mathbf{M} = \begin{pmatrix} \mathbf{M}^1 & \mathbf{M}^{12} \\ \mathbf{M}^{21} & \mathbf{M}^2 \end{pmatrix} \quad . \tag{2.54}$$

Moreover, $\mathbf{M}$ may be chosen so that

$$\mathbf{M} = -\mathbf{\Gamma}\mathbf{M}^{\mathrm{T}}\mathbf{\Gamma} \quad . \tag{2.55}$$

Using the block matrix representation of $\mathbf{M}$ in equation (2.54), this equation reads:

$$\begin{pmatrix} \mathbf{M}^1 & \mathbf{M}^{12} \\ \mathbf{M}^{21} & \mathbf{M}^2 \end{pmatrix} = -\begin{pmatrix} (\mathbf{M}^2)^{\mathrm{T}} & (\mathbf{M}^{12})^{\mathrm{T}} \\ (\mathbf{M}^{21})^{\mathrm{T}} & (\mathbf{M}^1)^{\mathrm{T}} \end{pmatrix} \quad . \tag{2.56}$$

Clearly there is always a matrix $\widetilde{\mathbf{M}}[v]$ with $\mathcal{H}_{\mathrm{eff}}[v] = \frac{1}{2}\,\bar{\mathbf{c}}^{\dagger}\,\widetilde{\mathbf{M}}[v]\,\bar{\mathbf{c}}$. But this matrix is in general not traceless. For this reason one has to prove why the condition $\mathrm{Tr}\,\mathbf{M}[v] = 0$ leads to the additional term in equation (2.53). The diagonal part of $\mathcal{H}$ is given by:

$$\mathcal{H}^{\mathrm{D}}_{\mathrm{eff}} = \sum_i \epsilon_i\, n_i \tag{2.57}$$

with $n_i = c_i^{\dagger} c_i$ and diagonal matrix elements $\epsilon_i[v]$ which might depend on v. On the other hand, using the matrix representation above leads to:

$$\begin{aligned} \mathcal{H}^{\mathrm{D}}_{\mathrm{eff}} &= \frac{1}{2}\sum_i \left(\mathbf{M}^1_{ii}\, c_i^{\dagger} c_i + \mathbf{M}^2_{ii}\, c_i c_i^{\dagger}\right) + \frac{1}{2}\mathrm{Tr}\,\mathbf{M}^1 & (2.58)\\ &= \frac{1}{2}\sum_i \left(\mathbf{M}^1_{ii} - \mathbf{M}^2_{ii}\right) c_i^{\dagger} c_i + \frac{1}{2}\mathrm{Tr}\,\mathbf{M}^2 + \frac{1}{2}\mathrm{Tr}\,\mathbf{M}^1 \quad . & (2.59) \end{aligned}$$

Comparing this equation with the expression for $\mathcal{H}^{\mathrm{D}}_{\mathrm{eff}}$ above yields:

$$\begin{aligned} \frac{1}{2}\left(\mathbf{M}^1_{ii} - \mathbf{M}^2_{ii}\right) &= \epsilon_i & (2.60)\\ \wedge\quad \mathrm{Tr}\,\mathbf{M} &= 0 \quad . & (2.61) \end{aligned}$$

From these equations it follows that the constraint $\mathrm{Tr}\,\mathbf{M} = 0$ causes no contradiction. On the other hand, the additional term $1/2\mathrm{Tr}\,\mathbf{M}^1$ cannot be omitted because this would lead to the following equations:

$$\begin{aligned} \frac{1}{2}\left(\mathbf{M}^1_{ii} - \mathbf{M}^2_{ii}\right) &= \epsilon_i & (2.62)\\ \wedge\quad \mathrm{Tr}\,\mathbf{M}^2 &= 0 \quad . & (2.63) \end{aligned}$$

However, if one uses the traceless condition for $\mathbf{M}$, namely $\mathrm{Tr}\,\mathbf{M} = \mathrm{Tr}\,(\mathbf{M}^1 + \mathbf{M}^2) = 0$, these equations are only valid if $\sum_i \epsilon_i = 0$, which is not true in general. The second

symmetry property in equation (2.55) can be derived using the anticommutation rules for the Nambu components in equation (2.52). In particular:

$$\begin{aligned}\bar{\mathbf{c}}^\dagger \mathbf{M} \bar{\mathbf{c}} &\doteq \sum_{\alpha\beta} \bar{c}^\dagger_\alpha \mathbf{M}_{\alpha\beta} \bar{c}_\beta \\ &= -\sum_{\alpha\beta} \bar{c}_\beta \mathbf{M}^{\mathrm{T}}_{\beta\alpha} \bar{c}^\dagger_\alpha + \mathrm{Tr}\,\mathbf{M} \\ &= -\bar{\mathbf{c}}^{\mathrm{T}} \mathbf{M}^{\mathrm{T}} \bar{\mathbf{c}}^{\dagger\mathrm{T}} \\ &= -\bar{\mathbf{c}}^\dagger \boldsymbol{\Gamma} \mathbf{M}^{\mathrm{T}} \boldsymbol{\Gamma} \bar{\mathbf{c}} \quad , \end{aligned} \tag{2.64}$$

where the last equation arises from the definition of the transposed Nambu vectors in equation (2.51). This shows that $\mathbf{M}$ may be chosen so that $\mathbf{M} = -\boldsymbol{\Gamma}\mathbf{M}^{\mathrm{T}}\boldsymbol{\Gamma}$. This equation implies that $(\mathbf{M}^2)^{\mathrm{T}} = -\mathbf{M}^1$ and with equation (2.61):

$$\mathbf{M}^1_{ii} = \epsilon_i \quad . \tag{2.65}$$

It should be mentioned that, due to terms with $g_i(q) > 0$, both the effective Hamiltonian $\mathcal{H}_{\mathrm{eff}}$ and hence the matrix $\mathbf{M}$ are not necessarily hermitian.

Now, whenever the v-dependence of one of the previously defined functionals is given by $\mathcal{H}_{\mathrm{eff}}[v]$, it may also be considered as a functional of $\mathbf{M}$. In the forthcoming sections and chapters we shall use both representations, the v-representation defined by $\mathcal{H}_{\mathrm{eff}}[v]$ and the $\mathbf{M}$-representation defined by $\mathcal{H}_{\mathrm{eff}}[\mathbf{M}]$. They are distinguished by the argument given in brackets. Occasionally we shall omit the argument, indicating that the functional dependence on v or $\mathbf{M}$ is of no interest or that the expression is valid for both representations.

For the calculations below it is useful to introduce a new symbol for the quadratic and the constant[2] part of the effective Hamiltonian, namely:

$$\mathcal{H}_{\mathrm{eff}}[v] = \mathcal{H}^{\mathrm{q}}_{\mathrm{eff}}[v] + \mathcal{H}^{\mathrm{c}}_{\mathrm{eff}}[v] \quad , \tag{2.66}$$

with

$$\mathcal{H}^{\mathrm{q}}_{\mathrm{eff}}[v] := \frac{1}{2}\bar{\mathbf{c}}^\dagger \mathbf{M}[v] \bar{\mathbf{c}} \quad \text{and} \tag{2.67}$$

$$\mathcal{H}^{\mathrm{c}}_{\mathrm{eff}}[v] := \frac{1}{2}\mathrm{Tr}\,\mathbf{M}^1[v] \quad . \tag{2.68}$$

Accordingly the effective free energy functional is also devided into two parts:

$$F_{\mathrm{eff}}[v] = F^{\mathrm{q}}_{\mathrm{eff}}[v] + \frac{1}{\beta}\int_0^\beta \mathcal{H}^{\mathrm{c}}_{\mathrm{eff}}[v] \quad , \tag{2.69}$$

[2]This means that it is no longer an operator but still a functional of the fields.

where $F^{q}_{\rm eff}[v]$ is the free energy functional given in equation (2.45) where $\mathcal{H}_{\rm eff}[v]$ has been replaced by $\mathcal{H}^{q}_{\rm eff}[v]$. Because $\mathrm{Tr}\,\mathbf{M}^{1}[v] = \sum_i \epsilon[v]$, only $F^{q}_{\rm eff}[v]$ needs to be calculated, which is shown in the next sections.

2.3.2 The Time Evolution Operator Corresponding to the Effective Hamiltonian

In order to calculate the functional derivatives of $F_{\rm eff}$, it is useful to introduce the time evolution operator which belongs to the effective Hamiltonian. As for any time-dependent Hamiltonian [Mahan90], it is definded by:

$$\tilde{\mathcal{S}}_{\rm eff}(\tau_2,\tau_1) := \mathrm{T}\exp\left(-\int_{\tau_1}^{\tau_2}\mathcal{H}_{\rm eff}(\tau')d\tau'\right) \quad . \tag{2.70}$$

This operator has some nice properties, including:

$$\begin{aligned}\tilde{\mathcal{S}}_{\rm eff}(\tau_2,\tau_1) &= \mathcal{S}_{\rm eff}(\tau_2)\mathcal{S}^{-1}_{\rm eff}(\tau_1)\\ \tilde{\mathcal{S}}_{\rm eff}(\tau_3,\tau_1) &= \tilde{\mathcal{S}}_{\rm eff}(\tau_3,\tau_2)\tilde{\mathcal{S}}_{\rm eff}(\tau_2,\tau_1) \quad ,\end{aligned}$$

where $\mathcal{S}_{\rm eff}(\tau)$ and its inverse $\mathcal{S}^{-1}_{\rm eff}(\tau)$ are defined by:

$$\mathcal{S}_{\rm eff}(\tau) := \mathrm{T}\exp\left(-\int_0^{\tau}\mathcal{H}_{\rm eff}(\tau')d\tau'\right) \tag{2.71}$$

$$\mathcal{S}^{-1}_{\rm eff}(\tau) := \overline{\mathrm{T}}\exp\left(\int_0^{\tau}\mathcal{H}_{\rm eff}(\tau')d\tau'\right) \quad . \tag{2.72}$$

Here T orders the products of time-dependent operators with decreasing time argument, while $\overline{\mathrm{T}}$ orders them with increasing time argument. The time-dependence of an arbitrary operator $\mathcal{A}$ is as usual given by

$$\mathcal{A}(\tau) := \mathcal{S}^{-1}_{\rm eff}(\tau)\mathcal{A}\mathcal{S}_{\rm eff}(\tau) \quad . \tag{2.73}$$

Furthermore one can introduce an effective partition function

$$Z_{\rm eff} := \mathrm{Tr}\,\mathcal{S}_{\rm eff}(\beta) \quad , \tag{2.74}$$

so that the effective free energy functional becomes:

$$F_{\rm eff} = -\frac{1}{\beta}\ln\left(Z_{\rm eff}\right) \quad . \tag{2.75}$$

The partition function is then given by:

$$Z = \int \mathcal{D}^2 v \, Z_{\text{eff}}[v] \, g[v] \quad , \tag{2.76}$$

where $g[v]$ is the Gaussian weight factor in equation (2.47).

As for the full effective Hamiltonian $\mathcal{H}_{\text{eff}}$, one can also define the time evolution operator and the partition function for the quadratic part $\mathcal{H}^{\text{q}}_{\text{eff}}$ just by replacing $\mathcal{H}_{\text{eff}}$ by $\mathcal{H}^{\text{q}}_{\text{eff}}$ in the formulae above. The resulting quantities should be indexed by an upper index $^{\text{q}}$. Because $\mathcal{H}^{\text{c}}_{\text{eff}}[v]$ is for every field distribution a $\mathbb{C}$–number, $\mathcal{S}^{\text{q}}_{\text{eff}}(\tau)$ is related to $\mathcal{S}_{\text{eff}}(\tau)$ via

$$\mathcal{S}_{\text{eff}}(\tau) = \mathcal{S}^{\text{q}}_{\text{eff}}(\tau) \, \mathcal{S}^{\text{c}}_{\text{eff}}(\tau) \quad , \tag{2.77}$$

with

$$\mathcal{S}^{\text{q}}_{\text{eff}}(\tau) \;:=\; \mathrm{T} \exp\left(- \int_0^\tau \mathcal{H}^{\text{q}}_{\text{eff}}(\tau') d\tau' \right) \quad \text{and} \tag{2.78}$$

$$\mathcal{S}^{\text{c}}_{\text{eff}}(\tau) \;:=\; \exp\left(- \int_0^\tau \mathcal{H}^{\text{c}}_{\text{eff}}(\tau') d\tau' \right) \quad . \tag{2.79}$$

Accordingly, the effective partition function is given by

$$Z_{\text{eff}} = \mathcal{S}^{\text{c}}_{\text{eff}}(\beta) Z^{\text{q}}_{\text{eff}} \quad , \tag{2.80}$$

and the free energy functional is

$$F_{\text{eff}} = -\frac{1}{\beta} \ln \left(Z^{\text{q}}_{\text{eff}} \right) - \frac{1}{\beta} \ln \left(\mathcal{S}^{\text{c}}_{\text{eff}}(\beta) \right) \quad , \tag{2.81}$$

which leads to the same expression as in equation (2.69).

2.3.3 Functional Derivative of the Effective Free Energy Functional

Using the chain rule, the partial functional derivative of $F^{\text{q}}_{\text{eff}}[\mathbf{M}]$ with respect to $\mathbf{M}_{\alpha,\beta}(\tau)$ is given by:

$$\frac{\partial F^{\text{q}}_{\text{eff}}[\mathbf{M}]}{\partial \mathbf{M}_{\alpha,\beta}(\tau)} = -\frac{1}{\beta Z^{\text{q}}_{\text{eff}}[\mathbf{M}]} \frac{\partial Z^{\text{q}}_{\text{eff}}[\mathbf{M}]}{\partial \mathbf{M}_{\alpha,\beta}(\tau)} \quad . \tag{2.82}$$

For the derivative of the effective partition function, one has to take into account the time ordered product within the defintion of $\mathcal{S}^{\mathrm{q}}_{\mathrm{eff}}(\beta)$. This yields for $\epsilon > 0$ and $\epsilon \to 0$:

$$\frac{\partial Z^{\mathrm{q}}_{\mathrm{eff}}[\mathrm{M}]}{\partial \mathrm{M}_{\alpha,\beta}(\tau)} = \frac{\partial \mathrm{Tr}\left(\tilde{\mathcal{S}}^{\mathrm{q}}_{\mathrm{eff}}(\beta,\tau+\epsilon)\tilde{\mathcal{S}}^{\mathrm{q}}_{\mathrm{eff}}(\tau+\epsilon,\tau-\epsilon)\mathcal{S}^{\mathrm{q}}_{\mathrm{eff}}(\tau-\epsilon)\right)}{\partial \mathrm{M}_{\alpha,\beta}(\tau)} \tag{2.83}$$

$$= \mathrm{Tr}\left(\tilde{\mathcal{S}}^{\mathrm{q}}_{\mathrm{eff}}(\beta,\tau+\epsilon)\frac{\partial \tilde{\mathcal{S}}^{\mathrm{q}}_{\mathrm{eff}}(\tau+\epsilon,\tau-\epsilon)}{\partial \mathrm{M}_{\alpha,\beta}(\tau)}\mathcal{S}^{\mathrm{q}}_{\mathrm{eff}}(\tau-\epsilon)\right) . \tag{2.84}$$

Because ϵ is infinitesimally small, the second factor becomes

$$\frac{\partial \tilde{\mathcal{S}}^{\mathrm{q}}_{\mathrm{eff}}(\tau+\epsilon,\tau-\epsilon)}{\partial \mathrm{M}_{\alpha,\beta}(\tau)} = -\frac{1}{2}\bar{c}^{\dagger}_{\alpha}\bar{c}_{\beta} \qquad \text{for} \qquad \epsilon \to 0 \ . \tag{2.85}$$

Inserting this in equation (2.84) and introducing an identity operator $\mathcal{S}_{\mathrm{eff}}(\tau)\mathcal{S}^{-1}_{\mathrm{eff}}(\tau)$ between the creation and the annihilation operator and an appropriate number of factors $\mathcal{S}^{\mathrm{c}}_{\mathrm{eff}}(\tau)(\mathcal{S}^{\mathrm{c}}_{\mathrm{eff}}(\tau))^{-1}$ yields:

$$\frac{\partial Z^{\mathrm{q}}_{\mathrm{eff}}[\mathrm{M}]}{\partial \mathrm{M}_{\alpha,\beta}(\tau)} = -\frac{1}{2}\mathrm{Tr}\left(\mathcal{S}^{\mathrm{q}}_{\mathrm{eff}}(\beta)\bar{c}^{\dagger}_{\alpha}(\tau)\bar{c}_{\beta}(\tau)\right) \ , \tag{2.86}$$

where the time–dependence of the creation and annihilation operators is defined by the full effective Hamiltonian in equation (2.73). Finally, the partial derivative of the effective free energy functional becomes

$$\frac{\partial F^{\mathrm{q}}_{\mathrm{eff}}[\mathrm{M}]}{\partial \mathrm{M}_{\alpha,\beta}(\tau)} = \frac{1}{2\beta}\left\langle \bar{c}^{\dagger}_{\alpha}(\tau)\bar{c}_{\beta}(\tau)\right\rangle_{\mathrm{eff}} \ , \tag{2.87}$$

where $\langle \ldots \rangle_{\mathrm{eff}}$ is an abbreviation for $\mathrm{Tr}\,(\mathcal{S}_{\mathrm{eff}}(\beta)\ldots)/Z_{\mathrm{eff}}[\mathrm{M}]$. Note that $\mathcal{S}_{\mathrm{eff}}(\beta)$ and $\mathcal{S}_{\mathrm{eff}}(\tau)$ are in general noncommutative operators due to the time–dependence of the effective Hamiltonian, so that the expectation value above is time–dependent as well.

2.3.4 The Greens Function

In order to calculate the right hand side of equation (2.87), one introduces a generalized field dependent one–particle Greens function matrix:

$$\mathbf{G}_{\mathrm{eff}}(\tau,\tau') := \left\langle \mathrm{T}\bar{\mathbf{c}}(\tau)\bar{\mathbf{c}}^{\dagger}(\tau')\right\rangle_{\mathrm{eff}} \ , \tag{2.88}$$

including both diagonal and nondiagonal — the anomalous — contributions. Here the time–dependence is defined by the effective time evolution operator according to equation

(2.73) and the time order operator T orders the operators with decreasing time argument. That is, due to the fermionic character of the creation and annihilation operators, $\mathbf{G}_{\text{eff}}$ is given by:

$$\mathbf{G}_{\text{eff}}(\tau,\tau') = \begin{cases} \left\langle \bar{\mathbf{c}}(\tau)\bar{\mathbf{c}}^{\dagger}(\tau')\right\rangle_{\text{eff}} & \text{for} \quad \tau > \tau' \\ -\left\langle \bar{\mathbf{c}}^{\dagger \mathrm{T}}(\tau')\bar{\mathbf{c}}^{\mathrm{T}}(\tau)\right\rangle_{\text{eff}}^{\mathrm{T}} & \text{for} \quad \tau < \tau' \quad . \end{cases} \tag{2.89}$$

In components:

$$\mathbf{G}_{\text{eff}}(\tau,\tau')_{\alpha,\beta} = \begin{cases} \left\langle \bar{c}_{\alpha}(\tau)\bar{c}^{\dagger}_{\beta}(\tau')\right\rangle_{\text{eff}} & \text{for} \quad \tau > \tau' \\ -\left\langle \bar{c}^{\dagger}_{\beta}(\tau')\bar{c}_{\alpha}(\tau)\right\rangle_{\text{eff}} & \text{for} \quad \tau < \tau' \quad . \end{cases} \tag{2.90}$$

The right hand side of equation (2.87) now results from the Greens function in the limit $\tau' \searrow \tau$. In fact:

$$\frac{\partial F^{\mathrm{q}}_{\text{eff}}[\mathbf{M}]}{\partial \mathbf{M}_{\alpha,\beta}(\tau)} = -\frac{1}{2\beta}\,\mathbf{G}_{\text{eff}}(\tau,\tau^{+})_{\beta,\alpha} \quad , \tag{2.91}$$

or, defining

$$\left(\frac{\partial F^{\mathrm{q}}_{\text{eff}}[\mathbf{M}]}{\partial \mathbf{M}}\right)_{\alpha,\beta} := \frac{\partial F^{\mathrm{q}}_{\text{eff}}[\mathbf{M}]}{\partial \mathbf{M}_{\beta,\alpha}(\tau)} \tag{2.92}$$

equation (2.87) may be rewritten in matrix form:

$$\frac{\partial F^{\mathrm{q}}_{\text{eff}}[\mathbf{M}]}{\partial \mathbf{M}} = -\frac{1}{2\beta}\,\mathbf{G}_{\text{eff}}(\tau,\tau^{+}) \quad . \tag{2.93}$$

2.3.5 The Equation of Motion

There exist several ways of calculating $\mathbf{G}_{\text{eff}}$. The most important and practical method is the derivation of an equation of motion with respect to its first time argument. Formally it is given by:

$$\frac{\partial}{\partial\tau}\mathbf{G}_{\text{eff}}(\tau,\tau') = \delta(\tau-\tau')\,\mathbf{1} + \left\langle \mathrm{T}\left[\mathcal{H}_{\text{eff}}(\tau),\bar{\mathbf{c}}\right](\tau)\,\bar{\mathbf{c}}^{\dagger}(\tau')\right\rangle_{\text{eff}} \quad . \tag{2.94}$$

Here the τ-dependence of $\mathcal{H}_{\text{eff}}$ according to the time dependence of v is explicitly indicated. The commutator has to be calculated for all components of $\bar{\mathbf{c}}$. Using the matrix representation of $\mathcal{H}_{\text{eff}}(\tau)$ yields

$$\begin{aligned}
\left[\mathcal{H}_{\text{eff}}(\tau), \bar{c}_\delta\right] &= \frac{1}{2}\sum_{\alpha\beta} \mathbf{M}_{\alpha\beta}(\tau)\left[\bar{c}^\dagger_\alpha \bar{c}_\beta, \bar{c}_\delta\right] \\
&= \frac{1}{2}\sum_{\alpha\beta} \mathbf{M}_{\alpha\beta}(\tau)\left\{\left(2\bar{c}^\dagger_\alpha \bar{c}_\delta - \delta_{\alpha\delta}\right)\bar{c}_\beta + \bar{c}^\dagger_\alpha\left(2\bar{c}_\beta \bar{c}_\delta - \Gamma_{\alpha\delta}\right)\right\} \\
&= \frac{1}{2}\sum_{\alpha\beta} \mathbf{M}_{\alpha\beta}(\tau)\left\{2\bar{c}^\dagger_\alpha \underbrace{\left[\bar{c}_\delta, \bar{c}_\beta\right]_+}_{=\Gamma_{\beta\delta}} - \delta_{\alpha\delta}\bar{c}_\beta - \Gamma_{\beta\delta}\bar{c}^\dagger_\alpha\right\} \\
&= -\frac{1}{2}\sum_{\beta} \mathbf{M}_{\delta\beta}(\tau)\bar{c}_\beta + \frac{1}{2}\sum_{\alpha\beta} \mathbf{M}_{\alpha\beta}(\tau)\Gamma_{\beta\delta}\bar{c}^\dagger_\alpha \quad . \qquad (2.95)
\end{aligned}$$

Note that the constant part of $\mathcal{H}_{\text{eff}}$ provides no contribution. The second term may be written as follows:

$$\sum_{\alpha\beta} \mathbf{M}_{\alpha\beta}(\tau)\Gamma_{\beta\delta}\bar{c}^\dagger_\alpha = \sum_{\alpha\beta} \Gamma_{\delta\beta}\mathbf{M}^{\mathrm{T}}_{\beta\alpha}(\tau)\bar{c}^\dagger_\alpha = \left(\boldsymbol{\Gamma}\mathbf{M}^{\mathrm{T}}\bar{\mathbf{c}}^{\dagger\mathrm{T}}\right)_\delta \quad . \qquad (2.96)$$

Using equations 2.50 and (2.55), this expression becomes the same as the first term, so that finally the commutator for all components is:

$$[\mathcal{H}_{\text{eff}}(\tau), \bar{\mathbf{c}}] = -\mathbf{M}(\tau)\,\bar{\mathbf{c}} \quad . \qquad (2.97)$$

Because of the time-ordered product one has to be careful introducing this result into the equation of motion (2.94) above. For $\tau > \tau'$ one obtains:

$$\left\langle [\mathcal{H}_{\text{eff}}(\tau), \bar{\mathbf{c}}](\tau)\,\bar{\mathbf{c}}^\dagger(\tau')\right\rangle_{\text{eff}} = -\mathbf{M}(\tau)\,\mathbf{G}_{\text{eff}}(\tau, \tau') \quad , \qquad (2.98)$$

and for $\tau < \tau'$:

$$\begin{aligned}
-\left\langle \bar{\mathbf{c}}^{\dagger\mathrm{T}}(\tau')\left[\mathcal{H}_{\text{eff}}(\tau), \bar{\mathbf{c}}^{\mathrm{T}}\right](\tau)\right\rangle^{\mathrm{T}}_{\text{eff}} &= -\left\langle \bar{\mathbf{c}}^{\dagger\mathrm{T}}(\tau')\,[\mathcal{H}_{\text{eff}}(\tau), \bar{\mathbf{c}}]^{\mathrm{T}}(\tau)\right\rangle^{\mathrm{T}}_{\text{eff}} \\
&= \left\langle \bar{\mathbf{c}}^{\dagger\mathrm{T}}(\tau')\,\bar{\mathbf{c}}^{\mathrm{T}}(\tau)\mathbf{M}^{\mathrm{T}}(\tau)\right\rangle^{\mathrm{T}}_{\text{eff}} \\
&= -\mathbf{M}(\tau)\,\mathbf{G}_{\text{eff}}(\tau, \tau') \quad .
\end{aligned}$$

That is, the final form of the equation of motion for the one-particle Greens function becomes:

$$\frac{\partial}{\partial\tau}\mathbf{G}_{\text{eff}}(\tau, \tau') = \delta(\tau - \tau')\,\mathbf{1} - \mathbf{M}(\tau)\,\mathbf{G}_{\text{eff}}(\tau, \tau') \quad . \qquad (2.99)$$

This is a system of coupled linear differential equations and can therefore be solved exactly. It should be emphasized that, due to the τ–dependence of $\mathbf{M}(\tau)$, a Fourier transformation method does not map this system onto a system of algebraic equations, so it has to be integrated directly.

2.3.6 The Effective Free Energy Formula

From equation (2.99) it becomes clear that the inverse of $\mathbf{G}_{\text{eff}}$ is given by:

$$\mathbf{G}_{\text{eff}}^{-1}(\tau,\tau') = \left(\frac{\partial}{\partial\tau} + \mathbf{M}(\tau)\right)\delta(\tau-\tau') \quad . \tag{2.100}$$

$\mathbf{G}_{\text{eff}}^{-1}$ is linear in $\mathbf{M}(\tau)$, so it is not very difficult to guess the functional dependence of the effective free energy on $\mathbf{G}_{\text{eff}}$ and hence on $\mathbf{M}$:

$$F_{\text{eff}}^{\text{q}} = -\frac{1}{2\beta}\,\text{Tr}\,\ln\left(-\mathbf{G}_{\text{eff}}^{-1}(\tau,\tau^+)\right) \quad , \tag{2.101}$$

where Tr includes both a matrix trace and a τ–integration from 0 to β. In order to prove this formula, one only has to calculate the functional derivative of the right hand side with respect to $\mathbf{M}$ and compare the result with equation (2.91). This yields:

$$\begin{aligned}
\frac{\partial F_{\text{eff}}^{\text{q}}[\mathbf{M}]}{\partial \mathbf{M}_{\alpha,\beta}(\tau)} &= -\frac{1}{2\beta}\int_0^\beta d\tau_1 \sum_{\gamma,\delta} \mathbf{G}_{\text{eff}}(\tau_1,\tau_1^+)_{\gamma,\delta}\,\frac{\partial \mathbf{G}_{\text{eff}}^{-1}(\tau_1,\tau_1^+)_{\delta,\gamma}}{\partial \mathbf{M}_{\alpha,\beta}(\tau)} \\
&= -\frac{1}{2\beta}\int_0^\beta d\tau_1 \sum_{\gamma,\delta} \mathbf{G}_{\text{eff}}(\tau_1,\tau_1^+)_{\gamma,\delta}\,\delta_{\delta,\alpha}\,\delta_{\gamma,\beta}\,\delta(\tau-\tau_1) \\
&= -\frac{1}{2\beta}\,\mathbf{G}_{\text{eff}}(\tau,\tau^+)_{\beta,\alpha} \quad .
\end{aligned}$$

Finally, the free energy functional $F^{\#}$ is given by:

$$\begin{aligned}
F^{\#}[v] &= -\frac{1}{2\beta}\,\text{Tr}\,\ln\left(-\mathbf{G}_{\text{eff}}^{-1}(\tau,\tau^+)\right) \\
&\quad + \frac{1}{\beta}\int_0^\beta \sum_{i,q} |g_i(q)|\,|v_i(q,\tau)|^2\,d\tau + \frac{1}{2\beta}\text{Tr}\,\mathbf{M}^1[v] \quad .
\end{aligned} \tag{2.102}$$

This formula will be used in the next chapter 3 dealing with approximations, in particular for the saddle point approximation.

2.4 The Functional Integral Representation for the NNSP Model

In this last section of this chapter we shall write down explicitly the functional integral representation of the NNSP model. The possible quadratic forms of the interaction term have already been derived in section 2.1 and are summarized in table 2.2. The first column gives the representation index and the second column its type. The third column shows the corresponding field operators, whereas the fourth and the fifth column define the field variables related to them and their nature, respectively. The last column summarizes the coupling constants. Introducing for each of the representations a real parameter $\lambda_i \geq 0$ with $\sum_i^3 \lambda_i = 1$, where i is the index in table 2.2, leads to an effective Hamiltonian of the following form:

$$
\begin{aligned}
&\mathcal{H}_{\text{eff}}[\rho, m, \Delta, \Omega] = \\
&\quad \mathcal{H}_0 + \lambda_3 \frac{Wz}{2} \sum_k n_k && \text{free part} \\
&\quad + \lambda_1 \frac{Wz}{2} L \sum_q S(q) \sqrt{\operatorname{sgn}(S(q))}\, \eta_q \rho(q,\tau) && \text{CDW} \\
&\quad - \lambda_1 2WzL \sum_q S(q) \sqrt{\operatorname{sgn}(-S(q))}\, s_q m(q,\tau) && \text{SDW} \\
&\quad + \lambda_2 WL \sum_q \sum_\alpha \left\{ P_\alpha^\dagger(q) \Delta_\alpha(q,\tau) + P_\alpha(q) \Delta_\alpha^*(q,\tau) \right\} && \text{Pairing} \\
&\quad - i\lambda_3 WL \sum_q \sum_\alpha \left\{ Q_\alpha^\dagger(q) \Omega_\alpha(q,\tau) + Q_\alpha(q) \Omega_\alpha^*(q,\tau) \right\} && \text{SF} \quad .
\end{aligned}
\tag{2.103}
$$

Remember that W is assumed to be negative. In the forthcoming treatment we shall neglect the SF representation, i. e. we select $\lambda_3 = 0$. In order to get rid of the square root in the second and third term in equation (2.103), it is useful to introduce a band index $\nu \in \{0, 1\}$ and restrict the q–sum to the inner half of the first Brioullin zone. This means that the q–sum is divided into two parts according to:

$$
\sum_q f(q) = \sum_{\nu,q}{}' f(q + \nu Q) = \sum_{\nu,q}{}' f_\nu(q) \quad , \tag{2.104}
$$

where f is an arbitrary function of q, which respects the lattice symmetry, and Q is the antiferromagnetic wave vector. The prime indicates the restricted q–sum. This formal procedure is depicted in figure 2.1 for a square lattice, where the first Brioullin zone is shown (thin dashed line). Introducing the band index means that one replaces the sum

Table 2.2: Quadratic representations of the interaction of the NNSP model

index	representation	field – operator	conj. field – variable	nature	coupling constant
1	CDW	$\eta_q = \eta_q^\dagger$	$\rho(q,\tau)$	real	$WzL\,S(q)/4$
	SDW	$s_q = s_q^\dagger$	$m(q,\tau)$	real	$-WzL\,S(q)$
2	Pairing	$\left\{P_\alpha^\dagger(q)\right\}_{\alpha=1\ldots z}$	$\left\{\Delta_\alpha(q,\tau)\right\}_{\alpha=1\ldots z}$	complex	WL
3	SF	$\left\{Q_\alpha^\dagger(q)\right\}_{\alpha=1\ldots z}$	$\left\{\Omega_\alpha(q,\tau)\right\}_{\alpha=1\ldots z}$	complex	$-WL$

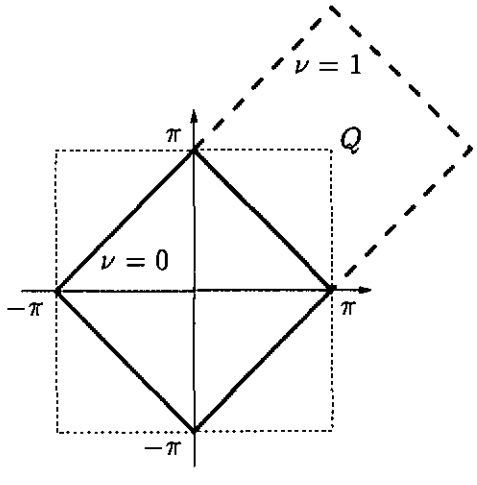

Figure 2.1: The first Brioullin zone for a square lattice of lattice constant one (thin dashed line). The thick solid line surrounds the inner half of it, whereas the thick dashed line marks this region shifted by $Q = (\pi, \pi)$.

over the first Brioullin zone by a sum over the two regions labeled by $\nu = 0$ and $\nu = 1$. This replacement is valid because the sum over the $\nu = 1$ region is equivalent to the sum over the four triangles left by subtracting the inside of the solid line from the first Brioullin zone. This procedure might seem a bit artificial but the advantage is that the sign of the structure function as defined in equation (1.10) is now fixed for both bands:

$$\left.\begin{array}{rcrcl} S_0(q) & = & S(q) & \geq & 0 \\ S_1(q) & = & -S(q) & \leq & 0 \end{array}\right\} \quad \forall q \in 1/2\,\mathrm{Bz} \quad . \tag{2.105}$$

Using this in equation (2.103), the effective Hamiltonian finally becomes:

$$\begin{aligned}
\mathcal{H}_{\text{eff}}[\rho, m, \Delta] \;=\; & \mathcal{H}_0 && \text{free part} \\
& + \lambda_1 \frac{Wz}{2} L \sum_{\nu,q}{}' S_\nu(q)\, i^\nu\, \eta_\nu(q) \rho_\nu(q,\tau) && \text{CDW} \\
& - \lambda_1 2WzL \sum_{\nu,q}{}' S_\nu(q)\, i^{(1-\nu)}\, s_\nu(q) m_\nu(q,\tau) && \text{SDW} \\
& + \lambda_2 WL \sum_q \sum_\alpha \left\{ P^\dagger_\alpha(q) \Delta_\alpha(q,\tau) + P_\alpha(q) \Delta^*_\alpha(q,\tau) \right\} && , \quad \text{Pairing}
\end{aligned} \tag{2.106}$$

where the ν–dependent field variables and operators have to be understood in the sense of equation (2.104). The partition function can now be expressed as a functional integral over the fields ρ, m and Δ. Explicitely:

$$Z = \int \mathcal{D}\rho \mathcal{D} m \mathcal{D}^2 \Delta \; \exp\left(-\beta F^{\#}[\rho, m, \Delta]\right) \quad , \tag{2.107}$$

with

$$\begin{aligned}
F^{\#}[\rho, m, \Delta] \;=\; & F_{\text{eff}}[\rho, m, \Delta] + \\
& + \frac{|W|\, zL}{\beta} \int_0^\beta d\tau \sum_q \left\{ |S(q)| \left(|\rho(q,\tau)|^2 + \frac{|m(q,\tau)|^2}{4} \right) + \frac{1}{z} \sum_\alpha |\Delta_\alpha(q,\tau)|^2 \right\} \quad .
\end{aligned} \tag{2.108}$$

As before, $F_{\text{eff}}[\rho, m, \Delta]$ is the field–, and therefore time–dependent effective free energy functional related to $\mathcal{H}_{\text{eff}}[\rho, m, \Delta]$. Note that in equation (2.108) above, the q–sum ranges over the entire first Brioullin zone because the introduction of the band index makes no sense in this context. The contributions in the curly brackets are all positive. Based on this expression many approximations are possible. In the next chapter 3 they are derived from a general point of view, whereas chapters 4 to 5 are dealing with the application of these approximatins to the NNSP model.

Chapter 3

Approximations

Is it worth this effort? This is a good and legitimate question. It can be answered with a few points. First of all, the derived effective Hamiltonian is one–particle operator, so that in principle $F^{\#}$ may be calculated exactly for every path $v_i(q,\tau)$. But practically this is in nearly all cases impossible. Furthermore, if one is able to calculate the free energy functional, the functional integration over all paths still remains which is also a nonsolvable task. To our knowledge, only Gaussian path integrals can be exactly evaluated. Hence, approximations are necessary. Here lies the real strength of this formalism. From the functional integral representation of the partition function, several approximation schemes may be derived. Furthermore it provides an idea on how to understand these approximations, about what is neglected and what one has to do in order to improve them. On top of most approximations is the restriction on time–independent fields. For this reason implications of this restriction are discussed in section 3.1. The saddle point and mean field approximations are described in section 3.2. The latter is related to the standard symmetry–broken Hartree Fock Bogoliubov approximation, which is not based on the functional integral formalism. It is derived from a variational point of view in section 3.3.

3.1 Time–Independent Fields and Computation of the Free Energy Functional

The time–independent field approximation (TIFA) is one of the most important approximations because it enables the explicit calculation of the effective Greens function matrix and of the free energy functional. Neglecting the time dependence means that the functional integral is only performed over time–independent fields $v_i(q)$. The effective Hamiltonian becomes then time–independent as well, and the time ordering operator becomes

the identity or can just be omitted. This yields:

$$Z = \int \mathcal{D}^2 v \, \exp\left(-\beta F_{\text{eff}}[v]\right) \, g[v] \tag{3.1}$$

with

$$F_{\text{eff}}[v] = -\frac{1}{\beta} \ln\left(\text{Tr} \exp\left(-\beta \mathcal{H}_{\text{eff}}[v]\right)\right) \tag{3.2}$$

$$g[v] = \exp\left(-\beta \sum_{i,q} |g_i(q)| \, |v_i(q)|^2\right) \quad , \tag{3.3}$$

where

$$\mathcal{H}_{\text{eff}}[v] = \mathcal{H}_0 + \sum_{i,q} \sqrt{\text{sgn}(-g_i(q))} \, g_i(q) \, \left(h_i^\dagger(q) v_i(q) + h_i(q) v_i^*(q)\right) \quad . \tag{3.4}$$

In this case the effective Greens function matrix $\mathbf{G}_{\text{eff}}(\tau, \tau')$ depends only on the time difference of its arguments, which leads to the definition of the Greens function with only one time argument:

$$\mathbf{G}_{\text{eff}}(\tau) := \mathbf{G}_{\text{eff}}(\tau, 0) \quad . \tag{3.5}$$

Because this is a fermionic Greens function, it obeys the typical antiperiodic feature:

$$\mathbf{G}_{\text{eff}}(\tau - \beta) = -\mathbf{G}_{\text{eff}}(\tau) \qquad \text{for} \qquad \tau \in \,]0, \beta] \quad , \tag{3.6}$$

which follows from the cyclic invariance of the trace operation and from $[\mathcal{S}_{\text{eff}}(\tau_1), \mathcal{S}_{\text{eff}}(\tau_2)] = 0$ for all τ_1, τ_2 due to the time-independence of $\mathcal{H}_{\text{eff}}$. For this reason, $\mathbf{G}_{\text{eff}}(\tau)$ may be expanded in a Fourier series in the region $-\beta < \tau \leq \beta$. We are using the following definition of the Fourier transformation:

$$\mathbf{G}_{\text{eff}}(\tau) = \frac{1}{\beta} \sum_n \mathbf{G}_{\text{eff}}(\omega_n) \, e^{i\omega_n \tau} \tag{3.7}$$

$$\mathbf{G}_{\text{eff}}(\omega_n) = \int_0^\beta d\tau \, \mathbf{G}_{\text{eff}}(\tau) \, e^{-i\omega_n \tau} \quad , \tag{3.8}$$

where the ω_n are the fermionic Matsubara frequencies given by

$$\omega_n = (2n+1)\frac{\pi}{\beta} \qquad \forall n \in Z \quad . \tag{3.9}$$

Usually one introduces a new symbol for the Fourier transfrom of $\mathbf{G}_{\text{eff}}(\tau)$, but we prefer to distinguish $\mathbf{G}_{\text{eff}}(\tau)$ and its Fourier transfrom $\mathbf{G}_{\text{eff}}(\omega_n)$ by their argument. With this

transformation, the equation of motion for $\mathbf{G}_{\text{eff}}(\tau)$ is mapped onto an algebraic equation for $\mathbf{G}_{\text{eff}}(\omega_n)$:

$$\Big(i\omega_n + \mathbf{M}[v]\Big)\mathbf{G}_{\text{eff}}(\omega_n) = \mathbf{1} \tag{3.10}$$

with the formal solution

$$\mathbf{G}_{\text{eff}}(\omega_n) = \frac{1}{(i\omega_n + \mathbf{M}[v])} \quad , \tag{3.11}$$

which means that $\mathbf{G}_{\text{eff}}(\omega_n)$ is the inverse of $(i\omega_n + \mathbf{M}[v])$. As in the case of a one-component Greens function for free fermions, the ω_n-sum in equation (3.7) can be calculated explicitly (see e. g. [Mahan90]). This yields:

$$\mathbf{G}_{\text{eff}}(\tau) = \exp\Big(-\mathbf{M}[v]\,\tau\Big)\Big\{\Big[1 - f(\mathbf{M}[v])\Big]\,\Theta(\tau) - f(\mathbf{M}[v])\,\Theta(-\tau)\Big\} \quad , \tag{3.12}$$

where $f(x)$ is the Fermi distribution function defined by

$$f(x) := \frac{1}{e^{\beta x} + 1} \quad . \tag{3.13}$$

Differentiating equation (3.12) leads back to the original equation of motion for $\mathbf{G}_{\text{eff}}(\tau)$. The limit $\mathbf{G}_{\text{eff}}(\tau, \tau^+)$ corresponds to the limit

$$\mathbf{G}_{\text{eff}}(\tau = 0^-) = -f(\mathbf{M}[v]) = -\frac{1}{e^{\beta\mathbf{M}[v]} + 1} \quad . \tag{3.14}$$

Hence, the functional dependence of F_{eff} on $\mathbf{M}[v]$ is given by

$$F_{\text{eff}}[\mathbf{M}[v]] = -\frac{1}{2\beta}\text{Tr}\,\ln\left(e^{\beta\mathbf{M}[v]} + 1\right) + \frac{1}{2}\text{Tr}\,\mathbf{M}^1[v] \tag{3.15}$$

or with $\text{Tr}\,\mathbf{M}[v] = 0$:

$$F_{\text{eff}}[\mathbf{M}[v]] = -\frac{1}{2\beta}\text{Tr}\,\ln\left(2\cosh\left(\frac{\beta\mathbf{M}[v]}{2}\right)\right) + \frac{1}{2}\text{Tr}\,\mathbf{M}^1[v] \quad . \tag{3.16}$$

This is one of the most important results concerning this approximation because it explicitly provides for the functional dependence of the free energy functional on the fields.

The physical meaning of the time-independent field approximation becomes clear if one goes back to the point where the time-dependence was introduced. It is therefore

exact if one is allowed to neglect the time–ordering operator within the Trotter–Suzuki decomposition, i. e. if the commutator of the kinetic and the interaction part of the original Hamiltonian vanishes. From this point of view, the time–independent field approximation neglects quantum correlations or fluctuations. But one cannot say that the original model described by $\mathcal{H}$ is approximated by a classical model because the creation and annihilation operators are still treated quantummechanically, i. e. their commutation or anticommutation rules are not neglected. Thermal fluctuations are included because the functional integration over the time–independent fields $v_i(q)$ still needs to be done, which is the reason why further approximations are necessary.

3.2 Saddle Point and Mean Field Approximation

3.2.1 General Saddle Point Approximation for Time–Dependent Fields

The basic idea behind a saddle point approximation is the assumption that the functional integral in equation (2.41) may be replaced by the value of the integrand related to the minimum of $F^{\#}$. A functional differentiation of $F^{\#}$ with respect to $v_i(q,\tau)$ yields to equations for the field variables which belong to a minimum, maximum or a saddle point of $F^{\#}$. They are in general coupled nonlinear integral equations which might have many solutions. However, one has to find the solution which belongs to the global minimum of $F^{\#}$. The functional differentiation of $F^{\#}$ with respect to $v_i(q,\tau)$ is performed using the technique described in chapter 2.3, which yields:

$$\frac{\partial F^{\#}[v]}{\partial v_i(q,\tau)} = \frac{\partial F_{\text{eff}}[v]}{\partial v_i(q,\tau)} + \frac{1}{\beta}\,|g_i(q)|\,v_i^*(q,\tau) \tag{3.17}$$

with

$$\frac{\partial F_{\text{eff}}[v]}{\partial v_i(q,\tau)} = \frac{1}{\beta}\sqrt{\text{sgn}(-g_i(q))}\,g_i(q)\,\left\langle h_i^{\dagger}(q,\tau)\right\rangle_{\text{eff}} \quad . \tag{3.18}$$

Note that $v_i(q,\tau)$ and $v_i^*(q,\tau)$ are treated here as independent variables instead of the imaginary and real part of $v_i(q,\tau)$. Finally the saddle point equations are:

$$v_i(q,\tau) = \text{sgn}(-g_i(q))^{3/2}\left\langle h_i(q,\tau)\right\rangle_{\text{eff}} \tag{3.19}$$

$$v_i^*(q,\tau) = \text{sgn}(-g_i(q))^{3/2}\left\langle h_i^{\dagger}(q,\tau)\right\rangle_{\text{eff}} \quad , \tag{3.20}$$

or taking the sign of the coupling constant explicitly into account, the first equation becomes:

$$v_i(q,\tau) = \begin{cases} -i \left\langle h_i(q,\tau) \right\rangle_{\text{eff}} & g_i(q) > 0 \\ \left\langle h_i(q,\tau) \right\rangle_{\text{eff}} & g_i(q) < 0 \end{cases} . \tag{3.21}$$

The equation for $v_i^*(q,\tau)$ is given by replacing $h_i(q,\tau)$ by its adjoint operator. These equations show that in a saddle point approximation the fields are more or less the expectation values of their corresponding field operators. A more detailed form of the selfconsistent equations may be derived using the Nambu representations of the field operators. Because $h_i(q,\tau)$ is a linear combination of products of the creation and annihilation operators, there exists a matrix $\mathbf{m}$ with

$$h_i(q) = \frac{1}{2}\bar{\mathbf{c}}^\dagger \mathbf{m}(i,q)\bar{\mathbf{c}} + \frac{1}{2}\mathrm{Tr}\,\mathbf{m}^1(i,q) \qquad \text{and} \tag{3.22}$$

$$h_i^\dagger(q) = \frac{1}{2}\bar{\mathbf{c}}^\dagger \mathbf{m}^\dagger(i,q)\bar{\mathbf{c}} + \frac{1}{2}\left(\mathrm{Tr}\,\mathbf{m}^1(i,q)\right)^* , \tag{3.23}$$

where $\mathbf{m}^\dagger = (\mathbf{m}^*)^{\mathrm{T}}$. The v–dependence of $\mathbf{M}[v]$ is therefore given by:

$$\mathbf{M}[v] = \mathbf{M}_0 + \sum_{i,q} \sqrt{\mathrm{sgn}(-g_i(q))}\, g_i(q) \left\{ \mathbf{m}^\dagger(i,q) v_i(q,\tau) + \mathbf{m}(i,q) v_i^*(q,\tau) \right\} , \tag{3.24}$$

where $\mathbf{M}_0$ is defined by:

$$\mathcal{H}_0 = \frac{1}{2}\bar{\mathbf{c}}^\dagger \mathbf{M}_0 \bar{\mathbf{c}} + \frac{1}{2}\mathrm{Tr}\,\mathbf{M}_0^1 \tag{3.25}$$

and is in general a diagonal matrix. This depends on the set of one–particle states defining the Nambu representation. The Nambu matrices for the field operators and for $\mathcal{H}_0$ obey the same symmetry properties as $\mathbf{M}$. In fact, the condition $\mathrm{Tr}\,\mathbf{M} = 0$ is equivalent to $\mathrm{Tr}\,\mathbf{m} = 0$ and $\mathrm{Tr}\,\mathbf{M}_0 = 0$ because the field variables are independent variables. Using equation (3.22) and (3.23), the selfconsistent equations are now given by:

$$v_i(q,\tau) = \frac{1}{2}\mathrm{sgn}(-g_i(q))^{3/2} \left\{ \mathrm{Tr}\,\mathbf{m}^1(i,q) - \mathrm{Tr}\,\left(\mathbf{G}_{\text{eff}}(\tau,\tau^+)\,\mathbf{m}(i,q)\right) \right\} . \tag{3.26}$$

The effective Greens function matrix can be calculated as a functional of all fields using the equation of motion method described in chapter 2. The equations above, including the complex conjugate equations, therefore define a complete set of selfconsistent equations for the saddle point fields. As mentioned above, they have, in general, many solutions. The solution which minimizes $F^{\#}$ should be named by $\bar{v}_i(q,\tau)$.

For the partition function and the free energy one obtains:

$$Z = \exp\left(-\beta F^{\#}[\overline{v}]\right) = Z_{\text{eff}}[\overline{v}]\, g[\overline{v}] \tag{3.27}$$

and

$$F = F^{\#}[\overline{v}] \quad . \tag{3.28}$$

For any kind of saddle point approximation the free energy is therefore indentical to the free energy functional evaluated at the saddle point fields $\overline{v}$.

In this approximation there is no more functional integration. For this reason thermal fluctuations of the fields are neglected. Quantum effects are included because the fields are still time dependent, which causes the problem of calculating the Greens function matrix and hence the mean values of the field operators. Combining both, the time–independent field and the saddle point approximation, overcomes this problem.

3.2.2 Time–Independent Saddle Point Approximation (TISPA)

For time–independent fields the free energy functional is explicitly given by:

$$F^{\#}[v] = -\frac{1}{2\beta}\,\mathrm{Tr}\,\ln\left(2\cosh\left(\frac{\beta \mathbf{M}[v]}{2}\right)\right) + \sum_{i,q} |g_i(q)|\,|v_i(q)|^2 + \frac{1}{2}\mathrm{Tr}\,\mathbf{M}^1[v] \quad . \tag{3.29}$$

Varying this expression with respect to $v_i^*(q)$ leads to the selfconsistent equations for time independent fields. The first term is just $F_{\text{eff}}^{\text{q}}[v]$ and using the chain rule, its functional derivative with respect to $v_i^*(q)$ is

$$\frac{\partial F_{\text{eff}}^{\text{q}}[\mathbf{M}[v]]}{\partial v_i^*(q)} = \sum_{\alpha,\beta} \frac{\partial F_{\text{eff}}^{\text{q}}[\mathbf{M}[v]]}{\partial \mathbf{M}_{\alpha,\beta}[v]}\, \frac{\partial \mathbf{M}_{\alpha,\beta}[v]}{\partial v_i^*(q)} \quad . \tag{3.30}$$

The second factor in the sum above may be directly calculated using equation (3.24), where the field operators are expressed by their Nambu representations. For the first factor the chain rule has to be used a second time. With the formula for $F_{\text{eff}}^{\text{q}}$ in equation (3.16), it is given by:

$$\begin{aligned}
\frac{\partial F_{\text{eff}}^{\text{q}}[\mathbf{M}[v]]}{\partial \mathbf{M}_{\alpha,\beta}[v]} &= -\frac{1}{4}\,\mathrm{Tr}\left(\tanh\left(\frac{\beta \mathbf{M}[v]}{2}\right)\frac{\partial \mathbf{M}[v]}{\partial \mathbf{M}_{\alpha,\beta}[v]}\right) \\
&= -\frac{1}{4}\sum_{\nu,\mu}\tanh\left(\frac{\beta \mathbf{M}[v]}{2}\right)_{\nu,\mu}\frac{\partial \mathbf{M}_{\mu,\nu}[v]}{\partial \mathbf{M}_{\alpha,\beta}[v]} \\
&= -\frac{1}{4}\tanh\left(\frac{\beta \mathbf{M}[v]}{2}\right)_{\beta,\alpha} \quad .
\end{aligned} \tag{3.31}$$

The functional derivative of the second and third term in equation (3.29) is straight forward, so that finally the selfconsistent equations for the time–independent saddle point approximation are:

$$v_i(q) = \frac{1}{2}\,\mathrm{sgn}(-g_i(q))^{3/2}\left\{\mathrm{Tr}\,\mathbf{m}^1(i,q) - \frac{1}{2}\,\mathrm{Tr}\left(\tanh\left(\frac{\beta\mathbf{M}[v]}{2}\right)\mathbf{m}(i,q)\right)\right\} \quad . \tag{3.32}$$

Thus, instead of differentiating $F^{\#}$ directly one can just use the general selfconsistent equations for time–dependent fields (3.26). For time–independent fields they read:

$$v_i(q) = \frac{1}{2}\,\mathrm{sgn}(-g_i(q))^{3/2}\left\{\mathrm{Tr}\,\mathbf{m}^1(i,q) - \mathrm{Tr}\,\left(\mathbf{G}_{\mathrm{eff}}(0^-)\mathbf{m}(i,q)\right)\right\} \quad . \tag{3.33}$$

Using the result for $\mathbf{G}_{\mathrm{eff}}(0^-)$ in equation (3.14), this equation becomes:

$$v_i(q) = \frac{1}{2}\,\mathrm{sgn}(-g_i(q))^{3/2}\left\{\mathrm{Tr}\,\mathbf{m}^1(i,q) + \mathrm{Tr}\,\left(f(\mathbf{M}[v])\mathbf{m}(i,q)\right)\right\} \quad . \tag{3.34}$$

Both equations (3.32) and (3.32) are equivalent because

$$f(-x) - f(x) = \tanh\left(\frac{\beta x}{2}\right) \quad , \tag{3.35}$$

$$f(-x) + f(x) = 1 \tag{3.36}$$

and $\mathrm{Tr}\,\mathbf{m}(i,q) = 0$ for all i and q. From the right–hand side of equation (3.32) or equation (3.32), it becomes explicitly clear that the selfconsistent equations are nonlinear integral equations. As above, the solution which minimizes the free energy functional should be named by $\overline{v}$.

As in the general time–dependent saddle point approximation, the free energy is now given by the free energy functional evaluated at $\overline{v}$:

$$F = F^{\#}[\overline{v}] = -\frac{1}{\beta}\ln\mathrm{Tr}\left(\exp\left[-\beta\left(\mathcal{H}_{\mathrm{eff}}[\overline{v}] + \sum_{i,q}|g_i(q)|\,|\overline{v}_i(q)|^2\right)\right]\right) \quad . \tag{3.37}$$

Moreover, the average value of an arbitrary operator $\mathcal{A}$ is given by:

$$\langle\mathcal{A}\rangle \overset{\mathrm{TISPA}}{=} \frac{\mathrm{Tr}\,\left(\exp\left(-\beta\mathcal{H}_{\mathrm{eff}}[\overline{v}]\right)\mathcal{A}\right)}{\mathrm{Tr}\,\exp\left(-\beta\mathcal{H}_{\mathrm{eff}}[\overline{v}]\right)} = \langle\mathcal{A}\rangle_{\mathrm{eff}} \quad , \tag{3.38}$$

because the common factor $g[\overline{v}]$ cancels out. For this reason, the TISPA might be understood in the way that the original Hamiltonian is replaced by $\mathcal{H}_{\mathrm{eff}}[\overline{v}] + \sum_{i,q}|g_i(q)|\,|\overline{v}_i(q)|^2$:

$$\mathcal{H} \overset{\mathrm{TISPA}}{\longrightarrow} \mathcal{H}_{\mathrm{TISPA}} := \mathcal{H}_{\mathrm{eff}}[\overline{v}] + \sum_{i,q}|g_i(q)|\,|\overline{v}_i(q)|^2 \quad . \tag{3.39}$$

From the calculation of the average value of $\mathcal{A}$, one might suggest that the TISPA is just the approximation where $\mathcal{H}$ is replaced by $\mathcal{H}_{\text{eff}}[\overline{v}]$. But because the free energy functional is calculated with respect to $\mathcal{H}_{\text{eff}}[\overline{v}] + \sum_{i,q} |g_i(q)|\,|v_i(q)|^2$, the quadratic terms have to be included. From this interpretation follows an important result: the field components $\overline{v}_i(q)$ for a non–hermitian field operator ($h_i^\dagger(q) \neq h_i(q)$) corresponding to positive coupling constants $g_i(q) \geq 0$ have to be zero. The proof of this statement is quite simple: the partition function and the free energy have to be real, and moreover $\langle \mathcal{A} \rangle = \langle \mathcal{A} \rangle_{\text{eff}}$ has to be real for any arbitrary hermitian operator $\mathcal{A}$. For this reason, $\mathcal{H}_{\text{TISPA}}$ and therefore all contributions to $\mathcal{H}_{\text{TISPA}}$, namely

$$\sqrt{\text{sgn}(-g_i(q))}\, g_i(q) \left(h_i^\dagger(q) v_i(q) + h_i(q) v_i^*(q) \right) + |g_i(q)|\,|v_i(q)|^2 \tag{3.40}$$

have to be hermitian. For a negative coupling constant this constraint is always satisfied. For positive coupling constants there are two cases. First, assume that the field operator is hermitian. In this case the expression above has to be replaced by[1]

$$2\,i\,g_i(q)\,h_i(q) v_i(q) + g_i(q) v_i(q)^2 \quad . \tag{3.41}$$

The substitution $v_i(q) \to i\,v_i(q)$ with $v_i(q) \in \mathbb{R}$ therefore yields a hermition operator:

$$2\,g_i(q)\,h_i(q) v_i(q) - g_i(q) v_i(q)^2 \quad , \tag{3.42}$$

which means that one can find an imaginary solution for the original field component. For a nonhermitian operator $h_i^\dagger(q) \neq h_i(q)$ and $g_i(q) > 0$, the field variable has to be a complex number and hence the substitution above cannot be used. For this reason the corresponding contribution to $\mathcal{H}_{\text{TISPA}}$ has to be zero.
Using this result, the effective Hamiltonian of the TISPA becomes

$$\mathcal{H}_{\text{TISPA}} = \mathcal{H}_0 + \sum_{i,q}{}^{*} g_i(q) \left\{ h_i^\dagger(q) v_i(q) + h_i(q) v_i^*(q) - |v_i(q)|^2 \right\} \quad , \tag{3.43}$$

where the starred sum indicates that the contributions for nonhermitian field operators corresponding to positive coupling constants are omitted and that for terms, including hermitian field operators corresponding to positive coupling constants, the variable transformation $v_i(q) \to i\,v_i(q)$ has been used. Finally, within this description, the selfconsistent equations for all fields become

$$v_i(q) = \left\langle h_i(q) \right\rangle \tag{3.44}$$

$$v_i^*(q) = \left\langle h_i^\dagger(q) \right\rangle \quad . \tag{3.45}$$

[1] See the Hubbard–Stratanovich transformation for real numbers on page 28.

In the same way as $\langle \mathcal{A} \rangle$ is replaced by $\langle \mathcal{A} \rangle_{\text{eff}}$, the one–particle Greens function matrix is given by the effective Greens function matrix[2]:

$$\mathbf{G}(\tau) \overset{\text{TISPA}}{\longrightarrow} \mathbf{G}_{\text{eff}}(\tau) \quad , \tag{3.46}$$

or

$$\mathbf{G}(\omega_n) \overset{\text{TISPA}}{\longrightarrow} \mathbf{G}_{\text{eff}}(\omega_n) = \frac{1}{i\omega_n + \mathbf{M}[\overline{v}]} = (i\omega_n + \mathbf{M}[\overline{v}])^{-1} \quad . \tag{3.47}$$

This leads to a nice interpretation of $\mathbf{M}[\overline{v}]$. Its eigenvalues are the excitation energies of the quasi particles and quasi holes, because $\det(i\omega_n + \mathbf{M}[\overline{v}])$ is the common denominator of all components of $\mathbf{G}_{\text{eff}}(\omega_n)$. Moreover, because $\mathbf{M}[\overline{v}]$ is now a hermitian matrix with real eigenvalues, the quasi–particles are stable, that is, they have an infinite lifetime. In other words, the TISPA includes no self–energy. The creation and annihilation operators of the quasi–particles might be derived by diagonalizing $\mathbf{M}[\overline{v}]$. If $\mathbf{U}$ is the unitary matrix which diagonalizes $\mathbf{M}[\overline{v}]$, the Nambu operator for the quasi particles is given by

$$\gamma = \mathbf{U}\overline{\mathbf{c}} \quad . \tag{3.48}$$

This is the generalization of the Bogoliubov transformation which is used within the BCS approximation to derive the excitation energies of the Cooper pairs [Nambu60].

The TISPA–Hamiltonian $\mathcal{H}_{\text{TISPA}}$ might also be derived using the ususal mean field decomposition

$$\mathcal{A}\mathcal{B} \longrightarrow \mathcal{A}\langle \mathcal{B} \rangle + \langle \mathcal{A} \rangle \mathcal{B} - \langle \mathcal{A} \rangle \langle \mathcal{B} \rangle \tag{3.49}$$

for the general expression of the interaction Hamiltonian in equation (2.27) on page 26. In fact, if one assumes that only terms with negative coupling constants and terms with positive coupling constants but hermitian field operators contribute, the replacement

$$\mathcal{H}_1 \longrightarrow \sum_{i,q}^{*} g_i(q) \left\{ h_i^{\dagger}(q) \left\langle h_i(q) \right\rangle + h_i(q) \left\langle h_i^{\dagger}(q) \right\rangle - \left| \left\langle h_i(q) \right\rangle \right|^2 \right\} \tag{3.50}$$

[2] In order to derive a functional integral representation for the one–particle Greens function matrix, one also has to decompose the time evolution operators defining the time–dependence of the creation and annihilation operators. This can be done in the same way as the decomposition for the partition function. Now, replacing all fields by the minimizing field $\overline{v}$ yields the relation above.

yields the Hamiltonian in equation (3.39). But now, from this point of view an important question arises: is the assumption above, namely the replacement

$$\sum_{i,q} \longrightarrow \sum_{i,q}^{*} \tag{3.51}$$

an additional constraint or does it result from the selfconsistent determination of the average values of the field operators?
This question cannot be answered in general. But experience shows that the selfconsistent equation for the expectation value of a hermitian field operator only has the trivial solution, namely zero, if the corresponding coupling constant is repulsive. For example, the gap equation within the BCS approximation, which is just the selfconsistent equation for the pairing operator, has a nonzero solution only if the coupling constant is negative. There are many other examples which show that the relation

$$g_i(q) > 0 \quad \wedge \quad h_i(q) \neq h_i^{\dagger}(q) \Longrightarrow \left\langle h_i(q) \right\rangle = 0 \tag{3.52}$$

holds. It seems as if this relationship is true in general and that in fact the restriction (3.51) in equation (3.50) is not really an additional assumption. This is a very interesting point because it shows that both, the TISPA within the functional integral formalism and the usual mean field decomposition for the quadratic representation of the interaction Hamiltonian, lead to the same result and are therefore equivalent.

3.2.3 Uniform Fields

The TIFA leads to an explicit expression for the free energy functional, while the additional saddle point approximation produces selfconsistent equations for the minimizing fields $\overline{v}_i(q)$, which form a set of coupled nonlinear integral equations. They might be considered as an "infinite" set of coupled nonlinear equations of order L. Even when using the general result from above, the number of equations is still of the order of the system size. For relatively small systems they can be solved numerically, using, for instance, an iteration method, but in order to describe a sharp phase transition one has to go to the thermodynamic limit. In order to reduce the number of equations to a finite number, symmetry arguments are helpful. In fact, a nonvanishing value of $\left\langle h_i(q) \right\rangle$ for $q \neq 0$ breaks the translational symmetry of the system with respect to q. For this reason, one only considers spacially constant fields, i. e. only the components of $v_i(q)$ with $q = 0$ are taken into account. This means that the spatial fluctuations of the fields are neglected. In some cases, however, if one wants to describe phase transitions with spacially varying order parameters, one has to include field components for the corresponding special values of q.

For example, a charge density wave order or an antiferromagnetic order is described by field variables corresponding[3] to $q = Q$. Finally, a finite set of variables remains, which is independent on the system size. This set should be indexed by a single roman index j. The effective Hamiltonian, the free energy functional and all other functionals of v now become ordinary functions of this finite set of variables $\{v_j\}$. The selfconsistent equations then read:

$$v_j = \frac{1}{2}\left\{\mathrm{Tr}\,\mathrm{m}_j - \frac{1}{2}\,\mathrm{Tr}\left(\tanh\left(\frac{\beta \mathrm{M}(\{v_j\})}{2}\right)\mathrm{m}_j\right)\right\} \quad , \tag{3.53}$$

where m_j is the Nambu matrix for h_j. Note that due to the renaming of the components of $v_i(q)$ the range of the index j might be different from the range of the previously used index i, which was introduced to distinguish the different quadratic representations of the interaction Hamiltonian.

This approximation is usually called the "mean field approximation", because the internal fields v_j are now uniform fields without any spatial modulation. To summarize, the mean field approximation includes three steps:

1. Within the functional integration only time–independent fields are concerned.

2. Only uniform fields and Fourier components corresponding to some physically important values for q are involved.

3. Saddle point approximation.

From this list it follows that a description which goes beyond the mean field approximation needs to abandon one or more of these points. For example point #3 may be skipped. In this case one has to perform a functional integral over constant fields, which may be done numerically. Omitting the second point leads to q–dependent fields, allowing for spatial fluctuations of the fields. Reintroducing time–dependent fields means studying the effect of quantum fluctuations.

[3] As shown in chapter 2, one can introduce a band index $\nu \in \{0, 1\}$ to split the Brioullin zone into two halfs. In that case the antiferromagnetic wave vector corresponds to $v = 1$ and $q = 0$.

3.3 Symmetry–Broken Hartree–Fock–Bogoliubov Approximation

3.3.1 The Variational Principle

In this section we derive the selfconsistent equations for time–independent fields from a slightly different point of view without using the functional integral formalism. It is a variational approach where the original Hamiltonian is approximated by a parametrized one–particle Hamiltonian of the following form:

$$\mathcal{H}_{\mathrm{HFB}}[w] = \mathcal{H}_0 + \sum_{i,\alpha,q} g_{i,\alpha}(q) \left\{ w_{i,\alpha}(q) h^{\dagger}_{i,\alpha}(q) + w^{*}_{i,\alpha}(q) h_{i,\alpha}(q) \right\} \quad , \tag{3.54}$$

where the terms $h_{i,\alpha}(q)$ are one–particle field operators corresponding to the various quadratic representations of the interaction Hamiltonian. They are defined in chapter 2. The fields $w_{i,\alpha}(q)$ are variational parameters. For a hermitian field operator $h^{\dagger}_{i,\alpha}(q) = h_{i,\alpha}(q)$, the expression in curly brackets should be replaced by

$$2 w_{i,\alpha}(q) h_{i,\alpha}(q) \quad . \tag{3.55}$$

Because the HFB approximation described in this section is a variational method, the effective coupling constants $g_{i,\alpha}(q)$ and the additional factor 2 for hermitian field operators may be absorbed. But for various reasons, including the comparison to the TISPA of the functional integral formalism, we separate them from the variational parameters. It should be noted that the Hamiltonian above is not the most general ansatz to start with. The most general quadratic Hamiltonian includes all distinct products of creation and annihilation operators as used for instance in [Bormann91b]. But from a practical point of view this approach is more than sufficient. Within the symmetry–broken Hartree–Fock–Bogoliubov (HFB) approximation, the fields $w_{i,\alpha}(q)$ and their complex conjugate fields are determined by minimizing the right hand side of the Bogoliubov inequality [Brenig83, Ring80]

$$F \leq F^{\#}_{\mathrm{HFB}} := F_{\mathrm{HFB}} + \left\langle \mathcal{H} - \mathcal{H}_{\mathrm{HFB}} \right\rangle_{\mathrm{HFB}} \quad , \tag{3.56}$$

where F_{HFB} and $\langle \ldots \rangle_{\mathrm{HFB}}$ have to be calculated with respect to the HFB Hamiltonian $\mathcal{H}_{\mathrm{HFB}}$. This inequality ensures the existence of a minimum because F is a lower bound for the HFB free energy functional $F^{\#}_{\mathrm{HFB}}$. It originates from the variation of the information entropy in the grand canconical ensemble in the space of all statistical operators ρ, which

leads to

$$F[\rho] = \frac{1}{\beta}\mathrm{Tr}\,(\rho \ln \rho) + \mathrm{Tr}\,(\rho\mathcal{H}) \leq F[\rho'] \quad , \tag{3.57}$$

for $\rho = \exp(-\beta\mathcal{H})$ and for all $\rho' \neq \rho$. In fact, the Bogoliubov inequality is derived for $\rho' = \rho_{\mathrm{HFB}} = \exp(-\beta\mathcal{H}_{\mathrm{HFB}})$. The variational principle now reads:

$$\delta F^{\#}_{\mathrm{HFB}} = 0 \quad . \tag{3.58}$$

Why is it called the symmetry–broken Hartree–Fock–Bogoliubov approximation? From equation (3.54) follows that the trial Hamiltonian might have a lower symmetry than the original Hamiltonian. On the other hand, if a trial Hamiltonian is used which has the same symmetry, the usual Hartree–Fock approximation is retained. But this approximation cannot describe any phase transition. For this reason, symmetry–breaking terms are necessary. For instance, in order to describe a superconducting phase transition, one has to add pair operators which break the $U(1)$ gauge–symmetry generated by the particle number operator. Such an approach leads to the BCS approximation. In order to describe antiferromagnetic order, a term proportional to the antiferromagnetic SDW–operator needs to be added. It violates the translational symmetry with respect to Q. That is, one has to add symmetry–breaking fields as they are used to calculate correlation functions. These fields are interpreted as internal fields and are determined selfconsistently.

3.3.2 Selfconsistent Equations

As shown below, the HFB free energy functional may be expressed in a natural way as a functional of w and $\langle h\rangle_{\mathrm{HFB}}$, i. e. as a functional of the variational parameters and the mean values of the field operators, including their complex conjugates. For this reason the variational principle in equation (3.58) reads explicitly:

$$\delta F^{\#}_{\mathrm{HFB}} = \sum_{i,\alpha,q} \Bigg\{ \frac{\partial F^{\#}_{\mathrm{HFB}}}{\partial w_{i,\alpha}(q)}\,\delta w_{i,\alpha}(q) + \frac{\partial F^{\#}_{\mathrm{HFB}}}{\partial \langle h_{i,\alpha}(q)\rangle_{\mathrm{HFB}}}\,\delta\langle h_{i,\alpha}(q)\rangle_{\mathrm{HFB}} + \text{complex conjugate terms} \Bigg\} = 0 \quad . \tag{3.59}$$

From this equation it follows that

$$\frac{\partial F^{\#}_{\mathrm{HFB}}}{\partial w_{i,\alpha}(q)} = 0 \qquad \text{and} \tag{3.60}$$

$$\frac{\partial F^{\#}_{\mathrm{HFB}}}{\partial \left\langle h_{i,\alpha}(q)\right\rangle_{\mathrm{HFB}}} = 0 \qquad \forall\, i,\alpha,q \quad , \tag{3.61}$$

which, including the complex conjugate equations, form the set of selfconsistent equations within the HFB approximation. Writing down the functional dependence of the HFB free energy functional on w and $\langle h \rangle_{\mathrm{HFB}}$ yields a more detailed form of the selfconsistent equations. Three terms F_{HFB}, $\langle \mathcal{H} \rangle_{\mathrm{HFB}}$ and $\langle \mathcal{H}_{\mathrm{HFB}} \rangle_{\mathrm{HFB}}$ are involved. First, the free energy with respect to $\mathcal{H}_{\mathrm{HFB}}$ should be treated. It is a functional of w and is defined by:

$$F_{\mathrm{HFB}}[w] = -\frac{1}{\beta} \ln \mathrm{Tr} \left(\exp \left[-\beta \mathcal{H}_{\mathrm{HFB}} \right] \right) \quad . \tag{3.62}$$

For this reason the functional derivative of F_{HFB} with respect to $w_{i,\alpha}(q)$ is proportional to the mean value of the corresponding field operator:

$$\frac{\partial F_{\mathrm{HFB}}[w]}{\partial w_{i,\alpha}(q)} = g_{i,\alpha}(q) \left\langle h^{\dagger}_{i,\alpha}(q) \right\rangle_{\mathrm{HFB}} \quad . \tag{3.63}$$

For the mean value of $\mathcal{H}_{\mathrm{HFB}} - \mathcal{H}_0$, one gets directly

$$\left\langle \mathcal{H}_{\mathrm{HFB}} - \mathcal{H}_0 \right\rangle_{\mathrm{HFB}} = \sum_{i,\alpha,q} g_{i,\alpha}(q) \left\{ w_{i,\alpha}(q) \left\langle h^{\dagger}_{i,\alpha}(q) \right\rangle_{\mathrm{HFB}} + w^{*}_{i,\alpha}(q) \left\langle h_{i,\alpha}(q) \right\rangle_{\mathrm{HFB}} \right\} \quad . \tag{3.64}$$

This is a functional of w and $\langle h \rangle_{\mathrm{HFB}}$ with

$$\frac{\partial \left\langle \mathcal{H}_{\mathrm{HFB}} - \mathcal{H}_0 \right\rangle_{\mathrm{HFB}}}{\partial w_{i,\alpha}(q)} = g_{i,\alpha}(q) \left\langle h^{\dagger}_{i,\alpha}(q) \right\rangle_{\mathrm{HFB}} = \frac{\partial F_{\mathrm{HFB}}[w]}{\partial w_{i,\alpha}(q)} \quad \text{and} \tag{3.65}$$

$$\frac{\partial \left\langle \mathcal{H}_{\mathrm{HFB}} - \mathcal{H}_0 \right\rangle_{\mathrm{HFB}}}{\partial \left\langle h^{\dagger}_{i,\alpha}(q) \right\rangle_{\mathrm{HFB}}} = g_{i,\alpha}(q)\, w_{i,\alpha}(q) \quad . \tag{3.66}$$

Finally, the mean value of $\mathcal{H}_1 = \mathcal{H} - \mathcal{H}_0$ with respect to $\mathcal{H}_{\mathrm{HFB}}$ needs to be calculated. Because the HFB Hamiltonian is a one–particle operator, Wick's Theorem may be used [Mahan90]. For this purpose one has to go back to the original form of the interaction Hamiltonian. For the NNSP model it is given by:

$$\mathcal{H}_1 = \frac{Wz}{L} \sum_{q,k,k'} S(q) c^{\dagger}_{k+q\uparrow} c_{k\uparrow} c^{\dagger}_{k'-q\downarrow} c_{k'\downarrow} \quad . \tag{3.67}$$

Using Wick's Theorem yields:

$$\begin{aligned} \left\langle \mathcal{H}_1 \right\rangle_{\mathrm{HFB}} = \frac{Wz}{L} \sum_{q,k,k'} S(q) \Big\{ & \left\langle c^{\dagger}_{k+q\uparrow} c_{k\uparrow} \right\rangle_{\mathrm{HFB}} \left\langle c^{\dagger}_{k'-q\downarrow} c_{k'\downarrow} \right\rangle_{\mathrm{HFB}} \\ & - \left\langle c^{\dagger}_{k+q\uparrow} c^{\dagger}_{k'-q\downarrow} \right\rangle_{\mathrm{HFB}} \left\langle c_{k\uparrow} c_{k'\downarrow} \right\rangle_{\mathrm{HFB}} \\ & + \left\langle c^{\dagger}_{k+q\uparrow} c_{k'\downarrow} \right\rangle_{\mathrm{HFB}} \left\langle c_{k\uparrow} c^{\dagger}_{k'-q\downarrow} \right\rangle_{\mathrm{HFB}} \Big\} \quad . \end{aligned} \tag{3.68}$$

Now, for all three terms the same variable transformations which have been used in the previous chapter 2 in order to derive the several quadratic representations of the interaction Hamiltonian may be applied. The first term therefore leads to SDW and CDW operators, the second term to pairing operators with different internal symmetry and the last term to SF operators. That is, the expectation value of $\mathcal{H}_1$ becomes:

$$\begin{aligned}\langle \mathcal{H}_1 \rangle_{\mathrm{HFB}} &= WzL \sum_q S(q) \left(\frac{1}{4} \left\langle \eta_q^\dagger \right\rangle_{\mathrm{HFB}} \left\langle \eta_q \right\rangle_{\mathrm{HFB}} - \left\langle s_q^\dagger \right\rangle_{\mathrm{HFB}} \left\langle s_q \right\rangle_{\mathrm{HFB}} \right) \\ &\quad + WL \sum_{q,\alpha} \left\langle P_\alpha^\dagger(q) \right\rangle_{\mathrm{HFB}} \left\langle P_\alpha(q) \right\rangle_{\mathrm{HFB}} \\ &\quad - WL \sum_{q,\alpha} \left\langle Q_\alpha^\dagger(q) \right\rangle_{\mathrm{HFB}} \left\langle Q_\alpha(q) \right\rangle_{\mathrm{HFB}} \quad . \end{aligned} \tag{3.69}$$

Finally one can introduce the general i-, α- and q-dependent field operators $h_{i,\alpha}(q)$ and the corresponding effective coupling constants $g_{i,\alpha}(q)$:

$$\langle \mathcal{H}_1 \rangle_{\mathrm{HFB}} = \sum_{i,\alpha,q} g_{i,\alpha}(q) \left\langle h_{i,\alpha}^\dagger(q) \right\rangle_{\mathrm{HFB}} \left\langle h_{i,\alpha}(q) \right\rangle_{\mathrm{HFB}} \quad . \tag{3.70}$$

It is not very difficult to show that this formula is true for general, non-retarded two-particle interactions. Moreover, for these interactions it is valid whenever Wick's Theorem holds. It should be emphasized that the right hand side of equation (3.70) does not include the parameters λ_i, which were introduced in the previous chapter 2 to sum over all the different quadratic representations. Now, from equations (3.63) and (3.65), it follows that the first set of selfconsistent equations, namely those which arise from the partial variation of $F_{\mathrm{HFB}}^{\#}$ with respect to w in equation (3.60), are identically satisfied. The second set remains, which reads:

$$\frac{\partial \left\langle \mathcal{H}_{\mathrm{HFB}} - \mathcal{H}_0 \right\rangle_{\mathrm{HFB}}}{\partial \left\langle h_{i,\alpha}^\dagger(q) \right\rangle_{\mathrm{HFB}}} = g_{i,\alpha}(q)\, w_{i,\alpha}(q) = \frac{\partial \left\langle \mathcal{H}_1 \right\rangle_{\mathrm{HFB}}}{\partial \left\langle h_{i,\alpha}^\dagger(q) \right\rangle_{\mathrm{HFB}}} \quad , \tag{3.71}$$

or evaluating the right hand side of this equation and including the complex conjugate equation yields the selfconsistent equations of the HFB approximation:

$$w_{i,\alpha}(q) = \left\langle h_{i,\alpha}(q) \right\rangle_{\mathrm{HFB}} \quad \text{and} \tag{3.72}$$

$$w_{i,\alpha}^*(q) = \left\langle h_{i,\alpha}^\dagger(q) \right\rangle_{\mathrm{HFB}} \quad \forall\, i, \alpha, q \quad . \tag{3.73}$$

From the more general equation (3.71), it follows that, if one adds a term $\tilde{w}\tilde{h}$ to the HFB Hamiltonian, where $\tilde{h}$ is not included in $\mathcal{H}_1$, the corresponding field variable $\tilde{w}$ needs to be zero. In fact, such a term would lead to the following equation:

$$\tilde{w} = \frac{\partial \left\langle \mathcal{H}_1 \right\rangle_{\mathrm{HFB}}}{\partial \left\langle \tilde{h} \right\rangle_{\mathrm{HFB}}} \quad , \tag{3.74}$$

and, because $\mathcal{H}_1$ does not depend on $\bar{h}$, it is equivalent to $\bar{w} = 0$. This proves the statement that, within the HFB approximation only those fields provide a contribution which are mediated by the interaction Hamiltonian. For instance in the attractive Hubbard model only s–wave superconductivity will occur, while in the NNSP model this type of pairing is not present.

3.3.3 Calculation of the HFB Free Energy Functional and Explicit Form of the Selfconsistent Equations

The right–hand sides of the selfconsistent equations and the HFB free energy functional integral can be calculated using the same technique as for the TISPA of the functional integral formalism. Namely, introducing the Nambu representation of the HFB Hamiltonian:

$$\mathcal{H}_{\mathrm{HFB}}[w] = \frac{1}{2}\bar{c}^{\dagger}\mathbf{M}_{\mathrm{HFB}}[w]\bar{c} + \frac{1}{2}\,\mathrm{Tr}\,\mathbf{M}^{1}_{\mathrm{HFB}}[w] \quad , \tag{3.75}$$

with

$$\mathbf{M}_{\mathrm{HFB}}[w] = \mathbf{M}_0 + \sum_{i,\alpha,q} g_{i,\alpha}(q)\left\{\mathrm{m}^{\dagger}(i,\alpha,q)w_{i,\alpha}(q) + \mathrm{m}(i,\alpha,q)w^{*}_{i,\alpha}(q)\right\} \tag{3.76}$$

yields:

$$\begin{aligned} F^{\#}_{\mathrm{HFB}}[w] &= -\frac{1}{2\beta}\,\mathrm{Tr}\,\ln\left(2\cosh\left(\frac{\beta\mathbf{M}_{\mathrm{HFB}}[w]}{2}\right)\right) - \sum_{i,\alpha,q} g_{i,\alpha}(q)\left|w_{i,\alpha}(q)\right|^2 \\ &\quad + \frac{1}{2}\,\mathrm{Tr}\,\mathbf{M}^{1}_{\mathrm{HFB}}[w] \quad , \end{aligned} \tag{3.77}$$

where additionally $\left\langle h_{i,\alpha}(q)\right\rangle_{\mathrm{HFB}}$ and $\left\langle h^{\dagger}_{i,\alpha}(q)\right\rangle_{\mathrm{HFB}}$ have been replaced by $w_{i,\alpha}(q)$ and $w^{*}_{i,\alpha}(q)$ according to the selfconsistent equations (3.72) and (3.73). Based on this expression one can derive an explicit form of the selfconsistent equations. Varying $F^{\#}_{\mathrm{HFB}}[w]$ with respect to $w^{*}_{i,\alpha}(q)$ yields:

$$w_{i,\alpha}(q) = \frac{1}{2}\left\{\mathrm{Tr}\,\mathrm{m}^{1}(i,\alpha,q) - \frac{1}{2}\,\mathrm{Tr}\left(\tanh\left(\frac{\beta\mathbf{M}_{\mathrm{HFB}}[w]}{2}\right)\mathrm{m}(i,\alpha,q)\right)\right\} \quad , \tag{3.78}$$

whereas the equation for $w^{*}_{i,\alpha}(q)$ is given by the complex conjugate equation. As in the TISPA, one can reduce the number of equations if one takes only a finite set of variational parameters into account. For instance, if one neglects spatial variations, only the $q = 0$ components will contribute. On the other hand, all components which correspond to nonhermitian field operators and positive coupling constants may be omitted[4]. That is

[4] We are using the same argument as before. Experience shows that for these components only the trivial solution, namely zero, minimizes the free energy functional.

one can replace the i, α, q – sum by the restricted sum $\sum^{*}_{i,\alpha,q}$ which was introduced in section 3.2.2. Including this restriction, a comparision between the TISPA and the HFB approximation is possible, which is discussed in the following paragraph.

Comparision to the TISPA

As in the TISPA, the free energy within the HFB approximation is given by the HFB free energy functional evaluated at the minimizing field $\overline{w}$. That is,

$$F \overset{HFB}{=} F^{\#}_{\mathrm{HFB}}[\overline{w}] \quad . \tag{3.79}$$

For this reason the original Hamiltonian $\mathcal{H}$ is replaced by the HFB Hamiltonian including the quadratic terms $\langle \mathcal{H} - \mathcal{H}_{\mathrm{HFB}} \rangle_{\mathrm{HFB}}$:

$$\mathcal{H} \overset{HFB}{\longrightarrow} \mathcal{H}_0 + \sum_{i,\alpha,q}{}^{*} g_{i,\alpha}(q) \left\{ \overline{w}_{i,\alpha}(q) h^{\dagger}_{i,\alpha}(q) + \overline{w}^{*}_{i,\alpha}(q) h_{i,\alpha}(q) - \left| \overline{w}_{i,\alpha}(q) \right|^2 \right\} \quad , \tag{3.80}$$

where, as mentioned above, the sum over all i, α and q is replaced by the restricted sum, excluding those terms which correspond to positive coupling constants and nonhermitian operators. This Hamiltonian appears like the TISPA Hamiltonian in equation (3.43), but there is a big difference. If one rewrites the TISPA Hamiltonian including the replacement $i \rightarrow i, \alpha$ and $g_i(q) \rightarrow \lambda_i g_{i,\alpha}(q)$ with $\sum_i \lambda_i = 1$ and $\lambda_i \geq 0$, one obtains:

$$\mathcal{H}_{\mathrm{TISPA}} = \mathcal{H}_0 + \sum_{i,\alpha,q}{}^{*} \lambda_i \, g_{i,\alpha}(q) \left\{ \overline{v}_{i,\alpha}(q) h^{\dagger}_{i,\alpha}(q) + \overline{v}^{*}_{i,\alpha}(q) h_{i,\alpha}(q) - \left| \overline{v}_{i,\alpha}(q) \right|^2 \right\} \tag{3.81}$$

From this equation it follows that both approximations are identical only for $\lambda_i = 1 \; \forall i$. This constraint causes no contradiction and both approximations are indeed identical if within the functional integral description only one quadratic representation is used. However, the TISPA and the HFB approximation are different from each other if two or more representations are taken into account, because the sum over all λ_i has to equal one, which cannot be satisfied for $\lambda_i = 1 \; \forall i$. For this reason one can ask if the TISPA with an appropriate choice of the parameters λ_i might lead to a better mean field approximation. Nevertheless, the HFB approximation is a variational method and leads to thermodynamically selfconsistent solutions for the variational parameters. For this reason it is used to study the NNSP model.

Chapter 4

Symmetry Hartree Fock Approximation for the NNSP Model: Formulae

Within the previous chapters a very technical formalism was introduced. This chapter is designated to apply this formalism to the NNSP model. Just writing down the functional integral as it was shown in the second chapter does not provide any information about the phase diagram of the model, but it gives an idea on how to construct a trial Hamiltonian for the symmetry–broken Hartree Fock Bogoliubov approximation. In fact, this approximation is one of the easiest ways to derive the phase diagram of a given model. If the proper trial Hamiltonian is used, it yields qualitatively good results. Furthermore, it is a thermodynamic selfconsistent approach. In this chapter a trial Hamiltonian is incorporated including antiferromagnetic and superconducting variational parameters and the selfconsistent equations are derived. Some remarks on the technique used for solving the selfconsistent equations simoultaneously are also included.

4.1 Trial Hamiltonian, Free Energy Functional and Self-consistent Equations

4.1.1 Construction of the Trial Hamiltonian

The antiferromagnetic phase diagram of the interaction Hamiltonian of the NNSP model was derived in chapter 1. In two dimensions it shows an antiferromagnetic phase transition for all fillings. On the other hand, a BCS approximation for the total Hamiltonian, kinetic and interaction part, leads to a superconducting phase transition [Schneider90a]. For this reason variational parameters which couple on one hand to the antiferromagnetic and on the other hand on the pairing field operators have to be included in a variational HFB

Table 4.1: Variational parameters and corresponding field operators for the symmetry broken HFB approximation of the NNSP model.

repr. – index	fieldoperator	variational parameter	nature	coupling constant
1	$\eta = \eta_{q=0} = \frac{1}{L}\sum_{k,\sigma} n_{k\sigma}$	ρ	real	$WzL/4$
1	$s_{\mathrm{AF}} = s_{q=Q} = \frac{1}{2L}\sum_{k} c^{\dagger}_{k+Q\uparrow}c_{k\uparrow} - c^{\dagger}_{k+Q\downarrow}c_{k\downarrow}$	m_{AF}	real	WzL
2	$\left\{P_\alpha(q=0) = \frac{1}{L}\sum_{k} c_{-k\downarrow}c_{k\uparrow} f_\alpha(k)\right\}_{\alpha=1\ldots z}$	$\left\{\Delta_\alpha\right\}_{\alpha=1\ldots z}$	complex	WL

approximation. Table 4.1 summarizes this minimum set of variational parameters and its corresponding field operators. The index in column 1 is the same index as in table 2.2 and enumerates the quadratic representation of the interaction Hamiltonian from which the field operator in the second column originates. It should be emphasized again that within the HFB approximation no parameters λ_i have to be introduced. The variational parameters and their nature are given in the third and forth column, while the last column lists the effective coupling constants. The first field operator describes a uniform charge distribution and leads to the usual Hartree approximation if no further terms are added to the trial Hamiltonian. As shown below, it renormalizes the chemical potential. Including the SDW operator in the second row allows for an antiferromagnetic phase transition, while including variational parameters corresponding to different types of pairing operators might lead to superconductivity with different symmetry. The corresponding field operators are given in the last row of table 2.2. Here the structure functions might be the cartesian or the group theoretical functions defined in chapter 2.1.2, or any other set of functions with

$$S(k-k') = \frac{1}{z}\sum_{\alpha} f_\alpha(k)\, f^{*}_\alpha(k') \quad . \tag{4.1}$$

Using this table and the general ansatz in equation (3.54), the trial Hamiltonian then reads:

$$\begin{aligned}
\mathcal{H}_{\mathrm{HFB}}[\rho, m_{\mathrm{AF}}, \Delta] \;=\; & \sum_{k,\sigma}(\epsilon_k - \mu) n_{k\sigma} && \text{free part} \\
& + 2\frac{WzL}{4}\rho\left(\frac{1}{L}\sum_{k,\sigma} n_{k\sigma}\right) && \text{density} \\
& + 2WzL\, m_{\mathrm{AF}}\left(\frac{1}{2L}\sum_{k} c^{\dagger}_{k+Q\uparrow}c_{k\uparrow} - c^{\dagger}_{k+Q\downarrow}c_{k\downarrow}\right) && \text{AF} \\
& + WL\sum_{\alpha}\left\{\left(\frac{1}{L}\sum_{k} c_{-k\downarrow}c_{k\uparrow}\, f_\alpha(k)\right)\Delta^*_\alpha + \text{h. c.}\right\} && \text{Pairing}
\end{aligned} \tag{4.2}$$

As already mentioned in the general considerations in chapter 3.3, the additional factor 2 in the density and antiferromagnetic contribution has been introduced because η and s_{AF} hermitian operators and hence their variational parameters may be chosen to be real. Exchanging the α–sum with the k–sum, the pairing term may be rewritten as follows:

$$WL\sum_{\alpha}\left\{\left(\frac{1}{L}\sum_{k} c_{-k\downarrow}c_{k\uparrow}\, f_\alpha(k)\right)\Delta^*_\alpha + \text{h. c.}\right\} = Wz\sum_{k}\left\{\Delta^*(k)\, c_{-k\downarrow}c_{k\uparrow} + \text{h. c.}\right\} \tag{4.3}$$

with a k–dependent superconducting variational parameter

$$\Delta^*(k) := \frac{1}{z}\sum_{\alpha}\Delta^*_\alpha\, f_\alpha(k) \quad . \tag{4.4}$$

In this form the pairing part of the trial Hamiltonian has the usual form as it is used in the BCS approximation for non–local interactions [Schneider90a] or in similar HFB approximations [Robaszkiewicz81b]. It should be noted that, if a general $\Delta^*(k)$ is used in the variational HFB approximation, one can see that it may be parametrized according to equation (4.4). With the HFB Hamiltonian above as well as the general expression in equation (3.77) and table 4.1, the free energy functional for the HFB approximation is given by:

$$F^{\#}_{\mathrm{HFB}}[\rho, m_{\mathrm{AF}}, \Delta] = F_{\mathrm{HFB}}[\rho, m_{\mathrm{AF}}, \Delta] - WzL\left\{\frac{\rho^2}{4} + m^2_{\mathrm{AF}} + \frac{1}{z}\sum_{\alpha}|\Delta_\alpha|^2\right\} \tag{4.5}$$

with

$$F_{\mathrm{HFB}}[\rho, m_{\mathrm{AF}}, \Delta] \;=\; -\frac{1}{\beta}\ln \mathrm{Tr}\, \exp\left(-\beta\mathcal{H}_{\mathrm{HFB}}[\rho, m_{\mathrm{AF}}, \Delta]\right) \tag{4.6}$$

$$= -\frac{1}{2\beta}\,\mathrm{Tr}\,\ln\left(2\cosh\left(\frac{\beta \mathbf{M}_{\mathrm{HFB}}[\rho, m_{\mathrm{AF}}, \Delta]}{2}\right)\right) + \frac{1}{2}\,\mathrm{Tr}\,\mathbf{M}^{1}_{\mathrm{HFB}}[\rho, m_{\mathrm{AF}}, \Delta] \quad , \tag{4.7}$$

where $\mathbf{M}_{\mathrm{HFB}}[\rho, m_{\mathrm{AF}}, \Delta]$ is the Nambu matrix associated with the trial Hamiltonian in equation (4.2). Using $\sum_k \epsilon_k = 0$, the last term becomes

$$\frac{1}{2}\,\mathrm{Tr}\,\mathbf{M}^{1}_{\mathrm{HFB}}[\rho, m_{\mathrm{AF}}, \Delta] = -L\left(\mu - \frac{Wz\rho}{2}\right) =: -L\,\overline{\mu} \quad , \tag{4.8}$$

where the right hand side of this equation defines the renormalized chemical potential $\overline{\mu}$. Now, in principle one can write down the Nambu matrix $\mathbf{M}_{\mathrm{HFB}}[\rho, m_{\mathrm{AF}}, \Delta]$ and it can be diagonalized so that the matrix trace in equation (4.7) can be derived explicitly. From the resulting expression for the free energy functional one can then derive the selfconsistent equations for the variational parameters. However, we prefer a Greens function method in order to calculate the right hand sides of the more formal selfconsistent equations in equations (3.72) and (3.73), which give the relation between the variational parameters and their corresponding field operators. For the variational parameters ρ, m_{AF} and Δ_α and their complex conjugates they read explicitly:

$$\rho = \frac{1}{L}\sum_{k,\sigma}\langle n_{k\sigma}\rangle_{\mathrm{HFB}} \tag{4.9}$$

$$m_{\mathrm{AF}} = \frac{1}{2L}\sum_{k}\left\{\left\langle c^{\dagger}_{k+Q\uparrow}c_{k\uparrow}\right\rangle_{\mathrm{HFB}} - \left\langle c^{\dagger}_{k+Q\downarrow}c_{k\downarrow}\right\rangle_{\mathrm{HFB}}\right\} \tag{4.10}$$

$$\Delta_\alpha = \frac{1}{L}\sum_{k}\left\langle c_{-k\downarrow}c_{k\uparrow}\right\rangle_{\mathrm{HFB}} f_\alpha(k) \tag{4.11}$$

$$\Delta^{*}_\alpha = \frac{1}{L}\sum_{k}\left\langle c^{\dagger}_{k\uparrow}c^{\dagger}_{-k\downarrow}\right\rangle_{\mathrm{HFB}} f^{*}_\alpha(k) \quad . \tag{4.12}$$

Before calculating the right hand sides of these equations we want to discuss an important point regarding the grand canconical description we have used up to now.

4.1.2 The Free Energy Functional for Fixed Particle Density

In a grand canonical description the chemical potential is fixed and the electron density is a fluctuating entity. For this reason the free energy functional above depends on ρ and, using a saddle point approximation, one gets a selfconsistent equation for ρ. Usually, however, one is interested in the physics for the fixed particle number density $n = N/L$, where N is the total number of particles and L the system size. In this case one can replace ρ by the fixed value of n and, because $\mathcal{H}_{\mathrm{HFB}}$ depends only on $(\mu - Wzn/2)$, the

chemical potential by the renormalized chemical potential $\overline{\mu}$, which has to be determined selfconsistently. Furthermore, one needs to introduce the canonical free energy functional

$$A^{\#}_{\mathrm{HFB}} := F^{\#}_{\mathrm{HFB}} + \overline{\mu} N \quad , \tag{4.13}$$

which, neglecting n–dependent terms, is explicitly given by

$$\begin{aligned} A^{\#}_{\mathrm{HFB}}[\overline{\mu}, m_{\mathrm{AF}}, \Delta] &= F_{\mathrm{HFB}}[\overline{\mu}, m_{\mathrm{AF}}, \Delta] - WzL\left\{ m^2_{\mathrm{AF}} + \frac{1}{z}\sum_{\alpha} |\Delta_\alpha|^2 \right\} \\ &\quad + \overline{\mu} L n \quad . \end{aligned} \tag{4.14}$$

The canonical free energy functional is written as a function of $\overline{\mu}$, m_{AF}, Δ_α and their complex conjugate variables, because the selfconsistent equations above may now be derived by minimizing the canonical free energy functional with respect to these variables. In particular, the first of the selfconsistent equations results from the condition

$$\frac{\partial A^{\#}_{\mathrm{HFB}}}{\partial \overline{\mu}} = 0 \quad , \tag{4.15}$$

which is an implicit equation for $\overline{\mu}$. This discussion seems at this point a bit artificial, but it is important for instance for the calculation of the specific heat in chapter 7.

4.1.3 Equations of Motion for Creation and Annihilation Operators

In order to calculate the right hand side of the selfconsistent equations (4.9) ... (4.12) using a Greens function method, it is very practical to start with the derivation of the equations of motion for the creation and annihilation operators. Their τ–dependence is defined with respect to the trial Hamiltonian and is given by

$$c^{\pm}_{k\sigma}(\tau) := e^{\mathcal{H}_{\mathrm{HFB}}\,\tau}\, c^{\pm}_{k\sigma}\, e^{-\mathcal{H}_{\mathrm{HFB}}\,\tau} \quad . \tag{4.16}$$

Here we have introduced the following notation:

$$c^{\alpha}_{k\sigma} = \begin{cases} c^{\dagger}_{k\sigma} & \text{for} \quad \alpha = + \\ c_{k\sigma} & \text{for} \quad \alpha = - \end{cases} \tag{4.17}$$

where σ is assumed to be -1 for spin down and $+1$ for spin up. Differentiating equation (4.16) with respect to τ yields the equation of motion for the creation and annihilation operators:

$$\frac{d}{d\tau} c^{\pm}_{k\sigma}(\tau) = \left[\mathcal{H}_{\mathrm{HFB}}, c^{\pm}_{k\sigma} \right](\tau) \quad . \tag{4.18}$$

The calculation of the commutator is a quite simple but long task and needs not be included here. The result is:

$$\frac{d}{d\tau}c^{\pm}_{k\sigma}(\tau) = \pm\left\{(\epsilon_k - \overline{\mu})\, c^{\pm}_{k\sigma}(\tau) + Wz\sigma\left(\Delta^{\pm}(k)\, c^{\mp}_{-k-\sigma}(\tau) + m_{\mathrm{AF}} c^{\pm}_{k+Q\sigma}(\tau)\right)\right\} \quad , \tag{4.19}$$

where $\Delta^{-}(k)$ is the k-dependent superconducting variational parameter $\Delta(k)$ as defined above and $\Delta^{+}(k)$ is its complex conjugate. In the first chapter we have made the general assumption that the model is considered on an bipartite lattice with transformation vector $Q = (\pi, \pi, \ldots)$. For this reason the following equations are valid for all integral numbers $l \in \mathrm{Z}$:

$$\begin{aligned} c^{\pm}_{k+nQ\,\sigma} &= c^{\pm}_{k\sigma} \qquad \text{for} \quad n = 2l \quad , \\ c^{\pm}_{k+nQ\,\sigma} &= c^{\pm}_{k+Q\,\sigma} \quad \text{for} \quad n = 2l+1 \quad . \end{aligned} \tag{4.20}$$

Based on these relations and with the equation of motion (4.19) one obtaines directly an equation of motion for $c^{\pm}_{k+Q\sigma}(\tau)$, which is given by:

$$\begin{aligned} \frac{d}{d\tau}c^{\pm}_{k+Q\,\sigma}(\tau) = \pm\Big\{ &(\epsilon_k - \overline{\mu})\, c^{\pm}_{k+Q\,\sigma}(\tau) + \\ &Wz\sigma\left(\Delta^{\pm}(k)\, c^{\mp}_{-k+Q\,-\sigma}(\tau) + m_{\mathrm{AF}} c^{\pm}_{k\sigma}(\tau)\right)\Big\} \quad , \end{aligned} \tag{4.21}$$

so that this equation (4.21), equation (4.19) and the equations for $-k$ and opposite spin, which result from equation (4.21) and (4.19) by replacing k by $-k$ and σ by $-\sigma$, define a complete set of time-dependent differential equations.

4.1.4 Greens Function

From the equation of motion for the creation and annihilation operators we obtain which one-particle Greens functions couple. Therefore it is not very useful to start from the general Greens function matrix defined in chapter 2.3.4. It is better to start directly from the following four Greens functions:

$$\mathrm{G}_{\sigma}(k,\tau) := \left\langle \mathrm{T}_{\tau} c_{k\sigma}(\tau) c^{\dagger}_{k\sigma} \right\rangle_{\mathrm{HFB}} \tag{4.22}$$

$$\mathrm{G}_{Q\sigma}(k,\tau) := \left\langle \mathrm{T}_{\tau} c_{k+Q\sigma}(\tau) c^{\dagger}_{k\sigma} \right\rangle_{\mathrm{HFB}} \tag{4.23}$$

$$\mathrm{F}^{\dagger}_{\sigma}(k,\tau) := \left\langle \mathrm{T}_{\tau} c^{\dagger}_{-k-\sigma}(\tau) c^{\dagger}_{k\sigma} \right\rangle_{\mathrm{HFB}} \tag{4.24}$$

$$\mathrm{F}^{\dagger}_{Q\sigma}(k,\tau) := \left\langle \mathrm{T}_{\tau} c^{\dagger}_{-(k+Q)-\sigma}(\tau) c^{\dagger}_{k\sigma} \right\rangle_{\mathrm{HFB}} \quad . \tag{4.25}$$

In addition, from the selfconsistent equations it becomes clear that it suffices to know these Greens functions in order to calculate the mean values of the field operators on the

right hand side of the selfconsistent equations. Using equations (4.19) and (4.21), the time derivatives of these Greensfunctions are:

$$\begin{aligned}
\frac{d}{d\tau}\mathrm{G}_\sigma(k,\tau) &= \delta(\tau) - (\epsilon_k - \overline{\mu})\mathrm{G}_\sigma(k,\tau) \\
&\quad -Wz\sigma\left(\Delta(k)\mathrm{F}^\dagger_\sigma(k,\tau) + m_{\mathrm{AF}}\mathrm{G}_{Q\sigma}(k,\tau)\right) \qquad (4.26)\\
\frac{d}{d\tau}\mathrm{G}_{Q\sigma}(k,\tau) &= -(\epsilon_{k+Q} - \overline{\mu})\mathrm{G}_{Q\sigma}(k,\tau) \\
&\quad -Wz\sigma\left(-\Delta(k)\mathrm{F}^\dagger_{Q\sigma}(k,\tau) + m_{\mathrm{AF}}\mathrm{G}_\sigma(k,\tau)\right) \qquad (4.27)\\
\frac{d}{d\tau}\mathrm{F}^\dagger_\sigma(k,\tau) &= (\epsilon_k - \overline{\mu})\mathrm{F}^\dagger_\sigma(k,\tau) \\
&\quad -Wz\sigma\left(\Delta^*(k)\mathrm{G}_\sigma(k,\tau) + m_{\mathrm{AF}}\mathrm{F}^\dagger_{Q\sigma}(k,\tau)\right) \qquad (4.28)\\
\frac{d}{d\tau}\mathrm{F}^\dagger_{Q\sigma}(k,\tau) &= (\epsilon_{k+Q} - \overline{\mu})\mathrm{F}^\dagger_{Q\sigma}(k,\tau) \\
&\quad -Wz\sigma\left(-\Delta^*(k)\mathrm{G}_{Q\sigma}(k,\tau) + m_{\mathrm{AF}}\mathrm{F}^\dagger_\sigma(k,\tau)\right) \quad , \qquad (4.29)
\end{aligned}$$

where the relations in equation (4.20) have also been incorporated. If only nearest neighbor hopping is under consideration, one can replace ϵ_{k+Q} by $-\epsilon_k$. If, however, the free particle dispersion relation includes the next nearest neighbor hopping terms, ϵ_k has to be replaced by $\epsilon_k + \epsilon'_k$ with $\epsilon_{k+Q} + \epsilon'_{k+Q} = -\epsilon_k + \epsilon'_k$. In this case, in the formulae above one has to replace ϵ_{k+Q} by $-\epsilon_k$ and $\overline{\mu}$ by $\overline{\mu} - \epsilon'_k$. In the forthcoming treatment, however, we assume only nearest neighbor hopping, bearing in mind that the generalization, including next nearest neighbor hopping, is obtained by replacing $\overline{\mu}$ by $\overline{\mu} - \epsilon'_k$. Now, using the Fourier transformation in equation (3.7), the set of ordinary differential equations may be mapped on a coupled set of algebraic equations by

$$\frac{d}{d\tau} \longrightarrow i\omega_n \quad \text{and} \quad \delta(\tau) \longrightarrow 1 \quad . \qquad (4.30)$$

As in the previous chapter 3 we do not introduce a new symbol for the Fourier transformed functions. They are distinguished by their argument. The algebraic set of equations for the frequency-dependent Greens functions then reads in matrix form:

$$\begin{pmatrix} \epsilon_1 & Wz\sigma m_{\mathrm{AF}} & Wz\sigma\Delta(k) & 0 \\ Wz\sigma m_{\mathrm{AF}} & \epsilon_2 & 0 & -Wz\sigma\Delta(k) \\ Wz\sigma\Delta^*(k) & 0 & \epsilon_3 & Wz\sigma m_{\mathrm{AF}} \\ 0 & -Wz\sigma\Delta^*(k) & Wz\sigma m_{\mathrm{AF}} & \epsilon_4 \end{pmatrix} \begin{pmatrix} \mathrm{G}_\sigma \\ \mathrm{G}_{Q\sigma} \\ \mathrm{F}^\dagger_\sigma \\ \mathrm{F}^\dagger_{Q\sigma} \end{pmatrix} = \begin{pmatrix} 1 \\ 0 \\ 0 \\ 0 \end{pmatrix} \qquad (4.31)$$

with

$$\begin{aligned}
\epsilon_1 &= (i\omega_n + \epsilon_k - \overline{\mu}) \\
\epsilon_2 &= (i\omega_n - \epsilon_k - \overline{\mu})
\end{aligned}$$

$$\begin{aligned} \epsilon_3 &= (i\omega_n - \epsilon_k + \overline{\mu}) \\ \epsilon_4 &= (i\omega_n + \epsilon_k + \overline{\mu}) \quad . \end{aligned} \tag{4.32}$$

Using an algebraic computer system like Mathematica [Mathematica], it is an easy task to invert the coefficient matrix above. The result is:

$$\mathrm{G}_\sigma = \frac{\epsilon_2\epsilon_3\epsilon_4 - W^2z^2m_{\mathrm{AF}}^2\epsilon_3 - W^2z^2|\Delta(k)|^2\epsilon_4}{(i\omega_n - E_1^2)(i\omega_n - E_2^2)} \tag{4.33}$$

$$\mathrm{G}_{Q\sigma} = \sigma W z\, m_{\mathrm{AF}} \frac{W^2z^2|\Delta(k)|^2 - \epsilon_2\epsilon_4 + W^2z^2m_{\mathrm{AF}}^2}{(i\omega_n - E_1^2)(i\omega_n - E_2^2)} \tag{4.34}$$

$$\mathrm{F}_\sigma^\dagger = \sigma W z\, \Delta^*(k) \frac{W^2z^2|\Delta(k)|^2 - \epsilon_3\epsilon_4 + W^2z^2m_{\mathrm{AF}}^2}{(i\omega_n - E_1^2)(i\omega_n - E_2^2)} \tag{4.35}$$

$$\mathrm{F}_{Q\sigma}^\dagger = W^2z^2\, m_{\mathrm{AF}}\, \Delta^*(k) \frac{\epsilon_3 - \epsilon_2}{(i\omega_n - E_1^2)(i\omega_n - E_2^2)} \tag{4.36}$$

Here the common denominator is the determinant of the coefficient matrix. Its roots define the excitation energy spectra of the quasi particles and quasi holes:

$$E_1^\pm = \pm\sqrt{W^2z^2|\Delta(k)|^2 + (E_{\mathrm{AF}} + \overline{\mu})^2} \tag{4.37}$$

$$E_2^\pm = \pm\sqrt{W^2z^2|\Delta(k)|^2 + (E_{\mathrm{AF}} - \overline{\mu})^2} \tag{4.38}$$

with

$$E_{\mathrm{AF}} = \sqrt{\epsilon_k^2 + W^2z^2m_{\mathrm{AF}}^2} \quad . \tag{4.39}$$

Without an upper index, E_i always refers to E_i^+.

4.1.5 Selfconsistent Equations and Free Energy

In a straight forward way, i.e. without using the general results from chapter 3 (see the end of this section), the expectation values on the right hand side of the selfconsistent equations may be calculated from the Greens functions G_σ, $\mathrm{G}_{Q\sigma}$ and the anomalous Greens function $\mathrm{F}_\sigma^\dagger$. In fact, in the limit $\tau \to 0^-$ one obtains:

$$\mathrm{G}_\sigma(k, 0^-) = -\langle n_{k\sigma}\rangle_{\mathrm{HFB}} \tag{4.40}$$

$$\mathrm{G}_{Q\sigma}(k, 0^-) = -\left\langle c_{k\sigma}^\dagger c_{k+Q\sigma}\right\rangle_{\mathrm{HFB}} \tag{4.41}$$

$$\mathrm{F}_\sigma^\dagger(k, 0^-) = -\left\langle c_{k\sigma}^\dagger c_{-k-\sigma}^\dagger\right\rangle_{\mathrm{HFB}} \tag{4.42}$$

$$\mathrm{F}_{Q\sigma}^\dagger(k, 0^-) = -\left\langle c_{k\sigma}^\dagger c_{-(k+Q)-\sigma}^\dagger\right\rangle_{\mathrm{HFB}} \quad , \tag{4.43}$$

so that the selfconsistent equations become

$$n = -\frac{1}{L}\sum_{k,\sigma} \mathrm{G}_\sigma(k, 0^-) \tag{4.44}$$

$$m_{\mathrm{AF}} = -\frac{1}{2L}\sum_k \left\{ \mathrm{G}_{Q\uparrow}(k,0^-) - \mathrm{G}_{Q\downarrow}(k,0^-) \right\} \tag{4.45}$$

$$\Delta_\alpha = -\frac{1}{L}\sum_k (\mathrm{F}^\dagger_\uparrow(k,0^-))^* f_\alpha(k) \tag{4.46}$$

$$\Delta^*_\alpha = -\frac{1}{L}\sum_k \mathrm{F}^\dagger_\uparrow(k,0^-)\, f^*_\alpha(k) \quad . \tag{4.47}$$

Note that the fourth Greens function is not used because no variational parameter corresponding to η–pairing [Yang89] has been included into the trial Hamiltonian. Nevertheless, this Greens function component may not be omitted in order to get a closed set of coupled equations of motions for all Greens functions. The inclusion of a η–pairing variational parameter and its implications is briefly discussed in chapter 8. Now, the limit $\tau \to 0^-$ may be calculated from the frequency dependent Greens functions. For this purpose it is useful to write them with simple denominators. All four Greens functions have the following form:

$$\mathrm{G}(k,i\omega_n) = \frac{\tilde{\mathrm{G}}(k,i\omega_n)}{(i\omega_n - E_1^2)(i\omega_n - E_2^2)} \tag{4.48}$$

where $\mathrm{G}(k,i\omega_n)$ represents one of the four Greens functions in equations (4.33) to (4.36), while $\tilde{\mathrm{G}}(k,i\omega_n)$ is the numerator of $\mathrm{G}(k,i\omega_n)$ and is a polynomial of third degree of $i\omega_n$. For this reason one can write (using again Mathematica [Mathematica])

$$\mathrm{G}(k,i\omega_n) = \frac{1}{E_2^2 - E_1^2}\sum_{i=1}^{2} \frac{(-1)^i}{2E_i} \left\{ \frac{\tilde{\mathrm{G}}(k,E_i)}{i\omega_n - E_i} - \frac{\tilde{\mathrm{G}}(k,-E_i)}{i\omega_n + E_i} \right\} \quad . \tag{4.49}$$

The advantage of this representation is that one now has obtained simple denominators of degree one and that the numerators do no longer depend on frequency. With

$$\frac{1}{\beta}\sum_n \frac{\exp(i\omega_n\tau)}{i\omega_n - \epsilon} = \begin{cases} \dfrac{\mathrm{e}^{\epsilon\tau}}{\mathrm{e}^{\epsilon\beta}+1} = \mathrm{e}^{\epsilon\tau} f(\epsilon) & \text{for} \quad \tau > 0 \\ -\dfrac{\mathrm{e}^{\epsilon\tau}}{\mathrm{e}^{-\epsilon\beta}+1} = -\mathrm{e}^{\epsilon\tau} f(-\epsilon) & \text{for} \quad \tau < 0 \quad , \end{cases} \tag{4.50}$$

the τ–dependent Greens functions for $\tau > 0$ are therefore given by:

$$\mathrm{G}(k,\tau>0) = \frac{1}{E_2^2 - E_1^2}\sum_{i=1}^{2} \frac{(-1)^i}{2E_i} \left\{ \mathrm{e}^{E_i\tau}\, \tilde{\mathrm{G}}(k,E_i)\, f(E_i) - \mathrm{e}^{-E_i\tau}\, \tilde{\mathrm{G}}(k,-E_i)\, f(-E_i) \right\} \tag{4.51}$$

and for $\tau < 0$ by:

$$\mathrm{G}(k,\tau<0) = \frac{1}{E_2^2 - E_1^2}\sum_{i=1}^{2} \frac{(-1)^{i+1}}{2E_i} \left\{ \mathrm{e}^{E_i\tau}\, \tilde{\mathrm{G}}(k,E_i)\, f(-E_i) - \mathrm{e}^{-E_i\tau}\, \tilde{\mathrm{G}}(k,-E_i)\, f(E_i) \right\} \quad , \tag{4.52}$$

from which the desired τ–limit can be calculated at once. The result is:

$$G(k,\tau=0^-)=\frac{1}{E_2^2-E_1^2}\sum_{i=1}^{2}\frac{(-1)^{i+1}}{2E_i}\Big\{\tilde{G}(k,E_i)f(-E_i)-\tilde{G}(k,-E_i)f(E_i)\Big\} \quad . \tag{4.53}$$

Finally one can replace the Fermi function by:

$$f(x)=\frac{1-\tanh(\beta x/2)}{2} \quad . \tag{4.54}$$

This leads to:

$$G(k,\tau=0^-)=\frac{1}{E_2^2-E_1^2}\sum_{i=1}^{2}\frac{(-1)^{i+1}}{2E_i}\Big\{\frac{\tilde{G}(k,E_i)-\tilde{G}(k,-E_i)}{2}+\frac{\tilde{G}(k,E_i)+\tilde{G}(k,-E_i)}{2}\tanh\left(\frac{\beta E_i}{2}\right)\Big\} \quad . \tag{4.55}$$

Using this formula and the expressions for the frequency–dependent Greens functions above in equation (4.33) to equation (4.36), from which the denominators $\tilde{G}(k,E_i)$ and $\tilde{G}(k,-E_i)$ can be directly obtained, the result for the time–dependent Greens functions in the limit $\tau\to 0^-$ is:

$$\begin{aligned}
G_\sigma(k,0^-) &= -\frac{1}{2}+\frac{1}{4E_{AF}}\Big\{(\epsilon_k-E_{AF})(E_{AF}+\overline{\mu})A_1+ \\
&\qquad (\epsilon_k+E_{AF})(E_{AF}-\overline{\mu})A_2\Big\} && (4.56)\\
G_{Q\sigma}(k,0^-) &= \frac{\sigma W z m_{AF}}{4E_{AF}}\Big\{(E_{AF}+\overline{\mu})A_1+(E_{AF}-\overline{\mu})A_2\Big\} && (4.57)\\
F^{\dagger}_{\sigma}(k,0^-) &= \frac{\sigma W z\Delta^*(k)}{4E_{AF}}\Big\{(E_{AF}-\epsilon_k)A_1+(E_{AF}+\epsilon_k)A_2\Big\} && (4.58)\\
F^{\dagger}_{Q\sigma}(k,0^-) &= \frac{\sigma W^2 z^2\Delta^*(k)m_{AF}}{4E_{AF}}\Big\{A_1-A_2\Big\} \quad , && (4.59)
\end{aligned}$$

where A_i is defined by

$$A_i:=\frac{1}{E_i}\tanh\left(\frac{\beta E_i}{2}\right) \quad \text{for} \quad i=1,2 \quad , \tag{4.60}$$

while the definitions of the quasi particle energies E_i and of the energy E_{AF} are given in equation (4.37), (4.38) and (4.39), respectively. Summing these expressions over k and σ yields the right hand sides of the selfconsistent equations. They are:

the equation for the chemical potential:

$$n=1+\frac{1}{2L}\sum_k\Big\{(E_{AF}+\overline{\mu})A_1-(E_{AF}-\overline{\mu})A_2\Big\} \quad , \tag{4.61}$$

the equation for the antiferromagnetic parameter:

$$m_{\rm AF} = -\frac{Wzm_{\rm AF}}{4L}\sum_k \frac{1}{E_{\rm AF}}\Big\{(E_{\rm AF}+\overline{\mu})A_1 + (E_{\rm AF}-\overline{\mu})A_2\Big\} \quad , \tag{4.62}$$

and the equations for the pairing parameter:

$$\Delta_\alpha = -\frac{Wz}{4L}\sum_k f_\alpha(k)\Delta(k)\Big\{A_1 + A_2\Big\} \quad \text{for} \quad \alpha = 1,\ldots,z \tag{4.63}$$

with

$$\Delta(k) = \frac{1}{z}\sum_\alpha \Delta_\alpha f_\alpha^*(k) \quad . \tag{4.64}$$

Note that the contributions in the equations for the pairing parameters which arise from the terms proportional to ϵ_k in the expression for the anomalous Greens function $\mathrm{F}^\dagger_\sigma(k,0^-)$ vanish, for a shift of $k \to k+Q$ changes the sign of ϵ_k while $f_\alpha(k)\Delta(k)$ remains invariant. These $2+2z$ equations (including the complex conjugate equations for the pairing parameters) have to be solved simultaneously. In order to find the solution which belongs to the global minimum of the free energy functional, it is useful to derive an explicit expression for it. This can be done by integrating the selfconsistent equations because they result from varying the (canconical) free energy functional with respect to $\overline{\mu}$, $m_{\rm AF}$ and the pairing parameters Δ_α and their complex conjugates. From the selfconsistent equations above it is not very difficult to obtain the analytic form of the free energy functional. It reads:

$$\begin{aligned} A^{\#}_{\rm HFB}[\overline{\mu}, m_{\rm AF}, \Delta] \;=\; & -\frac{1}{\beta}\sum_{k,i} \ln\left(2\cosh\left(\frac{\beta E_i}{2}\right)\right) + \overline{\mu}\,L\,(n-1) \\ & - WzL\left\{m_{\rm AF}^2 + \frac{1}{z}\sum_\alpha |\Delta_\alpha|^2\right\} \quad . \end{aligned} \tag{4.65}$$

This expression can be directly derived using the general results of chapter 3.2.2 and the quasi particle and hole excitation spectrum given in equations (4.37)...(4.39). In fact, because formally

$$F_{\rm HFB} = -\frac{1}{2\beta}\mathrm{Tr}\,\ln\left(2\cosh\left(\frac{\beta \mathbf{M}_{\rm HFB}}{2}\right)\right) - \overline{\mu}\,L \tag{4.66}$$

and the eigenvalues of $\mathbf{M}_{\rm HFB}$ are given by the excitation energies $E_i^\alpha(k)$ for $i = 1,2$ and $\alpha = \pm$ and for all k in the first Brioullin zone, the Nambu matrix $\mathbf{M}_{\rm HFB}$ may be replaced

by $E_i^\alpha(k)$, so that the trace operation reduces to a sum over i, α and k. Finally, the cosh-function is symmetric so that the α-sum causes a factor of 2. The results of this section are summarized in tables 4.2 and 4.3. They include the Hamiltonian of the NNSP model, the trial Hamiltonian, the canonical free energy functional, the quasi particle excitation energy spectra and finally the selfconsistent equations. The results listed here are valid for all dimensions. In the forthcoming sections, however, only the two dimensional case is considered.

Table 4.2: Summary of the formulae for the symmetry-broken HFB approximation for the NNSP model I: Hamiltonian and trial Hamiltonian.

Hamiltonian of the NNSP model:
$\mathcal{H} = \sum_{k,\sigma}(\epsilon_k - \mu)n_{k\sigma} + \frac{Wz}{L}\sum_{q,k,k'} S(q) c^\dagger_{k+q\uparrow} c_{k\uparrow} c^\dagger_{k'-q\downarrow} c_{k'\downarrow}$ with $S(q) = \frac{1}{z}\sum_\alpha e^{iq\delta_\alpha}$
Trial Hamiltonian of the HFB approximation:
$\mathcal{H}_{\mathrm{HFB}} = \sum_{k,\sigma}(\epsilon_k - \overline{\mu})n_{k\sigma} + 2WzL\, m_{\mathrm{AF}} \left(\frac{1}{2L}\sum_k c^\dagger_{k+Q\uparrow} c_{k\uparrow} - c^\dagger_{k+Q\downarrow} c_{k\downarrow}\right)$ $+ WL\sum_\alpha \left\{ \left(\frac{1}{L}\sum_k c_{-k\downarrow} c_{k\uparrow} f_\alpha(k)\right) \Delta^*_\alpha + \mathrm{h.\,c.} \right\}$ where the $f_\alpha(k)$ are defined by $S(k-k') = \frac{1}{z}\sum_\alpha f_\alpha(k)\, f^*_\alpha(k')$

Table 4.3: Summary of the formulae for the symmetry–broken HFB approximation for the NNSP model II: free energy functional, excitation spectra and selfconsistent equations.

Canonical free energy functional:

$$A^{\#}_{\mathrm{HFB}} = -\frac{1}{\beta}\sum_{k,i}\ln\left(2\cosh\left(\frac{\beta E_i}{2}\right)\right) + \overline{\mu}\,L\,(n-1) - WzL\left\{m^2_{\mathrm{AF}} + \frac{1}{z}\sum_{\alpha}|\Delta_\alpha|^2\right\}$$

Excitation spectra:

$$E^{\pm}_1 = \pm\sqrt{W^2z^2|\Delta(k)|^2 + (E_{\mathrm{AF}} + \overline{\mu})^2}$$

$$E^{\pm}_2 = \pm\sqrt{W^2z^2|\Delta(k)|^2 + (E_{\mathrm{AF}} - \overline{\mu})^2}$$

with

$$E_{\mathrm{AF}} = \sqrt{\epsilon^2_k + W^2z^2m^2_{\mathrm{AF}}}$$

and

$$\Delta(k) = \frac{1}{z}\sum_{\alpha}\Delta_\alpha f^*_\alpha(k)$$

Selfconsistent equations:

electron density and chemical potential:

$$n = 1 + \frac{1}{2L}\sum_{k}\Big\{(E_{\mathrm{AF}} + \overline{\mu})A_1 - (E_{\mathrm{AF}} - \overline{\mu})A_2\Big\}$$

antiferromagnetic parameter:

$$m_{\mathrm{AF}} = -\frac{Wzm_{\mathrm{AF}}}{4L}\sum_{k}\frac{1}{E_{\mathrm{AF}}}\Big\{(E_{\mathrm{AF}} + \overline{\mu})A_1 + (E_{\mathrm{AF}} - \overline{\mu})A_2\Big\}$$

pairing parameters:

$$\Delta_\alpha = -\frac{Wz}{4L}\sum_{k}f_\alpha(k)\Delta(k)\Big\{A_1 + A_2\Big\} \quad \text{for} \quad \alpha = 1\ldots z$$

with

$$A_i = \frac{1}{E_i}\tanh\left(\frac{\beta E_i}{2}\right)$$

4.2 Selfconsistent Equations for $D = 2$

4.2.1 Extended s–wave/d–wave Pairing and Relative Phase

In two dimensions ten coupled nonlinear equations have to be solved simultaneously. For singlet pairing the pairing parameter has to be an even function of the relative momentum vector k [Sigrist87], i. e.:

$$\Delta(k) = \Delta(-k) \quad . \tag{4.67}$$

Within the group–theoretical representation (see table 2.1 on page 23), this means that the p–wave components vanish identically or may just be omitted, so that the k–dependent superconducting variational parameter now becomes:

$$\Delta(k) = \frac{1}{z}\Big\{\Delta_{xs} f_{xs}(k) + \Delta_d f_d(k)\Big\} \tag{4.68}$$

with

$$f_{xs}(k) = (\cos(k_x) + \cos(k_y)) \tag{4.69}$$
$$f_d(k) = (\cos(k_x) - \cos(k_y)) \quad . \tag{4.70}$$

The two components Δ_{xs} and Δ_d, which describe xs–wave and d–wave superconductivity, respectively, are still complex numbers. It is very practical to introduce the phase of these parameters according to

$$\Delta_{xs} = |\Delta_{xs}|\, e^{i\phi_{xs}} \tag{4.71}$$
$$\Delta_d = |\Delta_d|\, e^{i\phi_d} \tag{4.72}$$

and the relative phase

$$\phi = \phi_{xs} - \phi_d \quad . \tag{4.73}$$

Because the free energy functional depends on the absolute value of the k–dependent superconducting variational parameter, which is now given by

$$|\Delta(k)|^2 = \frac{1}{z^2}\Big\{ |\Delta_{xs}|^2 f_{xs}^2(k) + |\Delta_d|^2 f_d^2(k) + 2\,|\Delta_{xs}|\,|\Delta_d|\, f_{xs}(k) f_d(k) \cos(\phi)\Big\} \quad , \tag{4.74}$$

and on the absolute values of Δ_{xs} and Δ_d in quadratic terms, only the relative phase is important. For this reason the two complex equations for Δ_{xs} and Δ_d reduce to three

real equations for $|\Delta_{xs}|$, $|\Delta_d|$ and ϕ. They may be derived either by introducing the phase factors in the selfconsistent equations for Δ_{xs} and Δ_d, or by differentiating the free energy functional with respect ot $|\Delta_{xs}|$, $|\Delta_d|$ and ϕ. The second method yields:

$$\frac{\partial A^{\#}}{\partial |\Delta_\alpha|} = -\frac{1}{2}\sum_{k,i} \tanh\left(\frac{\beta E_i}{2}\right) \frac{\partial E_i}{\partial |\Delta_\alpha|} - 2WL\,|\Delta_\alpha| \quad \text{for} \quad \alpha = xs, d \tag{4.75}$$

$$\frac{\partial A^{\#}}{\partial \phi} = -\frac{1}{2}\sum_{k,i} \tanh\left(\frac{\beta E_i}{2}\right) \frac{\partial E_i}{\partial \phi} \quad , \tag{4.76}$$

where

$$\frac{\partial E_i}{\partial |\Delta_{xs}|} = \frac{W^2}{E_i} f_{xs}\Big(f_{xs}\,|\Delta_{xs}| + f_d\,|\Delta_d|\cos(\phi)\Big) \tag{4.77}$$

$$\frac{\partial E_i}{\partial |\Delta_d|} = \frac{W^2}{E_i} f_d\Big(f_d\,|\Delta_d| + f_{xs}\,|\Delta_{xs}|\cos(\phi)\Big) \tag{4.78}$$

$$\frac{\partial E_i}{\partial \phi} = -\frac{W^2}{E_i}\,|\Delta_{xs}|\,|\Delta_d|\; f_{xs}\, f_d \sin(\phi) \quad . \tag{4.79}$$

The selfconsistent equations for $|\Delta_{xs}|$, $|\Delta_d|$ and ϕ now become:

$$|\Delta_{xs}| = -\frac{W}{4L}\sum_k f_{xs}(k)\Big(|\Delta_{xs}|\, f_{xs}(k) + |\Delta_d|\cos(\phi) f_d(k)\Big)\Big\{A_1 + A_2\Big\} \tag{4.80}$$

$$|\Delta_d| = -\frac{W}{4L}\sum_k f_d(k)\Big(|\Delta_{xs}|\cos(\phi) f_{xs}(k) + |\Delta_d|\, f_d(k)\Big)\Big\{A_1 + A_2\Big\} \tag{4.81}$$

$$0 = \frac{W^2}{2}\,|\Delta_{xs}|\,|\Delta_d|\sin(\phi)\sum_k f_{xs}(k)\, f_d(k)\Big\{A_1 + A_2\Big\} \quad . \tag{4.82}$$

Clearly the absolute values of the xs–wave and the d–wave components have to be real and positive. For this reason the range of solutions for $|\Delta_{xs}|$ and $|\Delta_d|$ can be restricted to $\mathbb{R}^+ \times \mathbb{R}^+$. As a function of ϕ, the free energy functional is periodic with period π, because a shift of ϕ by π yields

$$|\Delta(k)|^2\Big|_{\phi\to\phi+\pi} = \frac{1}{z^2}\Big\{\,|\Delta_{xs}|^2\, f_{xs}^2(k) + |\Delta_d|^2\, f_d^2(k) - 2\,|\Delta_{xs}|\,|\Delta_d|\, f_{xs}(k) f_d(k)\cos(\phi)\Big\} \quad , \tag{4.83}$$

i. e. the sign in front of the mixed term changes. Now one can exchange the k_x– with the k_y–sum in the expression for the free energy functional. This does not change the sign of $f_{xs}(k)$ but of $f_d(k)$, so that with

$$|\Delta(k)|^2\Big|_{\phi\to\phi+\pi, k_x\leftrightarrow k_y} = |\Delta(k)|^2 \tag{4.84}$$

the free energy functional remains invariant under the transformation $\phi \to \phi + \pi$, which means that it is periodic with period π. To summarize, the selfconsistent equations for the pairing parameters have to be solved in the range

$$\Big(|\Delta_{xs}|, |\Delta_d|, \phi\Big) \in \mathbb{R}^+ \times \mathbb{R}^+ \times [0, \pi[\quad . \tag{4.85}$$

The equation for ϕ can be solved analytically, which is shown in the next section.

4.2.2 $xs + id$ Pairing

or minimizing the free energy functional with respect to ϕ. First of all, from the free energy functional or explicitly from the selfconsistent equations, it becomes obvious that ϕ is irrelevant and has no more meaning if one of the two components $|\Delta_{xs}|$ or $|\Delta_d|$ vanish. In this case ϕ can be arbitrarily chosen without changing the result. Consider the mixed phase where both components $|\Delta_{xs}|$ and $|\Delta_d|$ are nonzero. The equation (4.82) for ϕ is therefore satisfied if

$$\sin(\phi) = 0 \tag{4.86}$$

$$\vee \sum_k f_{xs}(k)\, f_d(k) \left\{ A_1 + A_2 \right\} = 0 \ . \tag{4.87}$$

The solutions of the first of these equations are

$$\phi_{\max}(l) = l\pi \quad \forall\, l \in Z \tag{4.88}$$

and in the range $[0, \pi[$ only $\phi = \phi_{\max} = 0$. As we shall show below, these values of ϕ lead to maxima of the free energy functional. The solutions of the second equation are the odd multiples of $\pi/2$:

$$\phi_{\min}(l) = (2l+1)\frac{\pi}{2} \quad \forall\, l \in Z \tag{4.89}$$

and in the range $[0, \pi[$ only $\phi = \phi_{\min} = \pi/2$. They belong to minima of the free energy functional. Before we prove the maxima and minima properties of the free energy functional with respect to these values of ϕ, we need to show that in fact $\phi_{\min}(l)$ solves equation (4.87) and that there do not exist any further solutions. For $\phi = \phi_{\min}(l)$, the absolute square of $\Delta(k)$ becomes symmetric with respect to the exchange of the k_x- with the k_y-axis. On the other hand, the product of the two structure functions $f_{xs}(k)\, f_d(k)$ changes sign if k_x is replaced by k_y and vice versa. For this reason the odd multiples of $\pi/2$ solve equation (4.87). In order to see that there are no further solutions, it is useful to consider the derivative of the left hand side of equation (4.87) with respect to ϕ, which is given by:

$$\frac{\partial}{\partial\phi} \sum_k f_{xs}(k)\, f_d(k) \left\{ A_1 + A_2 \right\} = -W^2\, |\Delta_{xs}|\, |\Delta_d|\, \sin(\phi) \sum_{k,i} \frac{f_{xs}^2(k)\, f_d^2(k)}{E_i} \frac{\partial A_i}{\partial E_i} \tag{4.90}$$

with

$$\frac{\partial A_i}{\partial E_i} = \frac{\beta}{2E_i \cosh(\beta E_i/2)} \left\{ \frac{1}{\cosh(\beta E_i/2)} - \frac{\sinh(\beta E_i/2)}{\beta E_i/2} \right\} \leq 0 \quad , \tag{4.91}$$

which is less than or equal to zero because $\cosh(x) \geq 1$ and $\sinh(x) \geq x$ for all $x \in \mathbb{R}$ and β and E_i are always positive quantities. Moreover, it is negative for all $E_i > 0$ and vanishes for $E_i \to 0$. The set of (k_x, k_y)–pairs, for which $E_i = 0$ or $f_{xs}^2(k)\, f_d^2(k) = 0$ is a nonmeasurable set. For this reason the expression on the right hand side of equation (4.90) is greater than zero for all $\phi \in]0, \pi[$. For $\phi = 0$ or $\phi = \pi$, it becomes identically zero because of the pre–factor $\sin(\phi)$. Finally, this shows that the left hand side of equation (4.87) is a strictly monotonic increasing function of ϕ for $\phi \in]0, \pi[$, and hence proves that $\phi_{\min} = \pi/2$ is the only solution of equation (4.87) in this range and, because of the periodicity π, the odd multiples of $\pi/2$ are the only solutions of equation (4.87) for all ϕ. The derivative of the free energy functional with respect to ϕ is given by:

$$\frac{\partial A^{\#}}{\partial \phi} = \frac{W^2}{2} |\Delta_{xs}| |\Delta_d| \sin(\phi) \sum_k f_{xs}(k)\, f_d(k) \left\{ A_1 + A_2 \right\} \quad . \tag{4.92}$$

From the considerations above it follows that the k–sum is negative for $\phi \in [0, \pi/2[$, zero for $\phi = \pi/2$ and positive for $\phi \in]\pi/2, \pi[$. In the range $[0, \pi[$, $\sin(\phi)$ is always greater than or equal to zero. Therefore:

$$\frac{\partial A^{\#}}{\partial \phi} \begin{cases} < & 0 \quad \text{for} \quad \phi \in]0, \pi/2[\\ > & 0 \quad \text{for} \quad \phi \in]\pi/2, \pi[\\ = & 0 \quad \text{for} \quad \phi = 0, \pi/2 \end{cases} . \tag{4.93}$$

This shows that $A^{\#}$ as a function of ϕ has a maximum at $\phi = 0$ and, due to the periodicity, at all even multiples of $\pi/2$ and minima at all odd multiples of $\pi/2$. In figure 4.1 the free energy functional $A^{\#}/t$ is plotted as a function of ϕ for $T/t = 0$, $W/t = -4$ and $n = 1.2$, while the variational parameters $|\Delta_{xs}|$, $|\Delta_d|$, m_{AF} and $\overline{\mu}$ are determined selfconsistently. Figure 4.1 visualizes the general behavior described above, namely the minimum at $\phi = \pi/2$ and the maximum at $\phi = 0$ in the range of $[0, \pi[$, which is true for all parameters. Moreover, it shows that the difference between the maximum and the minimum values of $A^{\#}/t$ is not very large. For this reason the solutions of the selfconsistent equations depend not very sensitively on ϕ.

In this section, we have shown that the relative phase between the xs–wave and the d–wave component, which minimizes the free energy functional, is $\pi/2$ (or all odd multiples of $\pi/2$). This is usually refered as $xs + id$–pairing [Sigrist87]. For $\phi = \pi/2$, the selfconsistent

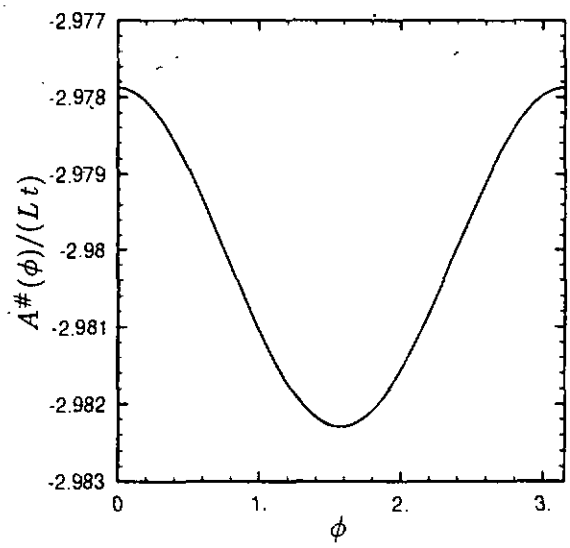

Figure 4.1: The canonical free energy functional as a function of the relative phase between the xs– and d–wave component of the superconducting variational parameter for $T/t = 0$, $W/t = -4$ and $n = 1.2$. The variational parameters, including the renormalized chemical potential, are determinded selfconsistently, i. e.: $|\Delta_d| = 0.182$, $|\Delta_{xs}| = 0.083$, $m_{\rm AF} = 0.378$ and $\overline{\mu} = 5.774$.

equations for the absolute values of Δ_{xs} and Δ_d then become:

$$|\Delta_{xs}| = -\frac{W\,|\Delta_{xs}|}{4L}\sum_k f_{xs}^2(k)\Big\{A_1 + A_2\Big\} \tag{4.94}$$

$$|\Delta_d| = -\frac{W\,|\Delta_d|}{4L}\sum_k f_d^2(k)\Big\{A_1 + A_2\Big\} \tag{4.95}$$

and the square of the absolute value of $\Delta(k)$ is given by:

$$|\Delta(k)|^2 = \frac{1}{z^2}\Big\{\,|\Delta_{xs}|^2\,f_{xs}^2(k) + |\Delta_d|^2\,f_d^2(k)\Big\} \quad , \tag{4.96}$$

which enters in the equations for the chemical potential and the antiferromagnetic variational parameter. The free energy functional and the selfconsistent equations for $D = 2$ are summarized in table 4.4.

Table 4.4: HFB free energy functional, excitation spectra and selfconsistent equations of the symmetry–broken HFB approximation for the NNSP model for $D = 2$ and $\phi = \pi/2$.

Canonical free energy functional:

$$A^{\#}_{\rm HFB} = -\frac{1}{\beta}\sum_{k,i} \ln\left(2\cosh\left(\frac{\beta E_i}{2}\right)\right) + \overline{\mu}\,L\,(n-1) - WL\Big\{4m^2_{\rm AF} + |\Delta_{xs}|^2 + |\Delta_d|^2\Big\}$$

Excitation spectra:

$$E^{\pm}_1 = \pm\sqrt{16W^2|\Delta(k)|^2 + (E_{\rm AF} + \overline{\mu})^2}$$

$$E^{\pm}_2 = \pm\sqrt{16W^2|\Delta(k)|^2 + (E_{\rm AF} - \overline{\mu})^2}$$

with

$$E_{\rm AF} = \sqrt{\epsilon^2_k + 16W^2 m^2_{\rm AF}}$$

$$|\Delta(k)|^2 = \frac{1}{16}\Big\{\,|\Delta_{xs}|^2\, f^2_{xs}(k) + |\Delta_d|^2\, f^2_d(k)\Big\}$$

$$f_{xs}(k) = \cos(k_x) + \cos(k_y) \quad \text{and} \quad f_d(k) = \cos(k_x) - \cos(k_y)$$

Selfconsistent equations:

electron density and chemical potential:

$$n = 1 + \frac{1}{2L}\sum_k \Big\{(E_{\rm AF} + \overline{\mu})A_1 - (E_{\rm AF} - \overline{\mu})A_2\Big\}$$

antiferromagnetic parameter:

$$m_{\rm AF} = -\frac{W m_{\rm AF}}{L}\sum_k \frac{1}{E_{\rm AF}}\Big\{(E_{\rm AF} + \overline{\mu})A_1 + (E_{\rm AF} - \overline{\mu})A_2\Big\}$$

xs–wave and d–wave pairing parameter:

$$|\Delta_\alpha| = -\frac{W\,|\Delta_\alpha|}{4L}\sum_k f^2_\alpha(k)\Big\{A_1 + A_2\Big\} \quad \text{for} \quad \alpha = xs, d$$

with

$$A_i = \frac{1}{E_i}\tanh\left(\frac{\beta E_i}{2}\right)$$

4.3 Numerical Remarks

Finding the roots of a single nonlinear equation is, in most cases, a simple numerical task. A Newton method is usually sufficient, or, if one is not able to calculate the derivative of the target function but is able to bracket the root (to find a value on the left and right hand side of the root), one can use a secant method or related methods, like a bisection or false position method [NumRec]. For a higher dimensional set of coupled nonlinear equations the situation is more difficult. One can also use a generalized Newton method, but it converges only if the starting point is very close to the root. Furthermore, at each iteration step the Jacobian has to be calculated, which requires a lot of computing time. For these reasons we have used a different but straightforward method. First of all it is quite easy to show that $n(\overline{\mu})$, defined by the right hand side of the first selfconsistent equation in table 4.4, is a monotonic increasing function of the renormalized chemical potential $\overline{\mu}$ for all parameters. Differentiating $n(\overline{\mu})$ with respect to $\overline{\mu}$ yields:

$$\frac{\partial n(\overline{\mu})}{\partial \overline{\mu}} = \frac{1}{2L}\sum_k \left\{ A_1 + A_2 + (E_{\mathrm{AF}} + \overline{\mu})\frac{\partial E_1}{\partial \overline{\mu}}\frac{\partial A_1}{\partial E_1} - (E_{\mathrm{AF}} - \overline{\mu})\frac{\partial E_2}{\partial \overline{\mu}}\frac{\partial A_2}{\partial E_2} \right\} \quad . \tag{4.97}$$

With

$$\frac{\partial E_1}{\partial \overline{\mu}} = \frac{(E_{\mathrm{AF}} + \overline{\mu})}{E_1} \tag{4.98}$$

$$\frac{\partial E_2}{\partial \overline{\mu}} = -\frac{(E_{\mathrm{AF}} - \overline{\mu})}{E_2} \quad , \tag{4.99}$$

the previous equation becomes:

$$\frac{\partial n(\overline{\mu})}{\partial \overline{\mu}} = \frac{1}{2L}\sum_k \left\{ A_1 + A_2 + \frac{(E_{\mathrm{AF}} + \overline{\mu})^2}{E_1}\frac{\partial A_1}{\partial E_1} + \frac{(E_{\mathrm{AF}} - \overline{\mu})^2}{E_2}\frac{\partial A_2}{\partial E_2} \right\} \quad . \tag{4.100}$$

Because $A_i \geq 0$, $(E_{\mathrm{AF}} + \overline{\mu})^2 \leq E_1^2$, $(E_{\mathrm{AF}} - \overline{\mu})^2 \leq E_2^2$ and $\partial A_i / \partial E_i \leq 0$ with

$$\begin{aligned} \left|\frac{\partial A_i}{\partial E_i}\right| &= -\frac{\partial A_i}{\partial E_i} \\ &= \frac{A_i}{E_i}\left\{ 1 - \frac{\beta E_i/2}{\sinh(\beta E_i/2)\cosh(\beta E_i/2)} \right\} \\ &\leq \frac{A_i}{E_i} \quad , \end{aligned} \tag{4.101}$$

the partial derivative $\partial n(\overline{\mu})/\partial \overline{\mu}$ is always positive or vanishes. Moreover, it is easy to show that $n(\overline{\mu})$ obeys the following two limits:

$$\lim_{\overline{\mu}\to\infty} n(\overline{\mu}) = 2 \tag{4.102}$$

$$\lim_{\overline{\mu}\to-\infty} n(\overline{\mu}) = 0 \quad . \tag{4.103}$$

For half–filling the renormalized chemical potential is always zero, i. e.

$$n(\overline{\mu}=0)=1 \quad . \tag{4.104}$$

This is an exact result and is reproduced by the HFB approximation. From these relations, it follows that $\overline{\mu}$ is always negative for $n<1$ and positive for $n>1$. Because of this nice behavior of $n(\overline{\mu})$, it is possible and very practical to use one of the one–dimensional methods to invert the first selfconsistent equation in order to get a function or procedure $\overline{\mu}(|\Delta_{xs}|,|\Delta_d|,m_{\mathrm{AF}},t,W,T,n)$ which calculates $\overline{\mu}$ for given but arbitrary variational parameters $|\Delta_{xs}|,|\Delta_d|,m_{\mathrm{AF}}$ and model parameters t,W,T and n. For that purpose we have implemented the false position method described in [NumRec], for it yields the fastest algorithm and even converges for discontinous target functions. For bracketing the root, we have multiplied or divided a starting value for $\overline{\mu}$ several times by a constant up to the point where two bracketing values have been found. The starting value for $\overline{\mu}$ has been chosen to be positive for $n>1$ and negative for $n<1$. Because of the behavior of $n(\overline{\mu})$ described above, the false position method together with this bracketing technique will always converge. Using this function within the evaluation of the right hand sides of the remaining selfconsistent equations reduces the number of equations by 1. The price to pay is the calculation of the chemical potential for every function evaluation. The advantage, however, is that now the three equations have all the same form, namely

$$m_{\mathrm{AF}} = m_{\mathrm{AF}}\, I_{\mathrm{AF}}(|\Delta_{xs}|,|\Delta_d|,m_{\mathrm{AF}}) \tag{4.105}$$

$$|\Delta_{xs}| = |\Delta_{xs}|\, I_{xs}(|\Delta_{xs}|,|\Delta_d|,m_{\mathrm{AF}}) \tag{4.106}$$

$$|\Delta_d| = |\Delta_d|\, I_d(|\Delta_{xs}|,|\Delta_d|,m_{\mathrm{AF}}) \quad , \tag{4.107}$$

where the functions I_{AF}, I_{xs} and I_d are defined by the right hand sides of the selfconsistent equations, and the renormalized chemical potential has been replaced by the numerical function $\overline{\mu}(|\Delta_{xs}|,|\Delta_d|,m_{\mathrm{AF}},t,W,T,n)$ described above. These equations can be iterated, i. e. starting from an initial guess for the parameters $|\Delta_{xs}|,|\Delta_d|$ and m_{AF}, a subsequent evaluation of the functions I_{AF}, I_{xs} and I_d might hopefully converge. This means one is looking for a stable fixed point of the dynamical system defined by the three functions I_{AF}, I_{xs} and I_d. This method works for almost all input parameters. It converges rather fast if the parameters are far from any phase transition, but it is nearly impossible to calculate sharp phase boundaries because near a phase boundary the free energy functional becomes too flat. Therefore we have chosen another method which can be motivated as follows. The minimum of a parabolic function in D dimensions can be found by minimizing it in each direction. This procedure needs D one–dimensional root finding processes. For an arbitrary function which is twice continuously differentiable, the neighborhood of a minimum appears parabolic. That is, if one has a good starting point, the one–dimensional root finding methods for each direction of the parameter space will hopefully

lead to the desired solution. Because the function is not exactly a parabolic function, one has to iterate this process. In particular, starting from an initial guess, one first solves the equation for the antiferromagnetic variational parameter. This leads to a new value for m_{AF} which, together with the other initial values for $|\Delta_{xs}|$ and $|\Delta_d|$, is used to solve the second equation. The result of this one–dimensional problem is a better value for $|\Delta_{xs}|$. In the last step of the first iteration step one uses the new values for m_{AF} and $|\Delta_{xs}|$ to calculate a new value for $|\Delta_d|$. If the free energy was a parabolic function, one iteration step would lead to the right solution. But for a nonparabolic function one has to use the new values for m_{AF}, $|\Delta_{xs}|$ and $|\Delta_d|$ to start a second iteration step and so on. If one starts not too far from the minimum, this iteration leads to the global minimum of the free energy functional. The advantage of this procedure is that within every one–dimensional step one can determine if for the corresponding variable only the trivial solution, namely zero, exists. This leads to sharp phase boundaries. The disadvantage is obviously computing time. Finally we have combined both methods. First we have iterated the selfconsistent equations up to 50 times. Second, if after these 50 iteration steps the solution is not found yet, the second method is used. In figure 4.2 the results of all three methods, the iteration method (figure 4.2 (a)), the method using one–dimensional root finding techniques (figure 4.2 (b)) and the method which combines both techniques (figure 4.2 (c)) are shown. In each diagram the values for m_{AF}, $|\Delta_d|$ and $|\Delta_{xs}|$ after each iteration step are plotted as a function of computing time for $W/t = -4$ and $n = 1.2$. On the left hand side they are plotted for $T = 0$ (far from the critical temperature), while on the right hand side they are shown for $T = 0.5$ (just above the critical temperature). Every point corresponds to one iteration step. For $T/t = 0$, the simple iteration method (a) is about seven times faster than the second method (b). The third method (c) is identical to the first one, because it converges after 40 iteration steps. On the other hand, near the critical temperature for $T/t = 0.5$, the simple iteration technique does not converge within a maximum number of 1000 iteration steps which makes it useless for this set of parameters. The second method converges as fast as far from the phase transition for $T/t = 0$ and the third method is comparable to the second one. These calculations reveal that the best choice is the third method, for it is as fast as the simple iteration technique far from any phase transition and comparable to the second method very close to a phase transition. The results shown in chapter 5 are calculated using this combined method.

Figure 4.2: (see next page) The variational parameters m_{AF} (+), $|\Delta_{xs}|$ (□) and $|\Delta_d|$ (•) as a function of computing time using the simple iteration method (a), the method using one-dimensional root finding techniques (b) and the method which combines both techniques (c). The curves are calculated for $W/t = -4$ and $n = 1.2$ for $T/t = 0$ (left side) and $T/t = 0.5$ (right side). The initial values are $|\Delta_d| = 0.2$, $|\Delta_{xs}| = 0.2$, $m_{\mathrm{AF}} = 0.3$, wheras the final values for $T/t = 0$ are $|\Delta_d| = 0.182$, $|\Delta_{xs}| = 0.083$, $m_{\mathrm{AF}} = 0.378$ and for $T/t = 0.5$: $|\Delta_d| = 0$, $|\Delta_{xs}| = 0$, $m_{\mathrm{AF}} = 0.379$.

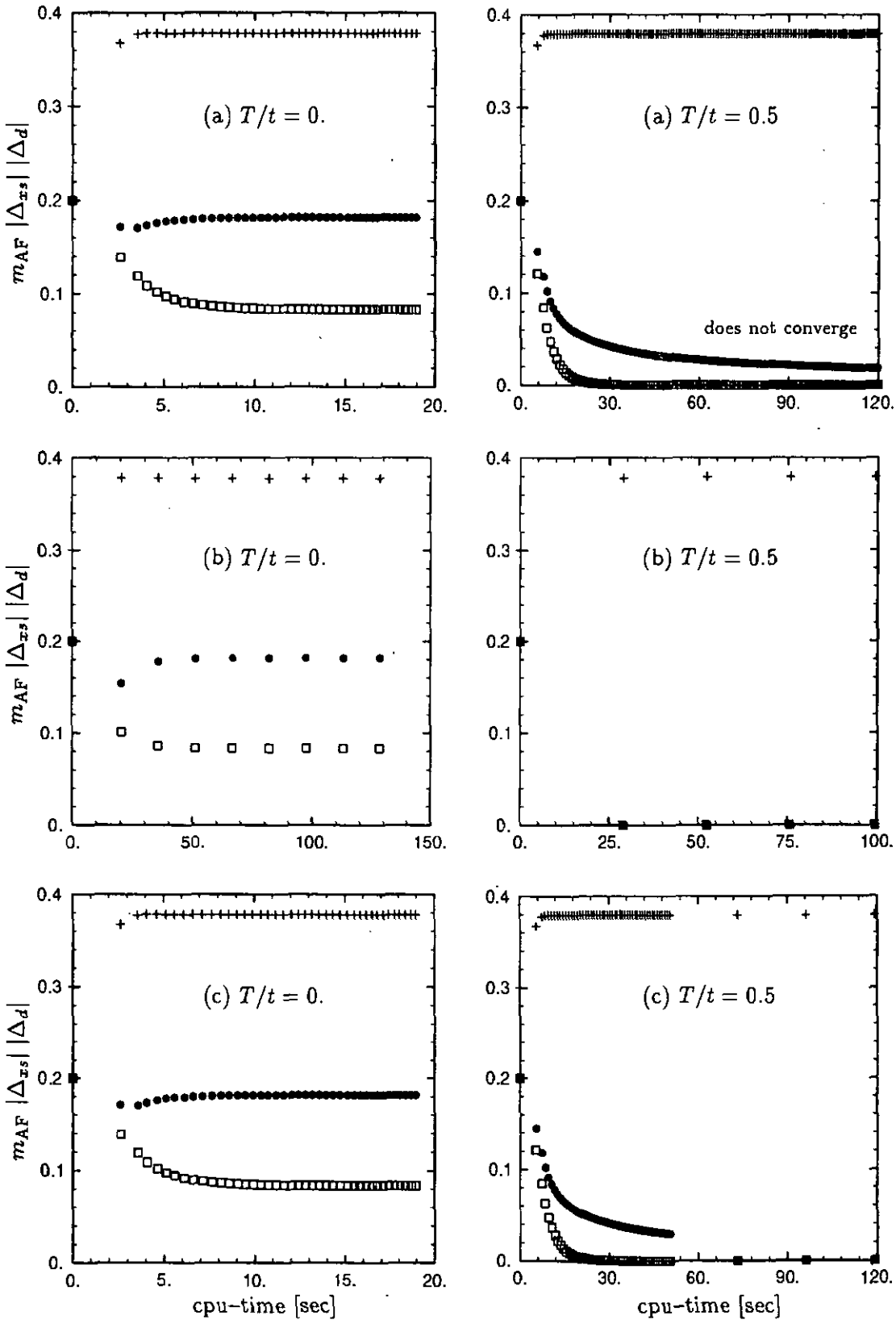
(a) $T/t = 0.$
(a) $T/t = 0.5$
does not converge
(b) $T/t = 0.$
(b) $T/t = 0.5$
(c) $T/t = 0.$
(c) $T/t = 0.5$
$m_{\rm AF}\ |\Delta_{xs}|\ |\Delta_d|$
cpu-time [sec]
cpu-time [sec]

Chapter 5

Solving the Selfconsistent Equations: Order parameter for $D = 2$

In the following sections of this chapter the numerical results for the order parameter are presented and discussed. In all figures the antiferromagnetic order parameter is drawn with a solid line, the absolute value of the xs–wave component of the superconducting order parameter with a dotted line and the absolute value of the d–wave component with a dashed line. Calculations of the free energy functional are used to verify that the solutions found by the iteration process described in the previous chapter 4 in fact minimize the free energy functional. Due to particle hole symmetry (only nearest neighbor hopping is taken into account) all functions of n are plotted as functions of $|n-1|$. All energies and temperatures are measured in units of the hopping integral t. The groundstate order parameters are considered in section 5.1. In section 5.2 their temperature behavior is studied, while in section 5.3 the HFB results are compared with the results obtained by the BCS approximation.

5.1 Groundstate Order parameter

5.1.1 Half–filling: $n = 1$

For half–filling the renormalized chemical potential is zero and both energy branches E_1 and E_2 are identical:

$$E_1 = E_2 = \sqrt{\epsilon_k^2 + 16W^2(|\Delta(k)|^2 + m_{\mathrm{AF}}^2)} \quad . \tag{5.1}$$

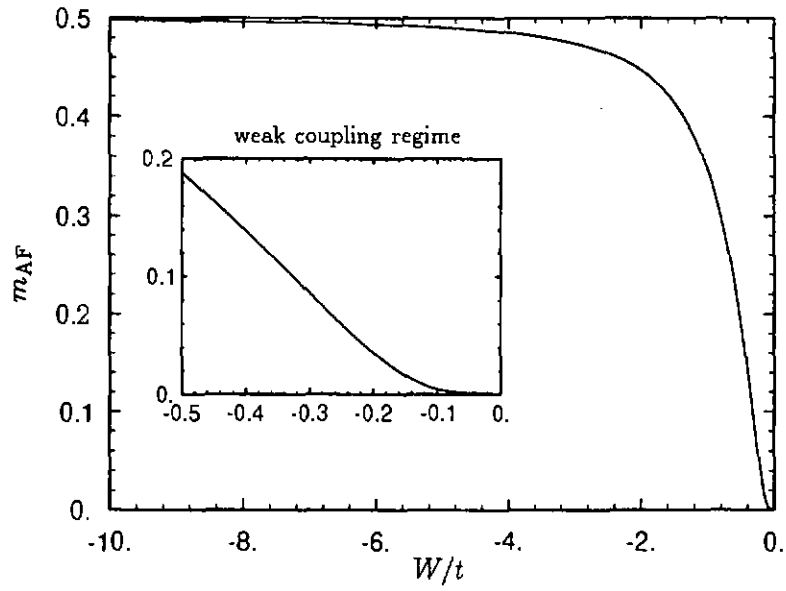

Figure 5.1: The selfconsistent solutions for half–filling ($n = 1$) and $T/t = 0.0$ as a function of W/t. Only for the antiferromagentic order parameter exists a nontrivial solution, which minimizes the free energy functional. Both $|\Delta_{xs}|$ and $|\Delta_d|$ vanish for all coupling constants, which shows that there is no superconductivity for half–filling. The inset zooms the weak coupling regime in the range $W/t = -0.5 \ldots 0$.

The selfconsistent equations for m_{AF}, $|\Delta_{xs}|$ and $|\Delta_d|$ now become very simple and read:

$$m_{\mathrm{AF}} = -\frac{2W m_{\mathrm{AF}}}{L} \sum_k A_1 \tag{5.2}$$

$$|\Delta_\alpha| = -\frac{W\,|\Delta_\alpha|}{2L} \sum_k f_\alpha^2(k) A_1 \quad \text{for} \quad \alpha = xs, d \quad . \tag{5.3}$$

Solving these equations leads to the important result that for half–filling there is no superconductivity for all parameters, i. e. both components $|\Delta_{xs}|$ and $|\Delta_d|$ are zero for all values of the coupling constants and all temperatures. This is shown in figure 5.1 for the groundstate ($T/t = 0.0$), where the selfconsistent solutions are plotted as a function of W/t. Only the antiferromagnetic order parameter m_{AF} is different from zero, increases with increasing absolute value of the coupling constant and approaches the maximum value of $m_{\mathrm{AF}} = 0.5$ as $|W/t|$ goes to infinity. In this limit the exact groundstate is the perfect Néel state and is reproduced by the HFB approximation. In fact for $t \to 0$ the right hand side of the selfconsistent equation for the antiferromagnetic order parameter in absence of any superconducting order becomes 1/2. The deviation from this maximum value for the antiferromagnetic order parameter in the weak coupling regime is due to quantum fluctuations which arise from the finite hopping amplitude. From the inset in figure 5.1 follows that the antiferromagnetic order parameter decreases exponentially for $W/t \to 0$.

To visualize the absence of superconductivity for half–filling, the free energy functional is plotted in figure 5.2 as a function of $|\Delta_{xs}|$ and $|\Delta_d|$ for $W/t = -4$ and $T/t = 0$. At

each point in the $|\Delta_{xs}|$-$|\Delta_d|$-plane, the antiferromagnetic order paramter is determined selfconsistently. From this figure it becomes obvious that indeed the global minimum of the free energy functional lies at $|\Delta_{xs}| = 0$ and $|\Delta_d| = 0$. It is quite easy to show that for a solution of the selfconsistent equations with finite value of the antiferromagnetic order parameter $m_{\mathrm{AF}} > 0$, the components $|\Delta_{xs}|$ and $|\Delta_d|$ of the superconducting order parameter have to be zero. In fact, with $f_\alpha^2(k) < 4$ for nearly all k-values and $f_\alpha^2(k) = 4$ for a nonmeasurable subset of the first Brioullin zone, the right-hand side of the selfconsistent equation for $|\Delta_\alpha|$ becomes:

$$\frac{|W|}{2L}\sum_k f_\alpha^2(k)A_1 < \frac{2\,|W|}{L}\sum_k A_1 = 1 \quad , \tag{5.4}$$

because of the finite value of m_{AF} which solves the antiferromagnetic selfconsistent equation. This inequality, however, does not prove that there do not exist any nontrivial solutions of the superconducting selfconsistent equations for vanishing antiferromagnetic order parameter, i. e. in the BCS limit. As shown in section 5.3, solutions of this type exist but have always a higher free energy as a solution with finite antiferromagnetic order

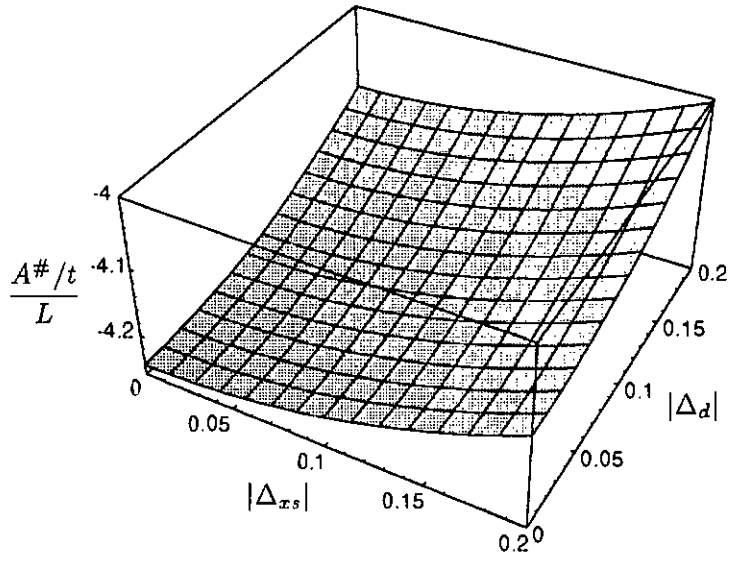

Figure 5.2: The free energy functional for half-filling with $W/t = -4$ and $T/t = 0$ as a function of the components of the superconducting order parameter $|\Delta_{xs}|$ and $|\Delta_d|$. At each point in the $|\Delta_{xs}|$-$|\Delta_d|$-plane m_{AF} and $\overline{\mu}$ are calulated selfconsistently. The absence of superconductivity for half-filling is obvious.

parameter, i. e.

$$A^{\#}(m_{\mathrm{AF}} > 0, |\Delta_{xs}|, |\Delta_d|)\Big|_{\mathrm{HFB}} < A^{\#}(m_{\mathrm{AF}} = 0, |\Delta_{xs}|, |\Delta_d|)\Big|_{\mathrm{BCS}} \quad , \tag{5.5}$$

where the left–hand side is evaluated at the antiferromagnetic solution with $m_{\mathrm{AF}} > 0$ and the right–hand side at the BCS solution with $m_{\mathrm{AF}} = 0$. Note that this inequality is also valid away from half–filling. For half–filling, however, it shows together with the first result in equation (5.4) the supression of superconductivity according to antiferromagnetic order.

In this context, a comparison to the negative U Hubbard model with on–site attraction is quite interesting. For this model a symmetry broken HFB approximation can also be carried out, including an s–wave variational pairing parameter Δ_s describing s–wave superconductivity and a CDW variational parameter $\rho_{q=Q} = \rho_{\mathrm{CDW}}$, which describes a nonuniform charge distribution corresponding to the wave vector Q [Robaszkiewicz81a]. The resulting formulae for the free energy functional and the quasi particle energy spectra are very similar to those of the NNSP model and read:

$$A^{\#}_{\mathrm{HFB}} = -\frac{1}{\beta}\sum_{k,i} \ln\left(2\cosh\left(\frac{\beta E_i}{2}\right)\right) + \overline{\mu}\, L\,(n-1) - UL\Big\{\frac{\rho^2_{\mathrm{CDW}}}{4} + |\Delta_s|^2\Big\} \quad , \tag{5.6}$$

with

$$E_1 = \sqrt{U^2|\Delta_s|^2 + (E_{\mathrm{CDW}} + \overline{\mu})^2} \tag{5.7}$$

$$E_2 = \sqrt{U^2|\Delta_s|^2 + (E_{\mathrm{CDW}} - \overline{\mu})^2} \tag{5.8}$$

and

$$E_{\mathrm{CDW}} = \sqrt{\epsilon_k^2 + U^2\rho^2_{\mathrm{CDW}}/4} \quad . \tag{5.9}$$

For half–filling the renormalized chemical potential vanishes and both excitation energy branches read:

$$E_1 = E_2 = \sqrt{\epsilon_k^2 + U^2(\rho^2_{\mathrm{CDW}}/4 + |\Delta_s|^2)} \quad . \tag{5.10}$$

From these formulae follows that the free energy functional for the HFB approximation for the attractive Hubbard model is a function of the combined variable $\rho^2_{\mathrm{CDW}}/4 + |\Delta_s|^2$, i. e. it is degenerate on all cirlces $\rho^2_{\mathrm{CDW}}/4 + |\Delta_s|^2 = R^2$ with radius R in the $\rho/2$–$|\Delta_s|$–plane. This symmetry does not exist for the HFB approximation for the NNSP model due to the nonlocal interaction which causes the k–dependence of the pairing functions. In fact,

the k–dependence of $f_{xs}(k)$ or $f_d(k)$ leads to inequality (5.4) and proves the suppression of superconductivity approaching half–filling. It should be noted that for the negative U Hubbard model the addition of an arbitrary small nearest neighbor interaction term favours the $CDW-$ solution for half–filling [Robaszkiewicz81a].

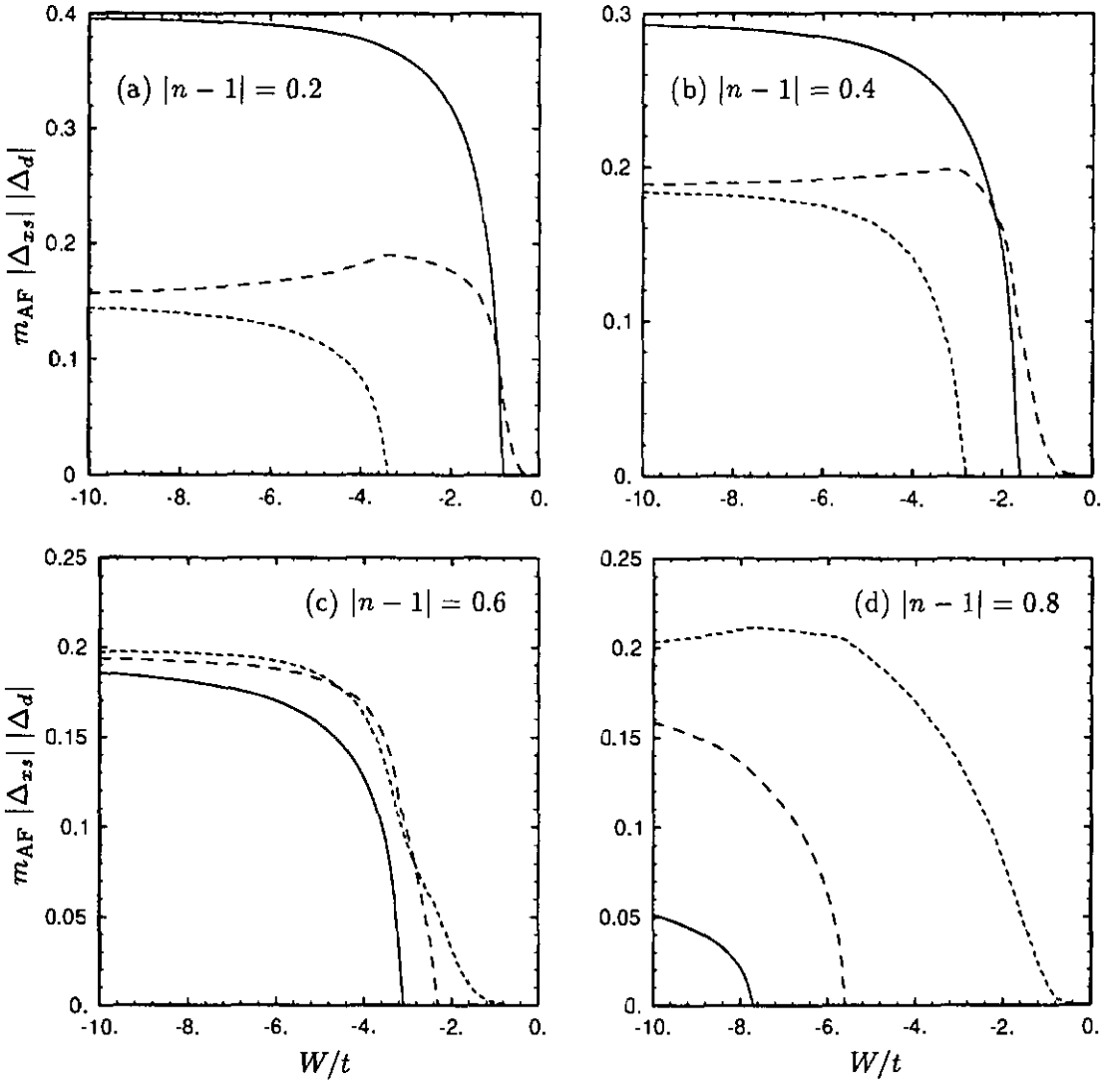

Figure 5.3: The order parameters m_{AF} (solid line), $|\Delta_{xs}|$ (dotted line) and $|\Delta_d|$ (dashed line) for $|n-1| = 0.2$(a), 0.4(b), 0.6(c), 0.8(d) and $T/t = 0$ as a function of W/t.

5.1.2 Away from Half–filling

The W/t–dependence of the groundstate order parameter away from half–filling is shown in figure 5.3 for different values of $|n-1|$. In figure 5.3(a) the antiferromagnetic order parameter (solid line), the xs–wave component (dotted line) and the d–wave component (dashed line) of the superconducting order parameter is plotted for $|n-1| = 0.2$, in figure 5.3(b) for $|n-1| = 0.4$, in figure 5.3(b) for $|n-1| = 0.6$ and in figure 5.3(b) for $|n-1| = 0.8$. It is interesting to observe that in contrast to the half–filled case in all four figures, either the absolute value of the xs–wave component or the absolute value of the d–wave component of the superconducting order parameter is nonzero for all $W/t < 0$,

which shows that away from half–filling the groundstate exhibits off–diagonal long range order and, if the system is noninsulating, superconductivity occurs[1] [Yang62, Rogovin76]. For $|n-1| = 0.2$ (a) and for $|n-1| = 0.4$ (b), the d–wave component is nonzero for all values of the coupling constant and one can observe an xs–wave phase boundary below which the xs–wave component becomes finite. On the other hand, for $|n-1| = 0.6$ (c) and $|n-1| = 0.8$ (d), the xs–wave component is nonzero for all values of the coupling constant and there is a finite d–wave phase boundary. It follows that in the weak coupling regime (say $|W/t| < 2, \ldots, 4$), the superconducting order parameter has d–wave symmetry near half–filling and below $|n-1| \approx 0.5$ and xs–wave symmetry above $|n-1| \approx 0.5$, i. e. in the low electron or low hole concentration regime. Approaching $W/t = 0$, the superconducting order parameter becomes exponentially small. In the strong coupling regime both components of the superconducting order parameter are different from zero and the symmetry is mixed $xs+id$–wave. Moreover, it seems that in the limit $|W/t| \to \infty$ both components saturate and approach each other. This behavior is discussed in the next section, where the order parameters are plotted as a function of density.

Regarding the antiferromagnetic order parameter it becomes obvious that away from half–filling there is a critical coupling strength below which the system shows antiferromagnetic long range order. This antiferromagnetic groundstate phase boundary depends on doping and decreases with increasing $|n-1|$. Moreover, because either the xs–wave component or the d–wave component of the superconducting order parameter is different from zero for all coupling constants, it is also a phase boundary below which superconductivity coexists with antiferromagnetism. As for half–filling the value of the antiferromagnetic order parameter increases monotonically with decreasing coupling constant and approaches its maximum value of $n/2$ in the limit $|W/t| \to \infty$, which is in agreement with the exact value obtained by the Monte Carlo simulation discussed in chapter 1. For this reason the HFB approximation predicts the exact ground state even in the strong coupling limit. It is generally accepted that mean field approximations give good results for small coupling constants, so that one can conclude that the HFB approximation describes the antiferromagnetic groundstate properties of the model for all coupling constants less than zero[2] very well. It has been argued [Nozieres85, Micnas90], that even in the superconducting case the HFB approximation leads to acceptable groundstate results for all coupling constants. In this context it is an interesting question which role the nonzero superconducting order parameters play in the strong coupling regime. Do they still describe superconductivity? In this limit the system becomes an insulator, so that they cannot describe superconduc-

[1] The additional constraint of being noninsulating is necessary, for there are systems which show off diagonal long range order but are not superconducting, e. g. the atomic limit of the attractive Hubbard model.

[2] For positive coupling constants other variational parameters have to be included in the variational HFB approximation.

tivity. They describe, however, the existence of a macroscopic number of localized electron pairs, which are indeed present in an antiferromagnetically ordered ground state.

Finally the competition between the different order parameters can be observed as a function of coupling strength. As shown, for instance in figure 5.3(a), $|\Delta_d|$ increases in a discontinuous way with the onset of the antiferromagnetic order but is suppressed at the xs–wave phase boundary, and in figure 5.3(d), $|\Delta_{xs}|$ is twice decreased at the d–wave and the antiferromagnetic phase boundary. The competition between antiferromagnetism and superconductivity becomes more obvious in a comparison of the HFB–approximation with a finite value of the antiferromagnetic order parameter and the BCS–approximation, where m_{AF} is set to zero. This is shown in section 5.3.

To verify the results shown in figure 5.3, we have calculated the free energy functional as a function of the components of the superconducting order parameter for different sets of parameters. At each point in the $|\Delta_{xs}|$–$|\Delta_d|$–plane the antiferromagnetic order parameter and the renormalized chemical potential are determined selfconsistently. The first free energy landscape in figure 5.4 shows its global minimum on the $|\Delta_d|$–axis. It belongs to $|n-1| = 0.2$, $W/t = -2$ and proves the pure d–wave symmetry of the superconducting order parameter. In figure 5.5 the free energy functional is plotted for $|n-1| = 0.2$ and in figure 5.6 for $|n-1| = 0.6$ in the strong coupling regime for $W/t = -6$. Both free energy surfaces have their minimum in a region with mixed $xs+id$–wave symmetry. The last free energy plot in figure 5.7 belongs to the low carrier density regime. For $|n-1| = 0.8$ and $W/t = -4$ it verifies pure xs–wave superconductivity.

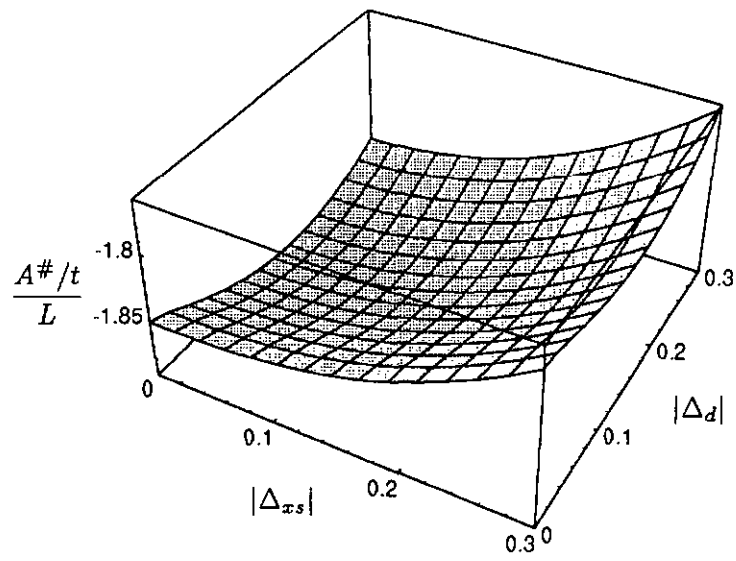

Figure 5.4: The free energy functional for $|n-1| = 0.2$, $W/t = -2.0$ and $T/t = 0.0$ as a function of the components of the superconducting order parameter $|\Delta_{xs}|$ and $|\Delta_d|$. At each point in the $|\Delta_{xs}|$-$|\Delta_d|$-plane m_{AF} and $\overline{\mu}$ are calculated selfconsistently. For these parameters the symmetry of the superconducting order parameter is pure d-wave.

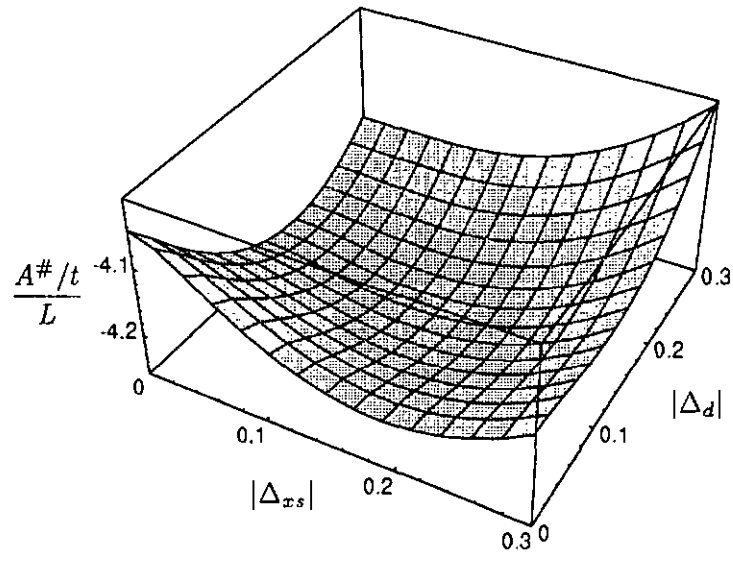

Figure 5.5: The free energy functional for $|n-1| = 0.2$, $W/t = -6$ and $T/t = 0$ as a function of the components of the superconducting order parameter $|\Delta_{xs}|$ and $|\Delta_d|$. At each point in the $|\Delta_{xs}|$-$|\Delta_d|$-plane m_{AF} and $\overline{\mu}$ are calculated selfconsistently. Here the symmetry of the superconducting order parameter is mixed $xs + id$-wave.

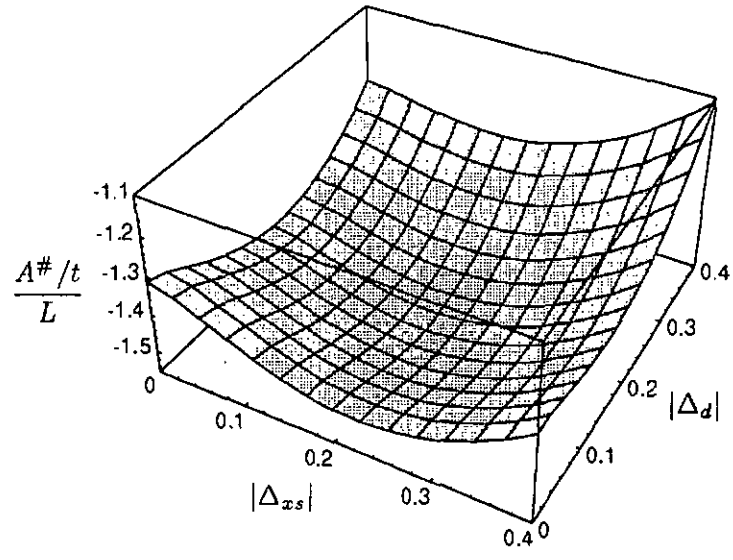

Figure 5.6: The free energy functional for $|n-1| = 0.6$, $W/t = -6$ and $T/t = 0$ as a function of the components of the superconducting order parameter $|\Delta_{xs}|$ and $|\Delta_d|$. At each point in the $|\Delta_{xs}|$-$|\Delta_d|$-plane m_{AF} and $\overline{\mu}$ are calculated selfconsistently. Here the symmetry of the superconducting order parameter is mixed xs+id-wave with $|\Delta_{xs}| \approx |\Delta_d|$.

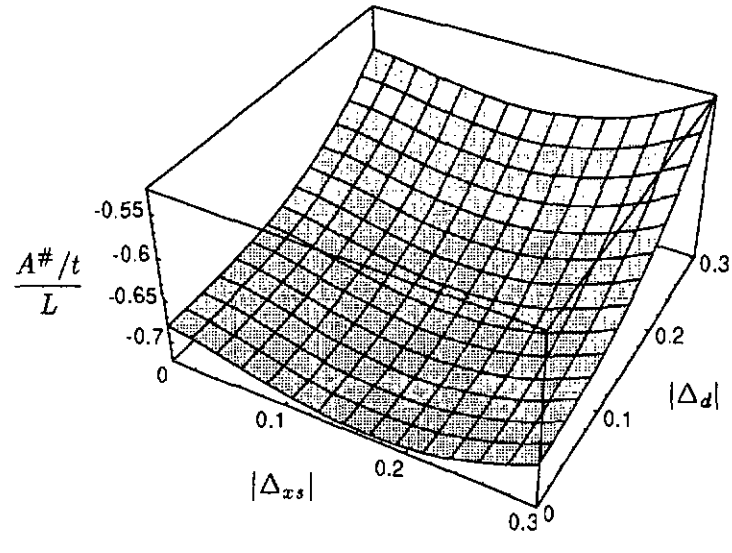

Figure 5.7: The free energy functional for $|n-1| = 0.8$, $W/t = -4$ and $T/t = 0$ as a function of the components of the superconducting order parameter $|\Delta_{xs}|$ and $|\Delta_d|$. At each point in the $|\Delta_{xs}|$-$|\Delta_d|$-plane m_{AF} and $\overline{\mu}$ are calculated selfconsistently. Here, in the low density limit, the symmetry of the superconducting order parameter is pure xs-wave.

5.1.3 The Groundstate Order parameter as a Function of Density

Most of the features described in the previous sections 5.1.1 and 5.1.2 become more clear if one plots the order parameter for fixed coupling constants as a function of $|n-1|$. The strong coupling regime for $|W/t| > 4$ is shown in figure 5.8, whereas the intermediate and weak coupling regime for $|W/t| \leq 4$ is shown in figure 5.9. In all figures the existence of superconductivity ($|\Delta_d| \neq 0$ or $|\Delta_d| \neq 0$) for all densities away from half-filling and the continous suppression of superconductivity approaching half-filling is visible. The symmetry of the superconducting order parameter depends strongly on density. In the strong coupling regime in figure 5.8 the superconducting order parameter is characterized

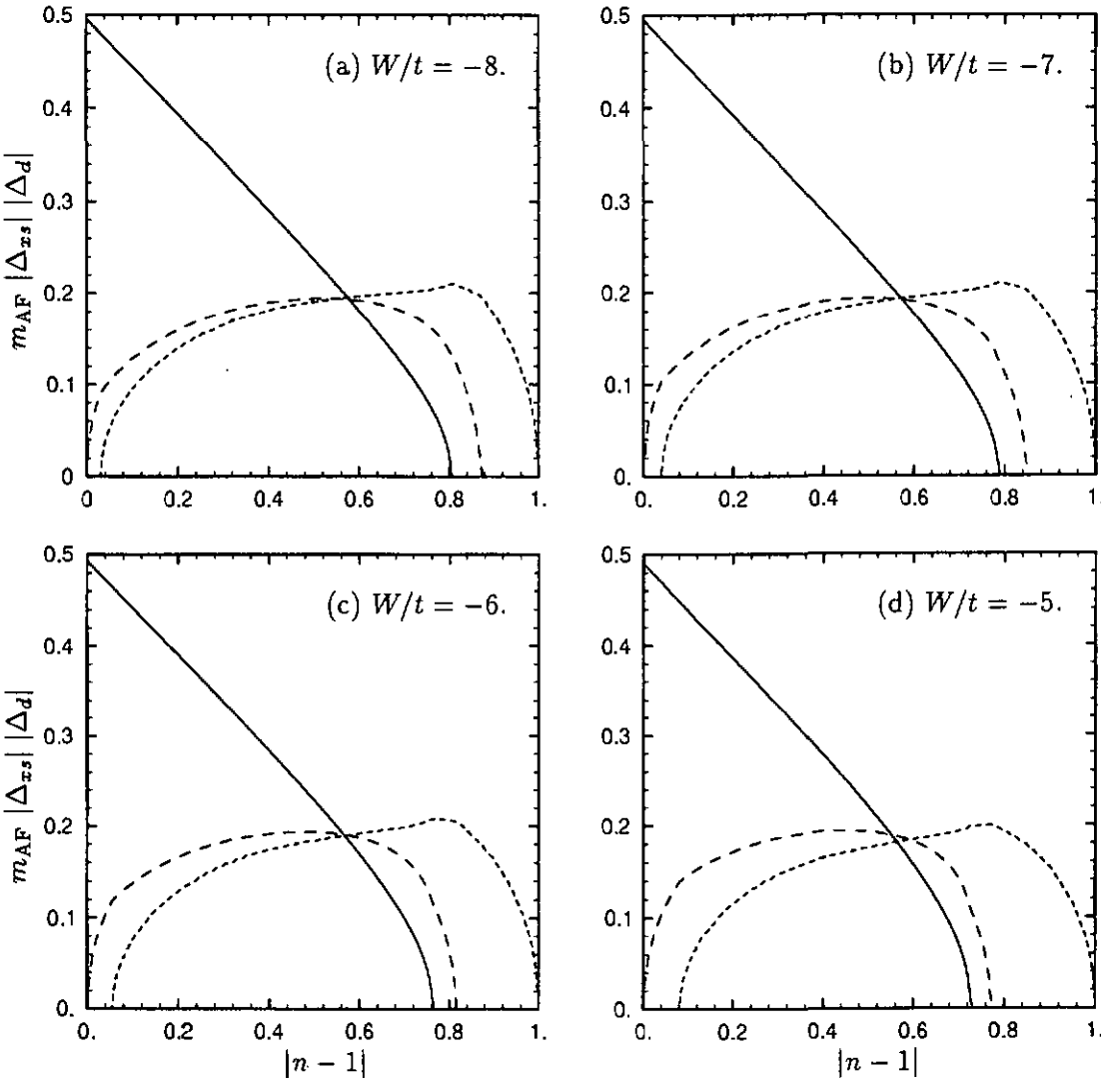

Figure 5.8: The groundstate order parameters m_{AF} (solid line), $|\Delta_{xs}|$ (dotted line) and $|\Delta_d|$ (dashed line) as a function of $|n-1|$ in the strong coupling regime for $W/t = -8.$(a), $W/t = -7.$(b), $W/t = -6.$(c), $W/t = -5.$(d).

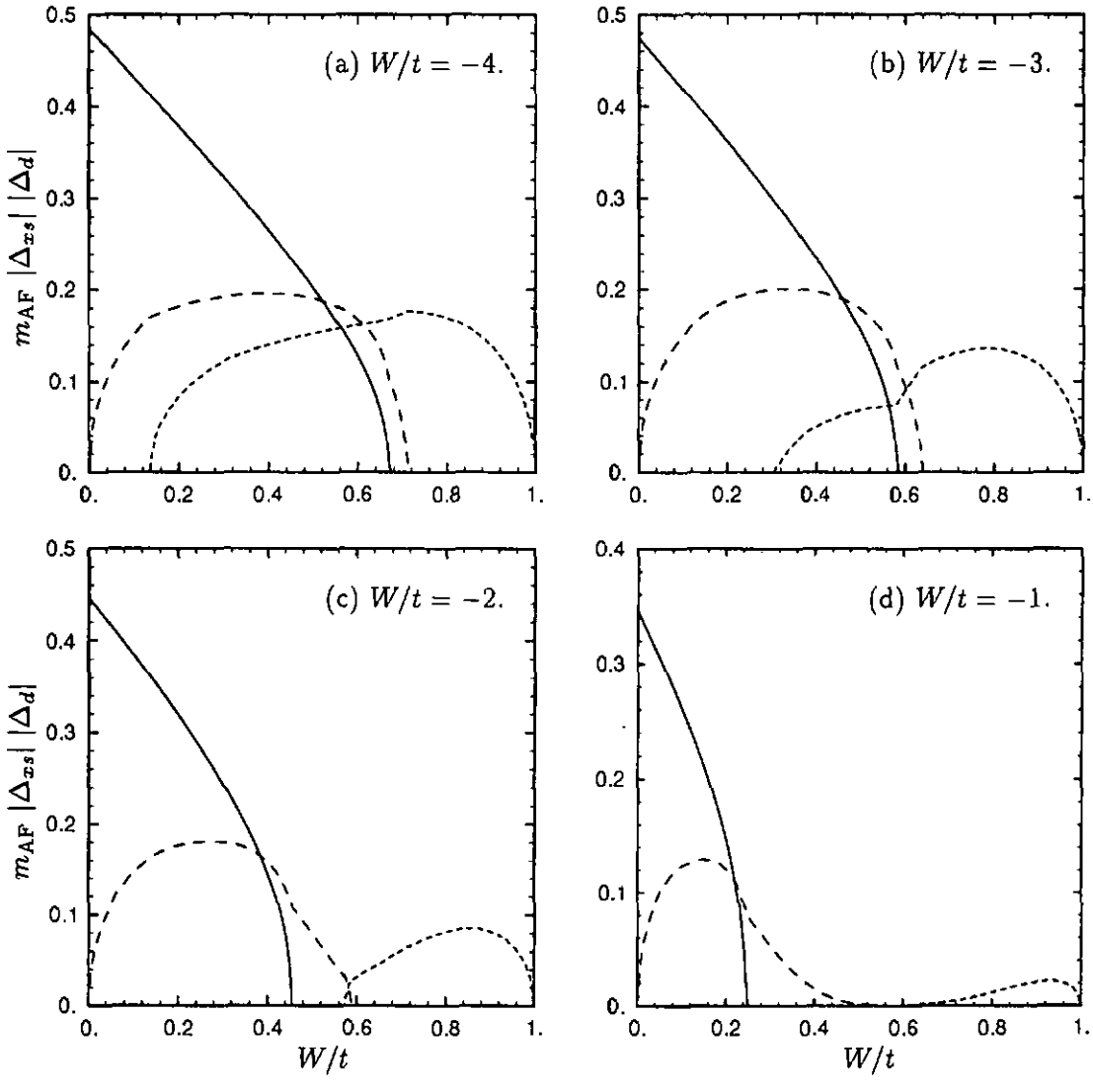

Figure 5.9: The groundstate order parameters m_{AF} (solid line), $|\Delta_{xs}|$ (dotted line) and $|\Delta_d|$ (dashed line) as a function of $|n-1|$ in the weak coupling regime for $W/t = -4.$(a), $W/t = -3.$(b), $W/t = -2.$(c), $W/t = -1.$(d).

by a very broad region in which both components $|\Delta_d|$ and $|\Delta_{xs}|$ are different from zero. Only in a very small region around half–filling is the symmetry of the superconducting order parameter pure d–wave and only in a very small region below $|n-1| = 1$ is it pure xs–wave. It appears that in the limit $|W/t| \to \infty$ both components become identical. This means that in the strong coupling regime the probability to find xs–wave superconductivity becomes equal to the probability to find d–wave superconductivity. Moreover, it shows that the larger the absolute value of the coupling constant is, the less the symmetry of the pairs plays any role. On the other hand, in the weak coupling regime for $|W/t| < 3$, the region of mixed $xs + id$–wave superconductivity shrinks to a very small region between $|n-1| = 0.55$ and $|n-1| = 0.6$ but it still exists and lies outside the antiferromagnetic

phase. The numerical data show that even for $W/t = -1$, there is a region around $|n-1| = 0.56$ with mixed $xs+id$–wave symmetry. In spite of this small overlap, the weak coupling regime is characterized by the nonexistence of mixed superconductivity, pure d–wave superconductivity near half–filling and below $|n-1| \approx 0.56$ and pure xs–wave superconductivity in the low carrier regime for $|n-1| > 0.56$.

The antiferromagnetic order parameter shows its maximum at half–filling and decreases monotonically with increasing values of $|n-1|$. It becomes zero at the antiferromagnetic groundstate phase boundary. In the strong coupling regime antiferromagnetic long range order exists for nearly all densities, whereas in the weak coupling regime the antiferromagnetic order parameter is different from zero in a relative small region around half–filling. Away from half–filling the nonzero antiferromagnetic and superconducting order parameters indicate a coexistence between superconductivity and antiferromagnetism. From a physical point of view a coexistence of antiferromagnetic order and superconductivity of the same electrons seems to be surprising, because antiferromagnetism involves localized and superconductivity very mobile electrons. The answer to this question is the occurence of a phase separated region of antiferromagnetically ordered domains and itinerent electrons which become superconducting below the critical temperature. This phase separation is discussed in chapter 6.

For all values of W/t there are three distinct phase boundaries for m_{AF}, $|\Delta_{xs}|$ and $|\Delta_d|$ in the region between halfilling and $|n-1| = 1$. As $|n-1|$ approaches half–filling, superconductivity is suppressed due to antiferromagnetism. Moreover, the superconducting order parameter also vanishes as $|n-1|$ approaches 1, which is not very surprising because of the disappearance of any mobile charge carriers for $n \to 0$ (no electrons) or $n \to 2$ (no holes). For this reason, $|n-1| = 0$ and $|n-1| = 1$ are superconducting phase boundaries. In particular, $|n-1| = 0$ is a phase boundary for the d–wave while $|n-1| = 1$ is a phase boundary for the xs–wave component. At all these phase boundaries, including $|n-1| = 0$ for $|\Delta_d|$ and $|n-1| = 1$ for $|\Delta_{xs}|$ the corresponding order parameter vanishes continuously, that is, the phase transitions are of second order. They are discussed in more detail in chapter 6.

Concerning the d–wave superconducting order parameter shown in figures 5.8 and 5.9, a strong correlation to the antiferromagnetic order parameter becomes visible. In fact, the region where $|\Delta_d|$ is different from zero is more or less identical to the region where the antiferromagnetic order parameter is different from zero. In addition, $|\Delta_d|$ increases with the onset of antiferromagnetic long range order, whereas it is suppressed approaching half–filling. This enhancement of $|\Delta_d|$ can very clearly be observed in figure 5.9 (c) at $|n-1| \approx 0.45$ or in figure 5.9 (d) at $|n-1| \approx 0.25$. The smaller the absolute value of the coupling constant is, the more visible is this effect, but it also exists in the strong coupling regime.

From these results one can conclude that the competition between the antiferromagnetic order parameter and the d–wave component of the superconducting order parameter is constructive at the antiferromagnetic phase boundary, whereas it is destructive near half–filling. On the other hand, the maximum of the xs–wave superconducting order parameter lies in regions where no antiferromagnetism exists, i. e. in regions where the number of electrons or holes is comparably small. The range of these regions depends on the coupling strength. In the strong coupling regime in figure 5.8 the xs–wave superconducting order parameter is always suppressed at the antiferromagnetic phase boundary, which is visible in figure 5.8 (a) and (b) at $|n-1| \approx 0.8$. In the intermediate regime for $W/t = -3$, $|\Delta_{xs}|$ seems to be stabilized with the onset of antiferromagnetic long range order. It should be noted that in none of the graphs in figures 5.8 and 5.9, $|\Delta_{xs}|$ and m_{AF} are different from zero while $|\Delta_d|$ vanishes, i. e. a coexistence of antiferromagnetism and superconductivity is always accompanied by a finite d–wave component. Finally, the competition between the two superconducting components $|\Delta_{xs}|$ and $|\Delta_d|$ is always destructive with respect to each other. In figure 5.9 (a), for instance, $|\Delta_d|$ is decreased by the onset of $|\Delta_{xs}|$ at $|n-1| \approx 0.15$ and in figure 5.9 (c) $|\Delta_{xs}|$ is suppressed by the finite value for $|\Delta_d|$ which occurs at $|n-1| \approx 0.64$.

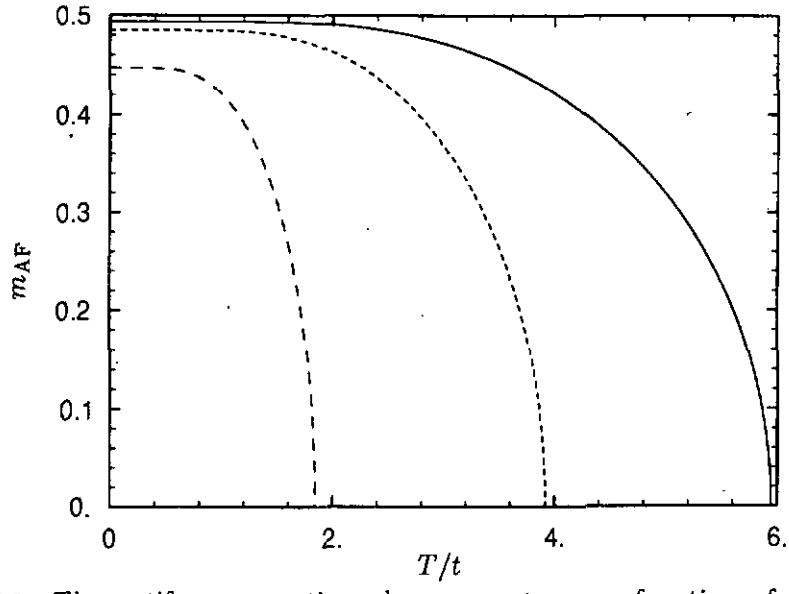

Figure 5.10: The antiferromagnetic order parameter as a function of temperature for half–filling and different values of the coupling constant: $W/t = -6$ (solid line), $W/t = -4$ (dashed line), $W/t = -2$ (dotted line).

5.2 The Order parameter as a Function of Temperature

In the previous section 5.1, the most important issues about solutions of the selfconsistent equations for $T/t = 0$ have been discussed. In this section the numerical results for finite temperatures are presented. They show how the groundstate solutions behave when the temperature is increased. From this behavior the Néel temperature for the antiferromagnetic and the critical temperature for the superconducting phase transition can be derived. In addition, the competition between several order parameters for finite temperatures is shown.

5.2.1 Half–filling

For half–filling only the antiferromagnetic order parameter is different from zero. Its temperature dependence is shown in figure 5.10 for $W/t = -6$ (solid line), $W/t = -4$ (dotted line) and $W/t = -6$ (dashed line). It is the usual mean field behavior with an exponent of $1/2$ in the neighborhood of the transition temperature [Binney92], which is defined by the value of T/t above which no nontrivial solution for the antiferromagnetic order parameter exists. The transition temperature is of order $|W/t|$. The deviation from this value is due to the kinetic energy of the electrons and becomes larger with decreasing absolute value of the coupling constant. Below the Néel temperature the antiferromagnetic order parameter increases monotonically with decreasing temperature. It saturates approaching $T/t = 0$.

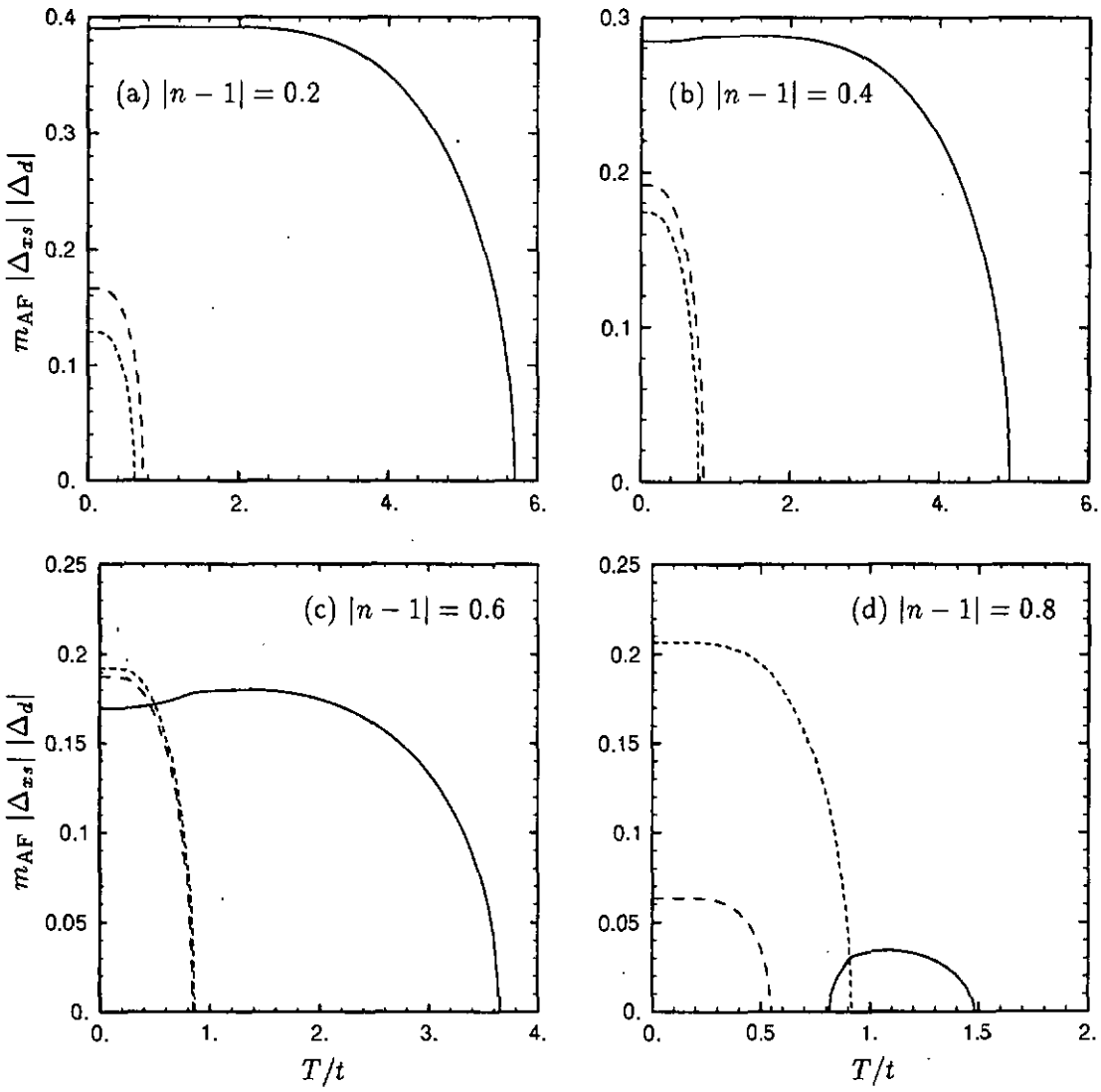

Figure 5.11: The order parameters m_{AF} (solid line), $|\Delta_{xs}|$ (dotted line) and $|\Delta_d|$ (dashed line) for $|n-1| = 0.2$(a), 0.4(b), 0.6(c), 0.8(d) and $W/t = -6$ as a function of T/t.

For this reason more and more electrons become localized and contribute to m_{AF} as the temperature is lowered. Because the perfect Néel state is not an eigenstate of the HFB hamiltonian, the maximum value of the antiferromagnetic order parameter for $T/t = 0$ is less than $n/2$ due to quantum fluctuations. These fluctuations become smaller as the absolute value of the coupling strength is increased.

5.2.2 Away from Half–filling

Because of the existence of both superconductivity and antiferromagnetism for $T/t = 0$, it is very interesting to study the temperature dependence of the order parameter away

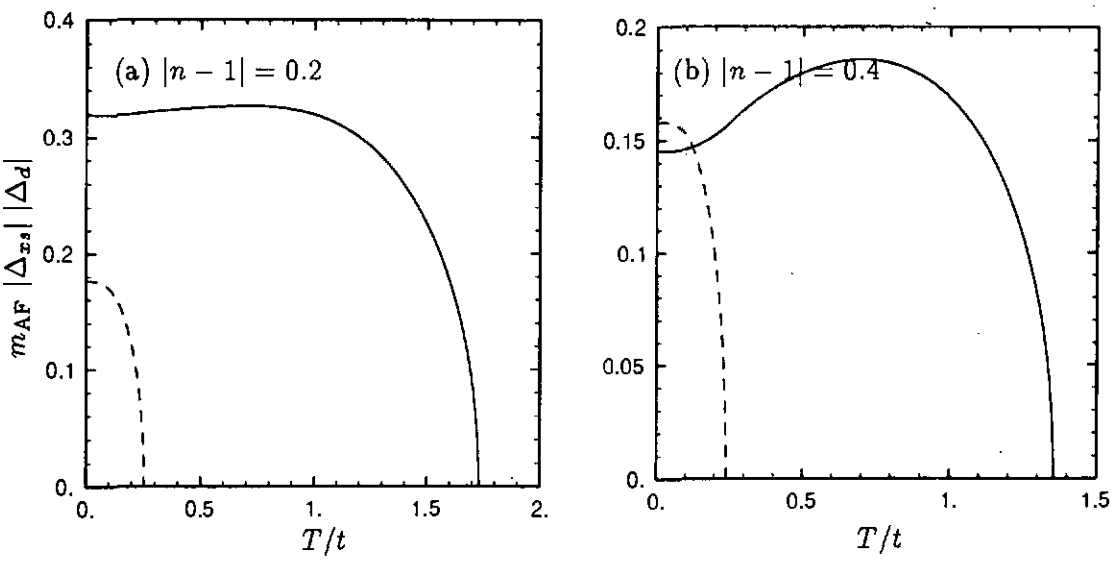

Figure 5.12: The order parameters m_{AF} (solid line), $|\Delta_{xs}|$ (dotted line) and $|\Delta_d|$ (dashed line) for $|n-1| = 0.2$(a), 0.4(b) and $W/t = -2$ as a function of T/t.

from half-filling. The order parameters are shown as a function of temperature T/t for $W/t = -6$ in figure 5.11 and for $W/t = -2$ in figure 5.12 for different values of $|n-1|$. Accordingly, figure 5.11 corresponds to the strong coupling and figure 5.12 to the weak coupling regime. In all graphs the three different and distinct phase boundaries for the occurence of antiferromagnetism, where m_{AF} (solid line) becomes different from zero, for the onset of xs–wave superconductivity where $|\Delta_{xs}|$ (dotted line) becomes different from zero and for the onset of d–wave superconductivity where $|\Delta_d|$ becomes different from zero, are clearly visible. In the neighborhood of each of these phase boundaries, the corresponding order parameter shows the typical mean field behavior, namely the disappearence with an exponent of 1/2, if one passes the phase boundary from low to high temperatures. Consider first the antiferromagnetic order parameter. Near half–filling, for $|n-1| = 0.2$ and $W/t - 6$ in figure 5.11 (a) and for $|n-1| = 0.2$ and $W/t - 2$ in figure 5.12 (a), the temperature dependence of m_{AF} is similar to the temperature behavior at half–filling. The Néel temperature is about the absolute value of W/t and m_{AF} approaches more or less monotonically its maximum value of $n/2$ as the temperature approaches zero. As doping is increased, the temperature behavior of the antiferromagnetic order parameter changes enormously. The Néel temperature decreases and $m_{AF}(T/t)$ shows its maximum at a finite value of temperature and not for the groundstate, as is the case for half–filling. This means that a fraction of electrons or holes which initally contribute to the antiferromagnetic order parameter become again itinerant if one lowers the temperature below the value for which m_{AF} takes on its maximum. This points to a phase separation between antiferromagnetically ordered and itinerant electrons which is discussed in more detail in chapter 6. The numerical data show that even very close to $n = 1$, the maximum

of $m_{\mathrm{AF}}(T/t)$ lies at a finite temperature. Concerning the superconducting order parameter, from figure 5.11 (b) or 5.11 (c) it follows that the suppression of the antiferromagnetic order parameter is strengthened with the occurence of a finite value of $|\Delta_{xs}|$ or $|\Delta_d|$, i. e. the onset of superconductivity is accompanied by the decrease of the number of carriers which contribute to the antiferromagnetically ordered domains. In other words, by the increase of the number of itinerant electrons, which now become superconducting. Note that the superconducting critical temperature, which is the maximum of the d–wave and the xs–wave phase boundary, lies always below the temperature where the maximum of the antiferromagnetic order parameter appears and hence is always smaller then the Néel temperature. Finally, figure 5.11 (d) shows that the suppression of $m_{\mathrm{AF}}(T/t)$ due to the phase separation and the occurence of superconductivity might be so strong that antiferromagnetism vanishes again at a lower temperature after it has become finite at a higher temperature. This is usually called the reentrance behavior of antiferromagnetism. In a region where no antiferromagnetism exists, e. g. in the weak coupling regime for $W/t = -2$ and $|n - 1| > 0.45$ (see the ground state order parameter in figure 5.9), the ususal BCS behavior of the superconducting order parameters is recovered. For this reason it is not discussed here.

5.3 Comparison to the BCS Approximation

In this section we would like to point out the differences between the HFB, including an antiferromagnetic variational parameter, and the BCS approximation. The latter results from the first for $m_{\mathrm{AF}} \equiv 0$. In the BCS approximation only the pairing variational parameters are taken into account. It neglects the antiferromagnetic features of the model. For this reason the comparison of the HFB and the BCS approximation shows very clearly the influence of antiferromagnetism on superconductivity and vice versa, e. g. the competition between both. In the first subsection 5.3.1 the groundstate free energy is discussed whereas the second subsection 5.3.2 reveales the differences for the order parameters.

5.3.1 Groundstate Free Energy

For half–filling the BCS approximation predicts superconductivity with a finite value of the superconducting variational parameters, whereas the HFB approximation shows antiferromagnetic order and no superconductivity. In figure 5.13, the free energy for half–filling is shown as a function of coupling strength. The solid line is the free energy functional evaluated at the antiferromagnetic solution of the HFB approximation, i. e. the free energy of the HFB approximation, and the dot–dashed line depicts the free energy for the BCS

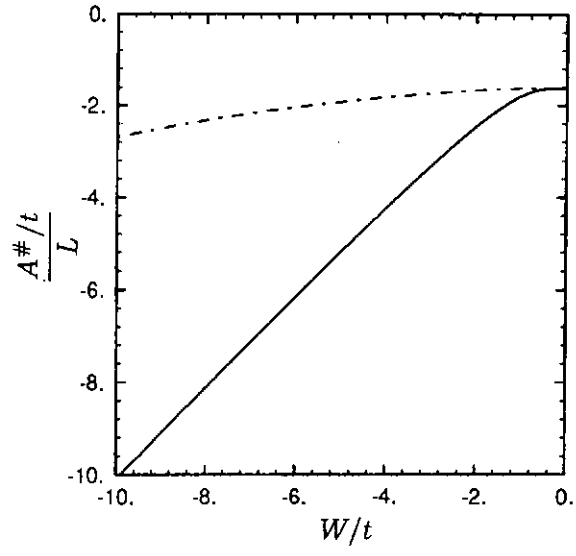

Figure 5.13: The ground state free energy for half-filling as a function of coupling strength. The solid line is the free energy for the HFB approximation, while the dot-dashed line is the free energy of the BCS approximation.

solution. From this figure it follows that the HFB approximation leads to a much lower free energy than the BCS approximation, which proves the absence of superconductivity for half-filling due to the occurrence of antiferromagnetism (see also section 5.1.1). The difference between the free energy of the BCS approximation and the HFB approximation becomes larger as the absolute value of the coupling strength is increased. This shows that for half-filling the BCS approximation becomes very bad in the strong coupling regime even for $T/t = 0$.

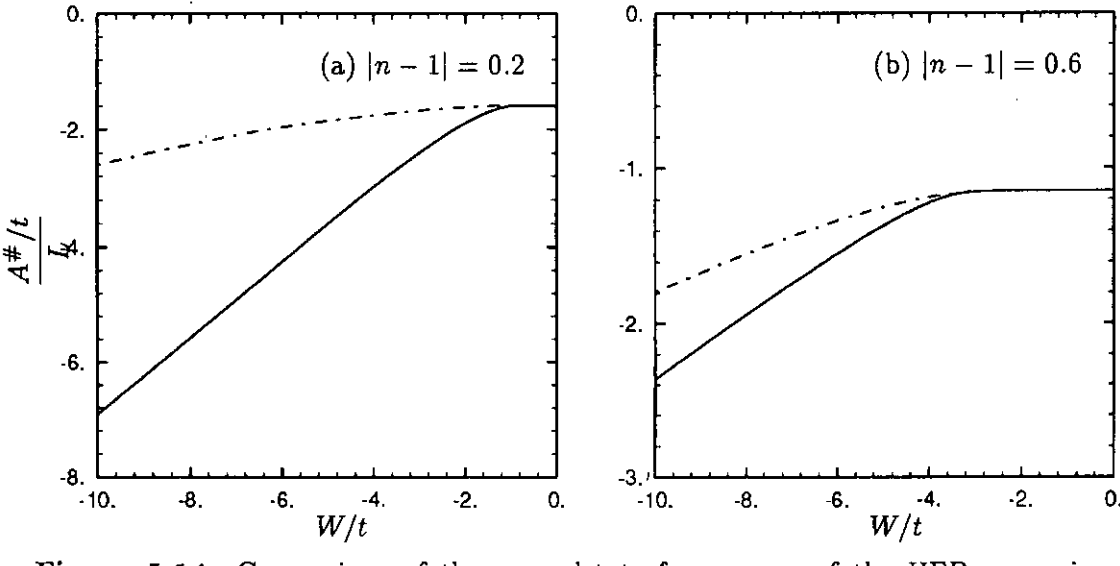

Figure 5.14: Comparison of the groundstate free energy of the HFB approximation (solid line), including an antiferromagnetic variational parameter and of the usual BCS approximation (dot-dashed line). The free energy is plotted as a function of coupling strength for $|n-1| = 0.2$ (a) and $|n-1| = 0.6$ (b).

Away from half-filling a similar behavior occurs as soon as the antiferromagnetic order

parameter becomes different from zero. As a function of coupling strength the free energy of the HFB and the BCS approximation is shown in figure 5.14 for $|n - 1| = 0.2$ (a) and for $|n - 1| = 0.6$ (b). From these figures it follows that as soon as antiferromagnetism occurs, the free energy is lowered with respect to the BCS solution. As for half-filling, the differences of the free energies increase with increasing absolute value of the coupling constant, which again shows the badness of the BCS approximation in the strong coupling regime. The differences become smaller, however, as the number of electrons ($n \to 0$) or holes ($n \to 2$) is decreased, i. e. in the low carrier regime. Outside the antiferromagnetic regime both the HFB and the BCS approximation are identical. In this regime the free energies are equal and the BCS approximation becomes valid.

5.3.2 Groundstate Order Parameter

Away from half-filling and for $T/t = 0$ both approximations predict superconductivity for all coupling constants and densities with slightly different phase boundaries for the xs-wave and d-wave components of the superconducting order parameter. The magnitude of the order parameters for the HFB and BCS approximation, however, differ more drastically from each other. This is shown in figure 5.15 as a function of coupling strength for $|n - 1| = 0.2$ (left side) and $|n - 1| = 0.6$ (right side) and in figure 5.16 as a function of density for $W/t = -6$ (left side) and $W/t = -2$ (right side). In both figures the first row shows the xs-wave component for the HFB approximation (solid line) in comparison to the BCS approximation (dot-dashed line), while in the second row the d-wave component is plotted. From these figures it follows that the existence of antiferromagnetism suppresses the superconducting order parameters. Only in a very small region in the neighborhood of the antiferromagnetic ground state phase boundary the superconducting order parameters are increased due to antiferromagnetism. The suppression becomes larger as half-filling is approached, where the superconducting order parameters vanish within the HFB approximation while they are nonzero for the BCS approximation. It should be noted that the d-wave component is more influenced by a nonvanishing antiferromagnetic order parameter than the xs-wave component. This is very clearly visible in figure 5.16 (c) and (d), where the d-wave superconducting order parameters for the HFB approximation differ obviously from the BCS solution, while the xs-wave components for both the HFB and the BCS approximation in figure 5.16 (a) and (b) show more or less the same behavior. This again shows the strong correlation between antiferromagnetism and d-wave superconductivity.

The comparisons above reveal that the HFB approximation yields much better results than the BCS approximation, in particular in the neighborhood of half-filling and in the strong coupling regime. Moreover, the discussion of the chemical potential and the phase

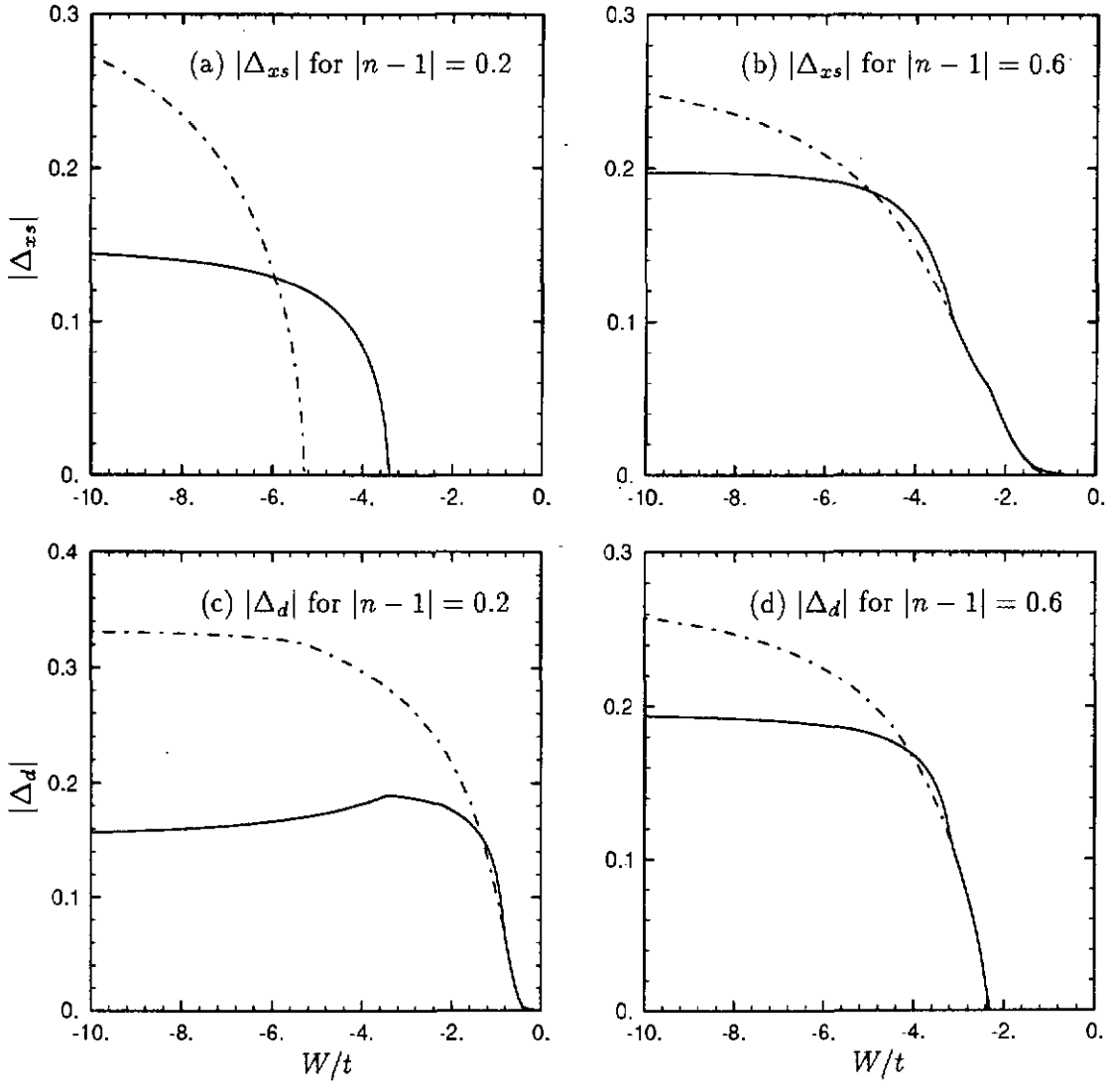

Figure 5.15: Comparison of the HFB approximation (solid line), including an antiferromagnetic variational parameter and the usual BCS approximation (dot–dashed line). The xs–wave parameter (a,b) and the d–wave parameter (c,d) are shown as a function of W/t for $T/t = 0$ and $|n-1| = 0.2$ (left side) and $|n-1| = 0.6$ (right side).

separation in chapter 6 show that even in the weak coupling regime the introduction of an antiferromagnetic variational parameter leads to a quite different phase diagram than the BCS approximation predicts.

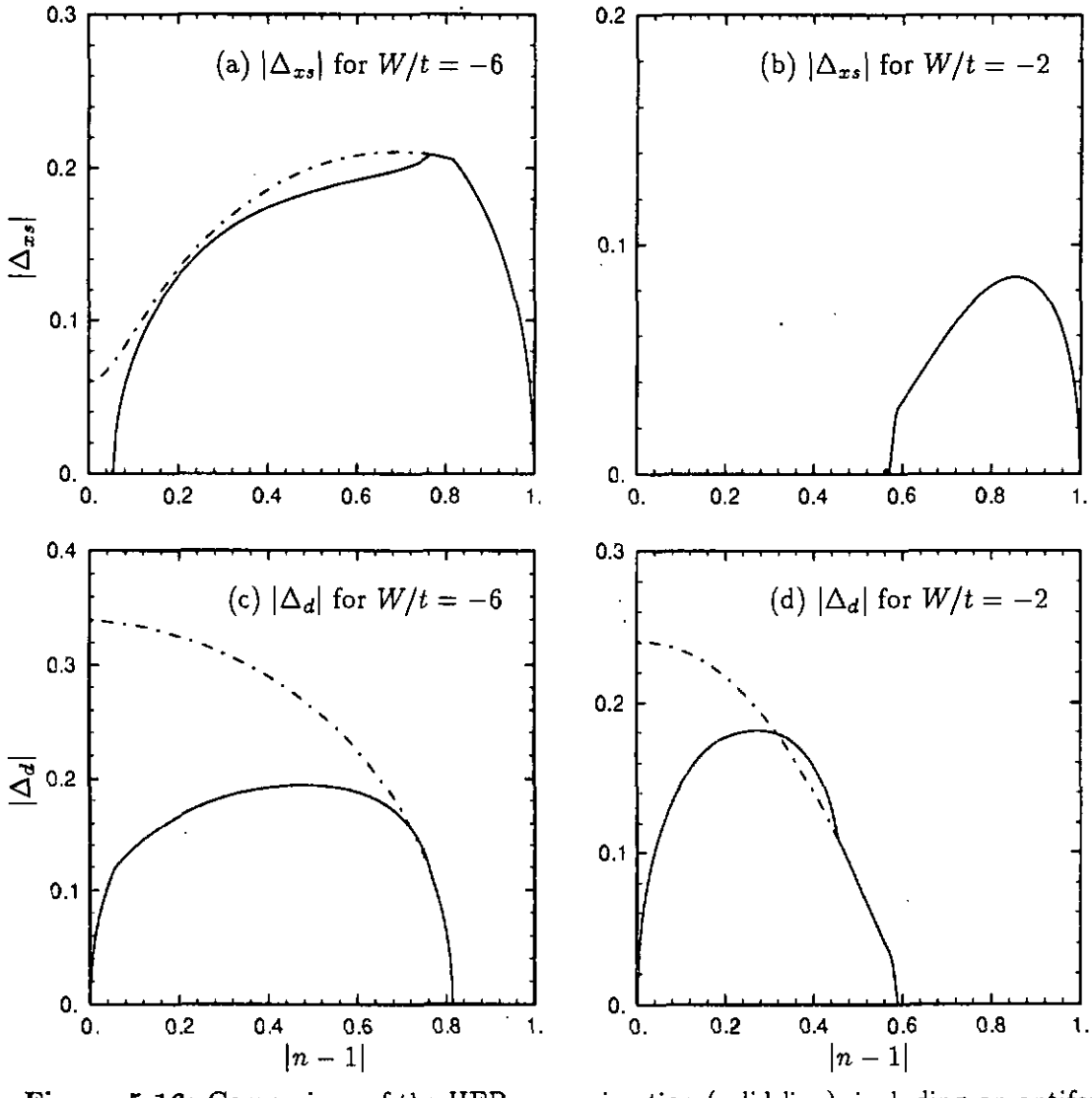

Figure 5.16: Comparison of the HFB approximation (solid line), including an antiferromagnetic variational parameter and the usual BCS approximation (dot dashed line). The xs–wave parameter (a,b) and the d–wave parameter (c,d) are shown as a function of $|n-1|$ for $T/t = 0$ and $W/t = -6$ (left side) and $W/t = -2$ (right side).

Chapter 6

Phase Diagrams of the Two–Dimensional NNSP Model

From an experimental point of view it is more interesting to study phase boundaries than order parameters, because in the superconducting case, the order parameters are not directly measureable, while the phase boundaries become visible in measurements of the specific heat or the conductivity. Nevertheless, the order parameters contain more information than the phase boundaries, where the order parameters vanish[1]. For this reason some of the results below were already discussed in the previous chapter 5, but only for a particular set of model parameters. The global behavior of the phase boundaries and its implications become more clear within phase diagrams where the phase boundaries are drawn as a function of the model parameters, for instance in a ground state W/t–$|n-1|$ phase diagram, or in a finite temperature phase diagram, where the behavior of the Néel temperature and the superconducting critical temperature are shown as functions of density or coupling strength. The phase boundaries for antiferromagnetism, xs–wave and d–wave superconductivity are defined by the disappearance of the order parameters m_{AF}, $|\Delta_{xs}|$ and $|\Delta_d|$, respectively. For this reason the phase boundaries may be calculated by computing the order parameters. Using a bisection algorithm near the disappearance of the order parameters allows for calculating the transition point with rather arbitrary precision. This method is in some particular cases very useful and even necessary but very slow. If one is only interested in phase diagrams of the model, one can calculate the phase boundaries directly using the fact that all transitions are of second order.

[1] For instance, that the phase transition is of second order.

6.1 Linearization of the Selfconsistent Equations

For a second order phase transition the order parameter vanishes continously at the transition point. Therefore the phase boundary might be calculated by linearizing the corresponding selfconsistent equations. The selfconsistent equations have the following form:

$$\begin{aligned} n &= I_n(m_{\mathrm{AF}}, |\Delta_{xs}|, |\Delta_d|, \overline{\mu}) \\ m_{\mathrm{AF}} &= m_{\mathrm{AF}}\, I_{\mathrm{AF}}(m_{\mathrm{AF}}, |\Delta_{xs}|, |\Delta_d|, \overline{\mu}) \\ |\Delta_{xs}| &= |\Delta_{xs}|\, I_{xs}(m_{\mathrm{AF}}, |\Delta_{xs}|, |\Delta_d|, \overline{\mu}) \\ |\Delta_d| &= |\Delta_d|\, I_d(m_{\mathrm{AF}}, |\Delta_{xs}|, |\Delta_d|, \overline{\mu}) \quad , \end{aligned} \tag{6.1}$$

where the functions I_n, I_{AF}, I_{xs} and I_d are defined by the right hand sides of the selfconsistent equations in table 4.4. They are quadratic functions of the order parameters because they depend indirectly on m_{AF}, $|\Delta_{xs}|$ and $|\Delta_d|$ via E_1, E_2 and E_{AF}. For this reason, linearizing the set of selfconsistent equations with respect to one of the order parameters is quite an easy task. In fact, the antiferromagnetic phase boundaries are determined by the following set of equations:

$$\begin{aligned} n &= I_n(0, |\Delta_{xs}|, |\Delta_d|, \overline{\mu}) \\ 1 &= I_{\mathrm{AF}}(0, |\Delta_{xs}|, |\Delta_d|, \overline{\mu}) \\ |\Delta_{xs}| &= |\Delta_{xs}|\, I_{xs}(0, |\Delta_{xs}|, |\Delta_d|, \overline{\mu}) \\ |\Delta_d| &= |\Delta_d|\, I_d(0, |\Delta_{xs}|, |\Delta_d|, \overline{\mu}) \quad , \end{aligned} \tag{6.2}$$

the phase boundaries for the xs-wave component of the superconducting order parameter are given by the solutions of

$$\begin{aligned} n &= I_n(m_{\mathrm{AF}}, 0, |\Delta_d|, \overline{\mu}) \\ m_{\mathrm{AF}} &= m_{\mathrm{AF}}\, I_{\mathrm{AF}}(m_{\mathrm{AF}}, 0, |\Delta_d|, \overline{\mu}) \\ 1 &= I_{xs}(m_{\mathrm{AF}}, 0, |\Delta_d|, \overline{\mu}) \\ |\Delta_d| &= |\Delta_d|\, I_d(m_{\mathrm{AF}}, 0, |\Delta_d|, \overline{\mu}) \quad , \end{aligned} \tag{6.3}$$

and finally the phase boundaries for the d-wave component of the superconducting order parameter are determined by solving

$$\begin{aligned} n &= I_n(m_{\mathrm{AF}}, |\Delta_{xs}|, 0, \overline{\mu}) \\ m_{\mathrm{AF}} &= m_{\mathrm{AF}}\, I_{\mathrm{AF}}(m_{\mathrm{AF}}, |\Delta_{xs}|, 0, \overline{\mu}) \\ |\Delta_{xs}| &= |\Delta_{xs}|\, I_{xs}(m_{\mathrm{AF}}, |\Delta_{xs}|, 0, \overline{\mu}) \\ 1 &= I_d(m_{\mathrm{AF}}, |\Delta_{xs}|, 0, \overline{\mu}) \quad . \end{aligned} \tag{6.4}$$

Four equations have to be solved for each of the phase boundaries for m_{AF}, $|\Delta_{xs}|$ or $|\Delta_d|$. Three equations of them are necessary to determine the renormalized chemical potential

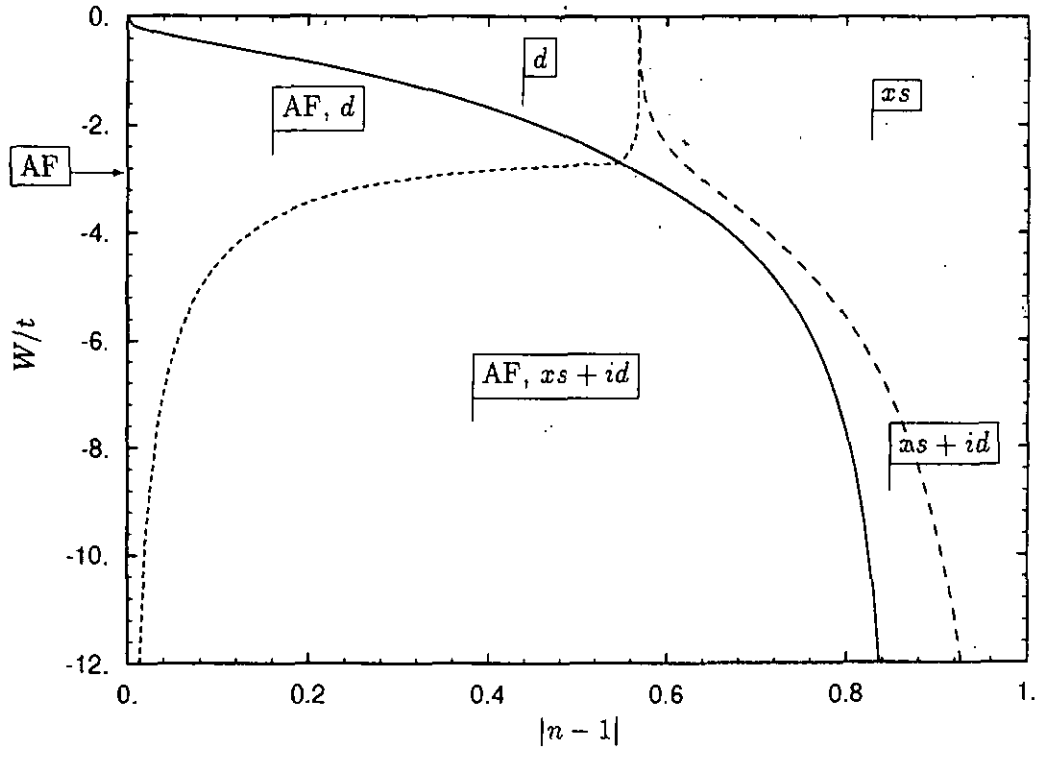

Figure 6.1: Groundstate phase diagram. The solid line marks the antiferromagnetic phase boundary above which m_{AF} becomes zero, the dotted line the phase boundary of the xs–wave component where $|\Delta_{xs}|$ vanishes, and the dashed line the phase boundary of the d–wave component of the superconducting order parameter where $|\Delta_d|$ becomes zero. The flags show which type of order exists within the specified regions.

and the remaining order parameters, while the fourth equation yields the value of the coupling constant, temperature or density at the transition point. A similar method as it was used to find the order parameters might be applied to solve these sets of equations. In particular, it is also very practical here to invert the first equation numerically in order to get rid of the chemical potential. In the following sections 6.2 and 6.3 the results are presented after solving these sets of equations with respect to W/t for the groundstate phase diagramm, or T/t for the finite temperature phase diagrams.

6.2 Groundstate Phase Diagram

The groundstate phase boundaries in the W/t–$|n-1|$–plane are shown in figure 6.1. The solid line is the antiferromagnetic phase boundary, the dotted line is the xs–wave phase boundary and the dashed line is the d–wave phase boundary. Accordingly, AF marks antiferromagnetism with $m_{\mathrm{AF}} \neq 0$, xs reflects superconductivity with xs–wave symmetry ($|\Delta_{xs}| \neq 0$), d describes superconductivity with d–wave symmetry ($|\Delta_d| \neq 0$) and $xs + id$,

describes superconductivity with mixed xs–wave, d–wave symmetry ($|\Delta_{xs}| \neq 0$ and $|\Delta_d| \neq 0$), where the relative phase of both components is $\phi = \pi/2$. These characterizations are given within the flags which point to the regions where the specified type of order exists.

For half–filling ($|n-1| = 0$) the system orders antiferromagnetically. In figure 6.1 this is indicated by the AF label which points to the line $|n-1| = 0$. It is therefore a phase boundary for superconductivity, or more precisely, for the d–wave component of the superconducting order parameter. For $n = 0$ and $n = 2$ superconductivity also vanishes due to the nonexistence of mobile charge carriers. For this reason the line $|n-1| = 1$ is also a phase boundary for superconductivity, in this case for the xs–wave component. The disappearance of superconductivity for $|n-1| \to 0$ and $|n-1| \to 1$ is more visible in T/t versus $|n-1|$ phase diagrams which are discussed in the next section 6.3. The horizontal $W/t = 0$ is a phase boundary for all considered types of order, because there are no nontrivial solutions of the selfconsistent equations for positive coupling constants.

The antiferromagnetic phase boundary (solid line) shows that for half–filling for all negative values of the coupling constant the antiferromagnetic groundstate order parameter is different from zero. For a given value of doping ($|n-1| > 0$), however, there is a critical value for W/t above which the groundstate has no more antiferromagnetic contribution. This threshold decreases monotonically with a decreasing number of electrons ($n \to 0$) or holes ($n \to 2$) and it is an interesting question whether there exists a maximum value for $|n-1|$ above which there does not exist any antiferromagnetism for all coupling constants. Because of the monotonic behavior of the antiferromagnetic phase boundary, this question can be answered in the limit $W/t \to -\infty$, i. e. for fixed values $W < 0$ and for $t \to 0$. In this limit and for $T = 0$, the set of equations for the antiferromagnetic phase boundary (equations (6.2)) read:

$$n - 1 = \frac{\overline{\mu}}{L} \sum_k \frac{1}{E_1}\Big|_{m_{AF}=0} \tag{6.5}$$

$$1 = \frac{2|W|}{L} \sum_k \frac{1}{E_1}\Big|_{m_{AF}=0} \tag{6.6}$$

$$|\Delta_\alpha| = \frac{|\Delta_\alpha|\,|W|}{2L} \sum_k \frac{f_\alpha(k)^2}{E_1}\Big|_{m_{AF}=0} \quad \text{for} \quad \alpha = xs, d \tag{6.7}$$

with

$$E_1\Big|_{m_{AF}=0} = E_2\Big|_{m_{AF}=0} = \sqrt{16W^2\,|\Delta(k)|^2 + \overline{\mu}^2} \quad . \tag{6.8}$$

Note that the solutions of this set of equations are independent of $|W|$ because the renormalized chemical potential might be rescaled by $|W|$. Now, let us assume that the solution of the set of equations above includes a nonzero superconducting order parameter, i. e. at

least one of the components $|\Delta_{xs}|$ or $|\Delta_d|$, which solve equation (6.7), has a finite value. From the equation for the nonzero component then follows

$$1 = \frac{|W|}{2L} \sum_k \frac{f_\alpha(k)^2}{E_1}\Big|_{m_{AF}=0} < \frac{2|W|}{L} \sum_k \frac{1}{E_1}\Big|_{m_{AF}=0} \quad , \tag{6.9}$$

because $f_\alpha(k)^2 < 4$ for nearly all wave vectors k and $f_\alpha(k)^2 = 4$ for a nonmeasurable subset of the first Brioullin zone, independent of α. For this reason there is no solution of equation (6.6) and hence for the whole set of equations (6.5) - (6.7). This means that the assumption of a finite superconducting order parameter at the antiferromagnetic phase boundary for $t = 0$ and $T = 0$ must be wrong. For $|\Delta_{xs}| = 0$ and $|\Delta_d| = 0$, however, it follows from equations (6.5), (6.6) and (6.8) that

$$(n-1)\Big|_{\text{AF phase boundary}} = \text{sgn}(\overline{\mu}) \tag{6.10}$$

$$|\overline{\mu}|\Big|_{\text{AF phase boundary}} = 2|W| \quad . \tag{6.11}$$

This means that the solution of the set of equations for the antiferromagnetic phase boundary in the limit $t \to 0$ and for $T = 0$ is given by $|n-1| = 1$, $\overline{\mu} = 2|W|\,\text{sgn}(n-1)$ and $|\Delta_\alpha| = 0$ for $\alpha = xs$ and $\alpha = d$. In other words, for $t \to 0$ and $T = 0$ the HFB approximation predicts antiferromagnetism for all densities. This is equivalent to the exact result obtained by the Monte Carlo simulation of the interaction Hamiltonian. Regarding the ground state phase diagram in figure 6.1, it rules out the existence of an upper bound for $|n-1|$, above which no antiferromagnetism exists for all coupling constants. In other words, this result shows that for all densities one can find a finite critical value for W/t below which the groundstate has an antiferromagnetic component. This result can be compared to a similar result for an extended Hubbard model with on–site attraction and repulsive spin–independent density–density interaction between nearest neighbors. In such a model the competition between s–wave superconductivity and CDW order plays an important role and in the groundstate phase diagram for strong on–site attraction there is an upper bound for $|n-1|$ above which the CDW component of the groundstate disappears for all coupling constants [Robaszkiewicz81b, Micnas90].

The xs–wave phase boundary in figure 6.1 (dotted line) separates the region of the W/t–$|n-1|$ plane on the right hand side of the phase boundary where a nontrivial solution of the selfconsistent equations for $|\Delta_{xs}|$ exists and therefore superconductivity with xs–wave symmetry appears, from the region on the left hand side of the phase boundary, where only the solution $|\Delta_{xs}| = 0$ leads to the global minimum of the free energy functional. For the d–wave component of the superconducting order parameter the situation is just the opposite: the region on the left hand side of the d–wave phase boundary in figure 6.1 (dashed line) is characterized by a nontrivial solution for $|\Delta_d|$, whereas only the trivial

solution exists in the region on the right hand side of the d–wave phase boundary. In the weak coupling regime ($|W/t| < 3$) the xs–wave phase boundary is nearly constant as a function of W/t and xs–wave superconductivity appears predominantly in the high doping regime for $|n-1| > 0.56$, which corresponds to a relatively low electron ($n < 0.44$) or hole ($n > 1.56$) concentration. The d–wave phase boundary (dashed line) follows more or less the xs–wave phase boundary and d–wave superconductivity appears in the neighborhood of half–filling and below $|n-1| \approx 0.56$. For this reason there is almost no coexistence of xs–wave and d–wave superconductivity in the weak coupling regime for all fillings. This scenario changes in the strong coupling regime. As the xs–wave phase boundary crosses the antiferromagnetic phase boundary at $W/t \approx -2.8$, a broad coexistence regime of xs–wave and d–wave superconductivity appears between the xs–wave and the d–wave phase boundary. In fact, the flat behavior of the xs–wave phase boundary as a function of filling for $W/t \approx -3$ might be used to define the separation line between the weak coupling and the strong coupling regime. The coexistence regime of xs–wave and d–wave superconductivity is labeled by $xs + id$ to emphasize the phase shift of $\phi = \pi/2$ between the xs–wave and d–wave component of the superconducting order parameter. The coexistence regime becomes broader as the absolute value of the coupling constant is increased and covers the entire density regime with the exception of half–filling as $|W/t|$ goes to infinity. In this region, both the order parameter for xs–wave and d–wave superconductivity become identical, i. e. the probability to find a pair with xs–wave symmetry becomes identical to the probability to find a pair with d–wave symmetry. One can say that the differences between d–wave superconductivity and xs–wave superconductivity disappear, which means that the internal structure of the pairs becomes unimportant.

Considering the coexistence regime of antiferromagnetism and superconductivity, it becomes obvious that in the weak coupling regime only d–wave superconductivity might coexist with antiferromagnetism. On the other hand, in the strong coupling regime the symmetry of the superconducting order parameter in the coexistence regime is predominantly mixed $xs + id$–wave. It should be noted that in the strong coupling regime the d–wave phase boundary follows the antiferromagnetic phase boundary, which shows the strong correlation between antiferromagnetism and d–wave superconductivity. Moreover, because the d–wave phase boundary lies always slightly above the antiferromagnetic phase boundary, a coexistence between antiferromagnetism and superconductivity is always accompanied with a nonzero d–wave component of the superconducting order parameter. This means that in the groundstate phase diagram there is no coexistence between pure xs–wave superconductivity and antiferromagnetism. For finite temperatures this is not necessarily true, which is shown in the next section 6.3. In section 6.5 on phase separation, the coexistence regime of antiferromagnetism and superconductivity will be interpreted

more accurately.

6.3 Finite Temperature Phase Diagrams

6.3.1 T/t versus n Phase Diagrams

From a physical point of view, phase diagrams which show the temperature behavior of the system are more interesting because in reality phase boundaries are usualy observed and studied by cooling the system. In figure 6.2, the Néel temperature for the antiferromagnetic phase (solid line), the xs–wave critical temperature for the occurence of xs–wave superconductivity (dotted line) and the d–wave critical temperature for the occurence of d–wave superconductivity (dashed line) are shown as a function of doping $|n-1|$ for $W/t = -6$ (a) and $W/t = -2$ (b) [2]. Because the system becomes superconducting either by the occurence of a finite value of the xs–wave pairing parameter or by the occurence of a finite value of the d–wave pairing parameter, the superconducting critical temperature T_c is just the envelope of the xs–wave and the d-wave phase boundary. As in the ground state phase diagram, the labels indicate the type of order. In addition, NO characterizes the region without any long range order. Only the trivial solutions for all order parameters exist in this region. Within the mean field picture, the NO region is described by the free particle Hamiltonian.

The most interesting point in both phase diagrams is the decrease of the superconducting critical temperature as doping approaches half–filling ($|n-1| = 0$). This shows the absence of superconductivity at half–filling for all temperatures. Moreover, the continuous decrease of T_c for $|n-1| \to 0$ shows the suppression of superconductivity due to antiferromagnetic correlations in a relatively wide doping range around half–filling. In fact, in the strong coupling regime it seems that the superconducting critical temperature is lowered as soon as the antiferromagnetic order parameter becomes different from zero. For $W/t = -6$ in figure 6.2 (a), this behavior is visible below the multicritical point at $|n-1| \approx 0.81$, where the antiferromagnetic phase boundary crosses the superconducting phase boundary. In the weak coupling regime, however, T_c seems to be increased at the multicritical point and its suppression appears below the density where the maximum of the d–wave phase boundary occurs. For $W/t = -2$ in figure 6.2 (b), this point lies approximately at $|n-1| = 0.3$. The suppression of the superconducting critical temperature due to antiferromagnetic order becomes more clear in a comparison to the phase boundaries

[2] These two values of W/t have been chosen to show the features in the strong and weak coupling regime, although the values for the transition temperatures are too high for a comparison to reality (see also chapter 7).

obtained by the BCS approximation, which is discussed in section 6.4. For $|n-1| \to 1$, the superconducting critical temperature decreases as well because of the disappearance of any mobile charge carriers as the band is totally filled ($n \to 2$) or the band becomes totally empty ($n \to 0$). The maximum value for $T_c(|n-1|)$ lies between $|n-1| = 0$ and $|n-1| = 1$. In the strong coupling regime there is only one maximum which appears at the multicritical point mentioned above. For $W/t = -6$, the maximum value for the superconducting critical temperature $(T_c/t)_{\max}$ approximately equals 1. In the weak coupling regime, however, there are two local maxima of $T_c(|n-1|)$. The first one lies in the low carrier regime and is the maximum of the xs–wave phase boundary. The second one is the global maximum and lies in the antiferromagnetic regime. It is the maximum of the d–wave phase boundary. For $W/t = -2$ its value is about 0.3. It should be noted that the valley between the two maxima of the superconducting critical temperatures might be filled up with the occurence of p–wave superconductivity, as it was discussed by Micnas et al. [Micnas88a, Micnas88b]. From the Pauli principle, however, it follows that for singlet pairing p–wave superconductivity is not allowed. For this reason the p–wave components have not been included in our treatment.

As the groundstate phase diagram has already shown, the symmetry of the superconducting order parameter depends on filling and on coupling strength. From the finite temperature phase diagrams it now becomes obvious that the symmetry of the superconducting order parameter depends also on temperature. In fact, in the strong coupling regime the symmetry might be pure d–wave or pure xs–wave just below the superconducting critical temperature but mixed $(xs + id)$–wave for lower temperatures. In figure 6.2 (a), this behavior occurs for instance at $|n-1| = 0.2$, where the symmetry is pure d–wave at $T/t = 0.7$ and mixed $(xs + id)$–wave at $T/t = 0.5$. Note that for a fixed value of the coupling constant there is only one multicritical density at which both the xs–wave and the d–wave component of the superconcting order parameter become different from zero at the same temperature. In all other cases the entrance in the mixed symmetry region splits into two phase transitions for the occurence of the xs–wave component and the d–wave component. This multicritical density has the same value as the density at which the xs–wave and the d–wave groundstate component become identical. Moreover, comparing figures 5.8 (c) and 6.2 (a), we note that for all densities for which the groundstate xs–wave component is larger than the groundstate d–wave component, the xs–wave transition temperature is higher than the d–wave transition temperature and vice versa. In the weak coupling regime a similar behavior only occurs in a very small doping regime around $|n-1| \approx 0.56$. Outside this region the symmetry of the superconducting order parameter is the same for all temperatures below T_c and so is the symmetry of the ground state order parameter. It should be noted that in the strong and the weak coupling regime the shape of the xs–wave and the d–wave critical temperature as a function of doping fol-

lows more or less the shape of the xs–wave and d–wave groundstate order parameter, respectively (compare figure 5.8 (c) with figure 6.2 (a) and figure 5.9 (c) with figure 6.2 (b)).

Another interesting point in these phase diagrams is the existence of antiferromagnetism above T_c and regions where antiferromagnetism might coexist with superconductivity. These regions lie on the left hand side of the antiferromagnetic phase boundary (solid line), which has its maximum at half–filling, decreases as doping is increased, surrounds the reentrance regime and vanishes at the antiferromagnetic ground state phase boundary. In both cases, for $W/t = -6$ in figure 6.2 (a) and for $W/t = -2$ in figure 6.2 (b), the maximum of the Néel temperature is about 6 times larger than the maximum of the superconducting critical temperature. In section 6.5 about phase separation, the antiferromagnetic phase boundary away from half–filling will be changed and the coexistence regime will be interpreted in a slightly different way. For this reason a discussion of the antiferromagnetic regime and the coexistence regime is omitted here.

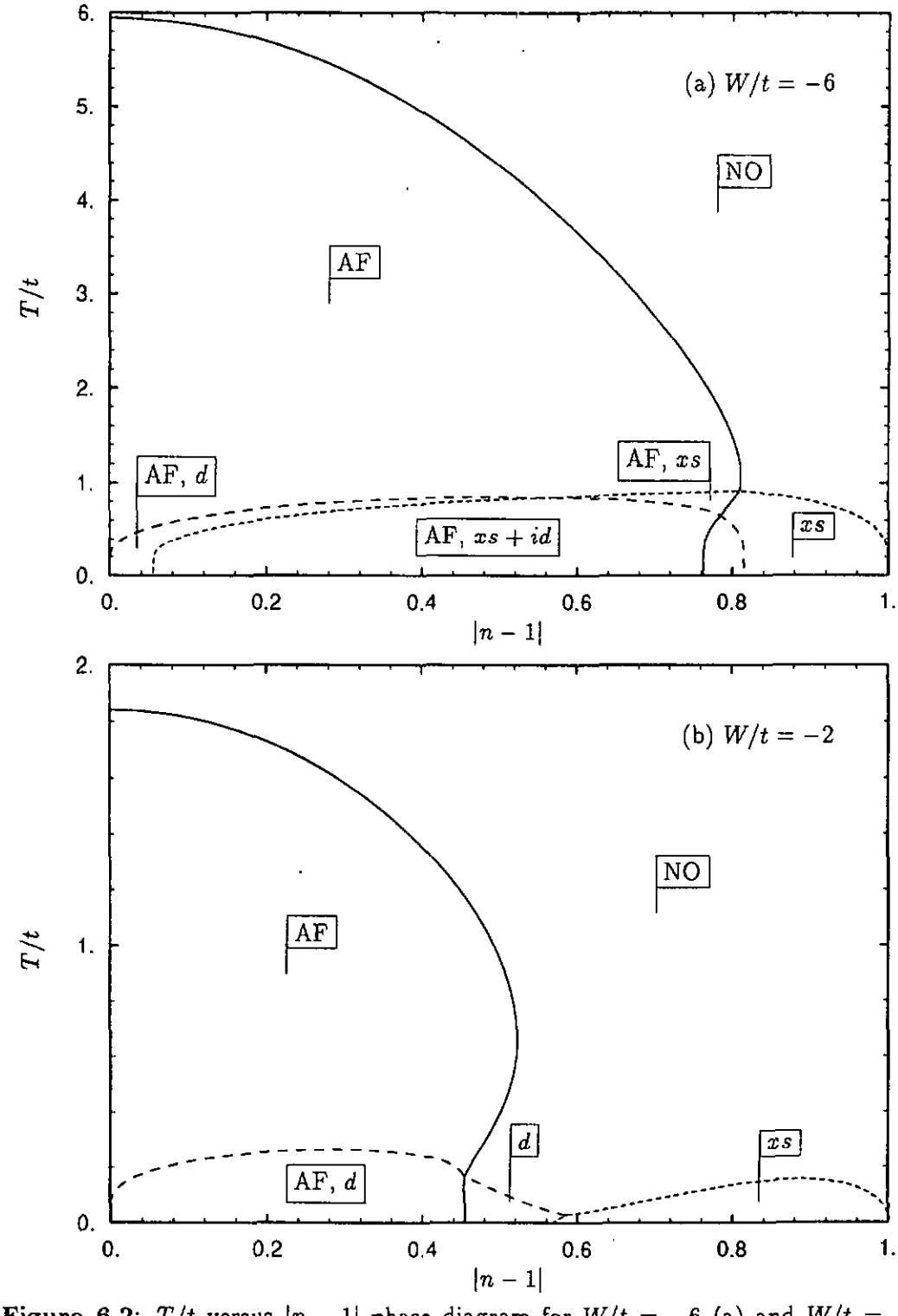

Figure 6.2: T/t versus $|n-1|$ phase diagram for $W/t = -6$ (a) and $W/t = -2$ (b). The solid line shows the Néel temperature, the dotted line the phase boundary of the xs–wave component and the dashed line the phase boundary of the d–wave component of the superconducting order parameter. The superconducting critical temperature is the envelope of the xs–wave and d–wave phase boundary. The flags show which types of order exist within the specified regions.

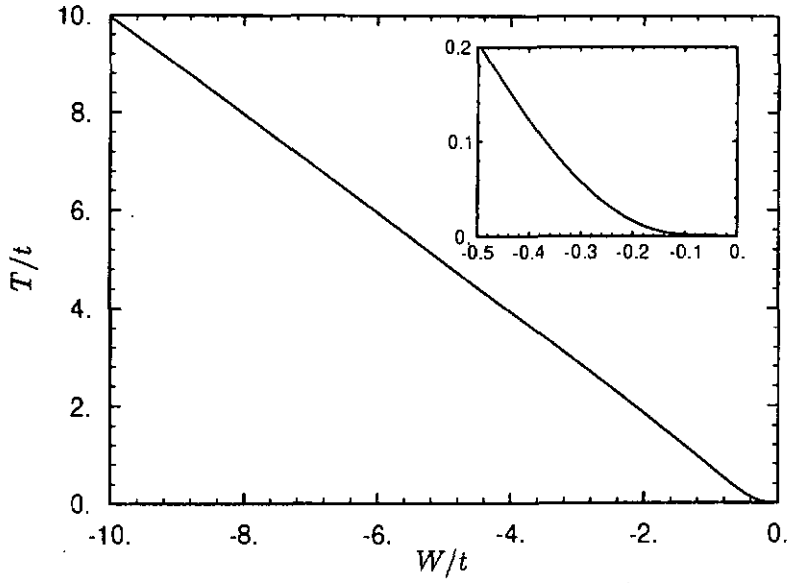

Figure 6.3: T/t–W/t phase diagram for half–filling ($n = 1$). Only the antiferromgnetic transition temperature is different from zero, which shows the absence of superconductivity for half–filling for all temperatures and coupling constants. The inset zooms the weak coupling regime in the range $W/t = -0.5 \ldots 0$.

6.3.2 T/t versus W/t Phase Diagrams

The final type of phase diagrams which should be discussed are T/t–W/t phase diagrams for different values of electron density. Owing to particle–hole symmetry they are classified by $|n-1|$. As before, the antiferromagnetic phase boundary is always drawn with a solid line, the xs–wave phase boundary with a dotted and the d–wave phase boundary with a dashed line. In figure 6.3, the Néel temperature is shown for half–filling. The inset zooms the weak coupling regime, where it shows an exponential behavior. In the strong coupling regime, however, it increases linearly with $|W|$. In fact, for $t = 0$ the Néel temperature becomes proportional to $|W|$ with proportionality constant equal to 1, i. e. the HFB approximation qualitatively leads to the exact result but yields a transition temperature which is about twice as high as the value obtained by the Monte Carlo simulation (see also chapter 1). The exact result is reduced due to thermal fluctuations, which are not fully included in mean field approximations [Binney92].

Away from halfilling, T/t–W/t phase diagrams are shown in figures 6.4 for $|n-1| = 0.2$ (a), $|n-1| = 0.4$ (b), $|n-1| = 0.6$ (c) and $|n-1| = 0.8$ (d). In all figures the Néel temperature becomes different from zero at the ground state phase boundary with infinite slope, surrounds the reentrance regime where transitions NO $\rightarrow$ AF $\rightarrow$ (NO or SC) are possible, and finally increases linearly with increasing absolute value of the coupling constant. As for half–filling, the linear behavior of the Néel temperature in the strong

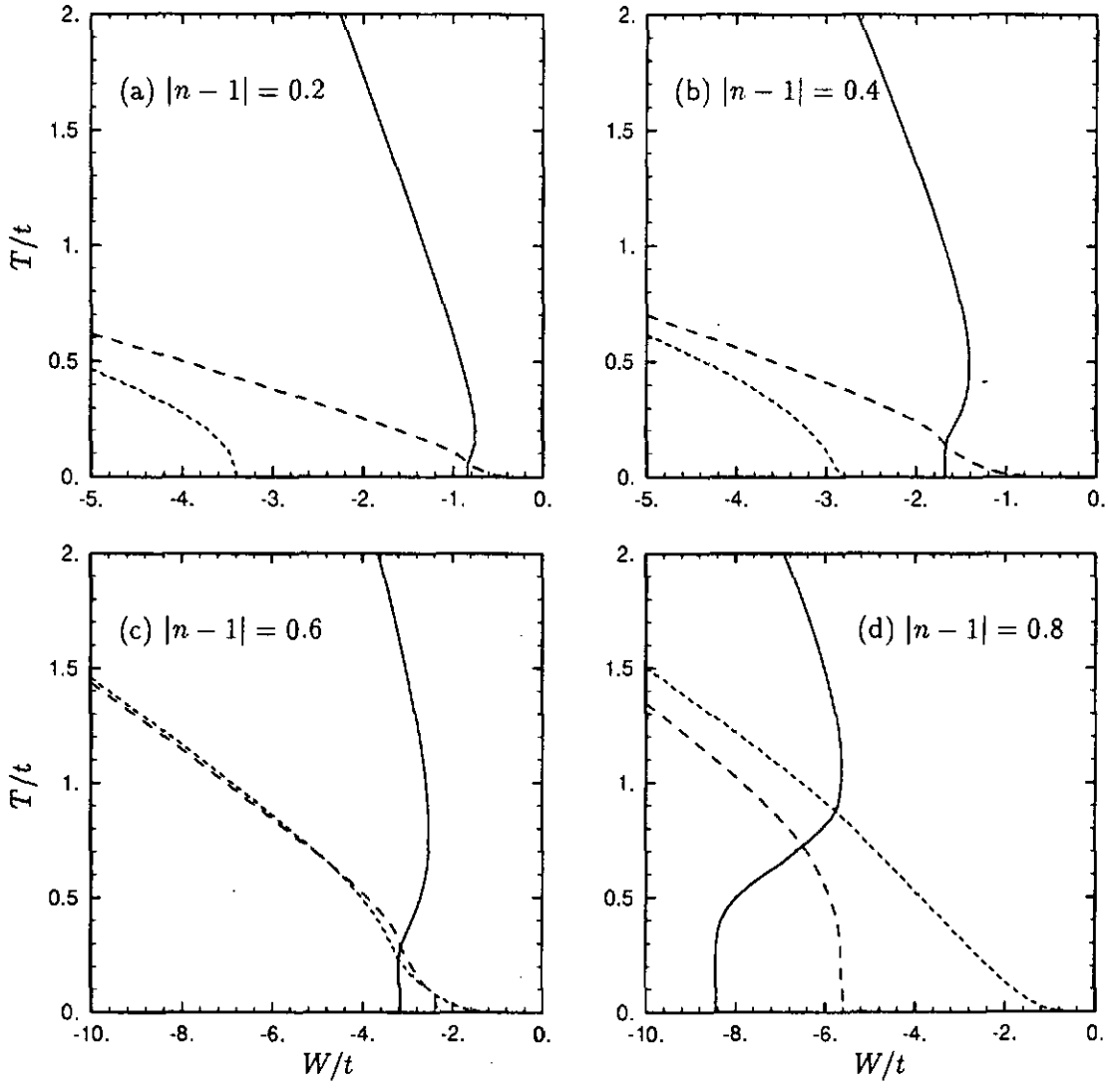

Figure 6.4: T/t versus W/t phase diagrams for different values of filling: $|n-1| = 0.2$ (a), $|n-1| = 0.4$ (b), $|n-1| = 0.2$ (c), $|n-1| = 0.2$ (d) As before, the solid line is the Néel temperature, the dotted line the xs–wave and the dashed line the d–wave phase boundary. The superconducting critical temperature is given by the higher value of the xs–wave and the d–wave transition temperature.

coupling regime is an exact result, but the proportionality constant derived within the HFB approximation has a wrong value in comparison to the Monte Carlo result.

The superconducting critical temperature is the maximum of the xs–wave and the d–wave transition temperature. It is different from zero for all coupling constants and all densities away from half–filling and it is zero for half–filling. In the weak coupling regime and in regions where no antiferromagnetism exists, it shows an exponential behavior and is identical to the transition temperature of the BCS–approximation. When the superconducting phase boundary enters the antiferromagnetic regime (AF) it signals the

coexistence of antiferromagnetism and superconductivity for lower temperatures. Comparing the BCS and the HFB phase diagrams in section 6.4 shows that the superconducting critical temperature is drastically decreased due to the occurence of antiferromagnetic long range order. In the strong coupling regime, T_c increases linearly with increasing $|W|/t$, but the proportionality constant is much smaller than for the Néel temperature. For the latter, this behavior is qualitatively exact, whereas for the superconducting critical temperature it leads to quite a wrong result. Why? As $|W|/t$ increases, the electrons or holes become more and more immobile, so that in the limit $|W| \to \infty$ the system becomes an insulator for all densities. It cannot be superconducting. For this reason the critical temperature should vanish as $|W|/t$ is increased. From this point of view the question arises why the mean field approximation yields to a qualitatively exact result for the Néel temperature and entirely fails in the superconducting case? The answer to this question is that the superconducting order parameter as defined in equations (4.4) and (4.12) does no longer describe the onset of superconductivity in the strong coupling regime. It is a static quantity which does not take into account the mobility of the charge carriers due to a finite hopping amplitude t which is related to the effective mass of the charge carriers. In the strong coupling limit it depends only on the ratio of coupling constant to temperature, which controls the disappearance of the order parameter and hence the phase boundary. This means that whatever approximation is used, the critical temperature in the strong coupling limit, which is calculated upon the pairing order parameter, becomes linear in the coupling strength. In fact, including fluctuations into the calculations of the critical temperature for the attractive Hubbard model also leads to linear behavior in the strong coupling regime [Sachdev91, Rodriguez94]. On the other hand, antiferromagnetism is a static type of long range order and the antiferromagnetic magnetization is the correct order parameter even in the strong coupling regime. For this reason the HFB–approximation yields a qualitatively good result for the antiferromagnetic transition temperature and fails in the superconducting case, so that the criteriom for superconductivity has to be modified. In particular, it should depend explicitely on t. From this point of view the criteria of Scalapino et al. in [Scalapino92, Scalapino93] are more appropriate because they describe the superconducting phase via the current–current correlation function which is directly connected to the Meissner–effect and is proportional to t. We suppose that their criterion might lead to the correct behavior of the superconducting critical temperature. In fact, their criterion is related to the ratio D/m^*, where D is the superfluid density and proportional to the pairing parameter and m^*, the effective mass of the electron pairs which is proportional to $1/t$. In the weak coupling regime, the effective mass is nearly constant as a function of coupling strength and the superconducting transition temperature is controlled by the pairing parameter. In this regime the predictions of the HFB approximation are correct. In the strong coupling regime, however, the charge carriers become more and more localized and the pairing parameter becomes constant, so that the

superconducting transition temperature is controlled by the effective mass and decreases with increasing absolute value of the coupling constant. The criteria of Scalapino et al. might also explain the Kosterlitz–Thouless criterion [Kosterlitz73, Binney92] used by Denteneer et al. [Denteneer91, Denteneer93] to derive the critical temperature in the strong coupling regime for the two–dimensional attractive Hubbard model.

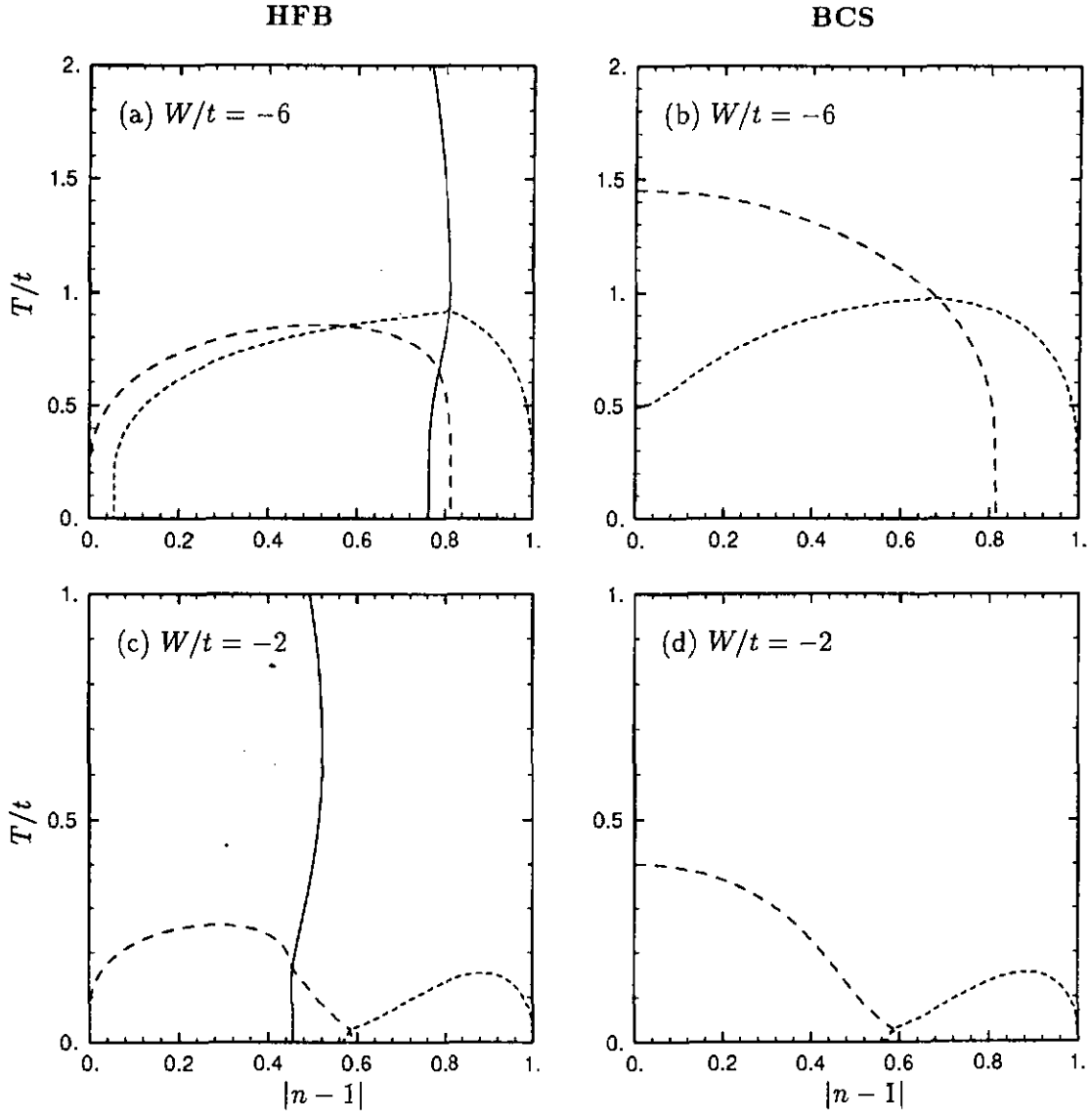

Figure 6.5: Comparison of the HFB and the BCS T/t versus $|n-1|$ phase diagrams for $W/t = -6$ (a,b) and $W/t = -2$ (c,d). In the HFB phase diagrams the solid line is the Néel temperature, while in the HFB and in the BCS phase diagrams the dotted line represents the xs–wave and the dashed line the d–wave phase boundaries. The superconducting critical temperature is given by the higher value of the xs–wave and the d–wave transition temperature.

6.4 Comparison to the BCS Approximation

As the groundstate order parameters for the HFB and the BCS approximations differ from each other, so do the transition temperatures. The T/t versus $|n-1|$ phase diagrams in figure 6.5 are estimated within the HFB approximation (left side) and the BCS approximation (right side) for $W/t = -6$ (first row) and for $W/t = -2$ (second row). In all

plots the xs–wave phase boundary is drawn with a dotted line while the d–wave phase boundary is drawn with a dashed line. The solid line in the HFB phase diagrams is the Néel temperature. It does not exist in the phase diagrams of the BCS approximation. Two major aspects follow from these figures. First, the suppression of superconductivity for half–filling is due to the finite value of the antiferromagnetic order parameter. Second, for nearly all model parameters (W/t and n) the superconducting critical temperature of the HFB approximation is lower than the critical temperature estimated within the BCS approximation, which means that the occurence of antiferromagnetism suppresses superconductivity. This is a first step towards an explanation of the expected decrease of the critical temperature in the strong coupling regime. In fact, because the system orders antiferromagnetically in the atomic limit and becomes an insulator, the critical temperature has to vanish for $|W/t| \to \infty$. The HFB approximation yields to a suppression due to antiferromagnetism, but still to a linear behavior of the critical temperature in the strong coupling regime. This indicates either a failure of the mean field picture or a misinterpretation of the pairing parameters, as was discussed in the previous section refsecTWPhdg.

Overall, the comparison of the HFB and the BCS approximation shows some very important aspects. First it shows that the BCS approximation for the NNSP model fails in the weak coupling regime near half–filling and in the strong coupling regime for nearly all densities. Second, it proves the strong competition between the different order parameters used in the variational HFB approximation, namely the suppression of superconductivity according to the occurence of antiferromagnetism, which is very clearly visible in the half-filled case. From this competition one can conclude that at least static many particle correlations are included in the variational HFB approximation, although it is a mean field type of approximation.

6.5 Phase Separation

The importance of the phase separation for the NNSP model has already been pointed out in chapter 1 where the antiferromagnetic features of the interaction Hmailtonian have been discussed. In fact, the wrong qualitative behavior of the mean field Néel temperature for the interaction Hamiltonian can be explained by the neglection of the phase separation within the mean field picture. In this section it is shown that even in a mean field approximation phase separation can be detected by studying the density dependence of the chemical potential. A Maxwell construction, which is introduced in the first section 6.5.1, leads to new phase boundaries within the HFB phase diagrams and to a better understanding of the coexistence regime of antiferromagnetism and superconductivity.

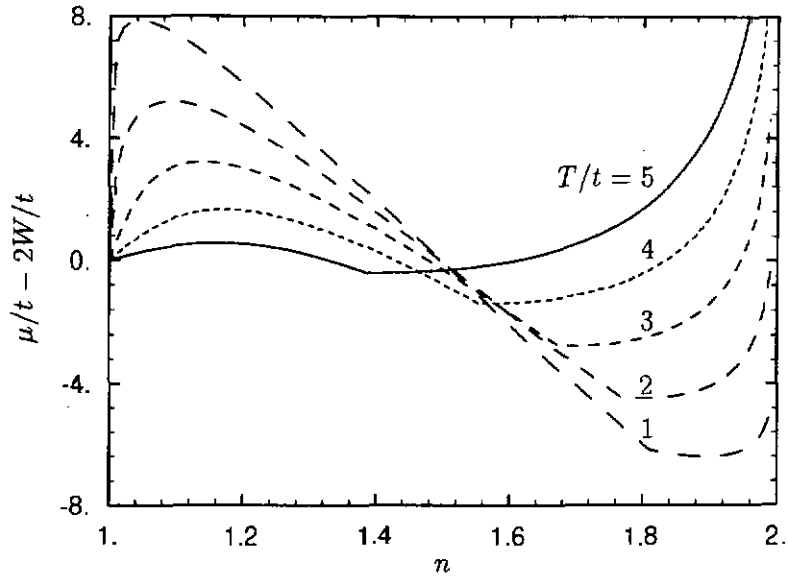

Figure 6.6: The chemical potential as a function of n for $W/t = -6$ and different values of temperature: $T/t = 5$ (solid line) and with increasing dash length $T/t = 4, 3, 2, 1$.

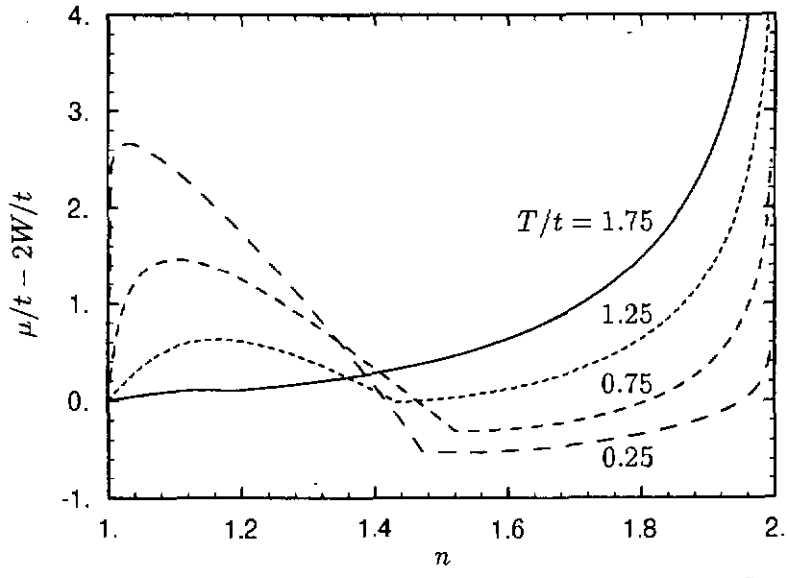

Figure 6.7: The chemical potential as a function of n in the range $[1,2]$ for $W/t = -2$ and different values of the temperature: $T/t = 1.75$ (solid line) and with increasing dash length $T/t = 1.25, 0.75, 0.25$.

This is shown in section 6.5.2 below. In section 6.5.3 the Maxwell construction is applied to the atomic limit. The new phase boundary shows better agreement with the transition temperature obtained by the Monte Carlo simulation. This supports the validity of the Maxwell construction.

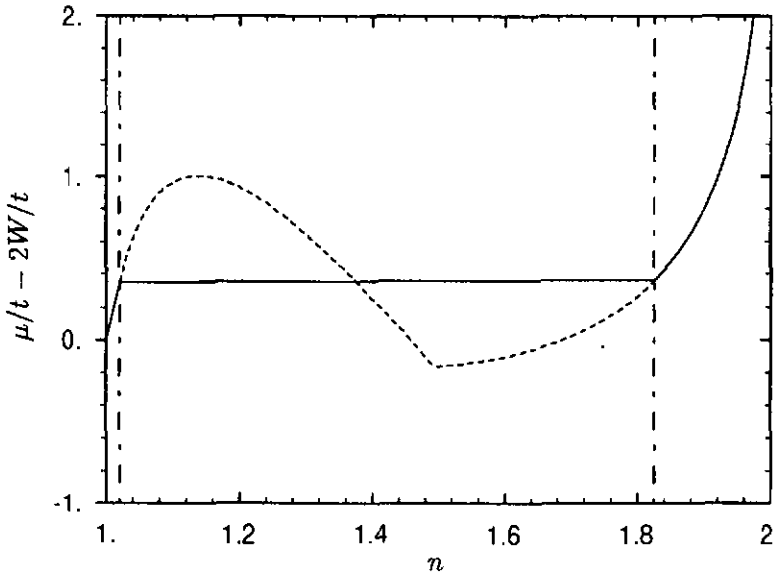

Figure 6.8: The chemical potential as a function of n in the range $[1,2]$ for $W/t = -2$ and $T/t = 1$ (solid line) after performing the Maxwell construction. The dotted line is the original selfconsistent solution for the chemical potential while the dash–dotted lines mark the boundaries for the coexistence region.

6.5.1 Chemical Potential and Maxwell Construction

Up to now only the order parameter and the phase boundaries were discussed. The chemical potential, which has to be determined selfconsistently as well, has not yet been considered. It is the subject of this section, in particular its dependence on filling above the superconducting critical temperature. It should be emphasized that, for the following discussion on phase separation, the chemical potential and not the renormalized chemical potential needs to be considered. Both quantities are related to each other via

$$\mu/t = \bar{\mu}/t + 2W\,n/t \quad . \tag{6.12}$$

Because of particle–hole symmetry the renormalized chemical potential is antisymmetric as a function of density with respect to half–filling. The chemical potential minus $2W$ has the same property. For this reason it suffices to discuss $\mu/t - 2W/t$ for densities $n \in [1,2]$. As all energies up to now, the chemical potential also has to be measured in units of the hopping integral t. In figure 6.6, $\mu/t - 2W/t$ is plotted in the range $n \in [1,2]$ for $W/t = -6$ for different values of temperature as indicated. In figure 6.7, $\mu/t - 2W/t$ is plotted in the same way for $W/t = -2$. Both figures obviously show a large density range where the slope of the chemical potential with respect to n becomes negative. This indicates a phase separated region [Gorbatsevich94]. In this region the chemical potential is pinned and in analogy, for instance, to the *van der Waals* theory for the liquid gas

transition, a *Maxwell* construction has to be carried out in order to get the correct value for the chemical potential and the proper behavior for the phase boundaries surrounding the phase separated region [Reichl80]. This is shown in figure 6.8 for $W/t = -2$ and $T/t = 1$. The dotted and the solid line in this figure show the chemical potential before and after the Maxwell construction, respectively. The region where it is constant defines the phase separated region. The phase boundaries are indicated by vertical dot-dashed lines. Within this region antiferromagnetic domains coexsist with free electrons above and with superconducting electron pairs below the superconducting critical temperature.

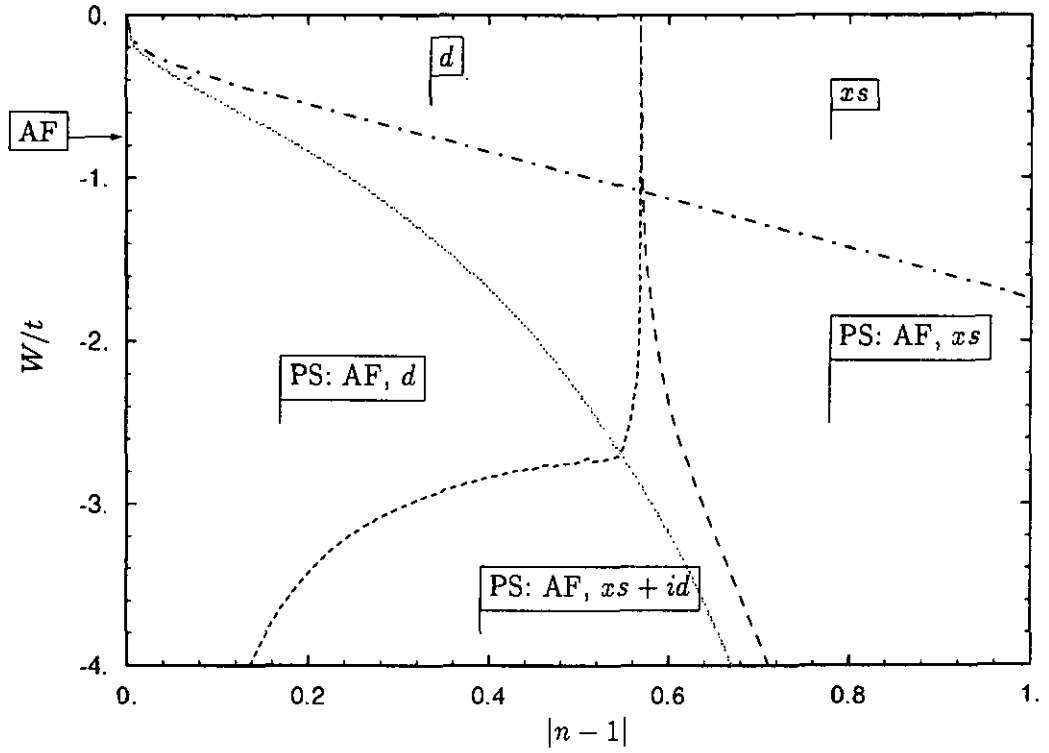

Figure 6.9: Groundstate phase diagram including the phase separation region. Antiferromagnetic long range order only exists at half-filling as indicated. Phase separation (PS) occurs below the dot-dashed region. As before the dotted line is the phase boundary of the xs-wave component and the dashed line the phase boundary of the d-wave component of the superconducting order parameter. The old antiferromagnetic phase boundary is drawn in light gray. The flags show which types of order exist within the specified regions.

6.5.2 Implications on the HFB Phase Diagrams

The Maxwell construction leads to a new antiferromagnetic phase boundary and a phase boundary below which phase separation occurs. For $T/t = 0$ this is shown in figure 6.9 for $W/t \in [-4, 0]$ and for finite temperature in T/t-$|n-1|$ phase diagrams in figure 6.10 for $W/t = -6$ (a) and $W/t = -2$ (b). In all three phase diagrams the new phase boundary

for the phase separation region is given by the dot-dashed line, while the old antiferromagnetic phase boundary is drawn in light gray. The dotted and dashed lines are the xs– and d–wave phase boundaries, respectively. The phase separated region is indicated by PS, whereas NO, AF, xs, d and $xs + id$ mark the nonordered, the antiferromagnetic region, superconductivity with xs–, d–, and mixed $xs + id$–wave symmetry, respectively. Due to the Maxwell construction, the old antiferromagnetic regime shrinks to a very small region around half–filling and is separated from the superconducting regime. For $T/t = 0$ antiferromagnetic long range order only occurs at half–filling as indicated. Above the superconducting critical temperature in figure 6.10 the phase separated region is surrounded by the antiferromagnetic region on the left hand side and the nonordered, metallic region on the right hand side. For this reason it describes a phase separation of antiferromagnetically ordered domains and free electrons and anomalous metallic behavior is expected. The mobile electrons become superconducting below the superconducting critical temperature. There is no more coexistence between antiferromagnetism and superconductivity. The former coexistence regime of antiferromagnetism and superconductivity is replaced by a phase separated region of antiferromagnetic domains and superconducting electron pairs with xs–, d–, or mixed $xs + id$–wave symmetry which depend on coupling strength, temperature and doping. In this regime superconductivity becomes unconventional. Conventional xs–wave or pure d–wave superconductivity occurs only in the extreme weak coupling regime above the phase separation line in figure 6.9. It should be emphasized that the superconducting phase boundaries have to be recalculated due to the new behavior of the chemical potential. However, because there is only a weak dependence of $\bar{\mu}$ on the components of the superconducting order parameter they remain unchanged. This new picture shows that in the weak as well as in the strong coupling regime for nearly all densities except half–filling both, mobile electrons and strong antiferromagnetic fluctuations exist above and even below the superconducting critical temperature. Moreover, superconductivity can only occur within the phase separation region. It seems that the antiferromagnetic correlations are necessary for the superconducting phase transition. The drop of T_c at half–filling is approached is now due to the decrease of the fraction of mobile charge carriers in comparison to the number of electrons which localize in antiferromagnetic domains. At half–filling all electrons localize and form at zero temperature the Néel state. In the next section the Maxwell construction is applied to the atomic limit and compared to the results of the Monte Carlo simulation of this limit. The results of this comparison show the validity of the Maxwell construction and its interpretation.

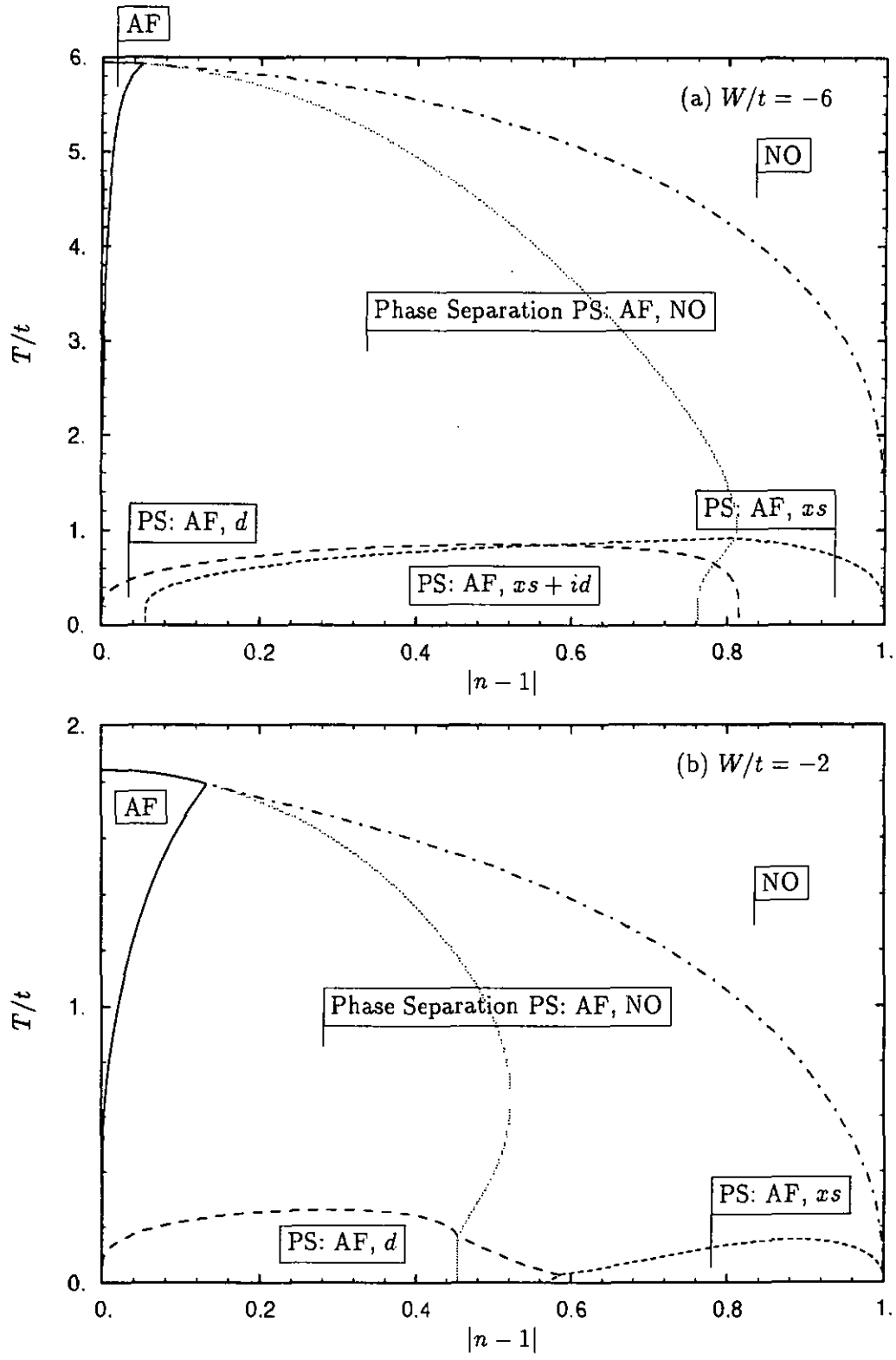

Figure 6.10: T/t versus $|n-1|$ phase diagram for $W/t = -6$ (a) and $W/t = -2$ (b) including the phase separation region (PS) obtained by the Maxwell construction. The solid line shows the new antiferromagnetic phase boundary, the dotted line the xs–wave, the dashed line the d–wave phase boundary and the dot–dashed line the upper bound of the phase separation region. The old antiferromagnetic phase boundary is drawn in light gray.

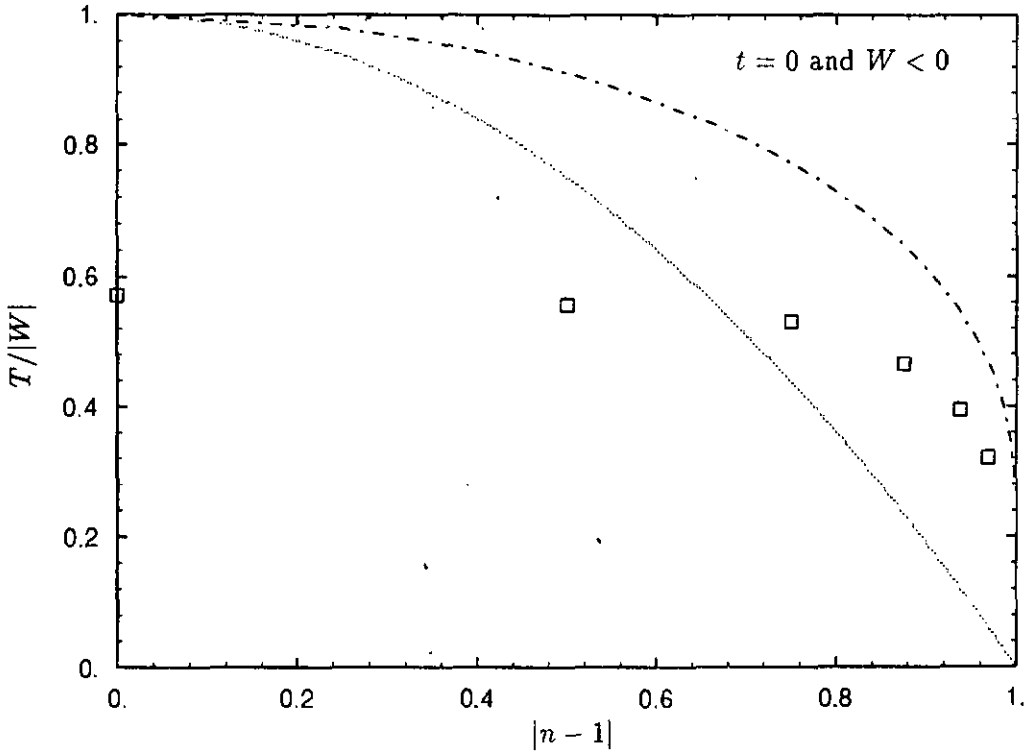

Figure 6.11: $T/|W|$ versus $|n-1|$ phase diagram for $t = 0$ and $W < 0$. The square dots are the Monte Carlo results for the phase transition, while the dot–dashed line is estimated using the Mean Field approximation including the Maxwell Construction to obtain the phase separation region (PS). The old mean field antiferromagnetic phase boundary is drawn in light gray.

6.5.3 Phase Separation in the Atomic Limit

In chapter 1 the phase diagram of the interaction Hamiltonian was presented using the results obtained by a classical Monte Carlo simulation. It was compared to the results of a simple mean field approximation, which results from the HFB approximation above if the pairing parameters are neglected and the hopping integral is chosen to be zero. The deviations from the exact results have to be explained by the neglection of fluctuations and of the phase separation in a mean field description. Using the Maxwell construction described above leads to the phase diagram in figure 6.11. In fact, the new phase separation line (dot dashed line) follows qualitatively the exact phase boundary of the Monte Carlo simulation. Especially the flat behavior as the electron density approaches half-filling and the nearly infinite slope of the phase boundary as $|n-1|$ approaches 1 are well described. The transition temperature is still too high. This is due to the neglection of fluctuations. From figure 6.11 it follows that the mean field approximation including the Maxwell construction yields the qualitatively correct results for all densities and describes the right physics. Regarding the HFB phase diagrams for the NNSP model, this implies that the

antiferromagnetic channel is well approximated by the HFB approximation including the Maxwell construction even in the strong coupling limit. This has some important implications on the interpretation of the NNSP model in comparison with reality, i. e. the high temperature superconductors.

Chapter 7

High Temperature Superconductors and the NNSP Model

Up to now about 100 pages were dealing with abstract theoretical considerations. In this chapter the comparison to reality is of interest. One of the most difficult issues in this framework is the determination of the model parameters t and W and the interpretation of the mean electron density n. Because both the antiferromagnetic and the superconducting properties of the high temperature superconductors should be described within the NNSP model, there is a unique and obvious solution. Its derivation is given in the first section 7.1 below. In the second section 7.2 the corresponding HFB phase diagram and its relation to the phase diagram of high temperature superconductors is discussed. Because of good agreement between both phase diagrams, electronic and thermodynamic implications are possible and meaningful. The density of states and the superconducting energy gap are discussed in section 7.3, while thermodynamic properties like the specific heat and the Pauli susceptibility are considered in section 7.4.

7.1 Fixing the Model Parameters

Because the NNSP model is a very simplified model which cannot account for the complicated details of the copper oxide materials and moreover a mean field type of approximation is used, which in general yields transition temperatures which are about twice as high as the exact results (see for instance the phase diagram of the atomic limit in figure 6.11), only the magnitude of the parameters is important. It is meaningless to care about a factor of two or three. The following considerations need in this sense to be understood. All energies and temperatures are measured in units of the hopping integral t, so its value should be estimated first. From energy band calculations a band

width of order 1 eV has been derived [Mattheiss87, Pickett88, Yu91], which is consistent with photoemission experiments [Minami89, Takahashi89, Olsen89]. In two dimensions and for the nearest neighbor hopping tight binding band in equation (1.9) the band width is $8t$, so that a hopping amplitude of order 0.1 eV or 1000 K is a good choice. In fact, $t = 0.25$ eV has been used by Monthoux and Pines [Monthoux92a], while Schneider et al. [Schneider90a, Frick90] have used $t = 0.07$ eV.

In order to estimate the coupling strength, it should be emphasized again that one of the main reasons to study a nearest neighbor singlet pairing interaction was the ability to describe both the antiferromagnetic and the superconducting features of high temperature superconductors. For this reason either the Néel temperature or the superconducting critical temperature can be used to determine W/t. In the previous chapters we have shown that, within the symmetry broken HFB approximation, the antiferromagnetic component is well described for all coupling constants and electron densities. On the other hand, we have argued that, for the superconducting critical temperature, the HFB approximation totally fails in the strong coupling regime. It is therefore wise to use the antiferromagnetic transition temperature to fix W/t. Moreover, because the undoped material is an antiferromagnetic insulator and shows no superconductivity which is described by the NNSP model, and if half–filling is interpreted as the undoped case, the Néel temperature for $n = 1$ should be used. In the intermediate and strong coupling regime the Néel temperature is given by $|W/t|$ and for $t = 1000$ K and $|W/t| > 1$ this yields $T_N > 1000$ K, which is much to high in comparison to $T_N \approx 250$ K for La_2CuO_4 and $T_N \approx 600$ K for $YBa_2Cu_3O_6$. For this reason, within the NNSP model high temperature superconductors should be described in the weak coupling regime. A second point which favors weak and rules out strong coupling constants is discussed in section 7.4.1 on the temperature dependence of the specific heat. In the weak coupling regime the Néel temperature for half–filling behaves exponentially as a function of $|W/t|$, so that values of about 0.7 or 0.8 for $|W/t|$ should be the appropriate ones. For the following discussion we shall take $W/t = -1$, which is consistent with estimates of the antiferromagnetic coupling constant for the undoped compounds of about 500 — 1000 K (see e. g. [Erice89] and references therein).

The last point which has to be checked is the role of the electron density n and its relation to δ, the number of holes per unit cell in the CuO_2 planes. Within the NNSP model the undoped material is described by half–filling and corresponds to $\delta = 0$. n reflects the mean number of electrons and $2 - n$ the mean number of holes per site of the square lattice, which has been assumed in all calculations. As argued in the introduction, each unit cell of the CuO_2 planes can be mapped onto one site of the lattice and, because the nearest neighbor hopping model shows particle hole symmetry, δ can be directly identified with $|n - 1|$. This interpretation is in sharp contrast to the interpretation of Schneider et

al. [Schneider90a, Schneider90b] and Micnas et al. [Micnas90]. Both authors used $\delta \sim n$ or $\delta \sim 2 - n$. Using $\delta = |n - 1|$ and the values for W/t and t from above, a phase diagram for high temperature superconductors can be derived.

7.2 Phase Diagram

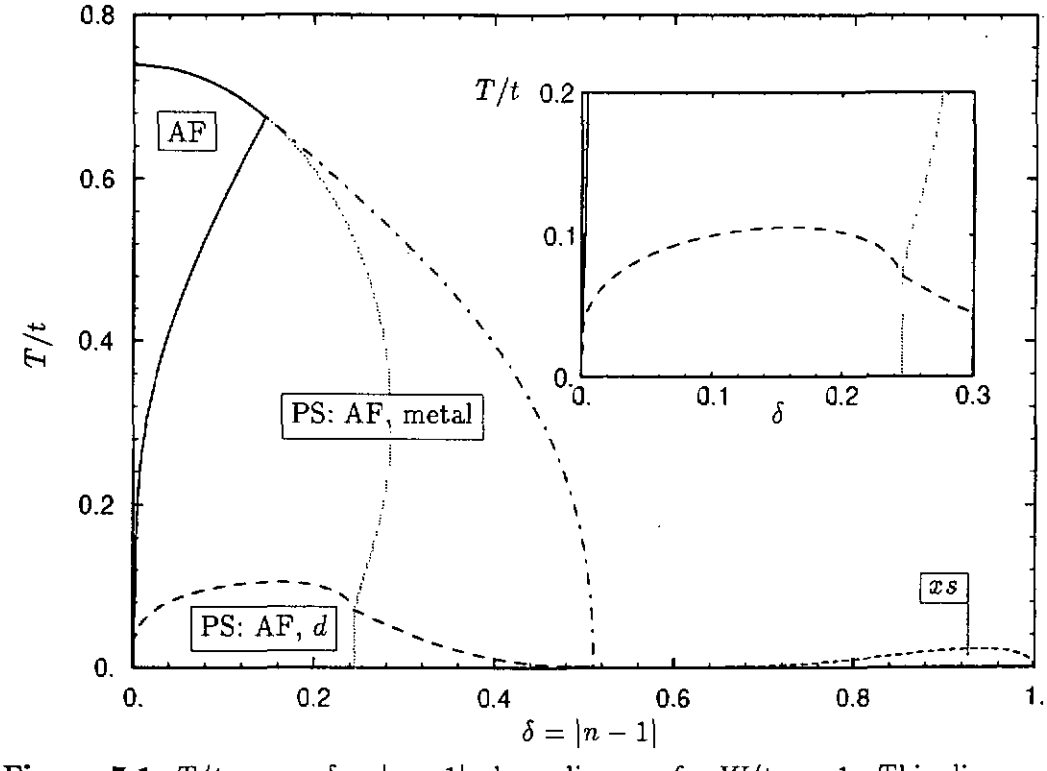

Figure 7.1: T/t versus $\delta = |n - 1|$ phase diagram for $W/t = -1$. This diagram shows the antiferromagnetic phase boundary (solid line), the phase separated region (below the dot–dashed line), the d–wave (dashed line) and the xs–wave (dotted line) transition temperature. The old antiferromagnetic phase boundary is drawn in light gray. The inset zooms the superconducting transition temperature in the doping range of interest for $\delta \in [0, 0.3]$.

The HFB phase diagram for $W/t = -1$ is shown in figure 7.1. It includes the phase separated region (solid line on the left hand side and dot–dashed line on the right hand side) as it is derived by the Maxwell construction described in chapter 6.5. The region where antiferromagnetic long range order appears is surrounded by the solid line. For $\delta \in [0, 0.5]$ the superconducting phase boundary is given by the d–wave transition temperature (dashed line), while in the extremely overdoped regime for $\delta > 0.5$ it is given by the xs–wave transition temperature (dotted line). The small inset shows the superconducting critical temperature in the interesting doping regime for $\delta \in [0, 0.3]$. The features of this phase diagram can be summarized as follows:

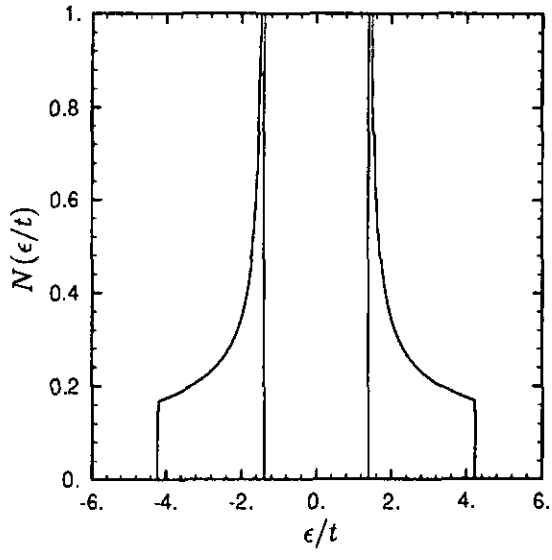

Figure 7.2: Density of states in the antiferromagnetically ordered system for half-filling, $T/t = 0$ and $W/t = -1$. The antiferromagnetic gap is given by $E_g/t = 2|W|/t\, z\, m_{\mathrm{AF}} = 2.76$ with $m_{\mathrm{AF}} = 0.34533$ and $z = 4$.

- In the undoped case ($\delta = 0$) the system orders antiferromagnetically and shows no superconductivity. For $t = 0.1$ eV the Néel temperature is about 700 K.
- Superconductivity occurs for $\delta > 0$. In the relevant doping range for $\delta \in [0., 0.3]$ the superconducting order parameter has d–wave symmetry. xs–wave superconductivity only appears beyond $\delta = 0.5$. This doping range, however, is not of any interest (is it possible to create extremly overdoped materials?).
- The superconducting critical temperature first increases in the underdoped regime for $\delta < 0.15$, shows a maximum at $\delta \approx 0.17$ and finally drops to zero as δ is further increased beyond 0.3.
- The critical temperature is about 100 K for the optimally doped system and for $t = 0.1$ eV, so that the ratio $T_{\mathrm{N}}(\delta = 0)/T_{\mathrm{c}}(\delta \approx 0.17)$ equals approximately 7.
- The phase separated region covers the whole doping range from $\delta = 0$ up to $\delta = 0.5$ and extends to temperatures comparable to the Néel temperature for half-filling.

Comparing the generic phase diagram of the copper oxide superconductors in figure 1.1 with these characteristic points of the phase diagram of the NNSP model for $W/t = -1$, some remarkable agreement is revealed. Not only the qualitative features, but also the quantitative estimates for the Néel temperature and the superconducting transition temperatures as a function of doping agree. For this reason the phase diagram of high temperature superconductors might be interpreted from the point of view of the NNSP model. The following physical scenario can be drawn: for half-filling the nearest neighbor pairing interaction drives the system into the antiferromagnetic state. As the density of states in figure 7.2 shows, a large antiferromagnetic gap opens below the Néel temperature and the single tight binding band splits into two sub-bands. For this reason the system becomes

an insulator for $T/t = 0$ [Scalapino93]. As the system is doped, antiferromagnetic long range order disappears and the system enters into a phase separated region. In fact, electronic phase separation has been discussed as one possible microscopical scenario for the doped copper oxide superconductors (see for instance [PS92, PS93] and references therein) and strong two–dimensional antiferromagnetic fluctuations have been observed in many experiments [Birgenau88a, Birgenau88b, Uemura87, Uemura88]. The phase separation of antiferromagnetic domains and metallic droplets above T_c is responsible for the unusual normal state behavior. In this region the system behaves as an antiferromagnetic Fermi liquid and shows unusual metallic behavior. The existence of a spin gap as it is for instance observed in NMR experiments [Pennington90, Mangelschots92a, Mangelschots92b] and which points to non Fermi liquid behavior is one consequence. The spin gap is more or less the energy required to extract an electron from an antiferromagnetic domain. On the other hand, the existence of a fermi surface which has been revealed in angle–resolved photoemission experiments [Abrikosov93, Aebi94], is due to the metallic component. It is reduced in intensity because the number of mobile charge carriers is only a fraction of δ. The other part is localized in antiferromagnetic domains. Only the mobile fraction is probed in transport experiments, for instance in measurements of the Hall coefficient and the resistivity. This explains the small carrier density of the order of 10^{21} in nearly all high temperature superconductors. The linear resistivity as a function of doping [Torrence89] is a consequence of the continuous increase of the mobile fraction as δ is increased. In angle–resolved photoemission experiments, however, both components become visible. In fact, the observed shadow bands [Abrikosov93, Aebi94] can be explained in terms of the phase separation. Also the unusual normal state behavior of the Pauli susceptibility as a function of temperature [Torrence89, Takigawa89] is a consequence of the existence of strong antiferromagnetic correlations. The temperature where the Pauli susceptibility shows a maximum remarkably agrees with the phase separation line in figure 7.1. To summarize: the bivalent behavior of high temperature superconductors in normal state — on one hand metallic behavior and on the other hand typical non–Fermi liquid antiferromagnetic characteristics — are a direct consequence of the electronic phase separation. As doping is increased the antiferromagnetic fraction decreases and the system becomes more and more a metal. Beyond the phase separation line usual Fermi liquid behavior occurs. This smooth transition to metallic behavior has also been observed in experiment [Torrence88, Torrence89]. Interesting enough, as the antiferromagnetic component vanishes in the overdoped regime, the superconducting critical temperature drops to zero. This strong correlation between antiferromagnetism and superconductivity has been clearly shown for a number of copper oxide compounds [Shafer90]. It seems that in the relevant doping range the antiferromagnetic fluctuations mediate the transition into the superconducting state with d–wave symmetry. On the other hand, if the number of mobile charge carriers decreases, the superconducting critical temperature should decrease

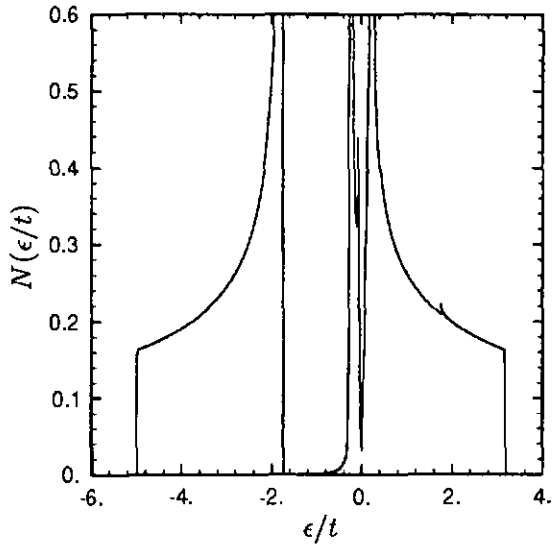

Figure 7.3: Density of states for the optimally doped system for $\delta = 0.15$, $T/t = 0$ and $W/t = -1$. The chemical potential lies at $\epsilon/t = 0$.

as well. In the phase separated region both scenarios are competing. In the underdoped regime the increase of the number of mobile charge carriers determines the increase of the superconducting transition temperature. In the overdoped regime, however, the antiferromagnetic fluctuations vanish, so that the d–wave transition temperature decreases. This leads to an optimal T_c at $\delta \approx 0.16$. Its relatively high value of about 100 K is due to the fact that within the NNSP model pairing takes place over the whole Brioullin zone. This is in contrast to the conventional BCS model[1], where only a small shell around the Fermi surface of the order of the Debye temperature is involved. The d–wave symmetry of the superconducting order parameter leads to unconventional superconductivity, which is in addition strongly influenced by antiferromagnetic fluctuations which still exist in the superconducting state. Some consequences are discussed in the next sections.

7.3 Density of States

7.3.1 Groundstate Density of States

For a free electron gas with dispersion relation ϵ_k, the density of states is defined by equation (1.13). For an interacting system this definition has to be generalized [Mahan90]:

$$N(\epsilon/t) = \frac{1}{L} \sum_{k\sigma} S_\sigma(k, \epsilon/t) \quad , \tag{7.1}$$

[1] It should be noted again that there is a difference between the BCS theory and a BCS type of approximation. The BCS theory starts from electron–phonon coupling which leads to conventional s–wave superconductivity. The BCS approximation, however, is a technique which might be applied to a large variety of models.

where $S_\sigma(k, \epsilon/t)$ is the spectral density function which is related to the normal Matsubara Greens function via

$$G_\sigma(k, i\omega_n) = \int dx \frac{S_\sigma(k, x)}{i\omega_n - x} \quad . \tag{7.2}$$

Using the formula for $G_\sigma(k, i\omega_n)$ in equation (4.33), an analytical expression for the spectral density function can be easily derived. With some limitations, the density of states is directly probed in tunneling experiments [Meservey69, Dynes94]. For this reason these experiments yield information about the quasiparticle excitation spectrum and can be used, for instance, to distinguish between different types of pairing in superconductors. In fact, one of the most interesting features of the phase diagram in figure 7.1 is the symmetry of the superconducting order parameter. In contrast to the BCS theory it is d–wave with an anisotropic energy gap which is given by

$$\Delta(k) = \frac{1}{4}\Delta_d(\cos(k_x) - \cos(k_y)) \quad . \tag{7.3}$$

From this equation follows that it becomes zero on the lines $k_x = \pm k_y$ in the first Brioullin zone and a pseudo gap in the density of states is expected [Zhou92, Wenger93]. Because of the competition between antiferromagnetism and superconductivity, however, the situation is much more complicated. In fact, the interplay between the antiferromagnetic order parameter, the chemical potential and the superconducting order parameter can alter this simple picture. In figure 7.3 the groundstate density of states for $W/t = -1$ and for optimal doping is drawn. The energy scale is shifted so that the chemical potential lies at the origin, namely $\epsilon/t = 0$. Two gaps are visible. The first gap, which is not symmetric with respect to the chemical potential, results from the finite antiferromagnetic order parameter and reflects the spin gap in the phase separated region. It also exists above T_c. The second gap is the superconducting gap which, in contrast to the antiferromagnetic gap, is more or less symmetric. In order to study the details of the superconducting gap as a function of doping, the density of states is plotted in the range $\epsilon/t \in [-1, 1]$ shown in figure 7.5 for different fillings. In the underdoped regime for $\delta = 0.02$ (a) and $\delta = 0.05$ (b), a real gap occurs which decreases as doping is increased. For fillings larger than $\delta = 0.05$, the real gap disappears and a pseudo gap with its characteristic V–shaped form occurs. For $\delta = 0.1$ this is shown in figure 7.5(c). For optimal doping for $\delta = 0.15$ (d), some internal structure appears within the superconducting gap. Finally in the overdoped regime for $\delta = 0.2$ (e) and $\delta = 0.25$ (f), where the antiferromagnetic fraction becomes very small, the typical d–wave gap occurs. It should be noted that these calculations of the densitiy of states are performed on the results of the HFB approximation without considering the modifcations mediated by the Maxwell construction to derive the phase separated region. For this reason the influence of the antiferromagnetic gap would be altered if the phase

separation would be taken into account. Especially in the overdoped regime which also lies within the phase separated region. The V–shaped form and the size of the superconducting gap, however, will be rather unchanged due to the weak correlation of the chemical potential and the superconducting order parameters. The density of states for optimal doping shown in figure 7.5 (d) can be compared to the experimental results on $YBa_2Cu_3O_{7-y}$ [Geerk89, Valles91]. Both the V–shaped form and the width of about 40 meV agree very well. In fact, for $t = 0.1$ eV the maximum width of the energy gap for optimal doping becomes 0.04 eV. The ratio of the zero temperature energy gap and the critical temperature has often been discussed. For the $YBa_2Cu_3O_{7-y}$ compounds it is about 4.4 (40 meV divided by 90K). Within the NNSP model the maximum gap for pure d–wave superconductivity is given by

$$E_g = 2 \times 2 \times |W| \times |\Delta_d| \quad . \tag{7.4}$$

The first factor 2 is due to the symmetry of the energy gap around the chemical potential, while the second factor 2 is the maximum of $(\cos(k_x) - \cos(k_y))$. In figure 7.4 the ratio E_g/T_c is plotted as a function of doping for $W/t = -1$ in the relevant doping range. It is weakly doping–dependent and over a wide range of about 4 – 5 in agreement with reality. It should be noted that this ratio is significantly larger than the BCS value of 3.53 for a conventional s–wave superconductor because of the anisotropic nature of the superconducting order parameter and the influence of the antiferromagnetic background on the quasiparticle excitation spectum.

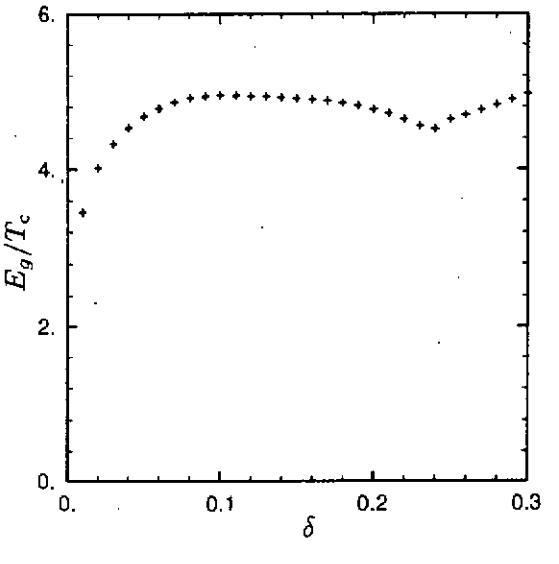

Figure 7.4: The ratio of the maximum energy gap in the groundstate density of states to the value of the transition temperature as a function of doping for $W/t = -1$.

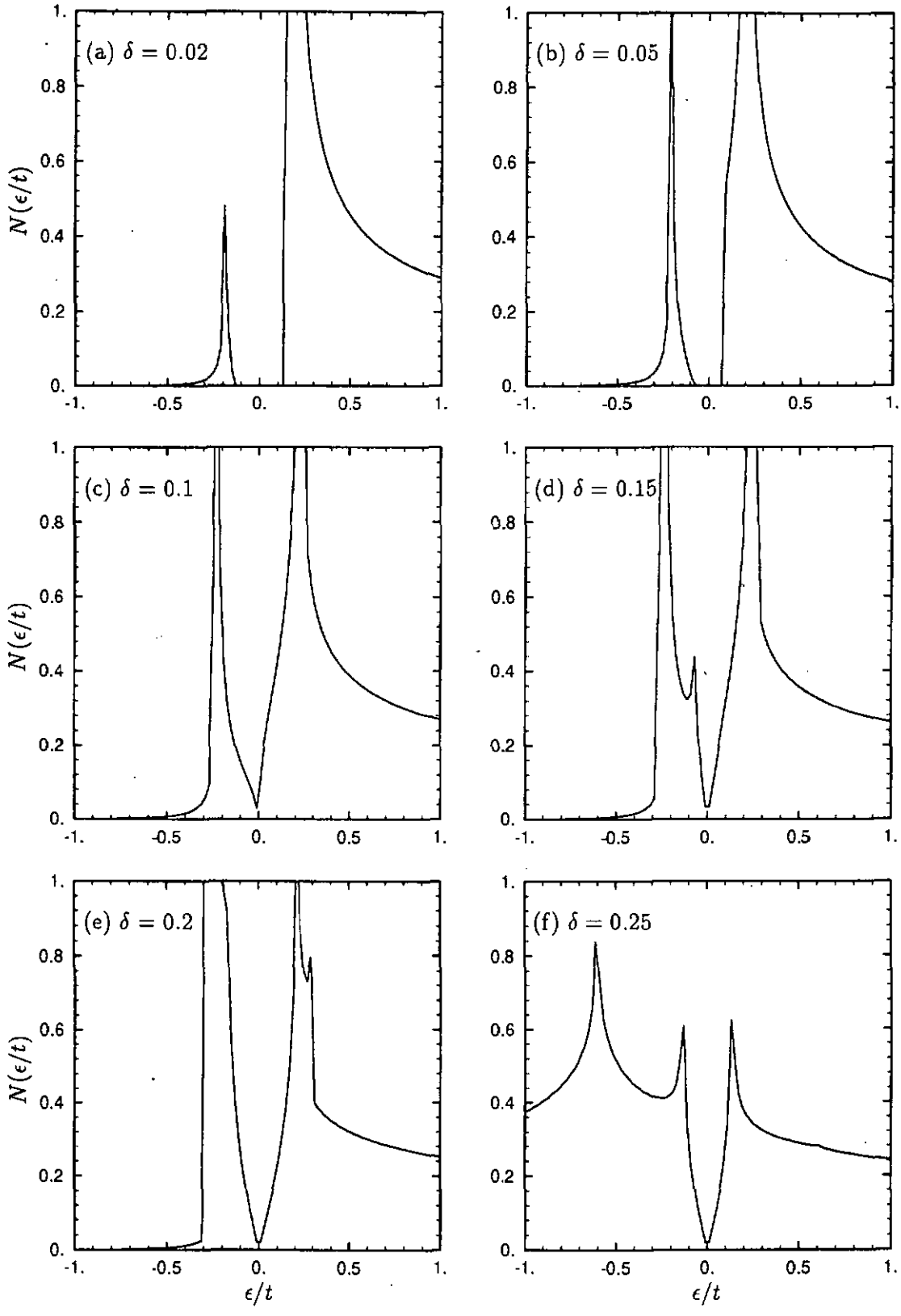

Figure 7.5: Groundstate density of states derived within the HFB approximation for $W/t = -1$ and various fillings: in the underdoped regime for $\delta = 0.02$ (a), $\delta = 0.05$ (b), $\delta = 0.1$ (c), for optimal doping $\delta = 0.15$ (d) and in the overdoped regime for $\delta = 0.2$ (e) and $\delta = 0.25$ (f).

7.3.2 Density of States near T_c

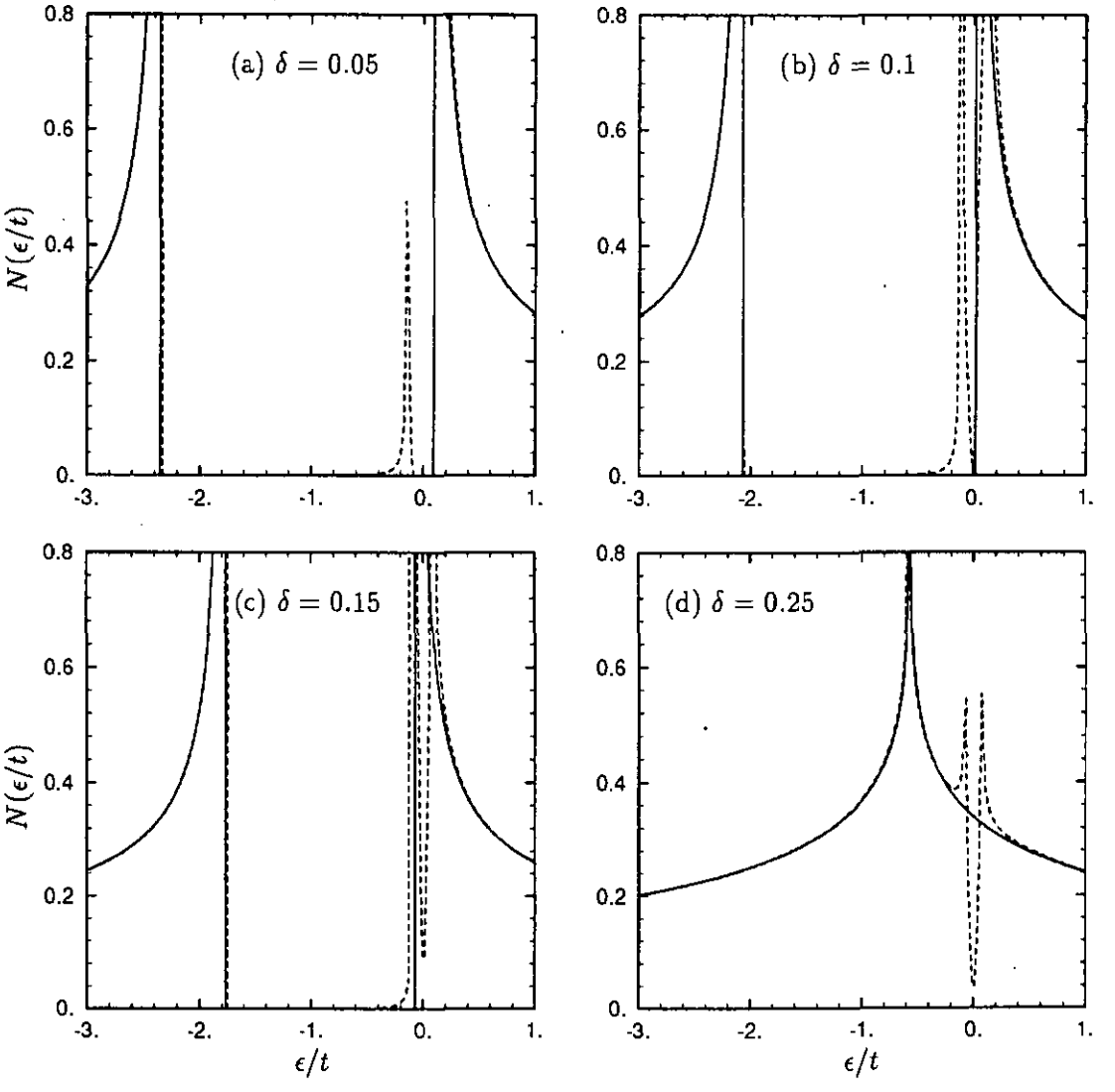

Figure 7.6: Density of states derived within the HFB approximation near the superconducting critical temperature for $W/t = -1$ and various various fillings: in the underdoped regime for $\delta = 0.05$ (a), $\delta = 0.1$ (b), for optimal doping $\delta = 0.15$ (c) and in the overdoped regime for $\delta = 0.25$ (d). The solid line is just above T_c, while the dotted line is the density of states immediately below T_c.

It is also interesting to study the density of states in the neighborhood of the superconducting critical temperature as a function of doping. For $W/t = -1$ and various fillings this is shown in figure 7.6. In all four graphs (a) – (d) the solid line corresponds to the normal state a few degrees of Kelvin above T_c, while the dotted line is the density of states immediately below the critical temperature. From (a) to (d) the density of states is given for $\delta = 0.05$, $\delta = 0.1$ $\delta = 0.15$ and $\delta = 0.25$. Two aspects can be derived from these graphs. As the system is cooled below the critical temperature, new quasiparticle states emerge

below the chemical potential at $\epsilon/t = 0$. This is very clearly visible in figure 7.6 (a) and (b) for the underdoped systems. It also appears for optimal doping in figure 7.6 (c) and in the overdoped regime in figure 7.6 (d), where the new states result in an opening of a superconducting gap and an increase of the density of states below the chemical potential. Because of these new states the free energy is lowered and superconductivity occurs.

The second interesting point is the position of the chemical potential. In the underdoped regime for $\delta = 0.05$ in figure 7.6 (a), the chemical potential lies within the antiferromagnetic gap. For this reason semiconducting properties are expected in the normal state just above the critical temperature. On the other hand, for $0.1 < \delta < 0.2$ the chemical potential lies in the upper band near the van Hove singularity. The maximum T_c occurs in this region, which supports the van Hove scenario [Gofron93, Dessau93]. Moreover, it has been argued that the high density of states and the flat dispersion are responsible for the linear in T behavior of the normal state resistivity as it is observed for the optimally doped compounds [Batlogg89, Torrence89]. In the overdoped regime the chemical potential shifts into the middle of the band and the normal state resistivity behaves more Fermi liquid like ($\sim T^2$). As already noted, this picture might change if the phase separation is taken into account. Nevertheless it points to the right direction in comparison to reality. In fact, the transition from semiconducting, over anomalous Fermi liquid to usual Fermi liquid behavior in the normal state just above the superconducting critical temperature as doping is increased, has been reported for various copper oxide superconductors and identified as a common and significant feature of these materials (see e. g. [GinsbergI]- [GinsbergIII] and references therein). From the point of view of the NNSP model this observation is due to the competition of antiferromagnetic fluctuations and metallic properties in the phase separated region above T_c.

7.4 Thermodynamic Properties

7.4.1 Specific Heat

In a canonical description the specific heat is the derivative of the entropy with respect to temperature for fixed particle number density [Reichl80], i. e.

$$C = T \left(\frac{\partial S}{\partial T} \right)_n \quad , \tag{7.5}$$

where the entropy itself is the first temperature derivative of the canonical free energy for fixed particle number density:

$$S = -\left(\frac{\partial A}{\partial T}\right)_n \quad . \tag{7.6}$$

It should be noted that due to the temperature dependence of the chemical potential, it is important to use the canonical free energy functional in equation (4.14) and not the free energy functional for the grand canonical description for fixed chemical potential given in equation (4.5). Moreover, in order to calculate the derivatives in equation (7.6) and equation (7.5), the implicit temperature dependence on the variational parameters of the HFB approximation has to be taken into account, i.e. first the total temperature derivative has to be computed and second the resulting expression has to be evaluated at the solution of the selfconsistent equations. In this sense the partial derivatives in equation (7.6) and equation (7.5) are somehow misleading. Because the first derivative of the canonical free energy functional with respect to the variational parameters vanish at the selfconsistent solution, the calculation of the entropy is quite easy. The result is

$$S = -\sum_{ki}\Big\{\Big(1-f(E_i)\Big)\ln\Big(1-f(E_i)\Big) + f(E_i)\ln\Big(f(E_i)\Big)\Big\} \quad , \tag{7.7}$$

where f is the Fermi function defined by

$$f(x) = \frac{1}{(e^{x/T}+1)} \quad . \tag{7.8}$$

The expression above reflects the information–theoretical interpretation of the entropy:

$$S = -\sum_l P_l \ln(P_l) \tag{7.9}$$

where the sum ranges over all microscopical states of the system and P_l is the probability of state $\# \, l$ being occupied. For the HFB approximation there are four quasiparticle bands $\pm E_i$ for $i = 1, 2$ with occupation probability distributions $f(E_i)$ and $f(-E_i) = 1 - f(E_i)$. The calculation of the specific heat, i.e. the second derivative of the canonical free energy functional is much more complicated. For this reason a numerical derivation method of the entropy data has been used. Moreover, the entropy density and the specfic heat density instead of its corresponding extensive quantities have been calculated.

For half–filling, i. e. the undoped system and $W/t = -1$, the entropy and the specific heat is shown in figures 7.7(a) and (b), respectively. The solid line is the HFB solution, while the dashed line is valid for free electrons. The discontinuity in the entropy indicates

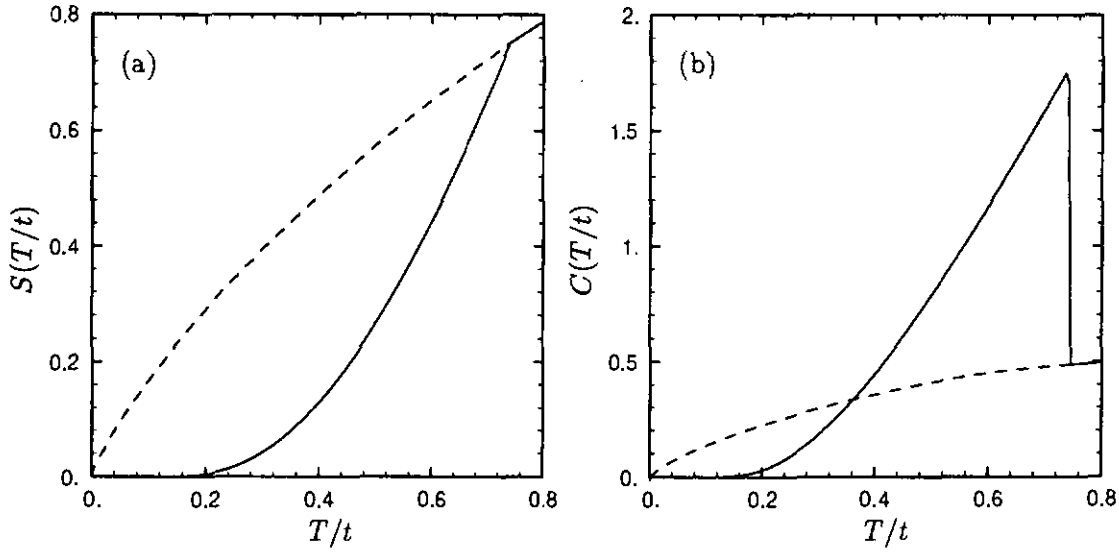

Figure 7.7: Entropy (a) and specific heat (b) for $w/t = -1$ and half–filling as a function of temperature. The solid line is derived within the HFB approximation, while the dashed line shows the entropy and the specific heat for free elecrons.

the transition into the antiferromagnetic state with long range order. Accordingly the specific heat shows a jump at T_N. The exponential decay for $T/t \to 0$ is due to the opening of a large antiferromagnetic gap below the Néel temperature. Both, the jump in the specific heat and the exponential decay has been observed in the undoped copper oxide compounds, which show antiferromagnetic long range order.

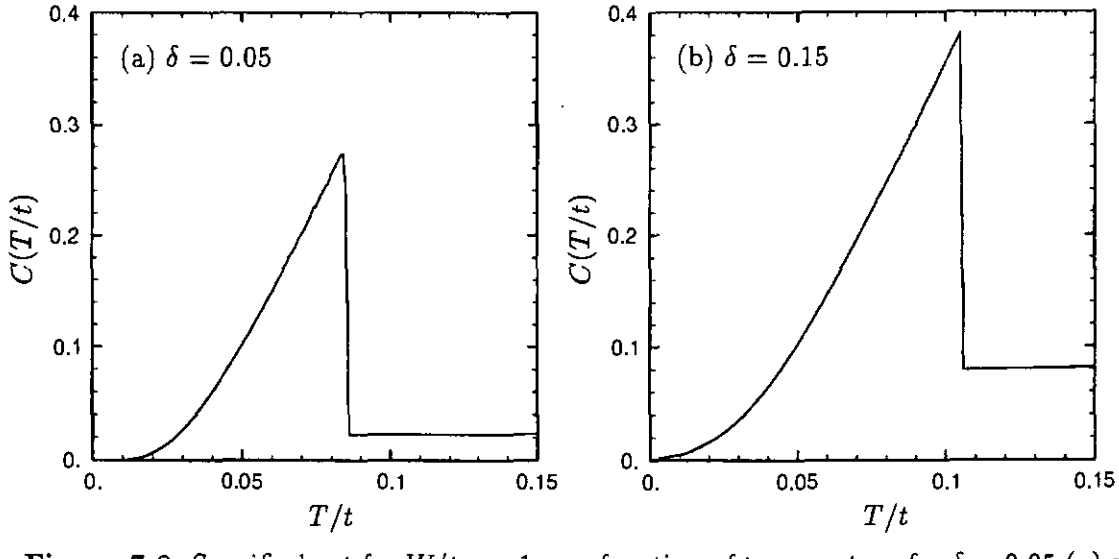

Figure 7.8: Specific heat for $W/t = -1$ as a function of temperature for $\delta = 0.05$ (a) and $\delta = 0.15$ (b).

Because the phase separation, revealed in the phase diagram of the NNSP model in figure 7.1, is very important for the normal state behavior but was not selfconsistently taken into account, the specific heat for the doped system is only studied in the low temperature regime where the implications of the d–wave character of the superconducting order parameter can be studied. In figure 7.8 the specific heat is plotted as a function of temperature for $W/t = -1$ and for $\delta = 0.05$ (a) and $\delta = 0.15$ (b). For the underdoped case an exponential behavior occurs due to the existence of a real gap in the density of states shown in figure 7.5 (b). On the other hand, the low temperature behavior of the specific heat is quadratic if a pseudo gap is present. This is shown for optimal doping in figure 7.8 (b).

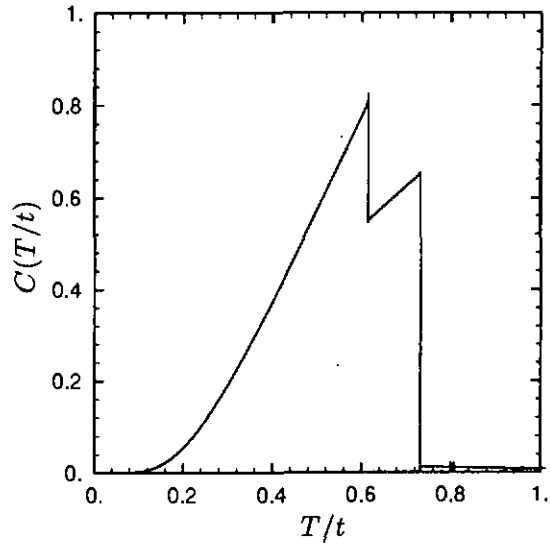

Figure 7.9: Specific heat as a function of temperature for $W/t = -6$ and $|n-1| = 0.2$. The first jump from the right marks the occurence of d–wave and the second jump of xs–wave superconductivity.

The specific heat in the strong coupling regime for $W/t = -6$ and $n = 1.2$ as a function of temperature is shown in figure 7.9. It shows a double jump according to the two distinct phase boundaries for the d–wave and the xs–wave component of the superconducting order parameter. Because such a splitted transition has not been observed in high temperature superconductors, they cannot be described by the NNSP model in the strong coupling regime. This conclusion is consistent with the estimation of the coupling strength upon the antiferromagnetic transition temperature for half-filling (see above). It cannot be used as a proof for the weak coupling regime because the HFB approximation fails in the superconducting case for strong coupling constants and finite temperatures. Nevertheless, the double peak structure of the specific heat should also emerge in approximations which go well beyond the HFB approximation because the groundstate phase diagram is well described in the HFB approximation even in the strong coupling regime [Nozieres85, Micnas90] and predicts mixed $xs+id$–wave superconductivity. A double peak structure of the specific heat has been observed in the heavy fermion superconductor UPt_3 [Stewart84, Ott87, Fisher89, Goltsev94]. From this point of view the strong or interme-

diate coupling regime, where $xs + id$–wave superconductivity occurs, might be used to describe the heavy fermion compounds. For this purpose, however, the model has to be solved in three dimensions.

7.4.2 Pauli Susceptibility

Finally the implications on the Pauli susceptibility should be discussed. The Pauli susceptibility is probed in measurements of the Knight shift in NMR experiments [Pennington90].

From the point of view of the HFB approximation, the most simple way to derive an analytic expression for the Pauli susceptibility is the calculation of the ferro–magnetization in a constant external magnetic field perpendicular to the square lattice. This leads to an additional Zeeman term in the Hamilton operator:

$$\mathcal{H} \rightarrow \mathcal{H} - \frac{B}{2} \sum_{i\sigma} \sigma \, n_{i\sigma} \quad , \tag{7.10}$$

where B is the magnetic field strength. This Zeeman term can be directly included into the effective Hamiltonian of the HFB approximation because it is a one–particle operator. Moreover, the magnetic field can be integrated into a spin–dependent chemical potential via

$$\overline{\mu} \rightarrow \overline{\mu} + \sigma \frac{B}{2} \quad , \tag{7.11}$$

so that the formulas for the Greens functions can easily be generalized. From the normal, now spin–dependent Greens function, the mean magnetization can be calculated. The result is:

$$m = \frac{1}{2L} \sum_k \sum_i \left[\tanh\left(\frac{\beta(E_i + B/2)}{2} \right) - \tanh\left(\frac{\beta(E_i - B/2)}{2} \right) \right] \quad . \tag{7.12}$$

The derivative of equation (7.12) with respect to B yields the Pauli susceptibility. Because the order parameter and the chemical potential depend quadratically on B, which follows from the generalized gap equations including the influence of the magnetic field, the Pauli susceptibility for $B = 0$ is given by

$$\chi = \frac{\beta}{16L} \sum_k \sum_i \operatorname{sech}^2\left(\frac{\beta E_i}{2} \right) \quad , \tag{7.13}$$

where the right hand side has to be evaluated at the selfconsistent solutions for the order parmeter without external field.

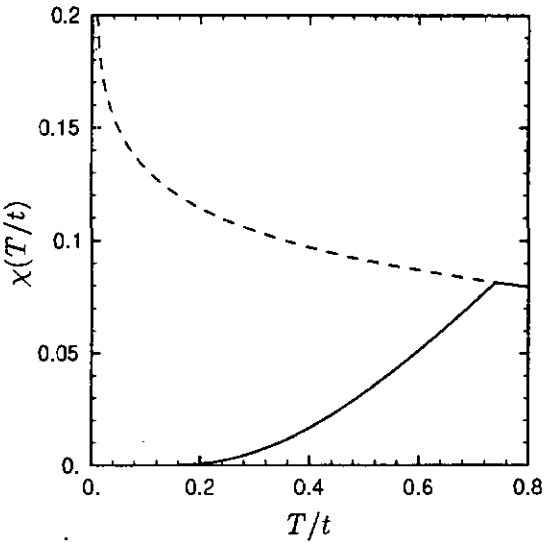

Figure 7.10: Pauli susceptibility as a function of temperature for $W/t = -1$ and $\delta = 0$. The solid line is the HFB solution, while the susceptibility for free electrons is given by the dashed line. The antiferromagnetic transition leads to a cusp and an exponential decay below the Néel temperature.

For the undoped system the Pauli susceptibility is shown in figure 7.10 for $W/t = -1$. Furthermore the susceptibility for free electrons is plotted for comparison (dashed line). The onset of antiferromagnetic long range order leads to a cusp at the Néel temperature. The exponential decay below the Néel temperature arises from the opening of the antiferromagnetic gap shown in the density of states in figure 7.2. A similar behavior has been observed in the antiferromagnetically ordered undoped high temperature superconductors (see e. g. [Erice89] and articles therein).

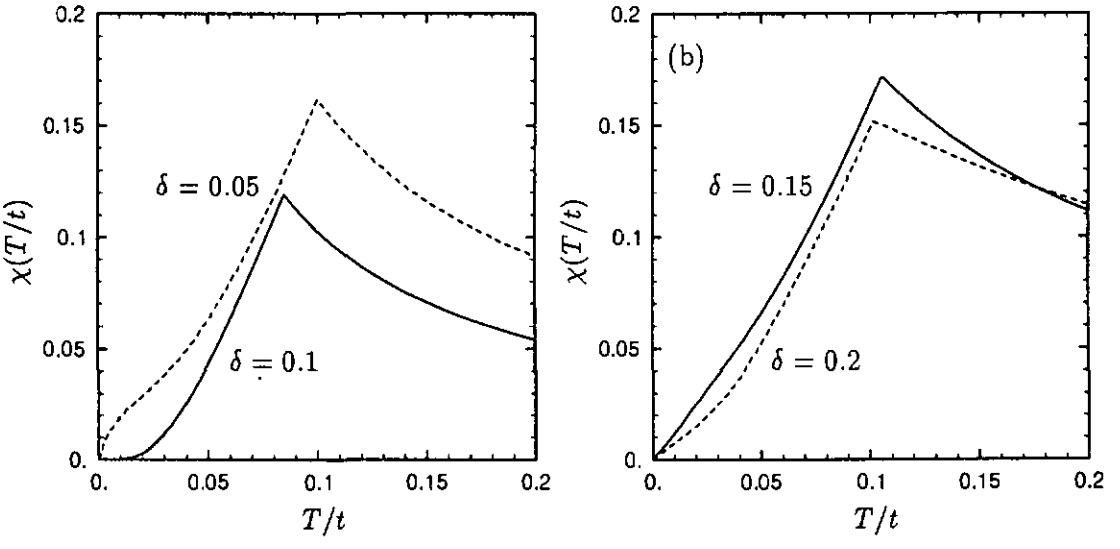

Figure 7.11: Pauli susceptibility for $W/t = -1$ as a function of temperature for $\delta = 0.05$ (solid line), 0.1 (dashed line) in (a) and for $\delta = 0.15$ (solid line), 0.2 (dashed line) in (b).

In figure 7.11 (a) the Pauli susceptibility is plotted as a function of temperature for $W/t = -1$ for $\delta = 0.05$ (solid line) and $\delta = 0.1$ (dashed line). In figure 7.11 (b) it is shown for optimal doping, i. e. $\delta = 0.15$ (solid line) and for $\delta = 0.2$ (dashed line), which lies

in the overdoped regime. At the superconducting transition temperature a cusp occurs which is maximal for optimal doping. In fact, the value of the Pauli susceptibility at the transition temperature seems to be related to the critical temperature. It increases with increasing critical temperature in the underdoped regime, reaches a maximum for optimal doping and drops with decreasing transition temperature in the overdoped regime. This behavior is in sharp contrast to the predictions of the BCS theory. Here the normal state is described by the free electron gas and the susceptibility above T_c is given by the dashed line in figure 7.10. From this figure follows a monotonic decrease of the Pauli susceptibility at T_c with increasing transition temperature. Because the only difference between the BCS and the HFB approximation used for the NNSP model is the inclusion of an antiferromagnetic variational paramter, the behavior of the Pauli susceptibility at the superconducting critical temperature has to be attributed to the existence of antiferromagnetic domains in the normal state above T_c. The same mechanism which controls the critical temperature as a function of doping is also responsible for this unusual behavior of $\chi(T_c/t)$. In the underdoped regime the decreasing antiferromagnetic fraction leads to an increase of $\chi(T_c/t)$, while in the overdoped regime the decrease of the number of electrons causes the drop of $\chi(T_c/t)$ as a function of doping.

In the low temperature regime the Pauli susceptibility reflects the groundstate density of states shown in figure 7.5. As soon as the superconducting energy gap becomes a pseudo gap for $\delta > 0.1$, the low temperature behavior changes from exponential to linear. Moreover, a reflection point is possible as is shown in figure 7.11 (a) for $\delta = 0.1$. Below the critical temperature the Pauli susceptibility drops to zero due to singlet pairing.

Chapter 8

Summary and Outlook

8.1 What has been done?

High temperature superconductors share several common properties. The most important ones are extreme anisotropic structure due to CuO_2 layers, antiferromagnetic long range order in the undoped case, doping–dependent singlet superconductivity and unusual normal state behavior due to antiferromagnetic fluctuations above the superconducting critical temperature, to name only a few of them. These features led to the introduction of the NNSP model which can be summarized as follows:

- The layered structure is modelled by a two–dimensional system.
- Due to the strong hybridization of the copper $d_{x^2-y^2}$ and the oxygen $2p\sigma$ orbitals, a single band description on a square lattice is introduced where each node corresponds to one unit cell of the CuO_2–planes.
- A nearest–neighbor hopping tight binding band takes tunneling processes between neighboring sites into account.
- To allow for antiferromagnetic flucutations and singlet superconductivity, an attractive density–density interaction between electrons of opposite spins on neighboring sites is added to the free tight binding Hamiltonian.

Two extreme limits, the free case and the "atomic limit", have been solved exactly. They show two and somehow excluding properties of the NNSP model, namely the metallic behavior in the free case and the occurence of two–dimensional antiferromagnetic long range order for all densities in the atomic limit, due to the Ising type of interaction.

The general case cannot been solved exactly. For this reason we considered the functional integral description of a quantum mechanical system. It provides a very useful formalism to study phase transitions in quantum mechanical systems from a microscopic point of view. Starting from a generic quadratic representation for the interaction Hamiltonian, the functional integral representation for the partition function has been derived. The results are independent on the NNSP model and can be used for a large variety of models. Moreover, we have generalized the functional integral formalism to competing order parameters. In fact, for the NNSP model a free energy functional has been explicitely derived including charge density, spin density and pairing field variables.

The functional integral representation leads to an exact expression for the partition function. It serves as a good starting point for approximations. Chapter 3 is attributed to this problem. Step by step, additional restrictions and assumptions have been introduced. The time–independent field approximation, saddle point approximations for time–dependent and time–independent fields and finally the mean field approximation for uniform fields have been discussed. General selfconsistent equations have been derived for time– and momentum–dependent fields. The nonlinear character and the fact that they are coupled equations reflect the competition between different types of fields. For a pairing model where only the pairing representation has been used to define the functional integral, these equations are the generalized gap equations, including time and momentum–dependent effects. They can be used, for instance, to study the role of the center of mass momentum of Cooper pairs or the influence of quantum mechanical fluctuations on the solutions of the gap equation. Within the time–independent saddle point approximation, we have shown that for hermitian field operators and positive effective coupling constants, only the trivial solutions for the corresponding fields exist. This shows, for instance, the absence of superconductivity for positive coupling constants in the pairing model mentioned above. For all other fields it has been proven that the selfconsistent solution for a field is given by the mean value of the corresponding field operator. If the field operator describes any long range order, a nontrivial solution therefore signals a phase transition. Finally the symmetry broken Hartree Fock Bogoliubov approximation has been derived from a variational principle. It is related to the time–independent saddle point approximation. In fact, we have shown that, if only one quadratic representation is used in the functional integral formulation, both approximations are identical. However, if the competition between different types of order is taken into account by the inclusion of more than one quadratic representation, they differ from each other. As the derivation of the functional integral representation, the approximations have been derived on the basis of the general quadratic form for the interaction Hamiltonian. For this reason they can be applied to a large class of models for correlated electron systems.

The symmetry–broken Hartree Fock Bogoliubov approximation has been used to study the NNSP model for the following reasons:

- it is a variational approximation and therefore leads to the best of its type,
- it is a thermodynamic selfconsistent approximation,
- it allows for phase transitions by the introduction of symmetry breaking fields,
- it can be used to describe the competition between different types of order, and
- it can be solved in the thermodynamic limit.

The minimum set of variational parameters which have been included into the trial Hamiltonian of the symmetry broken Hartree Fock Bogoliubov approximation is a real antiferromagnetic and a set of complex pairing parameters, which describe superconductivity with different internal symmetry. It has been shown that in two dimensions only d–, xs– or mixed $xs + id$–wave with a relative phase of $\pi/2$ are possible. The selfconsistent equations for the antiferromagnetic and superconducting parameters have been derived using a Greens function method, and a numerical technique has been applied to find the solution which minimizes the free energy functional. The main results can be summarized as follows:

- For half–filling the system orders antiferromagnetically and shows no superconductivity for all coupling constants, which is a consequence of the competition between antiferromagnetism and superconductivity. A large antiferromagnetic gap opens below the Néel temperature, so that the system becomes insulating for $T/t = 0$.
- Away from half–filling, superconductivity appears for all coupling constants and densities. The symmetry of the order parameter depends on filling, coupling strength and temperature. In the weak coupling regime only pure d– and pure xs–wave superconductivity exists, while in the strong coupling regime the symmetry of the superconducting order parameter is predominantly mixed $xs+id$–wave. The occurence of d–wave supeconductivity is strongly correlated to antiferromagnetic fluctuations, while xs–wave superconductivity occurs mainly in metallic regions.
- The selfconsistent solution of the chemical potential as a function of filling indicates a phase separation of antiferromagnetic domains and metallic droplets above T_c and superconducting electron pairs below the superconducting critical temperature. The boundary of the phase separated region has been calculated using a Maxwell construction.

- It has been shown that the HFB approximation describes the antiferromagnetic phase very well for all coupling constants and temperatures. The superconducting groundstate is well described for all coupling constants and in the weak coupling regime also for finite temperatures. However, the HFB approximation fails for the superconducting critical temperature in the strong coupling regime. We have argued that this fact is due to the static character of the pairing parameters which do not take the mobility of the charge carriers into account.

- The BCS approximation, which results from the HFB approximation if the antiferromagnetic component is neglected, is only correct in the extreme weak coupling regime and for small electron ($n \ll 1$) or hole ($n \gg 1$) concentrations. It totally fails for half–filling. Moreover, the comparison of both approximations clearly show the competition between antiferromagnetism and superconductivity included in the HFB approximation.

Because the HFB approximation describes the antiferromagnetic phase transition very well, the Néel temperature for half–filling has been used to estimate the coupling strength for a quantitative comparison of predictions of the NNSP model with properties of high temperature superconductors. For $t \approx 0.1$ eV, a coupling strength of about $W/t = -1$ and with $\delta = |n - 1|$, some remarkable agreement has been revealed. In fact, for these parameters the NNSP model predicts the following features:

- For half–filling ($\delta = 0$) the system is an insulating antiferromagnet. The Néel temperature is about 700 K for $t = 0.1$ eV.

- Due to the phase separation, strong antiferromagnetic fluctuations exist above and even below the critical temperature in the relevant doping regime. They decrease with an increasing number of holes.

- Superconductivity occurs for $\delta > 0$.

- For $\delta = 0.16$ the system is optimally doped with a maximum transition temperature of about 100 K for $t = 0.1$ eV.

- The superconducting critical temperature increases in the underdoped regime and decreases in the overdoped regime. For $\delta > 0.3$ it drops to zero Kelvin.

- The superconducting order parameter has d–wave symmetry in the relevant doping regime. Only for $\delta > 0.5$ conventional superconductivity occurs with xs–wave symmetry.

Implications on the normal state behavior above T_c, such as the density of states, the specific heat and the Pauli susceptibility have been discussed. We have shown that the normal state behavior emerges from semiconducting to anomalous and finally to usual Fermi liquid behavior as doping is increased, and that the shape of the superconducting gap and the low temperature behavior of the specific heat and the Pauli susceptibillity is related to this. In fact, in the underdoped regime for $\delta < 0.1$, semiconducting properties occur in the normal state and the groundstate density of states shows a real gap, although the symmetry of the superconducting order parameter is d–wave. Accordingly the specific heat and the Pauli susceptibility behave exponentially in the low temperature regime. This behavior is due to the strong influence of antiferromagnetic fluctuations and the fact that the chemical potential lies within the spin gap above T_c. As doping is increased, the chemical potential just above the superconducting critical temperature moves into the upper band and the antiferromagnetic fluctuations decrease. For this reason the normal state behavior changes from anomalous Fermi liquid behavior with a linear temperature dependence of the resistivity for hole concentrations around optimal doping to more or less usual Fermi liquid behavior with a quadratic temperature dependence of the resistivity in the overdoped regime. The superconducting energy gap becomes a pseudo gap and exhibits a V–shaped form, as it is expected for a d–wave superconductor and the low temperature behavior of the specific heat devided by T, and the Pauli susceptibility becomes linear in T. We have calculated the ratio of the maximum energy gap in the density of states to the transition temperature. This ratio is doping dependent and shows a mean value of about 4.5 in agreement with tunneling experiments on YBaCu [Geerk89, Valles91]. Although the HFB approximation of the NNSP model leads to surprisingly good results, there are still many open questions. Some of them are briefly discussed in the following sections.

8.2 Further Research

8.2.1 Phase Separation

In our treatment the phase separation has not been treated selfconsistently. In fact, a reintroduction of the pinned value for the chemical potential obtained by the Maxwell construction will lead to a wrong value for the particle number density. For this reason a first step towards a better description of the NNSP model is to use a method where the phase separation can be treated selfconsistently. Such a method requires the introduction of spatial fluctuations, for a phase separation cannot be longer described by a uniform antiferromagnetic internal field. For this purpose, the generalized selfconsistent equations of the time–independent saddle point approximation including momentum–dependent effects may be used.

8.2.2 Additional Parameters

Repulsive U

For high temperature superconductors it has been argued that a strong on-site repulsion on the in-plane copper ions is present[Emery87, Anderson87]. For this reason it should be interesting to study the influence of an on-site repulsion term on the phase diagrams of the NNSP model. In fact, in a first try it can be directly introduced into the HFB approximation if the coupling constant in front of the antiferromagnetic variational parameter is replaced by $Wz - U$. Because U does not enter into the pairing terms, the on-site repulsion favors the antiferromagnetic component, which will lead to a higher Néel temperature and antiferromagnetic order parameter. In a more sophisticated approach, also the ferro- and paramagnetic features of the repulsive Hubbard model should be taken into account [Hirsch85c].

η-Pairing

The basic principle of the HFB approximation is the concept of spontaneous symmetry breaking [Ring80, Bormann91b]. Within the HFB approximation for the NNSP model the translational symmetry with respect to the antiferromagnetic reciprocal lattice vector and a $U(1)$ gauge symmetry mediated by the particle number operator might be violated. In fact, a finite value for the antiferromagnetic order parameter breaks the translational symmetry, while the occurence of superconductivity is accompanied by a violation of the $U(1)$ gauge symmetry. From this point of view, the occurence of η-pairing [Yang89, Tian94] should be discussed as well. This is related to a spatially varying superconducting order parameter

$$\Delta_Q^*(k) \sim \left\langle c_{k\sigma}^\dagger c_{-(k+Q)-\sigma}^\dagger \right\rangle \quad , \tag{8.1}$$

and breaks both the translational and the gauge symmetry. Within this work, a finite value of the anomalous Greens function $\mathrm{F}_{Q\sigma}^\dagger$ signals the occurence of η-pairing, which occurs in the coexistence regime of antiferromagnetism and superconductivity. However, the η-pairing parameter has not been considered selfconsistenly. In this case variational parameters which couple onto the pairing operators $c_{k\sigma}^\dagger c_{-(k+Q)-\sigma}^\dagger$ and their complex conjugates have to be included into the trial Hamiltonian. For this reason the diagonalization of the trial Hamiltonian becomes much more complicated. Nevertheless, the implications of η-pairing parameters should be discussed in the future, because this might lead to a better understanding of the possible coexistence of antiferromagnetism and superconductivity.

Next Nearest Neighbor Hopping

From photoemmision experiments [Minami89, Takahashi89, Olsen89] and band calculations [Mattheiss87, Pickett88, Yu91], it follows that a tight binding band including both nearest and next nearest neighbor hopping is more suitable to describe the copper oxide superconductors. Because the formulae derived in chapters 5 and 6 for the Greens functions and selfconsistent equations can be easily generalized, the introduction of a nearest neighbor hopping term might be a good starting point for further development. As already shown in the introductory chapter, the additional next nearest neighbor hopping term destroys the particle–hole symmetry, so that hole–doped and electron–doped systems differ from each other. This will be mirrored in doping–dependent phase diagrams which become asymmetric with respect to half–filling or in the density of states. For instance, the maximum of the Néel temperature no longer appears for $n = 1$ and the identification $\delta = |n-1|$ must be replaced by $\delta = 1-n$ for hole doped ($n < 1$) and by $\delta = n-1$ for electron doped ($n > 1$) systems. For the BCS approximation, the implications of next nearest neighbor hopping on the phase boundaries of the components of the superconducting order parameter has been discussed by Micnas et al. [Micnas90]. Because in their treatment the competition between antiferromagnetism and superconductivity has not been taken into account, it seems worthwhile to generalize the HFB approximation including next nearest neighbor hopping effects.

8.2.3 Dynamic Criterion for Superconductivity

We have shown that the HFB approximation does not properly describe the superconducting phase transition in the strong coupling regime. We have argued, however, that the incorrect prediction of the superconducting critical temperature is due to the static nature of the pairing order parameter and that the mobility of the charge carriers has to be taken into account in the strong coupling regime. The criterion for superconductivity introduced by Scalapino et al. [Scalapino92, Scalapino93] might overcome this problem, for it describes the phase transition into the superconducting state by the London penetration depth, which is a dynamic quantity related to the superfluid density devided by the effective mass of the electron pairs. This might be successfully applied to the HFB approximation of the NNSP model.

8.2.4 Fluctuations

Although the HFB approximation yields acceptable predictions for both the antiferromagnetic and the superconducting component in the case of $W/t = -1$, which lies in

the weak coupling regime, fluctuations have to be introduced to improve our results, in particular in two dimensions, where fluctuations destroy any long range order in quantum mechanical systems. Moreover, it has been shown that fluctuations play an important role in high temperature superconductors [Schneider92a, Schneider92b, Ghiron93]. As mentioned above, a better description of the phase separation requires the introduction of spatial fluctuations, as well. In our belief, fluctuations which arise from spatially varying internal fields are the most important ones. They could be studied if the more general approximations of chapter 3 are used, or on the basis of a Ginzburg–Landau functional [Ginzburg65, Binney92, Amit84, Annett90a] which can be derived from the functional integral representation or directly from the HFB free energy functional for time–independent fields. Furthermore, a spin wave approximation for the antiferromagnetic component seems to be worthwhile for consideration because it describes the effect of collective modes on the HFB solution and therefore includes a spatially fluctuating antiferromagnetic component. A T–matrix approximation, as it has been used to study the attractive Hubbard model in the intermediate coupling regime [Fresard92, Rodriguez94], or a random phase approximation as it has been used to study the extended Hubbad model in the strong coupling regime [Robaszkiewicz81c, Robaszkiewicz81d, Micnas90] includes higher order correlation functions and might therefore lead to a better description of the NNSP model. It should be emphasized that in all these approximations both, antiferromagnetic and anomalous pairing correlation functions need to be incorporated. For this reason a thermodynamic selfconsistent treatment is very difficult to handle and requires some tremendous numerical effort.

8.2.5 The Problem of Two Dimensions

The quasi–two–dimensional character of copper oxide superconductors has been modeled by an exact two–dimensional system. This is a dangerous assumption because in a quantum mechanical system of two dimensions fluctuations destroy any long range order [Hohenberg67, Binney92]. Within the HFB approximation, which is a mean field type of approximation, these fluctuations are suppressed and long range order might appear. For this reason the NNSP model should be solved in three dimensions, taking the anisotropic structure of the high temperature superconductors explicitely into account by the introduction of at least an anisotropic hopping term [Frick90]. The interaction term includes an Ising spin–spin interaction and must not necessarily be replaced by its anisotropic three dimensional form. However, the predictions of the HFB approximation for an extreme anisotropic three–dimensional system differ only slightly from the predictions for the exact two–dimensional system [Micnas90]. Our results have to be interpreted within this framework.

8.3 Resume

In this project the essential features of the phase diagram of high temperature superconductors have been derived for the first time from a semi–microscopical point of view in a selfconsistent treatment. Both, the antiferromagnetic properties including quasi–two–dimensional antiferromagnetic long range order in the undoped case, and strong antiferromagnetic fluctuations above and even below the superconducting critical temperature due to the occurence of electronic phase separation and the superconducting properties, like the doping dependence of the critical temperature or the d–wave symmetry of the order parameter, have been revealed and explained. Because the singlet pairing interaction is somehow unphysical, the reason being the violation of the rotational spin symmetry, we can conclude that the extended Hubbard model including a next nearest neighbor singlet pairing interaction is as important for high temperature superconductors as the Ising model is for magnetic systems.

Bibliography

[Abrikosov93] A. A. Abrikosov, J. C. Campuzano, K. Gofron
Physica C, **214**, 73 (1993)

[Aebi94] P. Aebi, et al.
Phys. Rev. Lett, **72**, 2757 (1994)

[Aharony89] A. Aharony, R. J. Birgenau, M. A. Kastner
IBM J. Res. Develop., **33**, 287 (1989)

[Alloul90] H. Alloul, T. Ohno, D. Mendels
Phys. Rev. Lett., **63**, 1700 (1990)

[Amit84] D. J. Amit
Field Theory, the Renormalization Group, and Critical Phenomena
World Scientific, Singapore (1984)

[Anderson87] P. W. Anderson
Science, **235**, 1196 (1987)

[Anderson93] P. W. Anderson
J. Phys. Chem. Solids, **54**, 1457 (1993)

[Annett90a] J. F. Annett
Adv. Phys., **39**, 83 (1990)

[Annett90b] J. F. Annett
Adv. Phys., **39**, 83 (1990)

[Ashcroft76] N. W. Ashcroft, N. D. Mermin
Solid State Physics
CBS Publishing Asia LTD, Hong Kong (1976)

[BCS57] J. Bardeen, L. N. Cooper, J. R. Schrieffer
Phys. Rev., **108**, 1175 (1957)

[Batlogg89] B. Batlogg in
High Temperature Superconductivity. The Los Alamos Symposium — 1989
K. Bedall, D. Coffey, D. Meltzer, D. Pines and J. R. Schrieffer (eds.)
Addison Wesley Publishing Company, Redwood City, California (1989)

[Bednorz86] J. G. Bednorz, K. A. Muller
Z. Phys. B – Condensed Matter, **64**, 189 (1986)

[Bianconi87] A. Bianconi, A. C. Castellano, M. D. Santis, P. Rudolf, P. Lagarde, A. M. Flank
Solid State Comm., **63**, 1009 (1987)

[Binney92] J. J. Binney, N. J. Dowrick, A. J. Fisher, M. E. J. Newman
The Theory of Critical Phenomena: An Introduction to the Renormalization Group
Clarendon Press, Oxford (1992)

[Birgenau88a] R. J. Birgenau, D. R. Gabbe, H. P. Jenssen, M. A. Kastner, P. J. Picone, T. R. Thurston, G. Shirane, Y. Endoh, M. Sato, K. Yamada, Y. Hidaka, M. Oda, Y. Enomoto, M. Suzuki, T. Murakami
Phys. Rev. B, **38**, 6614 (1988)

[Birgenau88b] R. J. Birgenau, M. A. Kastner, A. Aharony
Z. Phys. B, **71**, 57 (1988)

[Birgenau89a] R. J. Birgenau, G. Shirane in
Physical Properties of High Temperatures Superconductors I
D. M. Ginsberg (ed.), World Scientific, Singapore (1989)

[Birgenau89b] R. J. Birgenau, Y. Endoh, Y. Hidaka, M. A. Kastner, T. Murakami, G. Shirane, T. R. Thurston, K. Yamada
IBM J. Res. Develop., **33**, 270 (1989)

[Bormann91a] D. Bormann, T. Schneider, M. Frick
Europhys. Lett., **14**, 101 (1991)

[Bormann91b] D. Bormann
Dissertation, Heidelberg (1991)

[Brenig83] W. Brenig
Statistische Theorie der Wärme: Gleichgewicht
Springer–Verlag, Berlin, Heidelberg, New York (1993)

[Chaikin75] P. M. Chaikin, P. Pincus, G. Beni
Phys. Rev. C, **8**, L65 (1975)

[Chaudhari94] P. Chaudhari, S. Lin
Phys. Rev. Lett., **72**, 1084 (1994)

[Chen94] J. Chen, e. al.
Phys. Rev. B, **49**, 3683 (1994)

[Coffey93] D. Coffey, L. Coffey
Phys. Rev. Lett., **70**, 1529 (1993)

[Cox88] D. E. Cox, C. C. Toradi, M. E. Subramanian, J. Gopalakrishman, A. W. Sleight
Phys. Rev. B, **38**, 6624 (1988)

[Dagotto90] E. Dagotto, J. Rierra, A. P. Young
Phys. Rev. B, **42**, 2347 (1990)

[Dagotta94] E. Dagotto
Rev. Mod. Phys., (July 1994)

[Denteneer91] P. J. H. Denteneer, A. Guozhong, J. M. J. v. Leeuwen
Europhys. Lett., **16**, 5 (1991)

[Denteneer93] P. J. H. Denteneer, A. Guozhong, J. M. J. v. Leeuwen
Phys. Rev. B, **47**, 6256 (1993)

[Dessau93] D. S. Dessau, e. al.
Phys. Rev. Lett., **71**, 2781 (1993)

[Dynes94] R. C. Dynes
Solid State Comm., **92**, 53 (1994)

[Eliashberg60] G. M. Eliashberg
Sov. Phys. JETP, **11**, 696 (1960)

[Emery87] V. J. Emery
Phys. Rev. Lett., **58**, 2794 (1987)

[Erice89] *Earlier and Recent Aspects of Superconductivity*,
Erice, Italy, 1989
J. G. Bednorz and K. A. Muller (eds.)
Springer–Verlag, Heidelberg (1990)

[Feynman65] R. P. Feynman, A. R. Hibbs
Quantum Mechanics and Path Integrals
McGraw-Hill, New York (1965)

[Fisher89] R. A. Fisher, S. Kim, B. F. Woodfield, N. E. Phillips, L. Taillefer, K. Hasselbach, J. Floquet, A. L. Giorgi, J. L. Smith
Phys. Rev. Lett., **62**, 1411 (1989)

[Fresard92] R. Fresard, B. Glaser, P. Wölfle
J. Phys Condens. Matt., **4**, 8565 (1992)

[Frick90] M. Frick, T. Schneider
Z. Phys. B - Condensed Matter, **81**, 337 (1990)

[Geerk89] J. Geerk, G. Linker, O. Meyer, Q. Li, R. V. Wang, X. X. Xi
Physica C, **162**, 837 (1989)

[Ghiron93] K. Ghiron, M. B. Salamon, M. A. Hubbard
Phys. Rev. B, **48**, 16188 (1993)

[GinsbergI] *Physical Properties of High Termperature Superconductors I*
D. M. Ginsberg (ed.), World Scientific, Singapore (1989)

[GinsbergII] *Physical Properties of High Termperature Superconductors II*
D. M. Ginsberg (ed.), World Scientific, Singapore (1990)

[GinsbergIII] *Physical Properties of High Termperature Superconductors III*
D. M. Ginsberg (ed.), World Scientific, Singapore (1992)

[Ginzburg65] V. L. Ginzburg
JETP, **20**, 1549 (1965)

[Gofron93] K. Gofron
J. Phys. Chem. Solids, **54**, 1193 (1993)

[Goltsev94] A. V. Goltsev
J. Phys. Condens. Matt., **6**, 1749 (1994)

[Gorbatsevich94] A. A. Gorbatsevich, Y. V. Kopaev, I. V. Tokatly
Physica C, **223**, 95 (1994)

[Hirsch85c] J. E. Hirsch
Phys. Rev. B, **31**, 4403 (1985)

[Hohenberg67] P. C. Hohenberg
Phys. Rev., **158**, 383 (1967)

[Hubbard59] J. Hubbard
Phys. Rev. Lett., **3**, 77 (1959)

[HubbardI] J. Hubbard
Proc. Roy. Soc., **A276**, 238 (1963)

[HubbardII] J. Hubbard
Proc. Roy. Soc., **A277**, 237 (1964)

[HubbardIII] J. Hubbard
Proc. Roy. Soc., **A281**, 401 (1964)

[Jorgensen87] J. D. Jorgensen, H. B. Schlütter, D. G. Hinks, D. W. C. II, K. Zhang, M. B. Brodsky, D. J. Scalapino
Phys. Rev. Lett., **58**, 1024 (1987)

[Jorgensen90] J. D. Jorgensen, B. W. Veal, A. P. Paulikas, L. J. Nomicki, G. W. Crabtree, H. Claus, W. K. Kwok
Phys. Rev. B, **41**, 1863 (1990)

[Kaufmann49a] B. Kaufmann
Phys. Rev., **76**, 1232 (1949)

[Kaufmann49b] B. Kaufmann, L. Onsager
Phys. Rev., **76**, 1244 (1949)

[Kitaoka93] Y. Kitaocka, et al.
J. Phys. Chem. Solids, **54**, 1385 (1993)

[Kosterlitz73] J. M. Kosterlitz, D. J. Thouless
J. Phys. C: Solid State Phys., **6**, 1181 (1973)

[Leggett75] A. Leggett
Rev. Mod. Phys., **47**, 331 (1975)

[Levi93] B. G. Levi
Physics Today, 17 (May 1993)

[Li93] Q. P. Li, B. E. C. Koltenbah, R. Joynt
Phys. Rev. B, **48**, 437 (1993)

[Liu92] Z. Liu, S. Manousakis
Phys. Rev. B, **45**, 2425 (1992)

[Mahan90] G. D. Mahan
Many Particle Physics
Plenum Press, New York (1990)

[Mangelschots92a] I. Mangelschots, M. Mali, J. Roos, D. Brinkmann, S. Rusiecki, J. Karpinski, E. Kaldis
Physica C, **194**, 277 (1992)

[Mangelschots92b] I. Mangelschots, M. Mali, J. Roos, R. Stern, M. Bankay, A. Lombardi, D. Brinkmann
IBM Research Report, (1992)

[Marder90] M. Marder, N. Papnicolaou, G. C. Psaltakis
Phys. Rev. B, **41**, 6920 (1990)

[Mathematica] registered trademark of Wolfram Research, Inc.

[Mattheiss87] L. F. Mattheiss
Phys. Rev. Lett., **58**, 1028 (1987)

[Mattis70] D. Mattis, W. Langer
Phys. Rev. Lett., **25**, 379 (1970)

[Meservey69] R. Meservey, B. B. Schwartz in
Superconductivity
R. D. Parks (es.), Marcel Dekker, New York (1969)

[Micnas88a] R. Micnas, J. Ranninger, S. Robszkiewicz
J. Phys. C: Solid State Physics, **21**, L145 (1988)

[Micnas88b] R. Micnas, J. Ranninger, S. Robaszkiewicz, S. Tabor
Phys. Rev. B, **37**, 9410 (1988)

[Micnas89] R. Micnas, J. Ranninger, S. Robaszkiewicz
Phys. Rev. B, **39**, 11653 (1989)

[Micnas90] R. Micnas, J. Ranninger, S. Robaszkiewics
Rev. Mod. Phys., **62**, 113 (1990)

[Minami89] F. Minami, T. Kimura, S. Takekava
Phys. Rev. B, **39**, 4788 (1989)

[Monien90] H. Monien, D. Pines
Phys. Rev. B, **41**, 6297 (1990)

[Monthoux91] P. Monthoux, A. V. Balatsky, D. Pines
Phys. Rev. Lett., **67**, 3448 (1991)

[Monthoux92a] P. Monthoux, A. V. Balatsky, D. Pines
Phys. Rev. B, **46**, 14803 (1992)

[Monthoux92b] P. Monthoux, D. Pines
Phys. Rev. Lett., **69**, 961 (1992)

[Monthoux93] P. Monthoux, D. Pines
Phys. Rev. B, **47**, 6069 (1993)

[Nambu60] Y. Nambu
Phys. Rev., **117**, 648 (1960)

[Negele88] J. W. Negele, H. Orland
Quantum Many–Particle Systems
D. Pines (ed.)
Addison–Wesley Publishing Company, Inc., Redwood City (1988)

[Nolting86] W. Nolting
Quantentheorie des Magnetismus II
Teubner, Stuttgart (1986)

[Nozieres85] P. Nozieres, S. Schmitt–Rink
J. Low Temp. Phys., **59**, 195 (1985)

[Nucker88] N. Nucker, J. Fink, J. C. Fuggle, P. J. Durham, W. M. Temmerman
Phys. Rev. B, **37**, 5158 (1988)

[NumRec] W. H. Press, S. A. Teukolsky, W. T. Vetterling, B. P. Flannery
Numerical Recipes in C
Cambridge University Press, Cambridge (1992)

[Olsen89] C. G. Olsen, R. Lin, A. -. Yang, D. W. Lynch, A. J. Arko, R. S. List, B. W. Veal, C. Y. Chang, P. Z. Jiang, A. B. Pantikas
Science, **245**, 731 (1989)

[Onsager44] L. Onsager
Phys. Rev., **65**, 117 (1944)

[Ott87] H. R. Ott in
Novel Superconductivity
S. A. Wolf and V. Z. Kresin (eds.), Plenum Press, New York (1987)

[Pennington90] C. H. Pennington, C. P. Slichter in
Physical Properties of High Temperature Superconductors II
D. M. Ginsberg (ed.), World Scientific, Singapore (1990)

[Pickett88] W. E. Pickett
Rev. Mod. Phys., **61**, 433 (1988)

[Pines91] D. Pines
Physica C, **185–189**, 120 (1991)

[PS92] *Phase Separtion in Cuprate Superconductors*,
Erice, Italy, 1992
K. A. Muller and G. Benedek (eds.), World Scientific, Singapore (1993)

[PS93] *Phase Separation in Cuprate Superconductors*,
Cottbus, Germany, 1993
E. Sigmund and K. A. Muller (eds.), Springer–Verlag, Heidelberg (1994)

[Reichl80] L. E. Reichl
A Modern Course in Statistical Physics
Edward Arnold LTD, (1980)

[Rice87a] T. M. Rice
Physica Scripta, **T19**, 246 (1987)

[Rice87b] T. M. Rice
Z. Phys. B – Condensed Matter, **67**, 141 (1987)

[Richmond69] P. Richmond
Solid State Comm., **7**, 997 (1969)

[Ring80] P. Ring, P. Schuck
The Nuclear Many Body Problem
Springer–Verlag, Heidelberg (1980)

[Robaszkiewicz81a] S. Robaszkiewicz, R. Micnas, K. A. Chao
Phys. Rev. B, **24**, 4018 (1981)

[Robaszkiewicz81b] S. Robaszkiewicz, R. Micnas, K. A. Chao
Solid State Comm., **40**, 403 (1981)

[Robaszkiewicz81c] S. Robaszkiewicz, R. Micnas, K. A. Chao
Phys. Rev. B, **23**, 1447 (1981)

[Robaszkiewicz81d] S. Robaszkiewicz, R. Micnas, K. A. Chao
Phys. Rev. B, **24**, 1579 (1981)

[Robaszkiewicz82] S. Robaszkiewicz, R. Micnas, K. A. Chao
Phys. Rev. B, **26**, 3915 (1982)

[Rodriguez94] R. Micnas, M. H. Pederson, S. Schafroth, T. Schneider, J. J. Rodriguez–Nunez, H. Beck
to be published in Phys. Rev. B

[Rogovin76] D. Rogovin, M. Scully
Phys. Rep., **25**, 175 (1976)

[Sachdev91] S. Sachdev, Z. Wang
Phys. Rev. B, 10229 (1991)

[Scalapino92] D. J. Scalapino, S. R. White, S. C. Zhang
Phys. Rev. Lett., **68**, 2830 (1992)

[Scalapino93] D. J. Scalapino, S. R. White, S. Zhang
Phys. Rev. B, **47**, 7995 (1993)

[Schneider89] T. Schneider, H. D. Raedt, M. Frick
Z. Phys. B – Condensed Matter, **76**, 3 (1989)

[Schneider90a] T. Schneider, M. P. Sörensen
Z. Phys. B – Condensed Matter, **81**, 3 (1990)

[Schneider90b] T. Schneider, M. Frick in
Earlier and Recent Aspects of Superconductivity
J. G. Bednorz and K. A. Mller (eds.), Springer–Verlag, Heidelberg (1990)

[Schneider92a] T. Schneider, H. Keller
Phys. Rev. Lett., **69**, 3374 (1992)

[Schneider92b] T. Schneider, D. Ariosa
Z. Phys. B – Condensed Matter, (1992)

[Schrieffer94] J. R. Schrieffer
Solid State Comm., **92**, 129 (1994)

[Shafer90] M. W. Shafer, T. Penney
Europ. J. Solid State Chem., **27**, 191 (1990)

[Shen87] Z. -. Shen, J. W. Allen, J. J. Jen, J. -. Kang, W. Ellis, W. Spicer, I. Lindau, M. B. Maple, Y. D. Dalichaouch, M. S. Torikshvili, J. Z. Sun, T. H. Geballe
Phys. Rev. B, **36**, 8414 (1987)

[Shen93] Z. -. X. Shen, et al.
Phys. Rev. Lett., **70**, 1553 (1993)

[Sigrist87] M. Sigrist, T. M. Rice
Z. Phys. B – Condensed Matter, **68**, 9 (1987)

[Sigrist91] M. Sigrist, K. Ueda
Rev. Mod. Phys., **63**, 239 (1991)

[Slichter93] C. P. Slichter
J. Phys. Chem. Solids, **54**, 1439 (1993)

[Steglich85] F. Steglich in
Theory of Heavy Fermions and Valence Fluctuations
K. Kasuya and T. Saso (eds.), Springer, New York (1985)

[Steglich93] F. Steglich
Phys. Bl., **49**, 395 (1993)

[Stewart84] G. R. Stewart
Rev. Mod. Phys., **56**, 755 (1984)

[Stratonovich57] R. L. Stratonovich
Dokl. Akad. Nauk. S.S.S.R., **115**, 1907 (1957)

[Stratonovich58] R. L. Stratonovich
Sov. Phys. Dokl., **2**, 416 (1958)

[Sun94] A. G. Sun, et al.
Phys. Rev. Lett., **72**, 2267 (1994)

[Takahashi89] T. Takahashi in
Strong correlations and superconductivity
H. Fukuyama, S. Maekawa and A. B. Malozemoff (eds.)
Springer, Heidelberg (1989)

[Takigawa89] M. Takigawa, P. C. Hammel, R. H. Heffner, Z. Fisk
Phys. Rev. B, **39**, 7371 (1989)

[Tanner94] A. Tanner
private communication (1994)

[Teubel90] A. Teubel, E. Kolley, W. Kolley
Phys. Stat. Sol. B, **157**, 389 (1990)

[Thelen93] D. Thelen, D. Pines, J. P. Lu
Phys. Rev. B, **47**, 9151 (1993)

[Tian94] G. -. Tian
Solid State Comm., **90**, 837 (1994)

[Tokura89] Y. Tokura, H. Takagi, S. Uchida
Nature, **337**, 345 (1989)

[Torrence88] J. B. Torrence, T. Yokura, A. I. Nazzal, A. Brezinge, T. C. Huang, S. S. Parkin
Phys. Rev. Lett., **61**, 1127 (1988)

[Torrence89] J. B. Torrence, A. Bezinge, A. I. Nazzal, T. C. Huang, S. S. P. Parkin, D. T. Keane, S. J. LaPlace, P. M. Horn, G. A. Held
Phys. Rev. B, **40**, 8872 (1989)

[Tralshawala91] N. Tralshawal et al.
Phys. Rev. B, **44**, 12102 (1991)

[Trotter59] H. F. Trotter
Proc. Am. Math. Soc., **10**, 545 (1959)

[Uemura87] Y. J. Uemura, W. J. Kossler, X. H. Yu, J. R. Kempton, H. E. Schone, D. Opie, C. E. Stronach, D. C. Johnston, M. S. Alvarez, D. P. Goshorn
Phys. Rev. Lett., **59**, 1045 (1987)

[Uemura88] Y. J. Uemure
Phys. Rev. B, **38**, 909 (1988)

[Valles91] J. M. Valles, et al.
Phys. Rev. B, **44**, 11986 (1991)

[Vollhardt90] D. Vollhardt, P. Wolfle
The Superfluid Phases in Helium 3
Taylor and Francis, London (1990)

[Wenger93] F. Wenger, S. Astlund
Phys. Rev. B, **47**, 5977 (1993)

[Wollman93] D. A. Wollman et al.
Phys. Rev. Lett., **71**, 2134 (1993)

[Yang62] C. N. Yang
Rev. Mod. Phys., **34**, 694 (1962)

[Yang89] C. N. Yang
Phys. Rev. Lett., **63**, 2144 (1989)

[YokoyaPP] Yokoya
preprint (1994)

[Yu91] J. Yu, A. J. Freeman
Phys. Chem. Solids, **52**, 1351 (1991)

[Zhou92] C. Zhou, H. J. Schulz
Phys. Rev. B, **45**, 7397 (1992)

The project presented here would neither have been started nor completed without the constant support and encouragement of numerous people.

Thanks is due first and foremost to my long–time advisor, Prof. Dr. H. Beck and to Prof. Dr. T. Schneider, whose patience, goodwill and perpetual support I have certainly tried over time. His inspiration, guidance and critique throughout the research and writing of the dissertation was invaluable. Also thanks to Prof. Dr. F. Wegner and Prof. Dr. P. F. Meier, who supported me in the first two years.

I am deeply indebted to my wife Beate for her (often long–distance) support and sacrifice. None of this would have occurred without her love, kindness and understanding patience. She has made this endeavor more meaningful.

Without the friendship of people from outside academia, as well as the support and encouragement of my parents and family over the past five years, this project would have never gotten out of its infancy.

Thanks for financial support go to the Swiss National Science Foundation, the German "Sonderforschungsbereich 123" and the IBM Research Laboratory in Rüschlikon, which provided the necessary work environment.

Several researchers have greatly contributed to the successful completion of this project: Drs. Dierk Bormann, Axel Tanner, Stefan Schafroth, Morten Pederson, J. J. Rodriguez–Nûnez, Robert Schulz, Christophe Rossel Jean–Pierre Locquet and his wife Iris Mangelschots for always being available for fruitful discussions.

Last but not least thanks to Dr. Andreas Lang, who spent several days in reading and bug–fixing of this dissertation.

Curriculum Vitae

zur Person

Name	Thomas Meintrup
Geburtsdatum	11.02.1964
Geburtsort	Stuttgart, Deutschland

schulischer Werdegang

1970–1973	Heiligenbergschule, Heidelberg–Handschuhsheim.
1973–1974	Grundschule in Massenbach.
1974–1980	Elly–Heuss–Knapp–Gymnasium, Heilbronn.
1980–1983	Technisches Gymnasium der Wilhelm–Maybach–Schule, Heilbronn.
Abschluß	Abitur im Mai 1983. Notendurchschnitt: 1,5.

Wehrdienst

Juli 1983 – Sept. 1984	Wehrdienst als Panzerjäger in Kühlsheim.

Studium

Okt. 1984 – Sept. 1990	Studium der Physik und Mathematik an der Ruprecht–Karls–Universität Heidelberg.
Schwerpunkte	Statistische Physik, Physik der kondensierten Materie, Computerunterstütze Physik, reine und angewandte Mathematik.
Diplomarbeit	bei Prof. Dr. K. H. Hoffmann am Institut für Theoretische Physik der Universität Heidelberg.
Thema der Diplomarbeit:	Lineare Antworttheorie für die Diffusion auf Hierarchien.
Abschluß	am 25. September 1990 als Diplomphysiker. Gesamturteil: sehr gut.

Promotion

Jan. 1991 – Feb. 1992	Wissenschaftlicher Angestellter der Universtät Heidelberg am Institut für Theoretische Physik, Doktorand von Prof. Dr. F. Wegner.
seit Feb. 1992	Wissenschaftlicher Mitarbeiter des IBM–Forschungslaboratoriums in Rüschlikon unter der Leitung von Prof. Dr. T. Schneider.
Feb. 1992 – Aug. 1992	Doktorand von Prof. Dr. P. F. Meier, Universität Zürich.
Aug. 1992 – Okt. 1994	Doktorand von Prof. Dr. H. Beck, Universität Neuchâtel.

beruflicher Werdegang

seit Nov. 1994	Mitarbeiter der IBM Informationssysteme GmbH, Wissenschaftszentrum Heidelberg, in der Gruppe von Prof. Dr. G. Dueck (Optimierung und Statistik)